

[Home](#) [Transactions on Electrical and Electronic Materials](#) [Article](#)

Jacobian Based Nonlinear Algorithms for Prediction of Optimized RF MEMS Switch Dimensions

Regular Paper Published: 03 August 2023 24, 447–458 (2023)



Transactions on Electrical and
Electronic Materials

[Aims and scope](#)[Submit manuscript](#)

[Lakshmi Narayana Thalluri](#) , [M. Aravind Kumar](#), [Mohamed Sultan Mohamed Ali](#), [N. Britto Martin Paul](#), [K. Srinivasa Rao](#), [Koushik Guha](#) & [S. S. Kiran](#)

 55 Accesses [Explore all metrics](#) →

[Cite this article](#)

Abstract

This communication discusses the role of nonlinear algorithms in training the neural network, which predicts the optimized RF MEMS switch dimensions. A dedicated dataset, i.e., *DrTLN-RF-MEMS-SWITCH-DATASET-v1*, was created by considering the most appropriate input and output variable suitable to predict the cantilever dimensions, crab leg and serpentine structure-based RF MEMS switches. The distinct artificial neural networks (ANN) performance is analysed using various training methods. The hardware implementation possible neural network algorithms, i.e., Fitting and Cascade Feed

Forward Network, are considered for learning and prediction. The ANN algorithm's performance in predicting and optimizing RF MEMS switch is analysed using nonlinear training methods like Levenberg–Marquardt (LM) and Scaled Conjugate Gradient (SCG). The cascaded forward network with LM training combination offers the best performance compared with other varieties. A comprehensive study is performed using neural networks and finite element simulation results. The study revealed that the error percentage is below 15.08% for most of the parameters.

 This is a preview of subscription content, [log in via an institution](#)  to check access.

Access this article

[Log in via an institution](#)

Buy article PDF 39,95 €

Price includes VAT (India)

Instant access to the full article PDF.

Rent this article via [DeepDyve](#) 

[Institutional subscriptions](#) →

References

1. R. Chaudhary, P.R. Mudimela, Pull-in response and eigen frequency analysis of graphene oxide-based NEMS switch. Mater. Today Proc. (2020).
<https://doi.org/10.1016/j.matpr.2020.01.560>

[Article](#) [Google Scholar](#)

2. Y. Naito, K. Nakamura, K. Uenishi, Laterally movable triple electrodes actuator toward low voltage and fast response RF-MEMS switches. *Sensors* (2019).
<https://doi.org/10.3390/s19040864>
[Article](#) [Google Scholar](#)
3. Z. Yan-qing, L. Han, M. Qin, Q.-a Huang, Novel DC-40 GHz MEMS series-shunt witch for high isolation and high power applications. *Sens. Actuators A* (2014).
<https://doi.org/10.1016/j.sna.2014.04.024>
[Article](#) [Google Scholar](#)
4. S. Heydari, K. Pedram, Z. Ahmed, F.B. Zarrabi, Dual band monopole antenna based on metamaterial structure with narrowband and UWB resonances with reconfigurable quality. *Int. J. Electron. Commun.* (2017). <https://doi.org/10.1016/j.aeue.2017.07.015>
[Article](#) [Google Scholar](#)
5. H. Mohammed, H. Mohamed, Performance comparison of feed-forward neural networks trained with different learning algorithms for recommender systems. *Computation* (2017). <https://doi.org/10.3390/computation5030040>
[Article](#) [Google Scholar](#)
6. M. Adrian, C. Angel, A. Răzvan, Learning in feedforward neural networks accelerated by transfer entropy. *Entropy* (2020). <https://doi.org/10.3390/e22010102>
[Article](#) [Google Scholar](#)
7. D.C. Sérgio, T. Slavisa, B. Marko, A feed-forward neural network approach for energy-based acoustic source localization. *J. Sens. Actuator Netw.* (2019).
<https://doi.org/10.3390/jsan10020029>
[Article](#) [Google Scholar](#)

8. R.R. Benoit, R.Q. Rudy, J.S. Pulskamp, R.G. Polcawich, Piezoelectric RF MEMS switches on Si-on-Sapphire substrates. *J. Microelectromech. Syst.* (2020).
<https://doi.org/10.1109/JMEMS.2020.3008201>
[Article](#) [Google Scholar](#)

9. J. Iannacci, RF–MEMS for high–performance and widely reconfigurable passive components—a review with focus on future telecommunications, internet of things (IoT) and 5g applications. *J. King Saud Univ. Sci.* (2017).
<https://doi.org/10.1016/j.jksus.2017.06.011>
[Article](#) [Google Scholar](#)

10. S.S. Attar, R.R. Masnour, Integration of niobium low temperature superconducting RF circuits with gold–based RF MEMS switches. *IEEE Trans. Appl. Supercond.* (2014). <https://doi.org/10.1109/TASC.2014.2364453>
[Article](#) [Google Scholar](#)

11. D.T. Huong Giang, N.H. Duc, G. Agnus, T. Maroutian, P. Lecoer, Fabrication and characterization of PZT string based MEMS devices. *J. Sci. Adv. Mater. Dev.* (2016).
<https://doi.org/10.1016/j.jsamd.2016.05.004>
[Article](#) [Google Scholar](#)

12. C. Amrita, G. Bhaskar, K.S. Binay, Design, fabrication and characterization of miniature RF MEMS switched capacitor based phase shifter. *Microelectron J* (2014).
<https://doi.org/10.1016/j.mejo.2014.05.009>
[Article](#) [Google Scholar](#)

13. L. Han, X. Gao, Modeling of bending characteristics on micromachined RF MEMS switch based on LCP substrate. *IEEE Trans. Electron Dev.* (2016).
<https://doi.org/10.1109/TED.2016.2593799>

[Article](#) [Google Scholar](#)

14. I. Comart, C. Cetintepe, E. Sagiroglu, S. Demir, T. Akin, Development and modeling of a wafer-level BCB packaging method for capacitive RF MEMS switches. *J. Microelectromech. Syst.* (2019). <https://doi.org/10.1109/JMEMS.2019.2912745>

[Article](#) [Google Scholar](#)

15. C. Chen, Y. Tzeng, E. Kohn, C.-H. Wang, J.-K. Mao, RF MEMS capacitive switch with leaky nanodiamond dielectric film. *Diam. Relat. Mater.* (2011). <https://doi.org/10.1016/j.diamond.2011.02.008>

[Article](#) [Google Scholar](#)

16. C.-T. Jasmina, A.L. Marco, G. David, P. Lluís, L. Antonio, G. Flavio, C. Sabrina, Analytical energy model for the dynamic behavior of RF MEMS switches under increased actuation voltage. *J Microelectromech Syst* (2014). <https://doi.org/10.1109/JMEMS.2014.2314752>

[Article](#) [Google Scholar](#)

17. E.E. Okoro, T. Obomanu, S.E. Sanni, D.I. Olatunji, P. Igbinedion, Application of artificial intelligence in predicting the dynamics of bottom hole pressure for under-balanced drilling: extra tree compared with feed forward neural network model. *Petroleum* (2021). <https://doi.org/10.1016/j.petlm.2021.03.001>

[Article](#) [Google Scholar](#)

18. T. Shaopeng, I.A. Noreen, T. Davood, S.A. Eftekhari, H. Maboud, Using perceptron feed-forward Artificial Neural Network (ANN) for predicting the thermal conductivity of graphene oxide-Al₂O₃/ water-ethylene glycol hybrid nanofluid. *Case Stud Thermal Eng* (2021). <https://doi.org/10.1016/j.csite.2021.101055>

[Article](#) [Google Scholar](#)

19. M. Zlatica, M. Vera, Ć Tomislav, V. Larissa, P.-R. Olivera, Artificial neural networks in RF MEMS switch modelling. *Facta Univ Ser Electron Energetics* (2016).

<https://doi.org/10.2298/FUEE1602177M>

[Article](#) [Google Scholar](#)

20. M. Viviana, Instability and drift phenomena in switching RF-MEMS microsystems. *Actuators* (2019). <https://doi.org/10.3390/act8010015>

[Article](#) [Google Scholar](#)

21. Zlatica, M., Taeyoung, K., Vera, M., Marija, M., Olivera, P.-R., Tomislav, C., Larissa, V. Artificial Neural Network based design of RF MEMS capacitive shunt switch, *ACES J.*, 31(7), 2016.

22. F.Z. Qazi, S.R. Mulpuri, Investigation of an efficient RF-MEMS switch for reconfigurable antenna using hybrid algorithm with artificial neural network. *J. Artif. Intell.* (2018). <https://doi.org/10.3923/jai.2018.79.84>

[Article](#) [Google Scholar](#)

23. Ć Tomislav, M. Zlatica, D. Rohan, P.-R. Olivera, M. Vera, Hybrid neural lumped element approach in inverse modeling of RF MEMS switches. *Facta Univ. Ser. Electron. Energetics* (2020). <https://doi.org/10.2298/FUEE2001027C>

[Article](#) [Google Scholar](#)

24. S. Balachandran, T. Weller, A. Kumar, S. Jeedigunta, H. Gomez, J. Kusterer, E. Kohn, Nanocrystalline diamond for RF-MEMS applications. *Emerg. Nanotechnol. Manuf.* (2009). <https://doi.org/10.1016/B978-0-323-28990-0.00012-9>

[Article](#) [Google Scholar](#)

25. B.-K. Maher, R.M. Raafat, High power latching RF MEMS switches. IEEE Trans. Microw. Theory Tech. (2014). <https://doi.org/10.1109/TMTT.2014.2376932>
- [Article](#) [Google Scholar](#)
26. L. Han, A reconfigurable microwave equalizer with different maximum attenuations based on RF MEMS switches. IEEE Sens. J. (2015). <https://doi.org/10.1109/JSEN.2015.2482999>
- [Article](#) [Google Scholar](#)
27. M.-R. Mohammadi, A. Hemmati-Sarapardeh, M. Schaffie, M.M. Husein, R. Mohammad, Application of cascade forward neural network and group method of data handling to modeling crude oil pyrolysis during thermal enhanced oil recovery. J. Petrol. Sci. Eng. (2021). <https://doi.org/10.1016/j.petrol.2021.108836>
- [Article](#) [Google Scholar](#)
28. King Y.C., Rodica R., Raafat R.M., Novel miniaturized RF MEMS staircase Switch Matrixl, IEEE Microw. Wirel. Compon Lett 22(3) 2012.
29. Mojgan D., Raafat R.M., Redundancy RF MEMS Multiport Switches and Switch Matrices, J Microelectromech Syst 16(2), 2007.
30. Jaewoo L., Chang H.J., Sungweon K., Chang-Auck C., A low-loss single-pole six-throw switch based on compact RF MEMS switches, IEEE Trans. Microw. Theory Tech. 53(11), 2005.
31. Ananda P. De Silva and Henry G. Hughes, “The Package Integration of RF-MEMS Switch and Control IC for Wireless Applications”, IEEE Transactions on Advanced Packaging, Vol. 26, No. 3, 2003.

32. J. Pal, Y. Zhu, J. Lu, D.Dao, and F.Khan, “High Power and Reliable SPST/SP3T RF MEMS Switches for Wireless Applications”, IEEE Electron Device Letters, Vol. 37, No. 9, 2016.
33. Hee-Chul Lee, Jae-Yeong Park, and Jong-Uk Bu, “Piezoelectrically Actuated RF MEMS DC Contact Switches With Low Voltage Operation”, IEEE Microwave And Wireless Components Letters, Vol. 15, No. 4, 2005.
34. Yuhao Liu, Yusha Bey, and Xiaoguang Liu, “High-Power High-Isolation RF-MEMS Switches With Enhanced Hot-Switching Reliability Using a Shunt Protection Technique”, IEEE Transactions on Microwave Theory And Techniques, 2017.

Author information

Authors and Affiliations

Department of Electronics and Communication Engineering, Andhra Loyola Institute of Engineering and Technology, Vijayawada, Andhra Pradesh, 520008, India

Lakshmi Narayana Thalluri & N. Britto Martin Paul

Department of Electronics and Communication Engineering, West Godavari Institute of Science and Engineering, Avapadu, Prakasraopalem, East Godavari District, Tadepalligudem, Andhra Pradesh, 534112, India

M. Aravind Kumar

Faculty of Electrical Engineering, Universiti Teknologi Malaysia, 81310, Johor Bahru, Malaysia

Mohamed Sultan Mohamed Ali

MEMS Research Center, Department of ECE, Koneru Lakshmaiah Educational Foundation (Deemed to Be University), Green Fields, Vaddeswaram, Guntur, 522502, India

K. Srinivasa Rao

National MEMS Design Center, Department of Electronics and Communication Engineering, National Institute of Technology, Silchar, Assam, 788010, India

Koushik Guha

Department of Electronics and Communication Engineering, Lendi Institute of Engineering and Technology, Viziangaram, Andhra Pradesh, 535005, India

S. S. Kiran

Department of Electrical Engineering, College of Engineering, Qatar University, Doha, Qatar

Mohamed Sultan Mohamed Ali

Corresponding author

Correspondence to [Lakshmi Narayana Thalluri](#).

Additional information

Publisher's Note

Springer Nature remains neutral with regard to jurisdictional claims in published maps and institutional affiliations.

Rights and permissions

Springer Nature or its licensor (e.g. a society or other partner) holds exclusive rights to this article under a publishing agreement with the author(s) or other rightsholder(s); author self-archiving of the accepted manuscript version of this article is solely governed by the terms of such publishing agreement and applicable law.

[Reprints and Permissions](#)

About this article

Cite this article

Thalluri, L.N., Kumar, M.A., Ali, M.S.M. *et al.* Jacobian Based Nonlinear Algorithms for Prediction of Optimized RF MEMS Switch Dimensions. *Trans. Electr. Electron. Mater.* **24**, 447–458 (2023). <https://doi.org/10.1007/s42341-023-00463-7>

Received

16 June 2022

Revised

12 October 2022

Accepted

18 July 2023

Published

03 August 2023

Issue Date

October 2023

DOI<https://doi.org/10.1007/s42341-023-00463-7>

Keywords

[Artificial neural networks](#)[RF MEMS switches](#)[Training methods](#)[Datasets](#)



Low-pressure air plasma-treated polytetrafluoroethylene surface for efficient triboelectric nanogenerator

Anas A. Ahmed^a, Talal F. Qahtan^b, Naveed Afzal^d, Marzaini Rashid^c, Lakshmi Narayana Thalluri^e, Mohamed Sultan Mohamed Ali^a  

Show more 

 Share  Cite

<https://doi.org/10.1016/j.mtsust.2023.100330> 

[Get rights and content](#) 

ABSTRACT

In this study, an Al-PTFE triboelectric nanogenerator (TENG) that converts mechanical energy into electricity was investigated. The finite element analysis simulation was performed to illustrate the influence of surface engineering of the Al-PTFE TENG on electrostatic properties, especially at the edges of the TENG. The triboelectric performance of the TENG was improved through surface modifications of the PTFE using low-pressure air plasma treatment. The output voltage increased from 13V in the untreated sample to 90V in the 6min plasma-treated sample under an applied force of 3N. The maximum power density of the 6min plasma-treated sample was calculated to be 24 times higher than that of the untreated sample. The enhanced triboelectric performance was attributed to the formation of nanostructured surface which had higher surface area of PTFE and better effective contact area between the Al and PTFE. The air plasma treatment modified the chemistry of the PTFE surface by creating new functional groups and carbon dangling bonds, which act as electron acceptor sites. Therefore, the electron transfer from Al to PTFE was facilitated, and better triboelectric performance was achieved. The 6min plasma-treated TENG successfully powered electronic devices such as stopwatches and calculators.

Introduction

Triboelectric nanogenerators (TENGs) have gained global recognition due to their potential ability to harvest energy from various low-frequency mechanical sources [[1], [2], [3], [4]]. The concept of TENG was first proposed by Wang et al. [5] in 2012, and since then, it has become an active area of research worldwide. TENG has certain advantages over other energy harvesting devices, such as its ease of fabrication, simple design, cost-effectiveness, high power density, and environmental friendliness [[6], [7], [8]]. Additionally, TENGs are highly capable of harvesting electrical energy from various energy sources, including water waves, wind, biomechanical movements, vibrations, and road transportations [[9], [10], [11], [12], [13]]. Due to their exceptional properties, TENGs have been utilized in a wide variety of applications, including healthcare [14], environmental monitoring [15], security [16], and wireless communications [17]. Additionally, TENGs are gaining a vital role in the era of smart cities and the Internet of Things [[18], [19], [20]].

Surface engineering of tribo-materials plays a key point in controlling and enhancing the performance of TENGs. Different methods, including the formation of nano-patterns, chemical functionalization, and ion injection have been used to engineer the surfaces of tribo-materials, thus enhancing the surface charge density and the output power of TENGs [21]. Recently, Liu et al. [22] exploited the spike-shaped microstructure of the ferrofluid material under the influence of a magnetic field to fabricate triboelectric pressure sensor. The sensor showed an ultrahigh sensitivity (21.48kPa^{-1}) due to the spiky microstructure. Xie et al. [23] employed LaZrO as electron blocking layer between polytetrafluoroethylene (PTFE) and ITO electrode to suppress electron transfer from PTFE to ITO electrode. The electrical output of the LaZrO based TENG was measured as 215V, $96.3\text{mA}/\text{cm}^2$, and $243.3\mu\text{C}/\text{m}^2$. Towards miniaturization of TENGs, Chen et al. [24] designed a conductor-dielectric microstructured triboelectric ultrasonic device based on highly doped conductive silicon (positive tribo-material) and silicon dioxide (negative tribo-material). Photolithography and RIE etching process were used to create vacuum cavities on silicon dioxide with depth of 9nm. Under applying ultrasound waves with 63kPa at 1MH, the device generated voltage signal of 16.8mV and 12.7mV through oil and sound-attenuation medium, respectively.

In addition, the selection of positive and negative tribo-materials plays an important role in determining the performance of TENGs [[25], [26], [27]]. The literature states that polymers exhibit good triboelectric properties and are considered to be suitable for TENG applications [[28], [29], [30]]. Researchers have investigated the performance of different polymers including fluorinated ethylene propylene (FEP) [31], polyvinylidene fluoride (PVDF) [32], polyethylene terephthalate (PET) [33], polydimethylsiloxane (PDMS) [34], and PTFE [35]. Wang et al.

[31] formed a nanostructured surface morphology of FEP using the inductively coupled plasma; the FEP-based TENG delivered a maximum output voltage of 191 V with an output power of 64 μ W under an applied force of 20 N. Next, Jin et al. [32] altered the relative permittivity and specific surface area of PVDF TENG by doping the PVDF with active carbon (AC). Compared to the pure PVDF TENG, the AC-doped PVDF TENG showed an improvement in the output current, voltage, and power by a factor of 3.5, 2.5, and 9.8, respectively. Shin et al. [33] functionalized the surface of PET with a poly-L-lysine solution to create a positive tribo-surface and trichloro (1H,1H,2H,2H-perfluorooctyl) silane to create a negative tribo-surface. The output voltage of the functionalized PET-TENG was about 80 times higher than that of the untreated PET-TENG. Zhang and colleagues [34] reported a high-performing PDMS TENG based on a single-step fluorocarbon plasma treatment using C_4F_8 as reactive gas.

Among the different polymers, PTFE has been the subject of extensive interest in TENGs technology due to its strong electronegativity. Mule et al. [36] modified the surface of PTFE using thermal imprinting lithography to improve its output performance. The output voltage and current were recorded as 2.9 and 2 times that of the unmodified PTFE, respectively. In addition, Zhang et al. investigated an expanded PTFE membrane-based TENG [37]. The morphology of the PTFE was modified due to the expansion; thus, the triboelectric performance was boosted. Under an expansion ratio of 100%, the open-circuit voltage and short-circuit current increased from 38.51 to 61.23 V and from 3.65 to 5.63 μ A, respectively. Xu et al. [38] sprayed a PTFE emulsion on a copper mesh to improve the surface roughness of PTFE and increase the triboelectric performance. In addition, plasma is an efficient technique to modify the PTFE surface. Most of the reported studies have used a combination of O_2 , Ar, and CF_4 gases to obtain nanostructured surface morphology for enhancing the triboelectric performance of PTFE TENGs [[39], [40], [41], [42]]. However, CF_4 gas is detrimental to both humans and the environment. As CF_4 can replace air, it is an asphyxiation hazard to humans. In addition, CF_4 is a very strong greenhouse gas with a warming potential that is 7390 times that of CO_2 , and its lifetime in the atmosphere is more than 50,000 years. Recently, Prada et al. [43] modified the surface of PTFE by a sequential O_2 /Ar plasma treatment without the use of CF_4 gas. The authors reported an increased output power of the plasma-treated PTFE-TENG as compared to the pristine sample. This increase was attributed to an increase in the triboelectric surface charges due to the development of nanostructures and functional groups on the surface of the plasma-treated PTFE. Harvesting wasted energies from the surrounding environment using TENGs is a promising research field for eco-friendly applications in the near future. Therefore, it is of high importance to invest more effort into this upcoming research field. In this study, a conductor-dielectric Al-PTFE TENG was used to harvest mechanical energy. The PTFE surface was modified using a simple, cost-effective, non-toxic, and environmentally-friendly low-pressure air plasma process. The influence of plasma treatment on the triboelectric performance of the Al-PTFE TENG was investigated based on the morphological and chemical modifications of the PTFE surface. In addition, the fundamental physics of the fabricated Al-PTFE TENG were studied with the aid of simulation to better understand the working principle and explore the fringing effect of electric field at the edges of the TENG.

Section snippets

Experimental work

The PTFE in the form of a sheet with a thickness of 1 mm, was cut into $2 \times 2 \text{ cm}^2$ pieces. The PTFE samples were cleaned in an ultrasonic bath using ethanol, isopropanol, and deionized water each for 15 min and then dried in pure nitrogen gas. The samples were loaded into the plasma chamber, and a rotary pump was used to vacuum the chamber to a low pressure ($\sim 1\text{--}10$ mbar). The air plasma was produced inside the chamber at RF power of 60 W. The PTFE samples were exposed to the low-pressure air...

Fundamental physics

To gain a clear picture on the C-S mode TENG, it is important to start with the fundamental physics based on electrostatics. Fig. 2a shows the layout of a dielectric-dielectric C-S TENG which is composed of two dielectric materials with metal electrodes. When the two dielectrics are brought into contact, the top dielectric (acting as the positive tribo-material) loses electrons. Then, due to the triboelectric effect, the bottom dielectric (acting as the negative tribo-material) gains these...

Results and discussion

In this section, the surfaces of the pristine PTFE and plasma-treated PTFE samples are analyzed using SEM, AFM, and XPS characterizations. In addition, the triboelectric characteristics results of the pristine PTFE and plasma-treated PTFE samples are evaluated based on the surface analysis....

Conclusions

An efficient Al-PTFE TENG was fabricated using low-pressure air plasma treatment of the PTFE surface. Increasing the time of plasma treatment led to improvements in triboelectric performance. It was found that the output voltage of the untreated PTFE was boosted from 13 to 90 V upon plasma treatment of the PTFE surface for 6 min. Based on the 6 min-treated sample, the output power density of the TENG was calculated as 3.2 W/m^2 , which is higher than that of the untreated sample (0.133 W/m^2) by a ...

Authors' statement

Anas Ahmed: Conceptualization, Methodology, Formal analysis, Writing – original draft, Writing–review & editing, Visualization. **Talal F. Qahtan:** Conceptualization, Methodology, Formal analysis, Visualization. **Naveed Afzal:** Writing–original draft. **Marzaini Rashid & Lakhmi Narayana Talluri:** Resources. **Mohamed Sultan Mohamed Ali:** Conceptualization, Writing–review & editing, Visualization, Supervision....

Declaration of competing interest

The authors declare that they have no known competing financial interests or personal relationships that could have appeared to influence the work reported in this paper....

Acknowledgement

This work was sponsored by Universiti Teknologi Malaysia under Professional Development Research University Fund (R/J130000.7113.06E14) and UTM Fundamental Research Grant Q. J130000.3823.22H55. Talal F. Qahtan acknowledges the financial support from Prince Sattam Bin Abdulaziz University under project number PSAU/2023/R/1444 which partially supported this research....

[Recommended articles](#)

References (76)

D. Tan *et al.*

[Bow-type bistable triboelectric nanogenerator for harvesting energy from low-frequency vibration](#)

Nano Energy (2022)

R. Ouyang *et al.*

[Copper particles-PTFE tube based triboelectric nanogenerator for wave energy harvesting](#)

Nano Energy (2022)

F.-R. Fan *et al.*

[Flexible triboelectric generator](#)

Nano Energy (2012)

Y. Zeng *et al.*

[Flexible triboelectric nanogenerator for human motion tracking and gesture recognition](#)

Nano Energy (2022)

H.-J. Ko *et al.*

[Self-suspended shell-based triboelectric nanogenerator for omnidirectional wind-energy harvesting](#)

Nano Energy (2022)

J. Pei *et al.*

[Review and analysis of energy harvesting technologies in roadway transportation](#)

J. Clean. Prod. (2021)

D. Lee *et al.*

[Toward effective irregular wind energy harvesting: self-adaptive mechanical design strategy of triboelectric-electromagnetic hybrid wind energy harvester for wireless environmental monitoring and green hydrogen production](#)

Nano Energy (2022)

J. Yun *et al.*

[Paint based triboelectric nanogenerator using facile spray deposition towards smart traffic system and security application](#)

Nano Energy (2021)

X. Zhao *et al.*

[Nanogenerators for smart cities in the era of 5G and Internet of Things](#)

Joule (2021)

A. Alagumalai *et al.*

[Towards smart cities powered by nanogenerators: bibliometric and machine learning–based analysis](#)

Nano Energy (2021)

[View more references](#)

Cited by (4)

[An enhanced distance-dependent electric field model for contact-separation triboelectric nanogenerator: Air-breakdown limit as a case study](#)

2023, Nano Energy

[Show abstract](#) 

[Ionogel based triboelectric nanogenerator textiles for high-precision human fall recognition](#)

2023, Chemical Engineering Journal

[Show abstract](#) 

[Influence of Thickness and Relative Permittivity of Triboelectric Materials on CS-TENG Performance: A Simulation Study \$\nearrow\$](#)

2024, Communications in Computer and Information Science

[Ionogel Based Triboelectric Nanogenerator Textile Sensor with Excellent Thermal Property for High-Precision Human Fall Recognition \$\nearrow\$](#)

2023, SSRN

[View full text](#)

© 2023 Elsevier Ltd. All rights reserved.



All content on this site: Copyright © 2023 Elsevier B.V., its licensors, and contributors. All rights are reserved, including those for text and data mining, AI training, and similar technologies. For all open access content, the Creative Commons licensing terms apply.



[Home](#) [Journal of Electrical Engineering & Technology](#) [Article](#)

Smart City IoT System Network Level Routing Analysis and Blockchain Security Based Implementation

Original Article Published: 10 October 2022 18, 1351–1368 (2023)

[Download PDF](#) 

Journal of Electrical Engineering & Technology

[Aims and scope](#)[Submit manuscript](#)

[Samuyelu Bommu](#), [Aravind Kumar M](#), [Kiranmai Babburu](#), [Srikanth N](#), [Lakshmi Narayana Thalluri](#) , [V. Ganesh G](#), [Anitha Gopalan](#), [Purna Kishore Mallapati](#), [Koushik Guha](#), [Hayath Rajvee Mohammad](#) & [S. Kiran S](#)

 2236 Accesses  5 Citations  1 Altmetric [Explore all metrics](#) →

[Cite this article](#)

Abstract

This paper demonstrates, network-level performance analysis and implementation of smart city Internet of Things (IoT) system with Infrastructure as a Service (IaaS) level cloud computing architecture. The smart city IoT network topology performance is analyzed at the simulation level using the NS3 simulator by extracting most of the

performance-deciding parameters. The performance-enhanced smart city topology is practically implemented in IaaS level architecture. The intended smart city IoT system can monitor the principal parameters like video surveillance with a thermal camera (to identify the virus-like COVID-19 infected people), transport, water quality, solar radiation, sound pollution, air quality (O₃, NO₂, CO, Particles), parking zones, iconic places, E-suggestions, PRO information over low power wide area network in 61.88 km × 61.88 km range. Primarily we have addressed the IoT network-level routing and quality of service (QoS) challenges and implementation level security challenges. The simulation level network topology analysis is performed to improve the routing and QoS. Blockchain technology-based decentralization is adopted to enrich the IoT system performance in terms of security.

[Use our pre-submission checklist →](#)



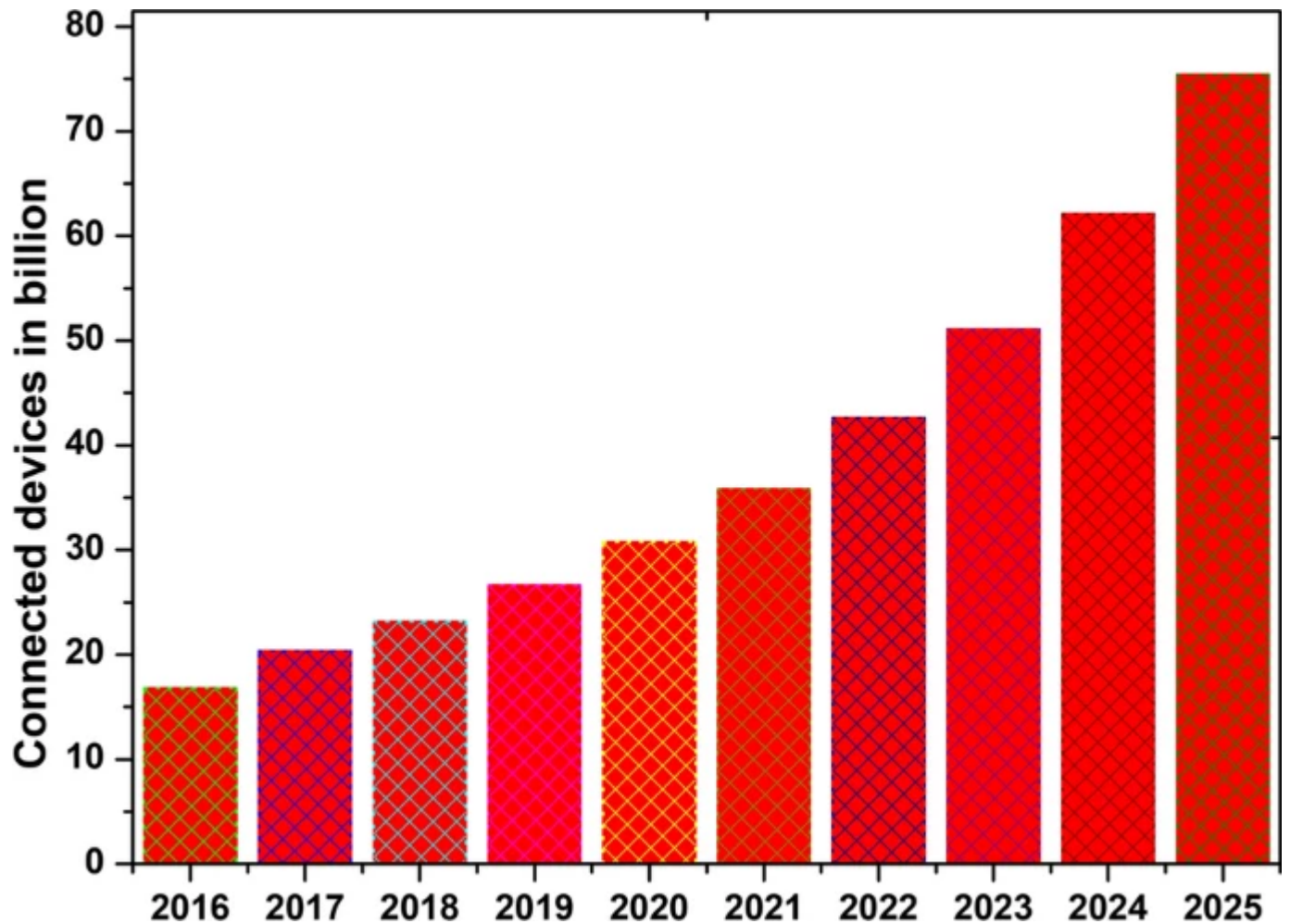
Avoid common mistakes on your manuscript.

1 Introduction

Because of its impressive performance and great potential, the IoT technology's role in the design of smart systems is thrived in many fields like smart cities [1,2,3], medical [4,5,6], aquaculture [7,8,9], industry [10,11,12], and smart home [13]. Industry 4.0 is aimed at mass customization and cyber-physical cognitive systems, in that IoT technology proved its ability and significance. When compared with RFID and smart device technology IoT plays a vital role in exploring smart applications [14].

The IoT device users count is growing rapidly as shown in Fig. 1, and this is the major motivating point for many kinds of researchers to choose IoT as a major domain of research [15]. However, the major research challenges in the implementation of IoT systems are maintaining high throughput, less delay, low power consumption, low path loss, good packet receive rate, quality of service(QoS), congestion control, reliability, heterogeneity, scalability, high security, and best network routing [16, 17]. The network-level IoT topology simulation helps to make the implementation cost-effective and the incorporation of blockchain technology in IoT will make the system more secure and sturdy [18].

Fig. 1



(Source: Statista)

IoT devices usage growth in billion

The present-day civil people are using more and more IoT devices and there is a significant demand for smart IoT systems like the design of smart transport, smart building, smart home, smart business [19], and smart grids [20]. However, the development of smart city applications using IoT is one of the potential research areas. Nowadays IoT systems for smart cities monitor viruses (like COVID-19) spread which is very essential. The vital smart city parameters are video surveillance, transport, water quality, solar radiation, sound pollution, air quality (O₃, NO₂, CO, Particles), parking zones, iconic places, E-suggestions, and public relational officer (PRO) information as shown in Fig. 2.

Fig. 2



Smart city parameters

The sensor, network, and implementation level challenges of a smart city-based IoT system as listed in Table 1. Identifying the best IoT routing topology for a smart city with good quality of services (QoS) is one of the network-level potential research challenges. Before the implementation, doing network level simulation analysis by extracting the parameters like throughput, delay, path loss, packets received, the distance between the mobile nodes and station nodes to access points ratio helps to improve the quality of service(QoS) [21,22,23]. Maintaining the exact distance between the nodes helps to improve the throughput of the system [24,25,26,27]. Security and reliability are the two

major challenges in IoT system implementation. Blockchain technology is useful to resolve the security challenges in IoT [28].

Table 1 Network and implementation level IoT challenges

Blockchain technology enables the decentralization of the database over a peer-to-peer network of nodes, each of which stores a copy of the whole database [29]. IoT devices produce massive volumes of data that must be stored and analyzed. Incorporation of blockchain technology with IoT helps to detect unofficial actions on stored IoT data with this the overall system security improves, is cost-effective, and speeds up the data transmission Process. The presented IoT system can majorly monitor atmospheric, traffic conditions, and identification of virus-infected people in the city [30].

This paper is described: in Sect. 2, we holistically investigate research gaps and possible solutions related to IoT-based smart city. Section 3 describes the simulation of network routing and parametric extraction to address the network quality of service. Smart city data collection and monitoring system implementation by incorporating distributive blockchain technology which offers high security is discussed in Sect. 4 and followed by Conclusions in Sect. 5.

2 Literature Survey

The smart city with the IoT paradigm is the most widely discussed area by both industry people and researchers. In this paper, we have primarily demonstrated network routing, quality of service, and security aspects in the smart city data monitoring IoT system. Monitoring the smart city parameters with IoT is considerably explored by many researchers, but still, we can find potential research gaps like defining the best network routing, improving quality of service (QoS), achieving high reliability or lifetime, getting the best scalability and providing high security as listed in Table 2. The smart city network simulation performance indices are listed in Table 3.

Table 2 Comprehensive study of smart city IoT related work

Table 3 Basic smart city and network topology parameters

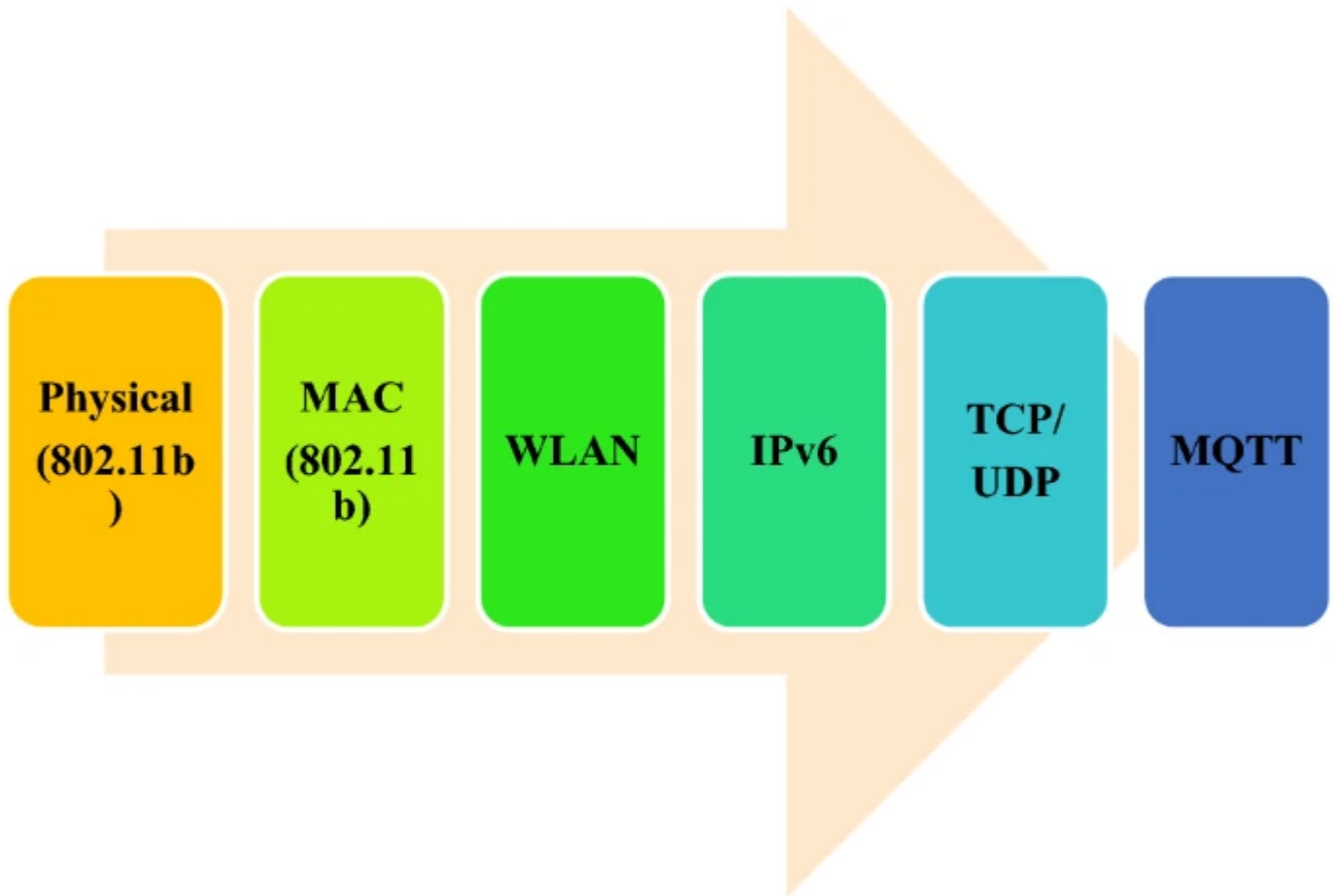
Different technologies involved in the design of IoT systems are listed in Table 4. The mathematical expressions for the topology performance analysis are listed in Table 5. IoT technology is emerged in many fields because of its great potential and unique ability to adapt to new technologies [64, 65]. Now there is a huge demand for the IoT in a wide area network, but in wide range offering reliability, scalability, proper network routing, congestion control, security, and quality of service (QoS) is a challenging task [66,67,68]. In this paper, we have addressed three potential research challenges in smart city IoT wide area networks i.e., network routing, QoS, and security. The blockchains are primarily classified as permissionless (public) and permission (private). Any type of blockchain incorporation in IoT enables decentralization which makes the network more secure and scalable.

Table 4 Comprehensive study on technologies involved in different layers of Internet of Things

Table 5 Basic IoT system network level mathematics [60,61,62,63]

3 Network Simulation Analysis of Smart City IoT Topology

Embedded systems that communicate with transducers and involve wireless communication are composed of IoT devices. In Ubuntu 18.0, we first compared compound TCP over Wi-Fi output with NS-3 simulator experiments. The smart city IoT system protocol stack is as in Fig. 3. It is made up of wireless equipment, a PC router on which a dummy net is mounted, a connection point, and a server. The Gateway and the A 22 Mbps Ethernet links to the server. We used the slandered IEEE 802.11a. There are systems with a Wi-Fi internal 802.11b card.

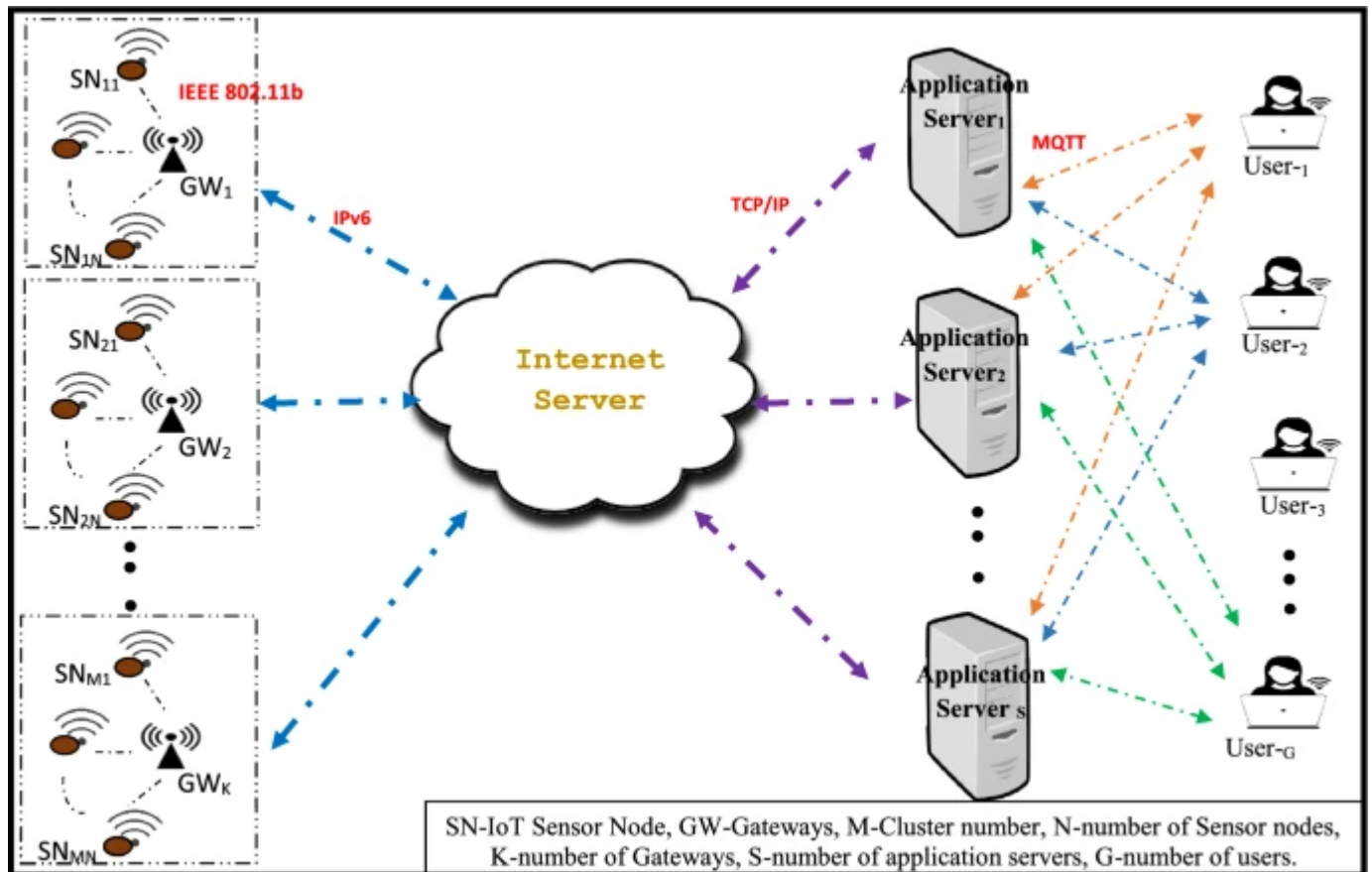
Fig. 3

Smart city IoT system protocol stack

The smart city network scenario is framed by considering Vijayawada city located in Andhra Pradesh state, India. Here, we performed the simulation level analysis on network performance by varying the number of sensor nodes ($M \times N$), the number of gateways (K), and the number of user counts (G). It is beneficial to build low-cost nodes to promote their large deployment, taking into account that the IoT system can monitor smart city parameters. This means saving money on the majority of the IoT architecture. The designed network parameters are listed in Table 6. The smart city model network topology is shown in Fig. 4. The smart city IoT scenario is virtually simulated in the ns-3 environment for 8000 s, it is offering a throughput of 22Mbps, Average power consumption of 2.6 mW, Delay of 80 ms, and Packet delivery ratio of 0.85%, and latency is 7.8. The network performance indices are as shown in Fig. 5.

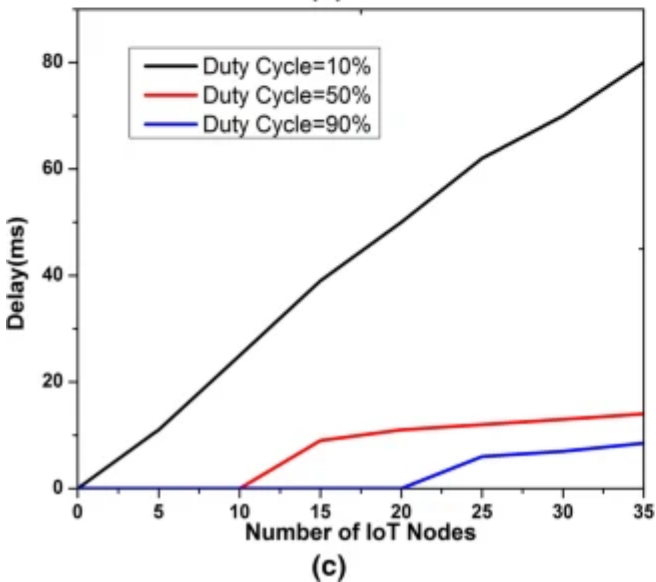
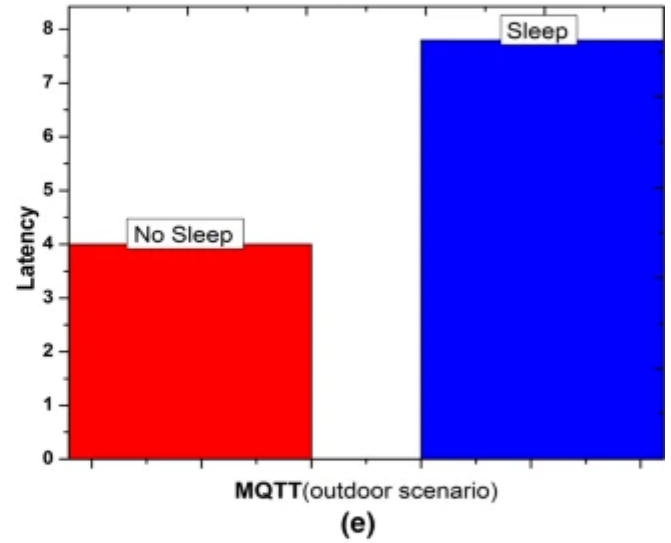
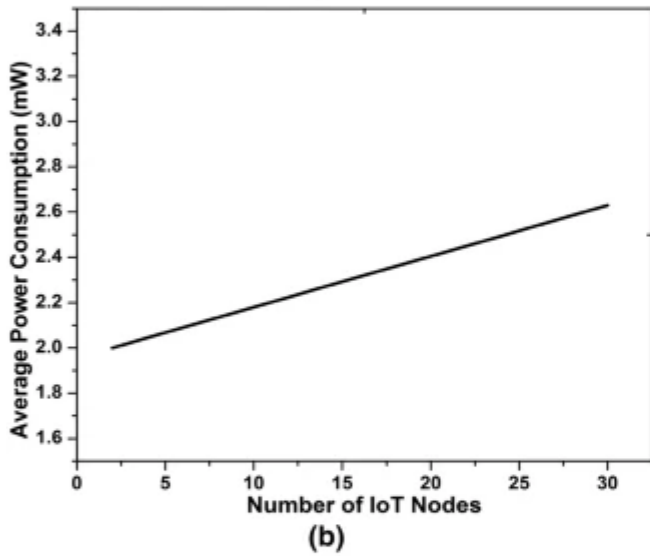
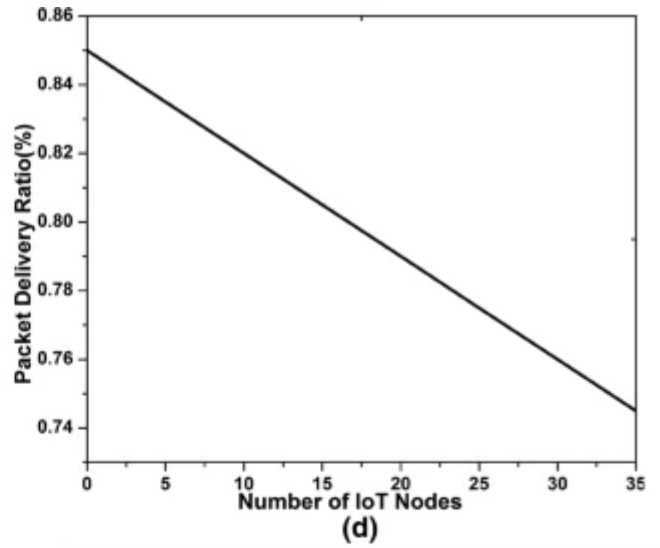
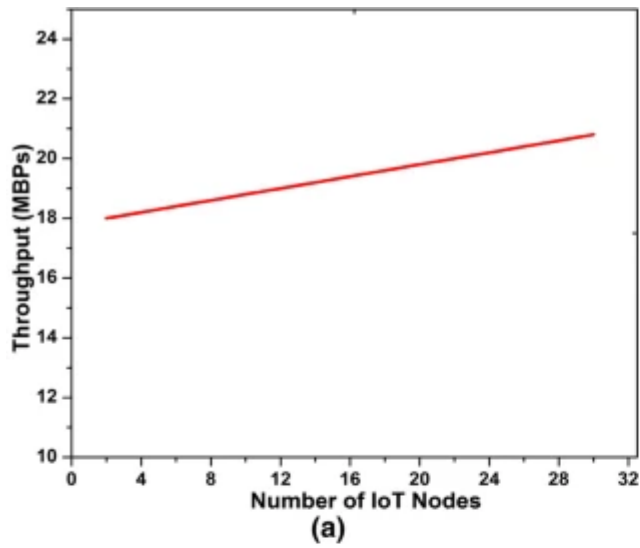
Table 6 Network Parameters

Fig. 4



Network topology for Vijayawada city, Andhra Pradesh, India

Fig. 5



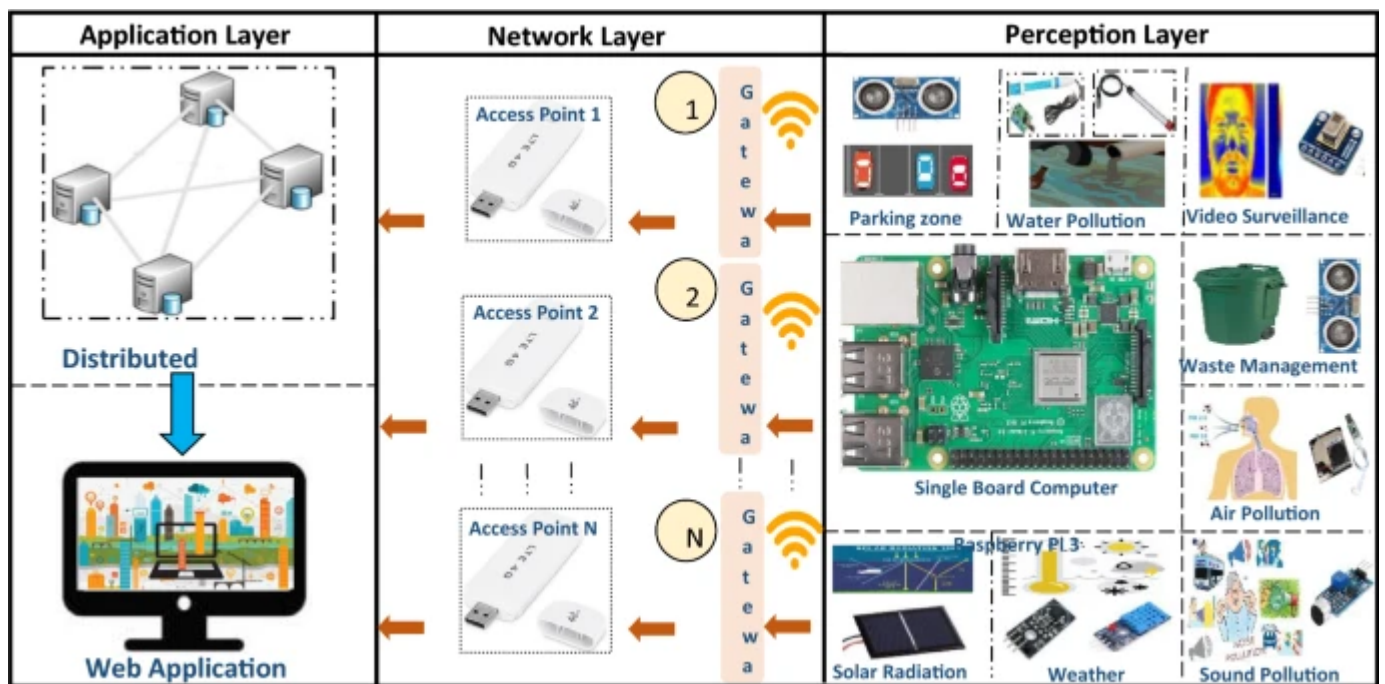
Network simulation parameters, a Throughput (MBPs), b Average Power Consumption (mW), c Delay(ms), d Packet Delivery Ratio, e Latency

4 Practical Realization Aspects

Monitoring the smart city parameters like air quality, sound pollution, parking zones, solar radiation, water quality, waste management, transportation, iconic places, e-

suggestions, public relations officer (PRO) information, video surveillance, human flow, and emergency services really help the civil people in the process of decision making [69,70,71]. In this paper, we have presented a smart city IoT system that can monitor the overall 13 parameters as illustrated in Fig. 6 related to the smart city. Primarily the air quality will depend on the levels of carbon monoxide (CO), ammonia (NH3), nitrogen dioxide (NO2), ozone (O3), sulphur dioxide (SO2), and particle matter 2.5, (PM2.5), particle matter 10 (PM10). The commercially available sensor to monitor the smart city parameters are listed in Table 7.

Fig. 6



Model structure of smart city IoT

Table 7 List of sensors incorporated with specifications [72,73,74]

4.1 Blockchain for Smart City IoT

The purpose of incorporating blockchain technology with smart city IoT is, which enables the decentralization of storage and server as shown in Fig. 7, with this the system security

improves and makes it more sturdy. The smart city IoT system performance is significantly improved with blockchain. The role of blockchain in presented smart city IoT is, that at the sensor level, the data was encrypted with the public key. The IoT device maker stores the associated public key in a blockchain block [[75](#),[76](#),[77](#)]. A network node sends a random challenge message to an IoT device, to which the IoT device responds with a signature. At the network level, other than centralized cloud, here we used decentralization of cloud services. With this, the system speed increased and the system is more scalable.

Fig. 7



(a)



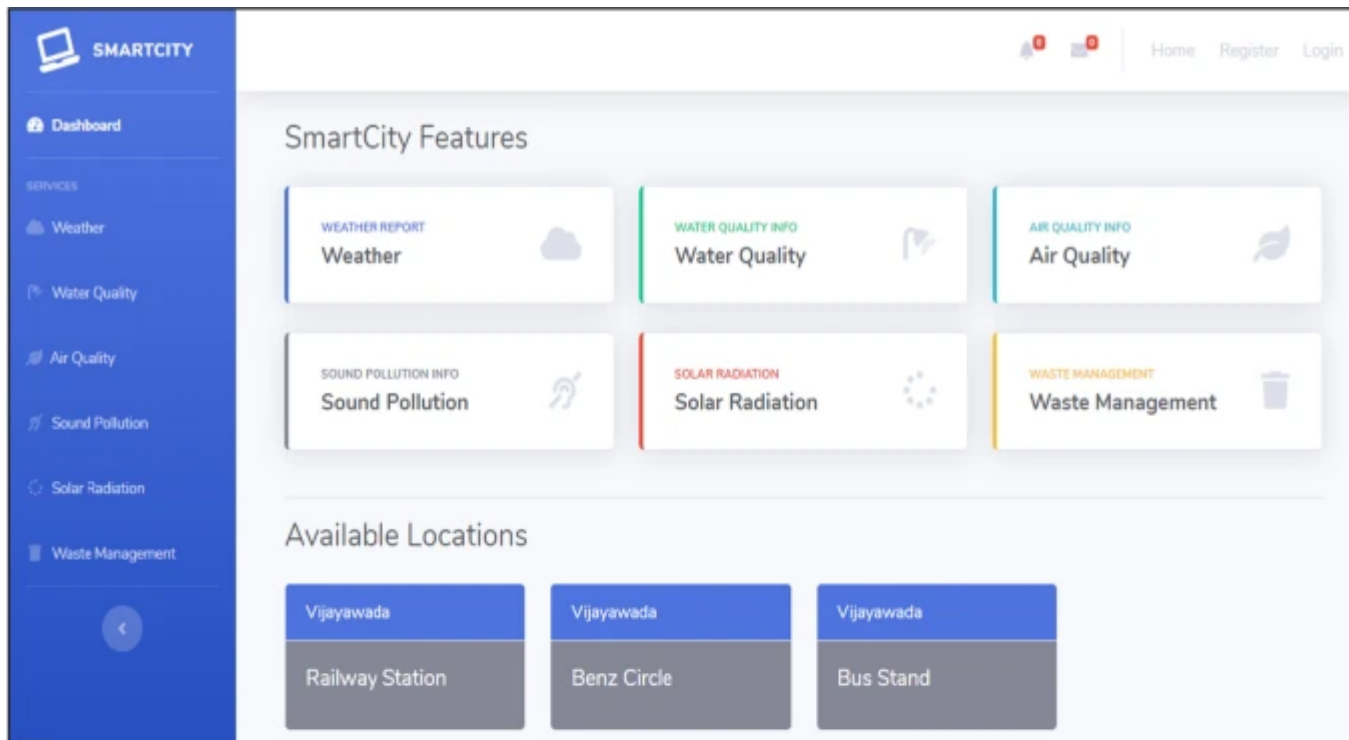
(b)

Smart city, a IoT system with centralized server, b Blockchain enabled IoT system with distributed server

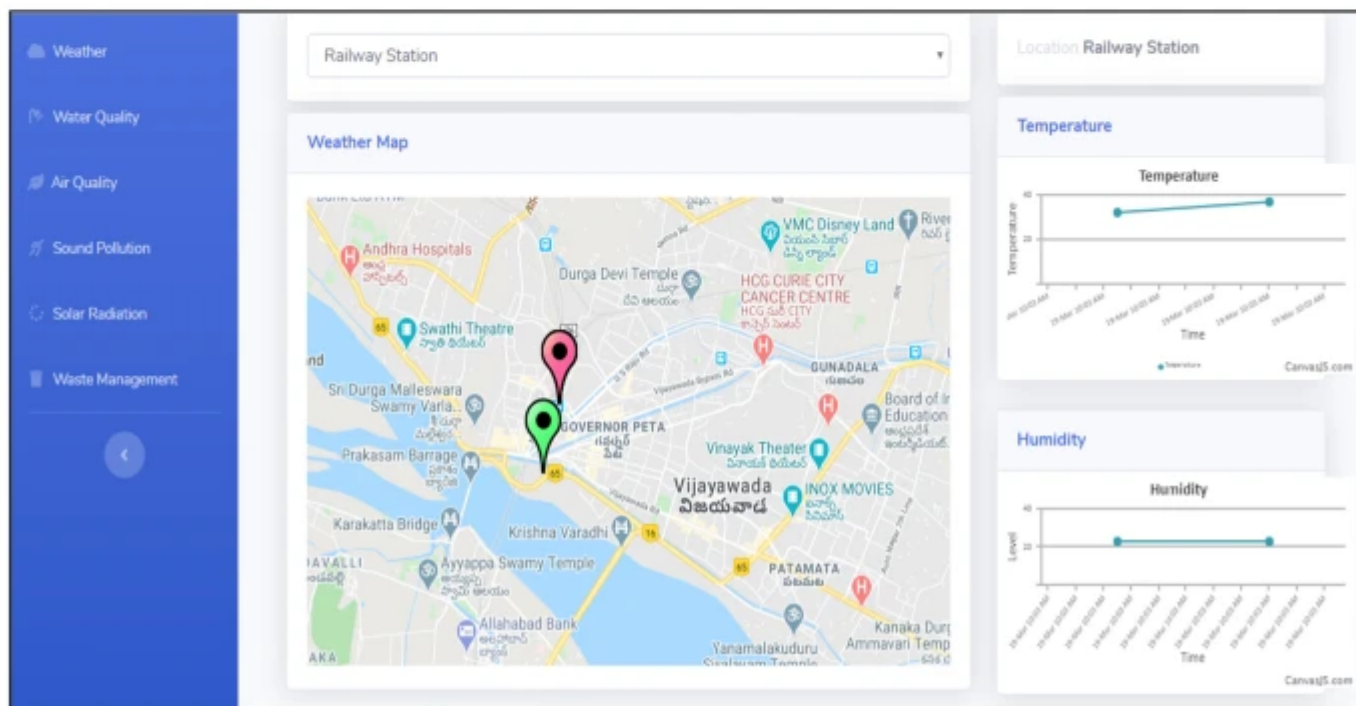
The smart city IoT application was designed by considering Vijayawada city in Andhra Pradesh state in India. Deployed multiple internet-enabled sensor nodes all over the city, those are capable to send the sensors data to the predefined destination API location.

Eventually, an application for the smart city for better monitoring and analysis of the data as shown in Fig. 8 was designed with blockchain security. The designed smart city application specifications are listed in Table 8. The sensor nodes are designed with Raspberry pi-3 and all the sensors related to smart city parameters are interfaced. The node is connected with an LTE access point for the internet. MongoDB and WinNMP are used as databases and servers respectively. MQTT IoT protocol was incorporated into the user access side. An application program interface (API) connector mechanism was used which enables highly secure data transmission to the destination. Overall the smart city IoT system was implemented with infrastructure as a service (IaaS) architecture.

Fig. 8



(a)



(b)

Smart city IoT application, a home page, b location based information monitoring

Table 8 Smart city IoT system implementation parameters

5 Conclusion

This article presented a smart city IoT system that helps to monitor essential parameters like video surveillance using a thermal camera, air quality, water quality, sound pollution, weather, solar radiation, waste management, parking zones, E-suggestions, and Iconic Places. Prior virtual simulation is performed on the smart city IoT network scenario using NS-3. Eventually, the IoT system is implemented with good quality of service and security. The incorporation of blockchain with the smart city makes the system more secure, highly scalable, and cost-effective.

References

1. Rahman MA, Rashid MM, Hossain MS, Hassanain E, Alhamid MF, Guizani M (2018) Blockchain and IoT-based cognitive edge framework for sharing economy services in a smart city. *IEEE Access* 7:18611–18621

[Google Scholar](#)

2. Santos PM, Rodrigues JGP, Cruz SB, Lourenc T , d'Orey OPM, Luis Y, Rocha C, Sousa S, Cris´ostomo S, Queir´os C, Sargento S, Aguiar A, Barros J (2018) PortoLivingLab: an IoT-based sensing platform for smart cities. *IEEE Internet of Things Journal* 5(2):523–532

3. Kumar K, Saraswat S, Jindal SK et al (2021) Experimental validation of an iot based device selective power cut mechanism using power line carrier communication for smart management of electricity. *J Electr Eng Technol* 16:67–77

[Google Scholar](#)

4. Xu B, Da Xu L, Cai H, Xie C, Hu J, Bu F (2014) Ubiquitous Data accessing method in IoT-based information system for emergency medical services. *IEEE Tran Ind Inf* 10(2)

5. Hebal S, Harous S, Mechta D (2021) Energy routing challenges and protocols in energy internet: a survey. *J Electr Eng Technol* 16:3197–3212

6. André da Costaa C, Pasluostab CF, Eskofierb B, Bandeira da Silvaa D, Righia RR (2018) Internet of health things: toward intelligent vital signs monitoring in hospital wards. *Artif Intel Med*, 89
 7. Aslam MM, Irshad MN, AZEEM, H. (2020) Cost effective and energy efficient intelligent smart home system based on IoT. *Afyon Kocatepe Üniversitesi Uluslararası Mühendislik Teknolojileri ve Uygulamalı Bilimler Dergisi* 3(1):10–20
- [Google Scholar](#)
8. Y.-B. Lin, and H.-C. Tseng (2018) FishTalk: An IoT-based Mini Aquarium System. *IEEE Access* 7
 9. Gao G, Xiao K, Chen M (2019) An intelligent IoT-based control and traceability system to forecast and maintain water quality in freshwater fish farms. *Comput Electron Agric*, 166
 10. Tzounis A, Katsoulas N, Bartzanas T, Kittas C (2017) Internet of Things in agriculture, recent advances and future challenges. *Biosyst Eng* 164(31)
 11. Zhang W, Guo W, Liu X, Liu Y, Zhou J, Li B, Lu Q, Yang S (2017) LSTM-based analysis of industrial IoT equipment. *IEEE Access* 13(9)
 12. Gronau N, Ullrich A, Teichmann M (2017) Development of the Industrial IoT competences in the areas of organization, process, and interaction based on the learning factory concept. *Proc Manuf* 9

13. Boyes H, Hallaq B, Cunningham J, Watson T (2018) The industrial internet of things (IIoT): an analysis framework,". *Comput Ind* 101:1–12

[Google Scholar](#)

14. Hafidh B, Al Osman H, Arteaga-Falconi J, Dong H, EL Saddik A (2017) SITE: the simple internet of things enabler for smart homes. *IEEE Access* 5:2034–2049

[Google Scholar](#)

15. Mehta R, Sahni J, Khanna K (2018) Internet of things: vision, applications and challenges. *Procedia Computer Science* 132:1263–1269

[Google Scholar](#)

16. Dachyar M, Zagloel TYM, Ranjaliba Saragih L (2019) Knowledge growth and development: internet of things (IoT) research, 2006–2018. *Heliyon* 5

17. Chernyshev M, Zeadally S, Baig Z, Woodward A (2018) Internet of things forensics. Theme Article: Cyberthreats And Security 20(3):40–49

[Google Scholar](#)

18. Al-Turjmana F, Malekloo A (2019) Smart parking in IoT-enabled cities: a survey. *Sustain Cities Soc* 49

19. Bello O, Zeadally S (2017) Toward efficient smartification of the internet of things (IoT) services. *Futur Gener Comput Syst* 92:663–673

[Google Scholar](#)

20. Srinidhi NN, Dilip Kumar SM, Venugopal KR (2019) Network optimizations in the internet of things: a review. *Eng Sci Technol Int J* 22:1–21

[Google Scholar](#)

21. Ranjan R et al (2018) Integrating the internet of things and data science. IEEE Cloud Comput 5(3)
22. Liu X,. Ansari N (2016) Green relay assisted D2D communications with dual batteries in heterogeneous cellular networks for IoT. IEEE Internet Things J x4(5)
23. Liu Y, Tong K-F, Wong K-K (2019) Reinforcement learning based routing for energy sensitive wireless mesh IoT networks. Electron Lett 55(17):966–968

[Google Scholar](#)

24. Pokhrel SR, Williamson C (2018) Modeling compound TCP Over WiFi for IoT. IEEE/ACM Trans Networking 26(2):864–878

[Google Scholar](#)

25. Jain B, Brar G, Malhotra J, Rani S (2017) A novel approach for smart cities in convergence to wireless sensor networks. Sustain Cities Soc 7:440–448
26. Kumar NM, Mallick PK (2018) Blockchain technology for security issues and challenges in IoT. Proc Comput Sci 132:1815–1823

[Google Scholar](#)

27. Li C, Palanisamy B (2018) Privacy in internet of things: from principles to technologies. IEEE Internet Things J 6(1):488–505

[Google Scholar](#)

28. Mahdavinejad MS et al (2018) Machine learning for Internet of Things data analysis: a survey. *Digital Commun Netw* 3(3):161–175

[Google Scholar](#)

29. Kumara NM, Mallickb PK (2018) Blockchain technology for security issues and challenges in IoT. *Proc Comput Sci* 132:1815–1823

[Google Scholar](#)

30. Xue M, Yang Q, Zhu G et al (2022) A position detection method for dynamic wireless inspection robots charging. *J Electr Eng Technol* 17:97–110

[Google Scholar](#)

31. Mirceaeremia LM (2017) The smart city concept in the 21st century. *Proc Eng* 181:12–19

[Google Scholar](#)

32. Araujo V, Mitra K, Saguna S, Åhlund C (2019) Performance evaluation of FIWARE: a cloud-based IoT platform for smart cities. *J Parall Distrib Comput* 132:250–261

[Google Scholar](#)

33. Yao H, Gao P, Wang J, Zhang P, Jiang C, Han Z (2019) Capsule network assisted IoT traffic classification mechanism for smart cities. *IEEE Internet Things J* 6(5):7515–7525

[Google Scholar](#)

34. Wazid M, Das AK, Odelu V, Kumar N, Conti M, Jo M (2017) Design of secure user authenticated key management protocol for generic IoT networks. *IEEE Internet Things J* 5(1):269–282

[Google Scholar](#)

35. Reyna A, Martín C, Chen J, Soler E, Díaz M (2018) On blockchain and its integration with IoT. Challenges and opportunities. *Futur Gener Comput Syst* 88:173–190

[Google Scholar](#)

36. Gan S, Rousstia D, Rifai FA (2020) Implementation of secure work from home system based on blockchain using NS3 simulation. In: International conference on electrical engineering, computer sciences and informatics (EECSI)

37. Kiki, MJM, Iddi I (2021) Improved LORA modulation output in LEO satellite internet of things. *J Electr Eng Technol*

38. Mick T, Tourani R, Misra S (2017) LAsER: lightweight authentication and secured routing for NDN IoT in smart cities. *IEEE Internet Things J* 5(2):755–764

[Google Scholar](#)

39. Marques P, Manfroï D, Deitos E, Cegoni J, Castilhos R, Rochol J, Pignaton E, Kunst R (2019) An IoT-based smart cities infrastructure architecture applied to a waste management scenario. *Ad Hoc Netw* 87:200–208

[Google Scholar](#)

40. Conti M, Kaliyar P, Rabbani MM, Ranise S (2019) Attestation-enabled secure and scalable routing protocol for IoT networks. *Ad Hoc Netw* 98(1)

41. Sanmartin P, Sierra R, Martinez E, Jabba D (2018) Objective Function BF-ETX for RPL Routing Protocol. *IEEE Latin Am Trans* 16(8)

42. Jia G, Zhu Y, Li Y, Zhu Z, Zhou L (2019) Analysis of the effect of the reliability of the NB-IoT network on the intelligent system. *IEEE Access* 7:112809–112820

[Google Scholar](#)

43. He J, Wei J, Chen K, Tang Z, Zhou Y, Zhang Y (2017) Multi-tier fog computing with large-scale IoT data analytics for smart cities. *IEEE Internet Things J* 5(2):677–686

[Google Scholar](#)

44. Yang J, Akyurek AS, Tilak S, Rosing TS (2017) Design of transmission manager in heterogeneous WSNs. *IEEE Trans Emerg Top Comput* 6(3):395–408

[Google Scholar](#)

45. Cheng B, Solmaz G, Cirillo F, Kovacs E, Terasawa K, Kitazawa A (2018) FogFlow: easy programming of iot services over cloud and edges for smart cities. *IEEE Internet Things J* 5(2):696–707

[Google Scholar](#)

46. Chen S, Yang C, Li J, Yu FR (2019) Full lifecycle infrastructure management system for smart cities: a narrow band IoT-Based platform. *IEEE Internet Things J* 6(5):8818–8825

[Google Scholar](#)

47. Arshad S, Azam MA, Rehmani MH, Loo J (2018) Recent advances in information-centric networking based internet of things (ICN-IoT). *IEEE Internet Things J* 6(2):2128–2158

[Google Scholar](#)

48. Abidoye AP et al (2017) Models for integrating wireless sensor networks into the Internet of Things. *IET Wireless Sensor Syst* 7(3):65–72

[Google Scholar](#)

49. Mohammad N, Muhammad S, Bashar A, Khan MA (2019) Formal analysis of human-assisted smart city emergency services. *IEEE Access*

50. Zhao L, Sun W, Shi Y, Liu J (2018) Optimal placement of cloudlets for access delay minimization in SDN-based internet of things networks. *IEEE Internet Things J* 5(2):1334–1344

[Google Scholar](#)

51. Li W, Song H, Zeng F (2017) Policy-based secure and trustworthy sensing for internet of things in smart cities. *IEEE Internet Things J* 5(2):716–723

[Google Scholar](#)

52. Ullah R, Faheem Y, Kim BS (2017) Energy and congestion-aware routing metric for smart grid AMI networks in smart city. *IEEE Access* 5:13799–13810

[Google Scholar](#)

53. Deebak BD, Al-Turjman F, Aloqaily M, Alfandi O (2019) An authentic-based privacy preservation protocol for smart e-healthcare systems in IoT. *IEEE Access* 7:135632–135649

54. Tahir Y, Yang S, McCann J (2017) BRPL: backpressure rpl for high-throughput and mobile IoTs. *IEEE Trans Mob Comput* 17(1):29–43

[Google Scholar](#)

55. Benayache A, Bilami A, Barkat S, Lorenz P, Taleb H (2019) MsM: A microservice middleware for smart WSN-based IoT application. *J Netw Comput Appl* 144:138–154
56. Farooq MS, Riaz S, Abid A, Abid K, Naeem MA (2019) A survey on the role of IoT in agriculture for the implementation of smart farming. *IEEE Access* 7:156237–156271
- [Google Scholar](#)
57. Ray PP, Thapa N, Dash D (2019) Implementation and performance analysis of interoperable and heterogeneous IoT-edge gateway for pervasive wellness care. *IEEE Trans Consumer Electron* 65(4)
58. Rajpoot SC, Pandey C, Rajpoot PS et al (2021) A dynamic-SUGPDS model for faults detection and isolation of underground power cable based on detection and isolation algorithm and smart sensors. *J Electr Eng Technol* 16:1799–1819
- [Google Scholar](#)
59. Shin D et al (2019) A security protocol for route optimization in DMM-based smart home IoT networks. *IEEE Access* 7:142531–142550
- [Google Scholar](#)
60. Wazid M et al (2019) LAM-CIoT: lightweight authentication mechanism in cloud-based IoT environment. *J Netw Comput Appl* 150:1–9
- [Google Scholar](#)
61. Zhang C, Ge J, Pan M, Gong F, Men J (2018) One stone two birds: a joint thing and relay selection for diverse IoT networks. *IEEE Trans Veh Technol* 67(6):5424–5434
- [Google Scholar](#)

62. Hasan MZ et al (2018) Analysis of cross-layer design of qualityof-service forward geographic wireless sensor network routing strategies in green internet of things. IEEE Access 6:20371–20389

[Google Scholar](#)

63. Ramezani P, Zeng Y, Jamalipour A (2018) Optimal resource allocation for multiuser internet of things network with single wireless-powered relay. IEEE Internet Things J 6(2):3132–3142

[Google Scholar](#)

64. Uddin R, Alghamdi AS, Uddin MH et al (2019) Ethernet-based fault diagnosis and control in smart grid: a stochastic analysis via markovian model checking. J Electr Eng Technol 14:2289–2300

[Google Scholar](#)

65. van Zoest V, Osei FB, Stein A, Hoek G (2019) Calibration of low-cost NO₂ sensors in an urban air quality network. Atmos Environ 210:66–75

[Google Scholar](#)

66. Collier-Oxandale A et al (2020) Field and laboratory performance evaluations of 28 gas-phase air quality sensors by the AQ-SPEC program. Atmos Environ 220

67. Shao W, Zhang H, Zhou H (2017) Mathematical modeling and parameter optimization of fine particle sensors based on laser light scattering. IEEE Sens J 17(20)

68. Phila M, Sithole P, Nwulu NI, Dogo EM (2019) Dataset for a wireless sensor network based drinking-water quality monitoring and notification system. Data Brief 27

69. Kang KD, KangH, Ilankoon IMSK, Chong CY (2020) Electronic waste collection systems using Internet of Things (IoT): household electronic waste management in Malaysia. *J Clean Prod* 252

70. Shrivastav K, Kulat KD (2020) Scalable energy efficient hexagonal heterogeneous broad transmission distance protocol in WSN-IoT networks. *J Electr Eng Technol* 15:95–120

[Google Scholar](#)

71. Ramos TRP et al (2018) The smart waste collection routing problem: alternative operational management approaches. *Expert Syst Appl* 103:146–158

[Google Scholar](#)

72. Rudniak J (2019) Comparison of local solar radiation parameters with data from a typical meteorological year. *Therm Sci Eng Prog* 16

73. Sultana T, Wahid KA (2019) Choice of application layer protocols for next generation video surveillance using internet of video things. *IEEE Access* 7

74. Sultana T, Wahid KA (2019) IoT-guard: event-driven fog-based video surveillance system for real-time security management. *IEEE Access* 7

75. Aliyu A et al (2018) Towards video streaming in IoT environments: vehicular communication perspective. *Comput Commun* 118:93–119

[Google Scholar](#)

76. Al-Turjman F, Malekloo A (2019) Smart parking in IoT-enabled cities: A survey. *Sustain Cities Soc* 49

- 77.** Aggarwal A, Gaba S, Mittal M (2021) A Comparative investigation of consensus algorithms in collaboration with IoT and blockchain Transforming Cyber security Solutions using Blockchain. Springer, Berlin

[Google Scholar](#)

Author information

Authors and Affiliations

Department of Electronics and Communication Engineering, PVP Siddhartha Institute of Technology, Vijayawada, 520007, Andhra Pradesh, India

Samuyelu Bommu

Department of Electronics and Communication Engineering, West Godavari Institute of Science and Engineering, Avapadu, Prakasraopalem, East Godavari District, 534112, Andhra Pradesh, India

Aravind Kumar M

Department of Electronics and Communication Engineering, Lendi Institute of Engineering and Technology, Vizianagaram, 535005, Andhra Pradesh, India

Kiranmai Babburu

Department of Electronics and Communication Engineering, St. Peters Engineering College, Medchal, 500043, Telangana, India

Srikanth N

Department of Electronics and Communication Engineering, Andhra Loyola Institute of Engineering and Technology, Dr. A. P. J. Abdul Kalam Research Forum, Vijayawada, 520008, Andhra Pradesh, India

Lakshmi Narayana Thalluri

Department of Electronics and Communication Engineering, Koneru Lakshmaiah Education Foundation, Vaddeswaram, 522502, Andhra Pradesh, India

V. Ganesh G

Department of Electronics and Communication Engineering, Saveetha School of Engineering, SIMATS, Thandalam, Chennai, 602105, Tamilnadu, India

Anitha Gopalan

Department of Electronics and Communication Engineering, KKR & KSR Institute Of Technology & Science, Vinjanampadu, Guntur, 522017, Andhra Pradesh, India

Purna Kishore Mallapati

National MEMS Design Center, Department of Electronics and Communication Engineering, National Institute of Technology, Silchar, 788010, Assam, India

Koushik Guha

Department of Electronics and Communication Engineering, PBR VITS, Kavali, 524201, Andhra Pradesh, India

Hayath Rajvee Mohammad

Department of Electronics and Communication Engineering, Lendi Institute of Engineering and Technology, Vizianagaram, 535005, Andhra Pradesh, India

S. Kiran S

Corresponding author

Correspondence to [Lakshmi Narayana Thalluri](#).

Additional information

Publisher's Note

Springer Nature remains neutral with regard to jurisdictional claims in published maps and institutional affiliations.

Rights and permissions

Springer Nature or its licensor holds exclusive rights to this article under a publishing agreement with the author(s) or other rightsholder(s); author self-archiving of the accepted manuscript version of this article is solely governed by the terms of such publishing agreement and applicable law.

[Reprints and Permissions](#)

About this article

Cite this article

Bommu, S., M, A.K., Babburu, K. *et al.* Smart City IoT System Network Level Routing Analysis and Blockchain Security Based Implementation. *J. Electr. Eng. Technol.* **18**, 1351–1368 (2023). <https://doi.org/10.1007/s42835-022-01239-4>

Received

11 April 2021

Revised

21 July 2022

Accepted

16 August 2022

Published

10 October 2022

Issue Date

March 2023

DOI

<https://doi.org/10.1007/s42835-022-01239-4>

Share this article

Anyone you share the following link with will be able to read this content:

[Get shareable link](#)

Provided by the Springer Nature SharedIt content-sharing initiative

Keywords

[IoT technology](#)

[Smart applications](#)

[Network simulation](#)

[Blockchain technology](#)

STRUCTURAL AND MATERIAL BASED COMPREHENSIVE PERFORMANCE ANALYSIS ON SHUNT CAPACITIVE RF MEMS SWITCH

SATHULURI MALLIKHARJUNA RAO^{1,2,*}, G. SASIKALA¹

¹Dept. of ECE, Vel Tech Rangarajan Dr.Sagunthala R&D Institute of Science and Technology (Deemed to be University), Avadi, Chennai, Tamilnadu, India

²Dept. of ECE, Andhra Loyola Institute of Engineering and Technology, Andhra Pradesh, India

*Corresponding Author: smr.aliet@gmail.com

Abstract

In this paper, we have presented the structural and material based comprehensive analysis on shunt capacitive RF MEMS switches. The switches properties are analysed by considering two structures, i.e., clamped-clamped and serpentine structure. The material analysis is done on different thin films like substrate, dielectric, and membrane. With the comprehensive analysis, it is clear that the serpentine structure is offering extraordinary features in the form of pull-in voltage and switching time. The material analysis is revealed that silicon, HfO₂, and Aluminium (Al) are the best material for substrate, dielectric, and membrane thin films. Finally, we designed a switch with improved performance, the switch offering an actuation voltage of 3.68 V, insertion losses of -0.55 dB, and isolation losses of -51 dB. The designed switch is suitable for K and Ka-band applications like radar and satellite applications.

Keywords: Material science, MEMS technology, Microstructure, RF switches, Thin films.

1. Introduction

Radio Frequency (RF) switches are very needy devices in future high-frequency mobile communication applications. Especially in the design of transceivers, the RF switches are primarily used for frequency tuning and frequency reconfigurability. Low power consumption is the potential research challenge in RF switches, which extremely influences the battery lifetime. Solid state technology and the MEMS technology offers fine performance RF switches.

However, the MEMS technology is the rapidly growing technology with great potential which offers low power consumption, high linearity, and high reliability. The solid-state technology RF switches, i.e., PiN diodes performance is not up to the level of requirement of 5G communication. But the MEMS centred RF switches are offering the finest performance when matched with solid state technology-based RF switches. Not only RF switches, MEMS technology proved its ability in the design of filters, varactors which are essential devices in mobile communication applications [1].

The RF MEMS switches are adopted by high-frequency potential applications because of offering great performance in terms of low power consumption, high isolation, and high linearity. Despite these features, the RF MEMS switches have some potential research challenges, i.e., high actuation voltage(20-80 V), high switching time (1-300 μ s), and low isolation. Prior performance analysis helps to advance the switches performance in mechanical, electrical and radio frequency multi-physics. These basically are classified as series and shunt. However, shunt type switches are appropriate for high frequency and series type switches are appropriate for low frequency applications.

K-band, and Ka-band covers the frequency in the range of 18-27 GHz, and 27-40 GHz respectively, which have some potential millimetre-wave applications like vehicle speed detection, satellite communication, satellite television, and radar astronomical observation and microwave communication [2].

With the motivation of research challenges of RF MEMS switches, in this paper, we have analysed and improved the performance of switches by doing simulations using FEM tools which are suitable for K-band, and K-band applications. Curiously and dedicatedly many researchers have proposed different shunt switches with different materials and membrane structures [3]. Cantilever, clamped-clamped, folded, and serpentine structures are adopted by many researchers. Proper selection of thin-films, i.e., substrate, dielectric, and membrane for the design of these switch helps to advance the switch performance [4-9]. In this paper, we analysed and enhance the performance of shunt capacitive switch with proper performance analysis, i.e., structural and material analysis.

2. Related Work

Several investigations advanced the research on micro electromechanical switches [10]. Improving the performance of these switch is a potential research aspect, so researchers curiously advanced the research on shunt switches. But because of the requirements in high-frequency communication applications, still these switches have few research challenges like low actuation voltage, high isolation, and low insertion.

Dubuc et al. [10] primarily described the parameters influencing the reliability of these switches, like dielectric chagrining. Bridge type micromechanical structure is incorporated in these switches. The authors proposed RF MEMS switches for future 5G communication applications.

Badia et al. [11] mainly demonstrated the shunt capacitive switch. The role of dielectric material on the performance is analysed. Si_3N_4 and AlN dielectric material are taken into consideration in the performance analysis. The switch with AlN as a dielectric material offering up-capacitance of 98.67 fF, and the down-capacitance of 1.295 pF.

Laxma and Shanmuganatham [12] proposed a novel shunt capacitive switch with AlN dielectric thin film for high capacitance ratio. The switch is offering an actuation voltage of 5 V for 1 μm gap, insertion of -0.5 dB, and isolation of -55 dB.

Table 1. Comprehensive study on shunt capacitive RF MEMS switches.

Ref.	Description	Limitations
[13]	Together with the analytical measurement tests, a numerical technique is provided to determine the release time of the gold cantilever switch which is thermally curled in micrometre size. Beam dimension is $400 \times 200 \times 2 \mu\text{m}$, frequency range 0.1-40 GHz, and input power is 0-10 W.	Actuation voltage is very high. Material analysis no performed.
[14]	A lateral-capacitive transition was actuated electro thermally processed built and assembled using bulk micromachining. In because of this turn, the HfO_2 was used as a dielectric substance which offers excellent legal and electric characteristics. Actuation voltage 40-80 V, spring constant 42 N/m, mass flow rate is 9.8×10^{-6} kg/s.	Switching time of the switch is not discussed.
[15]	Shunt capacitive switches with K-band control were built using GaAs III-V manufacturing method completely compliant with normal MMIC output.	Actuation voltage analysis is not performed.
[16]	A simplifies and coherent model of study using yang power simulation model was introduces perforated shunt turn considering fringing area impact attributable to scale of finite board, thickness of beam and each space.	Radio Frequency analysis is not performed.
[17]	It has been shown that a low cost and unorthodox imaging technique is effective for the optional characterisation of the capacitive switches suspended double-clamped bridge in switches. Capacitance ratio is in the range of 12-16.	Switching time of the switch is not discussed.
[18]	The FEM tool level analysis of a tunable antenna equipped with CPW stub, on which these switches are mounted. Air gap (d) 3 μm , C_{up} is 39.65 fF, and C_{down} is 2.2 pF.	Material analysis no performed.
[19]	SiN_x 's electrical properties with embedded CNT's by chance bunches arranged or vertically positioned, and Au nanorods were investigated. The electric properties are considered to be important affected by both embedded and directed nano filter. Actuation voltage 30 V, air gap 3 μm .	Actuation voltage analysis is not performed.

3.Problem Statement

RF MEMS is the emerging technology which is adopted the high frequency mobile communication applications. RF MEMS switches are already proved their ability

in offering high performance with low power consumption. Exploratory findings and the advancements observed from the related work, we have identified a few potential research challenges of shunt capacitive switches for k-band and Ka-band applications. RF MEMS technology deals with different multi-physics, i.e., electrostatic, electromechanical, and electromechanical. Pull-in voltage is related to electrostatic, and these switches require more actuation voltage compared with solid-state technology switches.

The switching mechanism in switches primarily depends on the electromechanical deformation of the membrane. The switching time of the switches is in the range of the millisecond, but the IC technology demands the communication devices using high switching speed in nanoseconds. The radio frequency properties of MEMS switches primarily depend on the dielectric material and the membrane structure, proper selection of the membrane, and the materials help to accelerate the performance. In this paper, we have primarily elevated the factors which majorly influences the performance of electrostatic ally actuated shunt capacitive RF MEMS switches, i.e., actuation voltage, switching time, and RF losses.

Table 2. Problem statement.

Multi-physics	Parameter	Solution
Electrostatic	Actuation voltage	Proper structural analysis helps to reduce the actuation voltage.
Electromechanical	Switching time	Low spring constant structures will offer high switching speed.
Electromagnetic	Insertion and isolation losses	The material analysis for the different thin films significantly improves the insertion and isolation properties.

4. Performance Analysis

In this paper, especially we have analysed two structures, i.e., clamped-clamped and serpentine structure. The performance of electrostatically actuated shunt capacitive these switches is analysed by considering the role of membrane structure and thin-film materials.

4.1. Theoretical analysis

The overall mass (m) of the micromechanical structure can be measure with $m = \rho \times l \times w \times t$, where ρ - material density, l - length, w - width, t - thickness. Spring constant will vary from flexure to flexure, for the clamped-clamped flexure the spring constant (k) can be expressed as [13, 14],

$$k = 4Ew \left(\frac{t}{l}\right)^3 \quad (1)$$

For the serpentine flexure with material young's modulus (E), the spring constant can be expressed as,

$$\frac{1}{K} = \frac{1}{K_1} + \frac{1}{K_2} + \frac{1}{K_3} + \frac{1}{K_4} \quad (2)$$

where,

$$K_{(1,2,3,4)} = \frac{Ewt^3}{l^3}$$

The switching time is one of the primary parameters which decides the switch performance, the switching time can be formulate with the help of resonant frequency. The free body analysis, as shown in Fig. 1, we can extract the expression for the resonant frequency, i.e.,

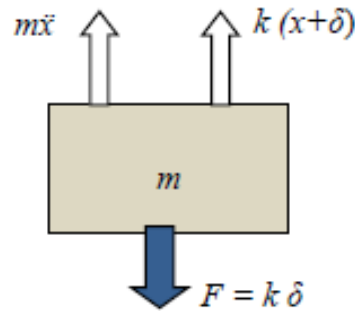


Fig. 1. Free body analysis.

$$m \ddot{x} + k(x+\delta) - F = 0 \quad (3)$$

$$m \ddot{x} + kx + k\delta - k\delta = 0$$

$$\ddot{x} + (k/m)x = 0$$

By comparing above equation with simple harmonic motion, i.e.,

$$\ddot{x} + \omega^2 x = 0 \quad (4)$$

Therefore,

$$\omega^2 = k/m$$

$$\omega = \sqrt{\frac{K}{m}}$$

$$f_r = \frac{1}{2\pi} \sqrt{\frac{K}{m}} \quad (5)$$

The switching time (t_s) of the clamped-clamped and serpentine flexure is expressed as,

$$t_s = 3.67 \frac{V_p}{v_s \omega_0} \quad (6)$$

The electrostatically actuated switch parameters mainly rely on the pull-in voltage, it can be expressed as,

$$V_{pull-in} = \sqrt{\frac{8kg^3}{27A\epsilon_0}} \quad (7)$$

Compared to series DC contact switches, shunt capacitive switches offer best performance at high frequency applications. The shunt capacitive switch upstate capacitance (C_{up}) and downstate capacitance (C_{down}) can be expressed as,

$$C_{up} = \frac{\epsilon_0 A}{g + \frac{t_d}{\epsilon_r}} + C_f \quad (8)$$

$$C_{down} = \frac{\epsilon_0 \epsilon_r A}{t_d} \quad (9)$$

where g - air gap, A - cross sectional area, ϵ_r - relative permittivity, t_d - dielectric thickness.

4.2. Structural Analysis

The parameters of the switch primarily be contingent on the micro mechanical structure incorporated. The actuation voltage is majorly influenced by the spring content of the micro mechanical structure.

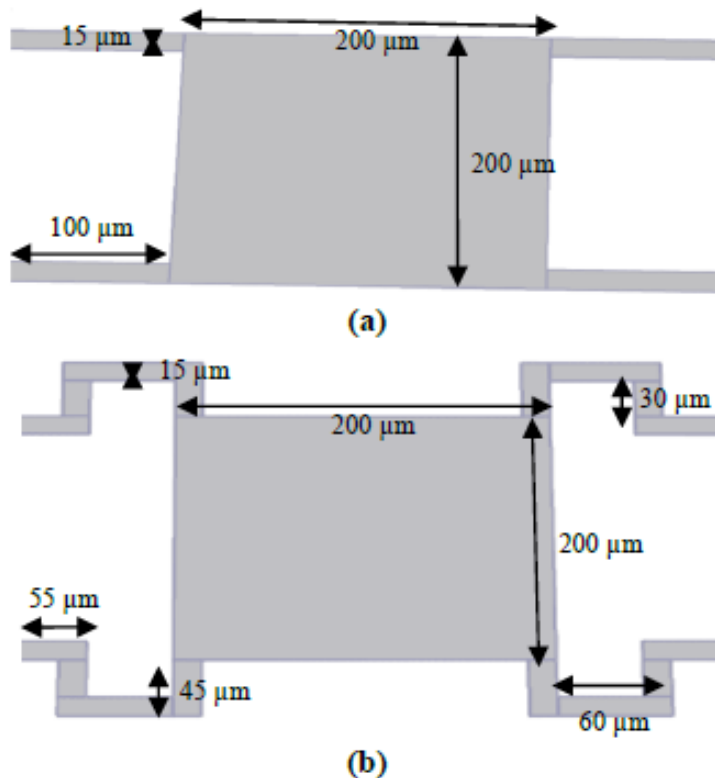


Fig. 2. Structural analysis, (a) clamped-clamped, (b) serpentine flexure with uniform meanders.

The low spring constant structure obviously offers low actuation voltage. Previously there are so many popular structures are proposed by different researchers, here we have taken clamped-clamped structure and serpentine structure shown in Fig. 2, for performance analysis. Gold material with young's modulus (E) of 70 GPa, and density (ρ) of 19300 kg/m³. The thickness of the structure is taken as 1 μm.

Both micro mechanical structures are designed with gold metal and actuated electrostatically. The actuation voltage of the structure with clamped-clamped flexure is 7.5 V and the structure with serpentine flexure is 5 V for one micrometre displacement as shown in Fig. 3.

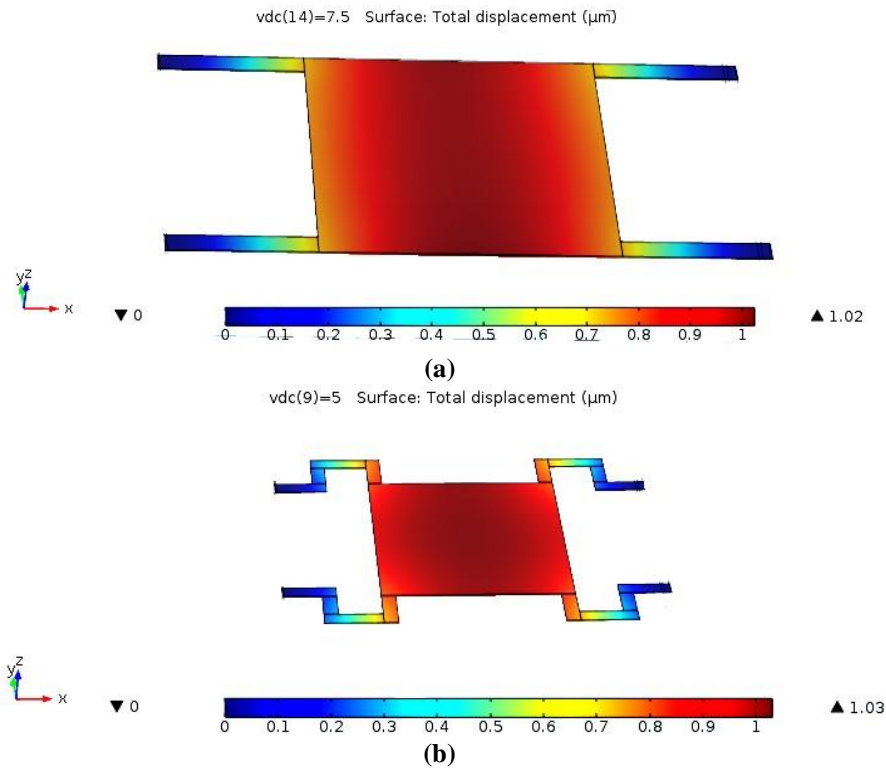
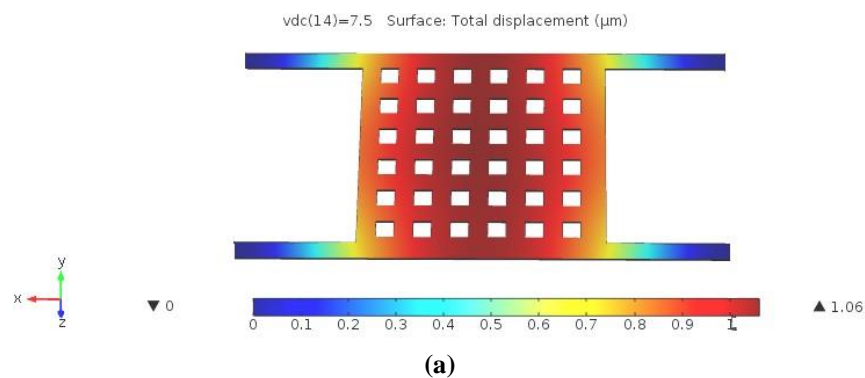


Fig. 3. Electrostatic actuation, (a) clamped-clamped, (b) serpentine structure.

4.3. Perforation analysis

Perforation to the micromechanical structure helps in the process of load distribution and improves the switch reliability. The perforation also helps to reduce the required actuation voltage in electro-statically actuated switches. Here we have perforated the micromechanical structure with holes of dimension $15\ \mu\text{m} \times 15\ \mu\text{m}$ as shown in Fig 4. Because of the perforation the required actuation voltage is reduced for both the structures. Because of the perforation the micromechanical structures displacement is increased an amount of $0.04\ \mu\text{m}$. It is clear that compared to the clamped-clamped flexure, serpentine flexure is offering low actuation voltage.



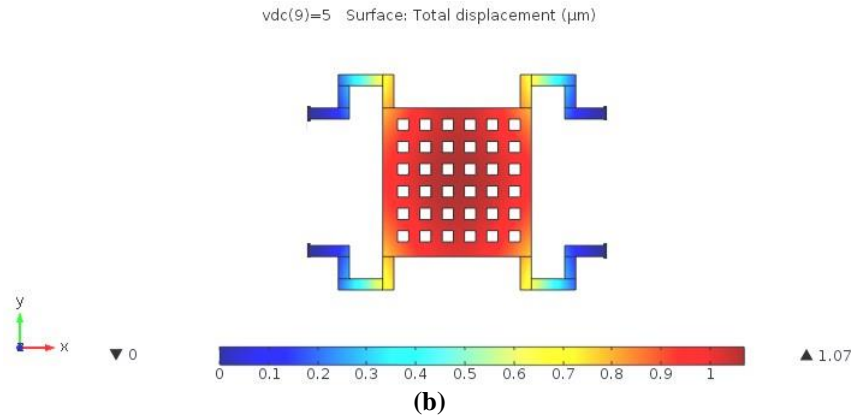


Fig. 4. Effect of perforation, a) clamped-clamped flexure, b) serpentine flexure with uniform meander.

So, further analysis is done on the serpentine structure. From the structural analysis it is clear that serpentine structure is offering low actuation voltage compared with clamped-clamped structure. The stiffness of the serpentine structure is very low when compared with clamped-clamped structure this is the primary reason of offering of low actuation voltage. So further analysis is performed on the serpentine structure.

4.4. Meander Analysis

Perfect design of membrane eventually decides the RF MEMS switch performance. From the previous analysis it is clear that the serpentine membrane with uniform meander is offering best performance compared with clamped-clamped structure. In this sub section, we analysed the role of type of meander, i.e., uniform and non-uniform meander of the serpentine membrane on the actuation voltage shown in Fig. 5.

After observing the electrostatic actuation, it is clear that compared to uniform meanders, the non-uniform meander serpentine structure is offering a low actuation voltage. The structure is offering a displacement of $1\ \mu\text{m}$ for $4.5\ \text{V}$ shown in Fig. 6. The above analysis is performed by considering the gold (Au) as the membrane material. Perforation to the membrane is an extra added advantage to the switch performance which helps to reduce actuation voltage.

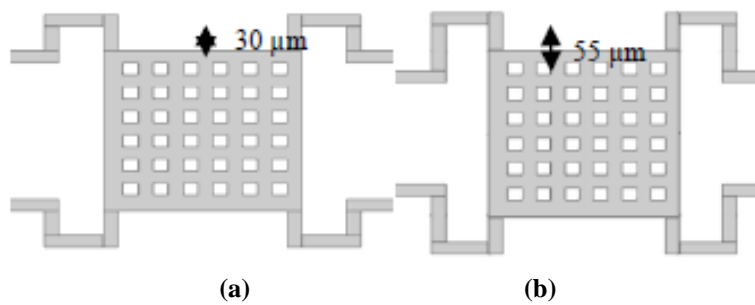


Fig. 5 Serpentine structure meander analysis, (a) uniform meanders, (b) non uniform meanders.

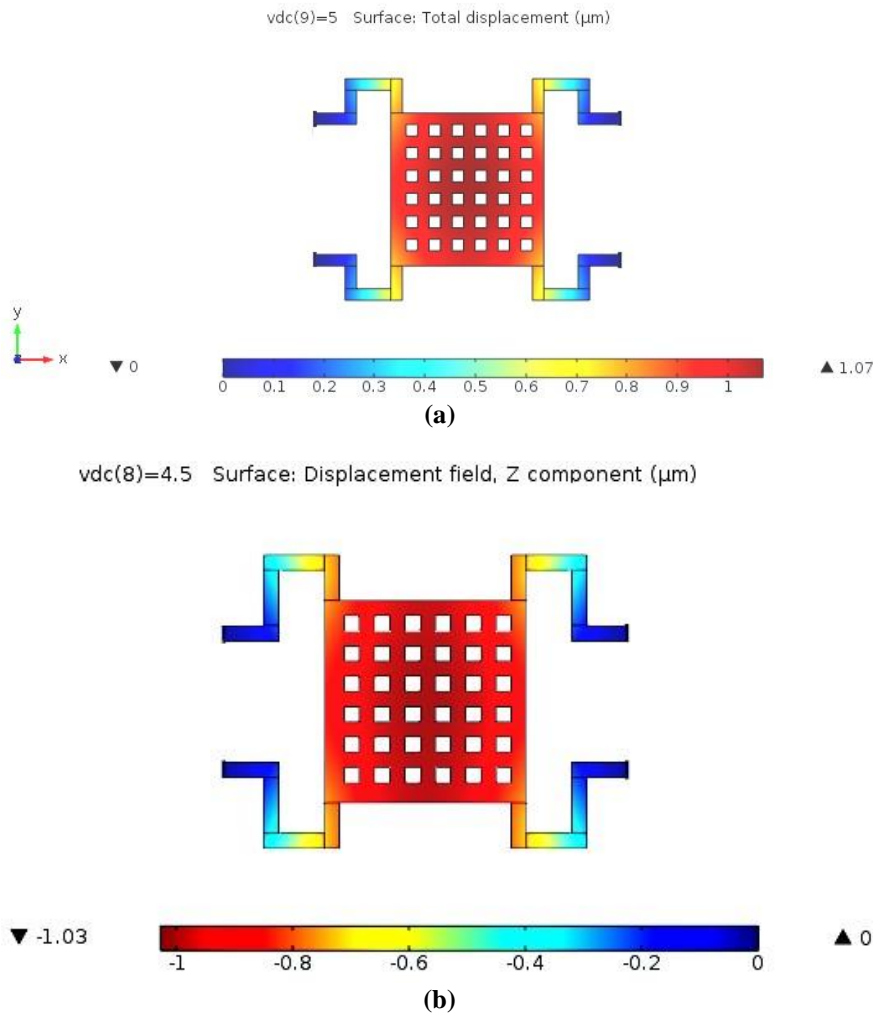


Fig. 6. Electrostatic actuation of serpentine flexure with, (a) uniform, (b) non-uniform meanders.

4.5. Switching time

The switching time (t_s) is generally defined as the time taken by the switch to complete ON and OFF action. The time taken by the membrane to come to down state after applying the appropriate DC voltage is known as the switch ON time represented with t_{ON} , similarly the time required to come to the upstate after applying Zero DC voltage is known as switch OFF time and is represented with t_{OFF} . The total switching time is combination of t_{ON} and t_{OFF} , i.e., $t_s = t_{ON} + t_{OFF}$. The spring constant of the micromechanical structure primarily influences the switching time. If the stiffness of structure low the switching time is low as shown in the Fig. 7. The serpentine structure with meanders is flexible and deforms for low voltages, because of this flexibility the structure is offering low switching time compared with clamped-clamped structure. The switching time of the serpentine structure is $45 \mu\text{s}$ and the clamped-clamped structure is $80 \mu\text{s}$.

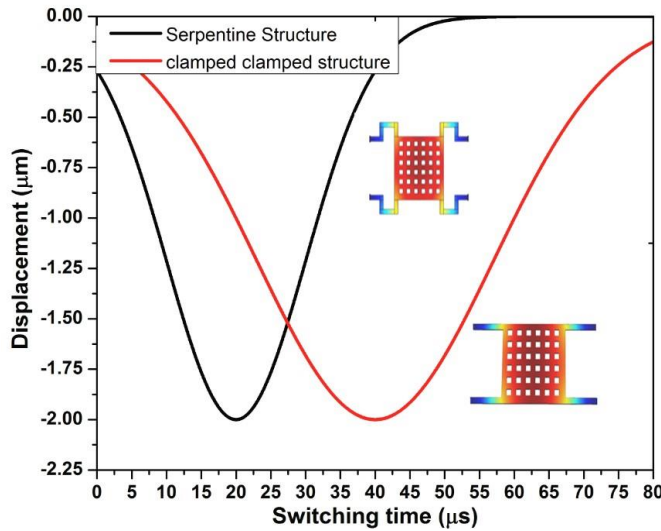


Fig. 7. Switching time (t_s) of the clamped-clamped and serpentine structures.

4.6. Material analysis

The shunt capacitive switch micro machined by deposition of different thin films, i.e., electromagnetic lines, dielectric thin film, membrane thin film on the substrate. The proper selection of the materials for these thin films helps to improve the performance. The serpentine membrane shown in Fig. 6, electrostatic actuation performance is analysed with different membrane materials, i.e., Al, Au, Ag, Cu, Cr, and W.

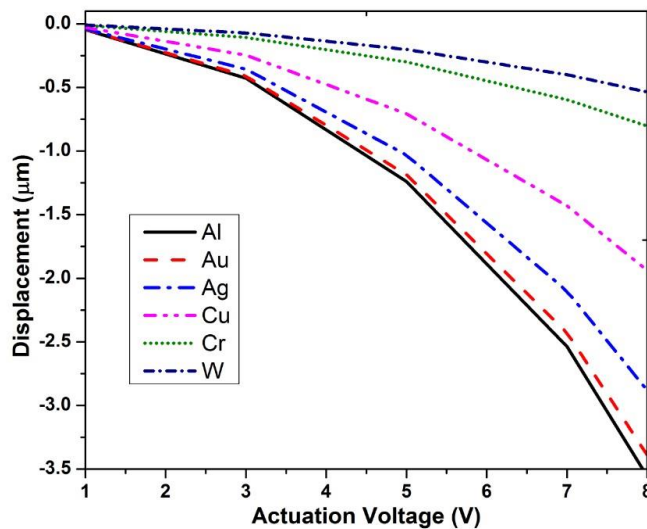


Fig. 8. Serpentine membrane material analysis.

The serpentine membrane material analysis revealed that the Al is offering low actuation voltage compared with the other metals, i.e., Au, Ag, Cu, Cr, and W. Light weight material deforms for less external force, here Al is a lightweight metal

compared with the others, so it deformed for low actuation voltage. The shunt capacitive switch performance relies on the capacitance offered by the switch when membrane in up and down state. Here we have performed the capacitance analysis by choosing different dielectric material, i.e., HfO_2 , AlN , ZnO , Si_3N_4 , Al_2O_3 , SiO_2 .

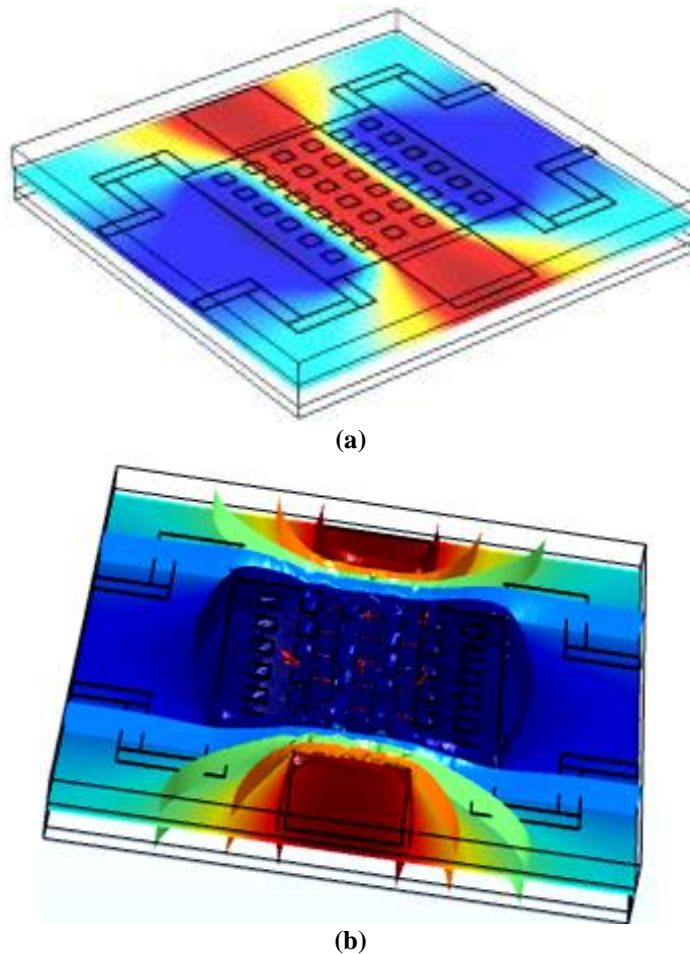
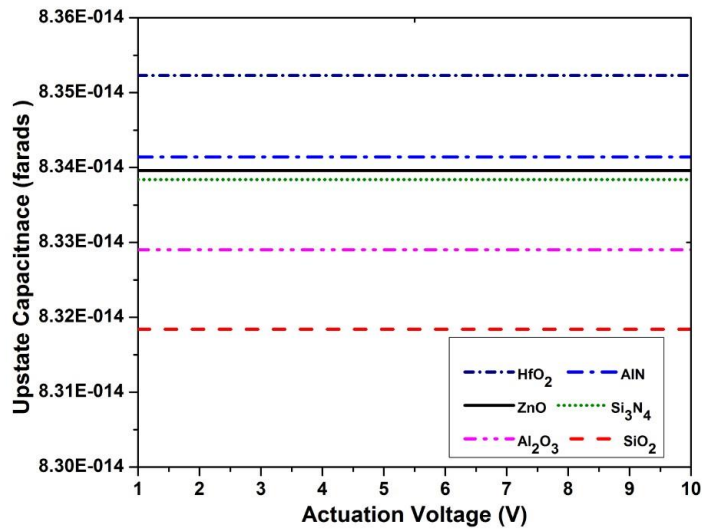
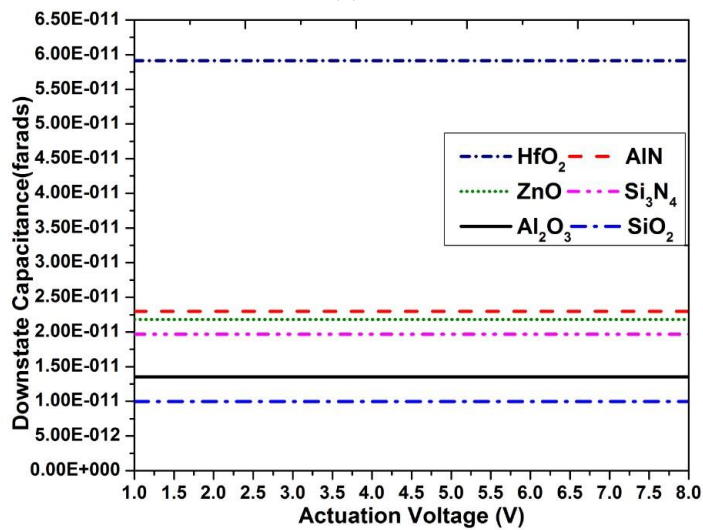


Fig. 9. Switch capacitance analysis, (a) Electrostatic analysis, (b) fringing fields.

When no actuation voltage applied, the micromechanical membrane is in upstate, and the capacitance presented by the switch is known as the upstate capacitance. If the applied actuation voltage is above the pull-in voltage the membrane will deform and come to down state, and the capacitance presented by the switch is known as the downstate capacitance. The Radio Frequency (RF) properties, i.e., insertion losses and the isolation losses are completely depending on the up and down capacitance of the switch. The dielectric material analysis with different materials, i.e., HfO_2 , AlN , ZnO , Si_3N_4 , Al_2O_3 and SiO_2 revealed that high relative permittivity material offers great performance in terms of capacitance. The relative permittivity of the HfO_2 is 25, and the up- capacitance is 83.52 fF and down- capacitance is 60 pF.



(a)



(b)

Fig. 10. Dielectric material capacitance analysis, (a) upstate capacitance, (b) downstate capacitance.

Table 3. Dielectric material capacitance analysis.

Material	Relative permittivity	Upstate capacitance (farads)	Downstate capacitance (farads)
HfO ₂	25	8.35 × 10 ⁻¹⁴	5.91 × 10 ⁻¹¹
AlN	9.8	8.342 × 10 ⁻¹⁴	2.30 × 10 ⁻¹¹
ZnO	9.7	8.339 × 10 ⁻¹⁴	2.18 × 10 ⁻¹¹
Si ₃ N ₄	9.6	8.336 × 10 ⁻¹⁴	1.97 × 10 ⁻¹¹
Al ₂ O ₃	5.7	8.33 × 10 ⁻¹⁴	1.35 × 10 ⁻¹¹
SiO ₂	4.2	8.32 × 10 ⁻¹⁴	0.98 × 10 ⁻¹¹

Prior performance analysis on shunt capacitance switch in terms of structure, material is revealed so many techniques, i.e., serpentine structure is offering low actuation voltage when compared with clamped-clamped structure, Al like lightweight materials also helps to improve the actuation voltage and the high relative permittivity material like HfO_2 as dielectric material helps to advance the capacitance ratio. By incorporating these all in the switch defiantly performance of the switch improves.

5. Proposed Model

Eventually we have designed a performance improved shunt capacitive switch on silicon substrate. Serpentine structure with non-uniform meanders designed with Al with $0.7 \mu\text{m}$ thickness. The membrane is perforated with $15 \mu\text{m} \times 15 \mu\text{m}$ size square holes which helped to reduce the actuation voltage. HfO_2 with relative permittivity (ϵ_r) of 25 is used as a dielectric material. By incorporation all the techniques revealed in the performance analysis in terms of structure and the material sure the overall performance is improved significantly. The coupled simulation is used in FEM tool with solid-mechanics and the electrostatic multi-physics. The spring constant, and membrane mass parameters are transferred between the physics. Extra fine meshing is used for better accuracy.

The switches design typically involves step by step deposition of different thin films, i.e., substrate, dielectric, and membrane thin film. Unlike previous designs, in this paper we are doing prior material analysis which helps to identify suitable material for different thin films. Completely the switch is micro machined on silicon substrate and $1 \mu\text{m}$ thickness SiO_2 is place in between substrate and CPW lines as an insulating layer.

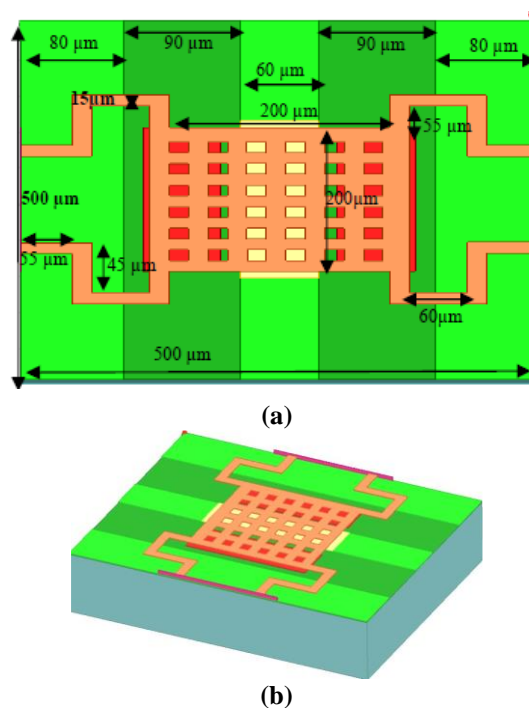


Fig. 11. Serpentine membrane switch, (a) top view, (b) side view.

Table 4. Dielectric material capacitance analysis.

Parameter	Material	Length×width×thickness in μm
Substrate	Si	500×500×800
Insulator	SiO ₂	500×500×1
CPW	Au	100×80×100
Dielectric	HfO ₂ ($\epsilon_r=25$)	220×80×0.05
Air Gap	-	2
Membrane	Al	2

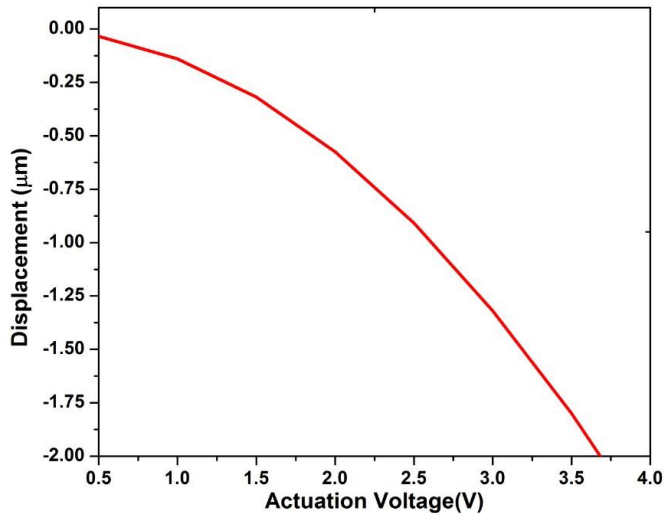


Fig. 12. Al 0.7 μm thickness membrane, actuation voltage (vs) Displacement.

If the applied DC voltage is below the pull-in voltage the micro mechanical membrane is in upstate, the RF signal is completely permitted to the output, so the switch is offering low insertion of -0.55 dB @ 23 GHz as shown in Fig. 13.

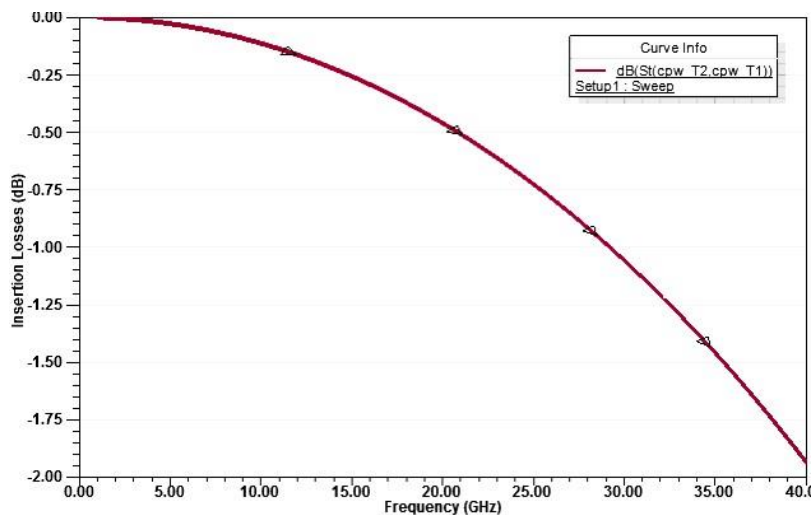


Fig. 13. Insertion Losses (dB).

The perforation to the membrane helps in uniform distribution of electrostatic force as shown in Fig.14. When the applied DC voltage is above the pull-in voltage, the structure will get deform and it will come to downstate as shown in Fig.15.

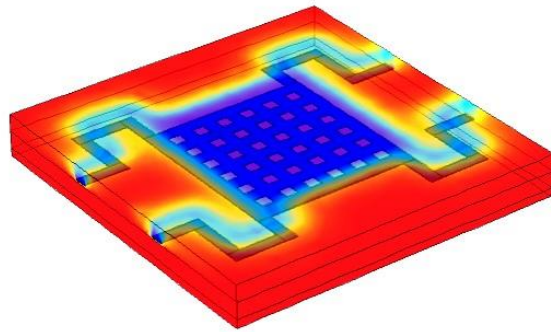


Fig. 14. Load distribution in non-uniform meander serpentine flexures.

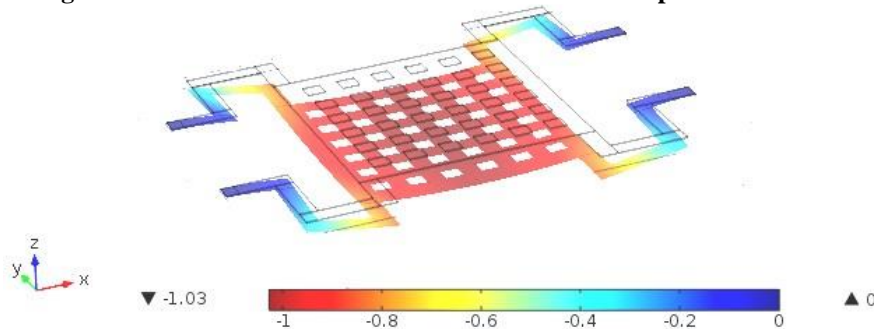


Fig. 15. Membrane is in downstate.

When the micromechanical structure is in down state the switch will offer high isolation of -51dB at 23 GHz. And the switch is offering an up-capacitance of 83.5 fF and the down-capacitance of 59.1 pF.

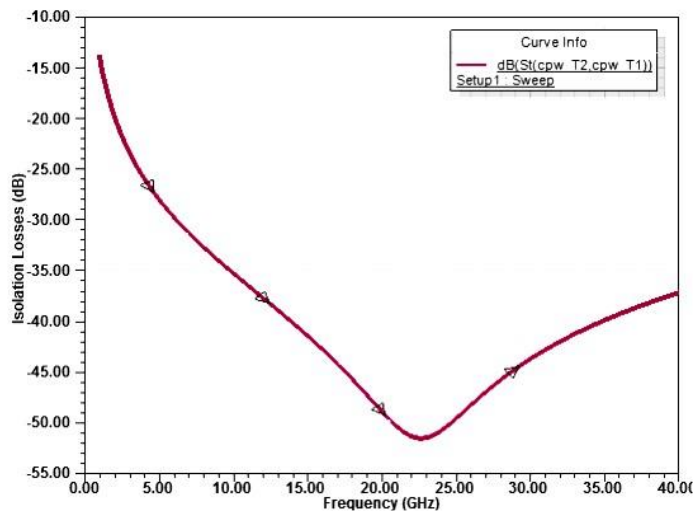


Fig. 16. Isolation losses (dB).

Eventually we have extracted most of the performance deciding parameters of the shunt capacitive switch and try to compare the theoretical and simulated values. Here the simulated results are near to the theoretical values. The mass of the serpentine structure is 783×10^{-12} kg. The serpentine structure with non-uniform meanders offered a low spring constant of 1.79 N/m. The Eigen frequency (or) natural frequency (or) resonant frequency is 7.445 kHz. The switch requires 3.68 V actuation voltage for 2 μm membrane downward deformation which created hope on possibility of integration of switches with IC technology. The novelty in the designed RF MEMS switch is incorporation of non-uniform meander based serpentine structure and high relative permittivity offering dielectric thin films. Because of this incorporation the switch performance is improved significantly.

Table 5. Dielectric material capacitance analysis.

Parameters	Serpentine with non-uniform meander	
	Theory	Simulation
Mass (m)	783×10^{-12} kg	783×10^{-12} kg
Spring constant (k)	2.07 N/m	1.79 N/m
Resonant frequency (f_r)	7785 Hz	7445 Hz
Actuation (V)	3.95 V	3.68 V
Upstate capacitance (C_{up})	80.39 fF	83.5 fF
Downstate capacitance (C_{down})	56.21 pF	59.1 pF

The major finding of this work is, because of incorporation of Al based serpentine membrane the required actuation voltage is reduced to 3.68 V. HfO_2 dielectric material, with high relative permittivity the switch is offered high capacitance ratio. Because of high capacitance ratio the switch offers high isolation of -51 dB.

Table 6. Dielectric material capacitance analysis.

Parameter	[20]	[21]	Our work
Mass (m)	---	---	783×10^{-12} kg
Spring constant (k)	---	---	1.79 N/m
Resonant frequency (f_r)	---	---	7445 Hz
Actuation Voltage	19.2 V	25.2 V	3.68 V
Upstate capacitance (C_{up})	22 fF	---	83.5 fF
Downstate capacitance (C_{down})	2.21 pF	---	59.1 pF
Insertion Losses (dB)	- 0.05 dB	- 0.1dB	- 0.55 dB
Isolation Losses (dB)	-12dB @ 61.5 GHz	-40 dB @ 11 GHz	-51 dB

6. Conclusions

Prior performance analysis with respect to structure and material definitely helped to improve the performance of switch. The structural analysis is performed on clamped-clamped and serpentine structures, and it is revealed that the serpentine structure is offering low actuation voltage. The material analysis is primarily aimed to select best material for the membrane and the dielectric thin films. The serpentine membrane with Al material of 0.7 μm thickness offers a low actuation voltage of 3.68 V. HfO_2 of 0.05 μm thickness is selected as a dielectric material which offers best up-capacitance of 83.5 fF and the down-capacitance of 59.1 pF. Eventually the

switch offers an insertion loss of -0.55 dB and isolation of -51 dB. The designed switch is suitable for K and Ka-band applications.

Nomenclatures

C_{down}	Downstate capacitance
C_{up}	Upstate capacitance
f_r	Resonant frequency
K	Spring constant
m	Membrane mass

Abbreviations

FEM	Finite Element Method
-----	-----------------------

References

1. Nabet, M.; Rack, M.; Hashim, N.Z.I.; de Groot, C.H.; and Raskin, J.-P. (2019). Behavior of gold-doped silicon substrate under small- and large-RF signal. *Solid-State Electronics*, 168, 107718.
2. Chaudhary, R.; and Mudimela, P.R. (2020). Pull-in response and eigen frequency analysis of graphene oxide-based NEMS switch. *materialstoday: Proceedings*, 28(Part 1), 196-200.
3. Angira, M.; Bansal, D.; Kumar, P.; Mehta, K.; and Rangra, K. (2019). A novel capacitive RF-MEMS switch for multi-frequency operation. *Super lattices and Microstructures*, 133, 106-204.
4. Thalluri, L.N.; Guha, K.; Rao, K.S.; Prasad, G.V.H.; Sravani, K.G.; Sastry, K.S.R.; Kanakala, A.R.; and Babu, P.B. (2020). Perforated serpentine membrane with AlN as dielectric material shunt capacitive RF MEMS switch fabrication and characterization. *Microsystem Technologies*, 26, 2029-2041.
5. Ouakad, H.M.; Sedighi, H.M.; and Younis, M.I. (2017). One-to-one and three-to-one internal resonances in mems shallow arches. *Journal of Computational and Nonlinear Dynamics*, 12(5): 051025 (11 pages)
6. Ouakad, H.M.; and Sedighi, H.M. (2019). Static response and free vibration of MEMS arches assuming out-of-plane actuation pattern, *International Journal of Non-Linear Mechanics*, 110, 44-57.
7. Sedighi, H.M. (2014). Size-dependent dynamic pull-in instability of vibrating electrically actuated microbeams based on the strain gradient elasticity theory. *Acta Astronautica*, 95, 111-123.
8. Sedighi, H.M.; and Shirazi, K.H (2015). Dynamic pull-in instability of double-sided actuated nano-torsional switches, *Acta Mechanica Solida Sinica*, 28(1), 91-101.
9. Nasr, M.E.; Abouelregal, A.E.; Soleiman, A.; and Khalil, K.M. (2021). Thermoelastic vibrations of nonlocal nanobeams resting on a pasternak foundation via DPL model. *Journal of Applied and Computational Mechanics*, 7(1), 34-44.

10. Dubuc, D.; Grenier, K.; and Iannacci, J. (2018). RF-MEMS for smart communication systems and future 5G applications. *Smart Sensors and MEMS*, 2018, 499-539.
11. Badia, M.F.-B.; Buitrago, E.; and Ionescu, A.M. (2012). RF MEMS shunt capacitive switches using AlN compared to Si₃N₄ dielectric. *Journal of Microelectromechanical Systems*, 21(5), 1229 - 1240.
12. Laxma, R.B.; and Shanmuganatham, T. (2014). Design of Novel Capacitive RF MEMS Shunt Switch with Aluminum Nitride (AlN) Dielectric. *Procedia Materials Science*, 6, 692-700.
13. Jensen; B.D.; Saitou, K.; Volakis, J.L.; and Kurabayash, K. (2003). Fully Integrated electrothermal multidomain modeling of RF MEMS switches. *IEEE Microwave and Wireless Components Letters*, 13(9), 364-366.
14. Barbato, M.; Giliberto, V.; Cester, A.; and Meneghesso, G. (2014). A Combined Mechanical and Electrical Characterization Procedure for Investigating the Dynamic Behavior of RF-MEMS Switches. *IEEE Transactions on Device and Materials Reliability*, 14(1), 13-20.
15. Cheulkar. L.N.; Sawant, V.B.; and Mohite, S.S. (2020). Evaluating performance of thermally curled microcantilever RF MEMS switches. *materialstoday: Proceedings*, 27(Part 1), 12-18.
16. He, X.J.; Lv, Z.Q.; Liu, B.; and Li, Z.H. (2012). High-isolation lateral RF MEMS capacitive switch based on HfO₂ dielectric for high frequency applications. *Sensors and Actuators A: Physical*, 188, 342-348.
17. Persano, A.; Tazzoli, A.; Farinelli, P.; Meneghesso, G.; Siciliano, P.; and Quaranta, F. (2012). K-band capacitive MEMS switches on GaAs substrate: Design, fabrication, and reliability. *Microelectronics Reliability*, 52(9-10), 2245-2249.
18. Guha, K.; Kumar, M.; Agrawal, S.; and Baishya, S. (2015). A modified capacitance model of RF MEMS shunt switch incorporating fringing field effects of perforated beam. *Solid-State Electronics*, 114, 35-42.
19. Persano, A.; Quaranta, F.; Martucci, M.C.; Siciliano, P.; and Cola, A. (2015). On the electrostatic actuation of capacitive RF MEMS switches on GaAs substrate. *Sensors and Actuators A: Physical*, 232, 202-207.
20. Pertin, O.; and Kurmendra (2018). Pull-in-voltage and RF analysis of MEMS based high performance capacitive shunt switch. *Microelectronics Journal*, 77, 5-15.
21. Younis, S.; Saleem, M.M.; Zubair, M.; and Zaidi, S.M.T. (2018). Multiphysics design optimization of RF-MEMS switch using response surface methodology. *Microelectronics Journal*, 71, 47-60.

LOCALIZATION AND DEBUGGING OF MULTIPLE FAULTS IN ARITHMETIC CIRCUITS

Mr.P.Bose Babu,M-Tech(Ph.D)
Professor Department of ECE
Andhra Loyola Institute of Engineering
and Technology,Vijayawada,
India.
E-mail:pbosebabu@alieta.ac.in

Mule.Madhava Reddy
Student,DepartmentofECE,
Andhra Loyola Institute of Engineering
and Technology,Vijayawada,
India.
E-mail:mulemadhava724@gmail.com

Kosuri Charan Naga Sai
Student, Department of ECE,
Andhra Loyola Institute of
Engineering and Technology,
Vijayawada, India.
E-mail:charannagasai2001@gmail.com

Puppala Dunesh Siva Kumar
Student, Department of ECE,
Andhra Loyola Institute of Engineering
and Technology, Vijayawada, India.
E-mail:duneshpuppala@gmail.com

Abstract—Optimised and custom arithmetic circuits are widely used in embedded systems such as multimedia applications, cryptography systems, signal processing and console games. Debugging of arithmetic circuits is a challenge due to increasing complexity coupled with non standard implementations. However, bug localization remains a major issue. simulation based validation using random or constrained-random tests are not effective for complex arithmetic circuits due to bit-blasting. In this model it will present an automated test generation and bug localization technique for debugging arithmetic circuits

Finally our model is fully automated. In other words this model is capable of producing a correct implementation of arithmetic circuits with out any manual interaction. Our experimental results demonstrate that the proposed approach can be used for automated debugging of large and complex arithmetic circuits

Keywords—Arithmetic circuits, Multiplier, Bugs, Independent bug, Dependent bug, Hybrid bug, Error Localization, Error Detection and Error Correction.

I. INTRODUCTION

A bug is just an error that has to be corrected in localization words. All problems (errors) found during localization testing are recorded in a database that keeps track of these entries. Then, a tester assigns each bug's resolution to the proper party, based on the software's knowledge requirements, linguistic ability, and source of the mistake. For instance, developers must fix various internationalisation problems. Most problems in source code or its design are the result of human error. When a programme has numerous defects that interfere with its functionality and produce unintended outcomes, it is said to be buggy.

Software bugs can result from misunderstandings and errors occurring when deriving requirements from users, planning a program's design, developing its source code, and interacting with people, hardware, and other programmes, including operating systems or libraries. Often, a programme is said to be buggy if it has numerous, or significant, defects. Errors caused by bugs may have repercussions. The effects of bugs can range from subtle, like unexpected text

formatting, to more overt, such as crashing a programme, locking up the computer, or breaking hardware. Other flaws fall under the category of security flaws and could, for instance, allow a hostile user to evade access controls and get unauthorised rights.

II. LITERATURE SURVEY

In [1] In order to rectify all provided counterexamples, this approach finds logic gates that need to be swapped out for alternative logic functions

In [2] The introduction of bug patterns lengthens the time that SMT solvers take to run. We provide a more effective approach that uses programme slicing and constraints created from the counterexamples to decrease the running time while also reducing the quantity of the design description that needs to be translated to an SMT formula and the number of bug candidates

In [3] The introduction of bug patterns lengthens the time that SMT solvers take to run. We provide a more effective approach that uses programme slicing and constraints created from the counterexamples to decrease the running time while also reducing the quantity of the design description that needs to be translated to an SMT formula and the number of bug candidates.

In [4] Bugs must be detected and repaired as early in the development process as is practical. This is the main rule for semiconductor design and verification. It's commonly believed that finding a bug at each new project stage increases the cost by 10.

In [5] The standard specifies how Verilog HDL's semantics are used, among other things, to specify level- and edge-sensitive logic. Additionally, it explains the language's grammar in terms of what must be supported and what must not be supported for interoperability

In [6] We provide BLUIR, a structured retrieval method that incorporates our insights, and demonstrate that BLUIR outperforms the current cutting-edge IR-based bug localization techniques

In [7] They developed Csmith, a tool for randomly generating test cases, to enhance the quality of C compilers, and they spent three years hunting for compiler flaws with it. Over the course of this time, we notified compiler

III. PROPOSED ARCHITECTURE

The primary goal of the project is to detect and correct the faults in arithmetic circuits, we are using three types of bugs in our proposed model those are Independent bug, Dependent bug and Hybrid bug. To detect and correct these bugs, the algorithms used are Error Localization, Error Detection and error Correction. In this proposed model we used process called BIST (Built In Self Test).

- A. Generating the Multiplier
- B. Synthesizing
- C. Bug Localization
- D. Bug Correction

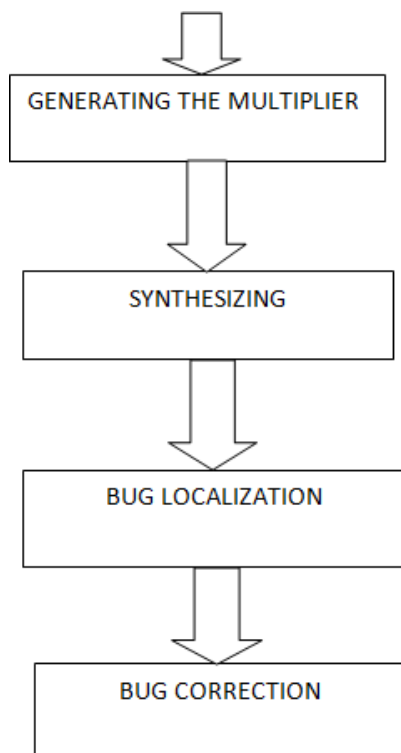


Figure 1: Proposed Model

1. Multiplier

Many high performance systems depend on multipliers as essential parts. However, as speed and area are frequently at odds with one another, increasing speed primarily leads to larger areas. As a result, a wide range of multipliers with various area-speed constraints have been created using fully parallel architecture. These multipliers perform only averagely in terms of speed and area. No matter how big the multiplier is, the benefit of pipelining at the digit level is constant operation speed.

By multiplying each bit of the multiplicand by each bit of the multiplier to get the partial products, the circuit implements a two-bit by two-bit multiplier. The total product is then calculated by weighting and adding the partial products.

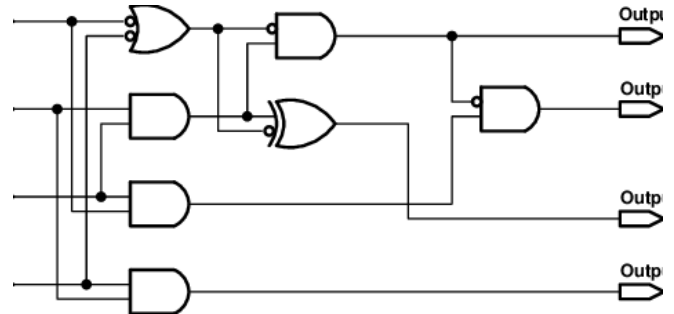


Figure 2 :2-Bit Multiplier

3. 4-bit Multiplier

The algorithm will finish in no more than 4 cycles for a 4-bit multiplication. The method is only lengthy multiplication. The lengthy multiplication of two 4-bit data to yield an 8-bit output is seen below.

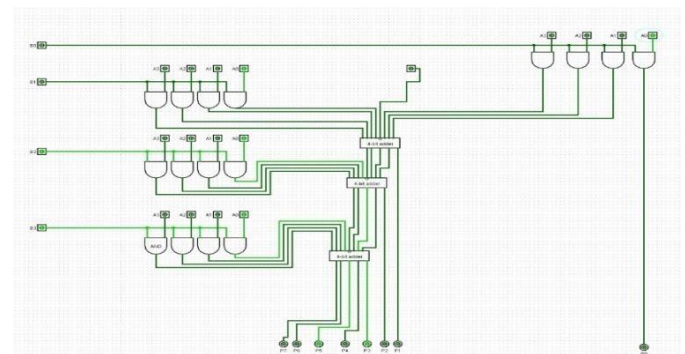


Figure 3 :4-Bit Multiplier

IV. Results

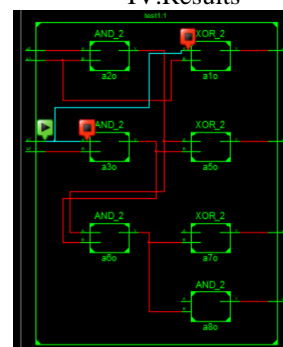


Figure 4 : Faulty 2-Bit Independent RTL Schematic Circuit

The above figure shows a schematic circuit with an independent bug present inside the circuit, where a1 a2 b1 and b2 are the inputs and o1 o2 o3 and o4 are the outputs of the circuit, where as o5,o6,o7 and o8 are the bug outputs. When outputs o1 and o5 are different, then an error e1 arises. But when the outputs o1 and o5 are same then there will not be any error. (Error free).

When outputs o2 and o6 are different, then an error e2 arises. But when the outputs o2 and o6 are same then there will not be any error. (Error free).

When outputs o3 and o7 are different, then an error e3 arises. But when the outputs o3 and o7 are same then there will not be any error. (Error free).

When outputs o4 and o8 are different, then an error e4 arises. But when the outputs o4 and o8 are same then there will not be any error. (Error free)

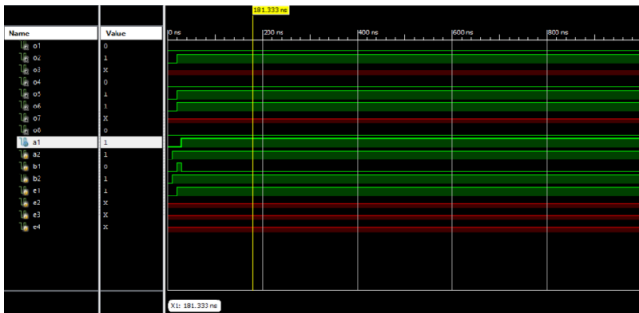


Figure 5 : Error Localization of 2-Bit Independent Circuit

In the above figure o1 and o5 are not equal so error is localized to correct the error we have to use the error correction logic using Xilinx tool.



Figure 6 : Error Correction of 2-Bit Independent Circuit

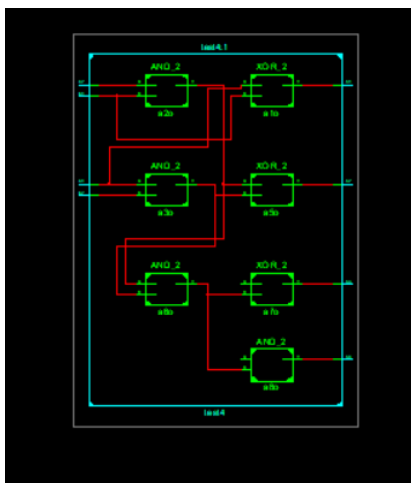


Figure 7 : Faulty 2-Bit Dependent RTL Schematic Circuit

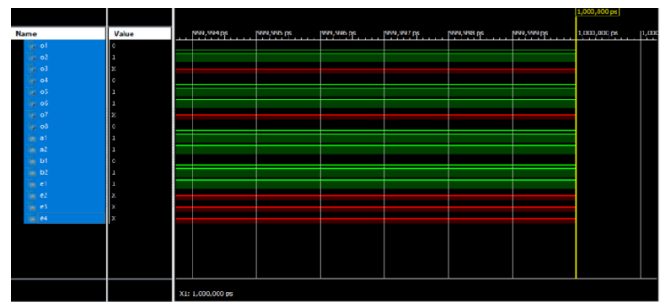


Figure 8 : Error Localization of 2-Bit Dependent Circuit

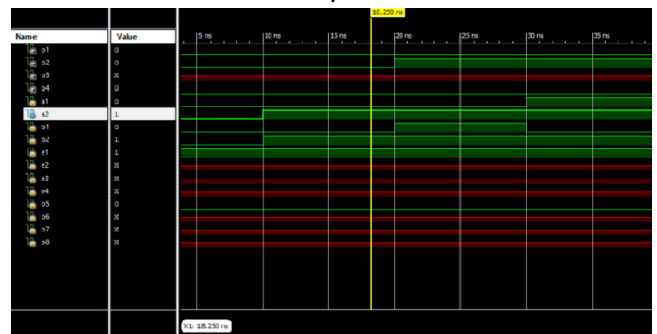


Figure 9 : Error Correction of 2-Bit Dependent Circuit

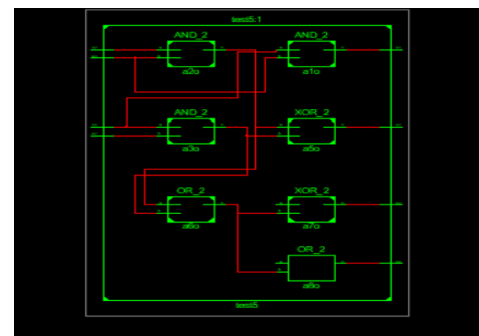


Figure 10 : Faulty 2-Bit Hybrid RTL Schematic Circuit

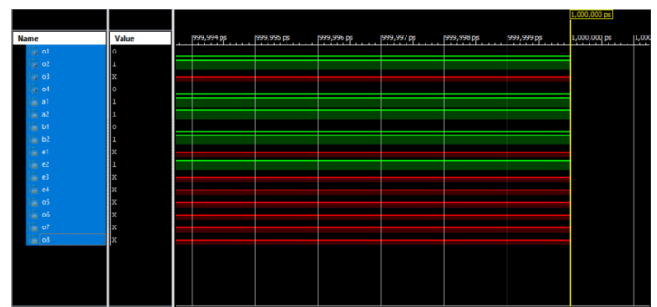


Figure 11 : Error Localization of 2-Bit Hybrid Circuit

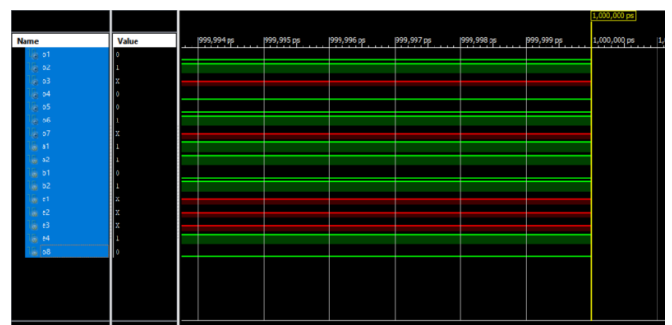


Figure 12 : Error Correction of 2-Bit Hybrid Circuit

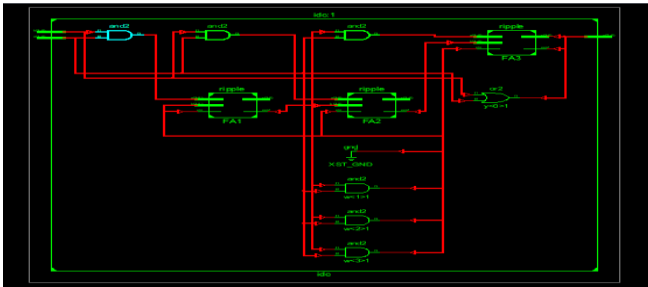


Figure 13 : Faulty 4-Bit Independent RTL Schematic Circuit

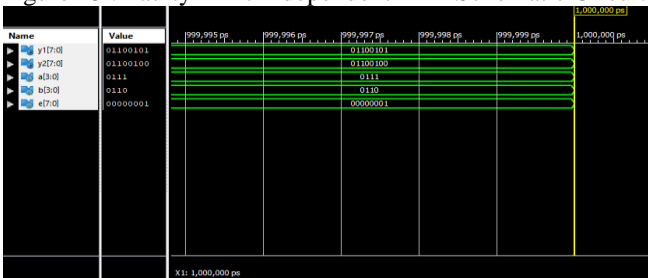


Figure 14 : Error Localization of 4-Bit Independent Circuit

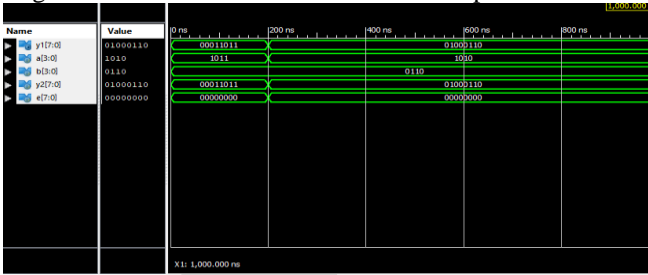


Figure 14 : Error Correction of 4-Bit Independent Circuit

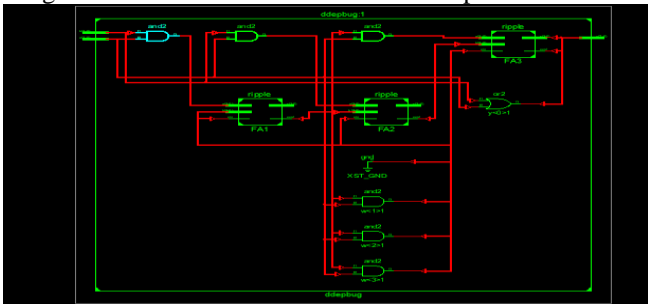


Figure 13 : Faulty 4-Bit Dependent RTL Schematic Circuit

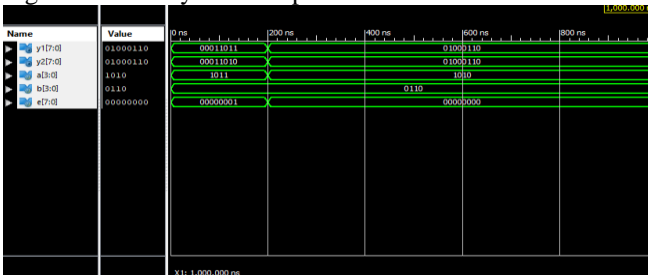


Figure 15 : Error Localization of 4-Bit Dependent Circuit

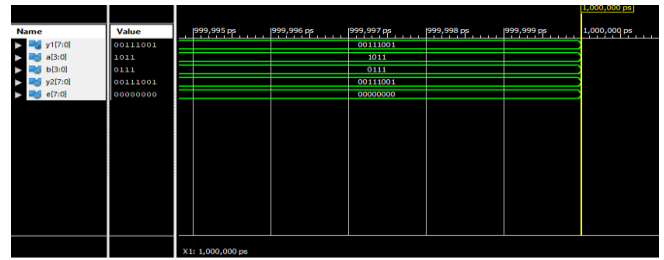


Figure 15 : Error Correction of 4-Bit Dependent Circuit

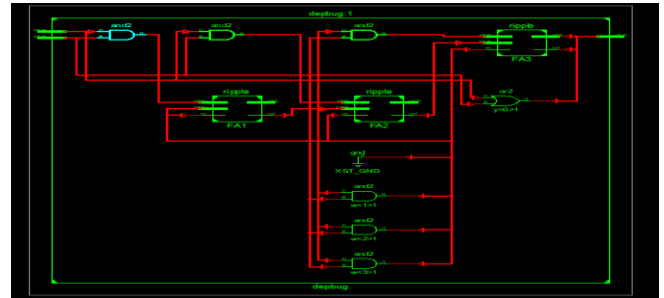


Figure 16 : Faulty 4-Bit Hybrid RTL Schematic Circuit

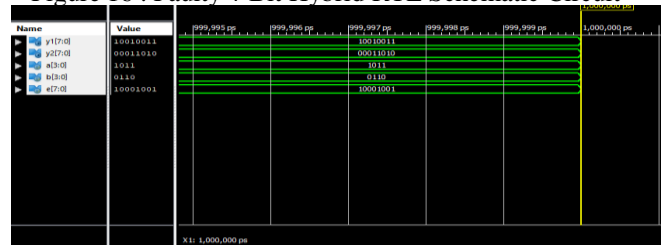


Figure 17 : Error Localization of 4-Bit Hybrid Circuit

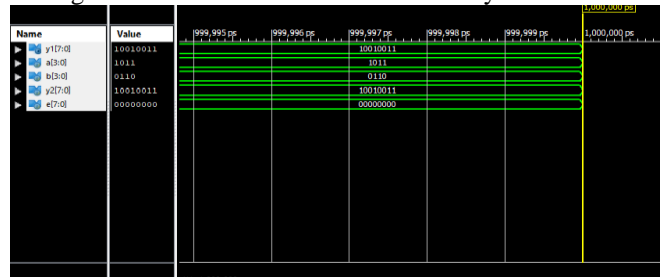


Figure 18 : Error Correction of 4-Bit Hybrid Circuit

Comparison of different parameters of 2-Bit multiplier and 4-Bit Multiplier

Test Cases	Number of LUT'S Used	Maximum Path Delay	CPU TIME	Total Time
Test-1 (localization)	3	9.063ns	5.94ns	11.75ns
Test-1(correction)	3	9.063ns	5.81ns	
Test-2 (localization)	3	9.109ns	5.89ns	9.34ns
Test-2(correction)	3	9.109ns	3.45ns	
Test-3 (localization)	3	9.063ns	3.44ns	6.87ns
Test-3(correction)	3	9.063ns	3.43ns	
Test-4 (localization)	3	9.063ns	3.47ns	7.00ns
Test-4(correction)	3	9.063ns	3.53ns	
Test-5 (localization)	3	9.109ns	3.63ns	7.13ns
Test-5(correction)	3	9.109ns	3.50ns	

Table 1 : comparison of different parameters for 2-Bit Multiplier

Test Cases	Number of LUT'S Used	Maximum Path Delay	CPU TIME	Total Time
Test-1 (localization)(Independent bug)	23	3.839ns	14.45ns	27.00ns
Test-1 (correction)(Independent bug)	23	3.839ns	12.55ns	
Test-2 (localization) (Dependent bug)	23	3.839ns	12.99ns	25.49ns
Test-2 (correction) (Dependent bug)	23	3.839ns	12.50ns	
Test-3 (localization) (Hybrid bug)	23	3.839ns	13.39ns	26.11ns
Test-3(correction)(Hybrid bug)	23	3.839ns	12.72ns	

Table 2 : comparison of different parameters for 4-Bit Multiplier

V. CONCLUSION

In the proposed model, the automated methodology for debugging arithmetic circuits. Our methodology consists of efficient , bug localization, and bug correction algorithms. We used the BIST produced by equivalence checking methods to generate directed tests that are guaranteed to activate the source of the bug when the bug is unknown. We used the generated tests to localize the source of the bug and find suspicious areas in the design. We also developed an efficient debugging algorithm that to locate and correct the bug without any manual intervention. We extended the proposed approach to automatically fix multiple bugs for 2-bit and 4-bit multiplier.

REFERENCES

- [1] M. J. Ciesielski, C. Yu, W. Brown, D. Liu and A. Rossi, "Verification of gate-level arithmetic circuits by function extraction," in IEEE/ACM International Conference on Computer Design Automation(DAC), 2015, pp.
- [2] A. Sayed-Ahmed, D. Große, U. Kuhne, M. Soeken, and R. Drechsler, "Formal verification of integer multipliers by combining grobner basis with logic reduction," in " Design, Automation & Test in Europe Conference & Exhibition (DATE), 2016. IEEE, 2016, pp. 1048–1053..
- [3] M. Chen and P. Mishra, "Functional test generation using efficient property clustering and learning techniques," IEEE Transactions on Computer-Aided Design of Integrated Circuits and Systems, vol. 29, no. 3, pp. 396–404, 2010
- [4] M. Chen, X. Qin, H. Koo, and P. Mishra, System-level Validation - high-level modeling and directed test generation techniques. Springer, 2012.
- [5] J. Lv, P. Kalla and F. Enescu, "Efficient grobner basis reductions for formal verification of galois field multipliers," in Design Automation and Test in Europe Conference(DATE), 2012, pp. 899–904.
- [6] F. Farahmandi and B. Alizadeh, "Grobner basis based formal verification of large arithmetic circuits using gaussian elimination and cone-based polynomial extraction," in Microprocessor and Microsystems - Embedded Hardware Design, 2015, pp. 83–96
- [7] F. Farahmandi, P. Mishra, and S. Ray, "Exploiting transaction level models for observabilityaware post-silicon test generation," in Proceedings of the 2016 Conference on Design, Automation & Test in Europe. EDA Consortium, 2016, pp. 1477–1480
- [8] D. Ritirc, A. Biere, and M. Kauers, "Improving and extending the algebraic approach for verifying gate-level multipliers," in Design, Automation & Test in Europe Conference & Exhibition (DATE), 2018. IEEE, 2018, pp. 1556–1561.
- [9] Y. Lyu, X. Qin, M. Chen, and P. Mishra, "Directed test generation for validation of cache coherence protocols," IEEE Transactions on Computer-Aided Design of Integrated Circuits and Systems, 2018.
- [10] A. Ahmed, F. Farahmandi, and P. Mishra, "Directed test generation using concolic testing on rtl models," in Design, Automation & Test in Europe Conference & Exhibition (DATE), 2018. IEEE, 2018, pp. 1538–1543

AN INTERACTIVE FEATURE PROPAGATION FOR IMAGE MATTING

¹Mr. K. Srinivasa Rao, ²M. Alekhya, ³P. Sindhu, ⁴M. Usha Sree, ⁵M. Rishita Rao.

¹Assist Prof., ECE Department, ALIET, JNTUK, Vijayawada, Andhra Pradesh, India.

² Student, ECE Department, ALIET, JNTUK, Vijayawada, Andhra Pradesh, India.

³Student, ECE Department, ALIET, JNTUK, Vijayawada, Andhra Pradesh, India.

⁴ Student, ECE Department, ALIET, JNTUK, Vijayawada, Andhra Pradesh, India.

⁵ Student, ECE Department, ALIET, JNTUK, Vijayawada, Andhra Pradesh, India.

ABSTRACT: With advanced digital cameras, matting techniques are widely used to create innovative compositions to facilitate other editing tasks and these techniques have gained increasing benefits from professionals and consumers alike. Image matting technology is a key step in the image and video editing image translation and locating objects in a scene in filmmaking. Image matting methods are divided into three categories sampling-based, propagation-based, and learning-based. a mixture of sampling-based and propagation-based to enhance alpha matte results. Various image matting techniques and systems have been proposed to efficiently extract high-quality matte from images.

Keywords: Deep CNN, Trimap, alpha matte, deep learning, Image Matting.

1. INTRODUCTION

Image matting refers to the task of precisely separating foreground objects from the background and accurately estimating the opacity per pixel near the boundaries. It has been studied for years by academia and industry. Typical applications include image processing, film productions, and virtual backgrounds for video conferencing. Given an input image I , this can be formulated as mathematical optimization problems as follows:

$$I_i = \alpha_i F_i + (1 - \alpha_i) B_i \quad (1)$$

Where $\alpha_i \in [0,1]$ denotes the opacity of a foreground object at pixel i . we can observe that for each pixel, the problem has 7 unknowns to solve from only 3 known values. It is therefore a highly morbid question.

Deep image matting is a learning-based approach to image matting that uses deep neural networks to estimate the alpha value of each pixel in an image. The basic idea behind deep image matting is to use a neural network to learn the mapping between an input image and the corresponding alpha values.

Traditional image matting methods rely on handmade features and heuristics, which may not capture the complex and diverse visual characteristics of real images. In contrast, deep image matting uses deep learning methods that can automatically learn complex features and patterns from large data sets of annotated images.

The basic workflow of deep image matting involves training deep neural networks to predict an alpha matte from an input image the training data consists of pairs of input images and ground truth alpha mattes. During training, the neural network learns to minimize the difference between its alpha matte and the ground truth alpha matte using a loss function such as mean square error or cross-entropy loss. The architecture of deep neural networks used in deep image matting consists of encoder-decoder networks with skip connections. The encoder array extracts the features from the input image and gradually reduces the spatial resolution of the feature map .while the decoder network Upsamples the feature maps to the original image and generates the final alpha matte. Skip connections help in preserving fine detail in input images during encoding and decoding.

Deep image matting achieves remarkable performance on multiple measures, outperforming traditional matting methods and other modern methods of deep learning. one of the main advantages of deep image matting is its ability to handle complex and challenging scenes such as transparent objects, fine hair, and motion blur. Features and patterns learned in the neural network can capture the subtle and intricate details of such scenes resulting in a more accurate alpha matte.

2. PROPOSED SYSTEM

Deep image matting can be implemented using the VGG16 neural network architecture. VGG 16 is a widely used CNN architecture consisting of 16 layers, including convolutional, pooling and fully connected layers.

Here is a high-level overview of the steps involved in implementing DIM using VGG16:

Data preparation: Collect a large dataset of image background pairs and their corresponding alpha blocks. Preprocess the data by resizing the image and its corresponding alpha matte to a fixed size.

Model building: create a Vgg16 MODEL with pre-trained weights on large image classification datasets such as imageNet. Freeze the weights of the pre-trained layers and add new trainable layers above the model to adapt it to the DIM task. The new layer should consist of a network of decoders to generate a coarse alpha matting and a blending module to combine the features of the image, background and coarse alpha matting to generate the final alpha matting

Train model: Train a model on prepared data using appropriate loss functions such as alpha predication loss, component loss, and gradient difference loss. alpha prediction loss measures the difference between the predicted alpha carpet and the ground truth alpha matte. synthesis loss measures the difference between composed images (foreground objects on a new background) and ground truth images.

Gradient differences loss measures the difference between the gradients of the predicted alpha matte and the ground truth alpha matte.

Evaluate Model: Evaluate the model trained on the set of validation images and their corresponding alpha matte. measure the accuracy of predicted alpha blocks and composed images using appropriate metrics such as an absolute error and structural similarity index.

Test Model: tests the trained model on a set of test images and their corresponding backgrounds. use the model to predict the alpha matte of the foreground object in the test image and use the predicted alpha matte to extract the foreground object Apply Post-processing techniques such as smoothing or thinning to improve the quality of extracted objects.

3. DEEP LEARNING:

Deep learning has a become popular technique for many computer vision tasks, including deep image matting as it has proven to be very effective in learning complex features and relationships in large datasets. deep learning models are able to automatically learn and extract the most relevant features from raw data, making them ideal for tasks where manually designing features is difficult or impossible.

In the case of deep image matting, deep learning models can learn to identify and separate foreground and background pixels, as well as deal with lighting and blurring effects and complex shade. This is especially important for natural images, which often have complex and variable backgrounds and lighting conditions.

In addition, deep learning models can be trained on large datasets which is critical for achieving high accuracy in deep image matting.

Large datasets such as the adobe composition-1k dataset and deep automatic portrait matting dataset containing thousands of high-quality images with ground truth alpha matting, provide a rich data source of training for deep learning model

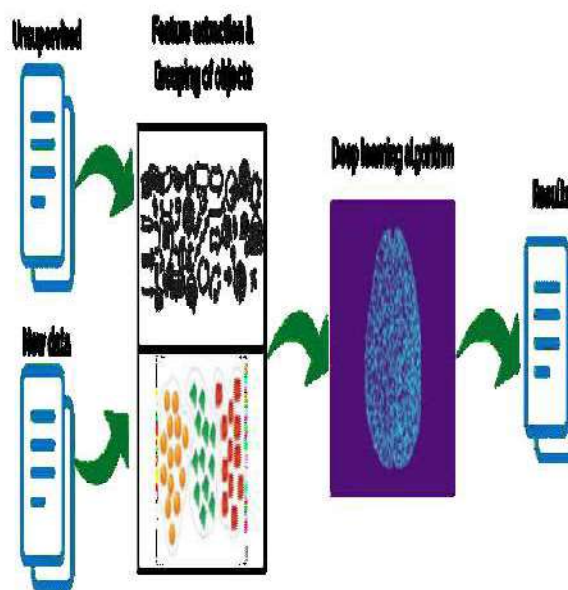


Fig1. Image of Deep learning

3a. CNN

A convolutional neural network is a type of artificial neural network particularly well suited for image and video processing tasks. They aim to automatically learn and extract features from input images in a hierarchical manner, enabling more accurate image classification and object recognition.

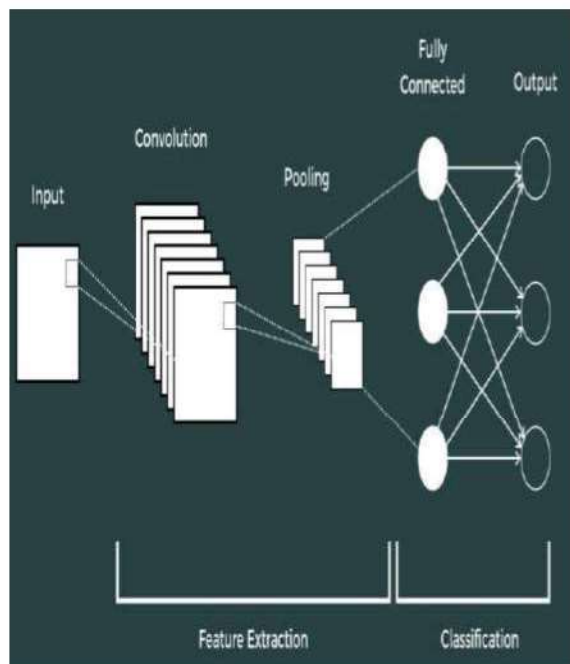


Fig.2. Image of CNN

3b.VGG16:

The vgg16 architecture is a deep convolution neural network for image classification the vgg16 model can be broken down into the following steps:

input image: the vgg16 architecture expects an input image with a fixed size of 224 x 224 pixels the images are introduced in the first layer of the network

convolution layers the input image passes through a series of convolution layers each convolution layer applies a set of filters to the input image to extract features. the vgg16 architecture has 13 convolution layers.

Activation functions: after each convolution layer an activation function is applied to introduce non-linearities in the model.

Pooling layer: to reduce the spatial size of the output volume maximum pooling is applied after some convolution layers. The Vgg16 architecture contains a maximum of 5 layers of grouping.

Fully Connected layers: after the input image has passed through all convolution and clustering layers the resulting feature map is flattened into a 1D vector and passed through a series of fully connected layers.

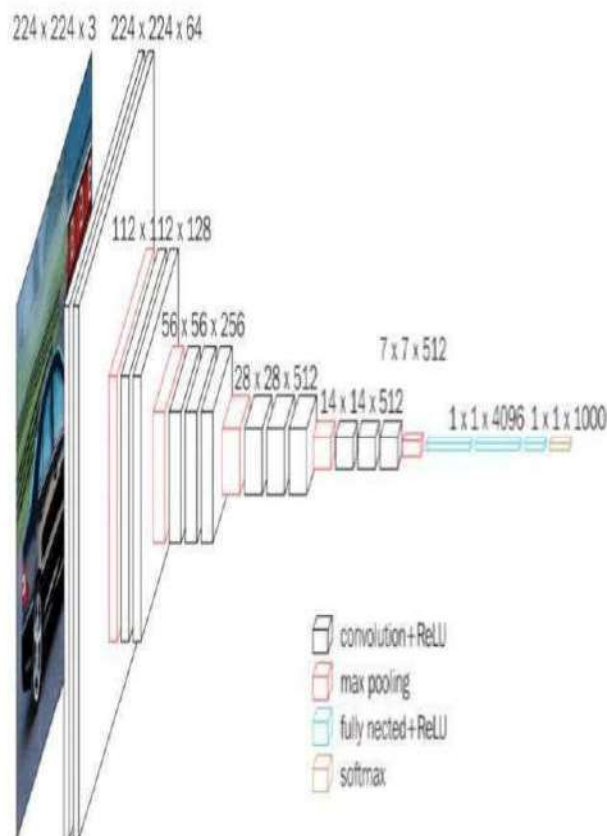


Fig.3. Image of VGG16

GUI Representation: The GUI may have a file import button where the user can select an image to process and an export button to save the processed image the GUI may also have options to adjust the parameters of the deep image matting algorithms such as threshold used to separate foreground and background. once the user has selected the image and adjusted the parameters the algorithm can be run by clicking the process button the processed image can then be displayed on a graphical interface for the user to view and save.

Additionally, the GUI has a section to display the results of the algorithm such as the alpha channel foreground objects, and background. this can allow the user to refine the results and adjust the settings as needed.

In general, the deep image matting GUI can provide users with a friendly interface to process the image and adjust the parameters of the algorithm

4. RESULTS:

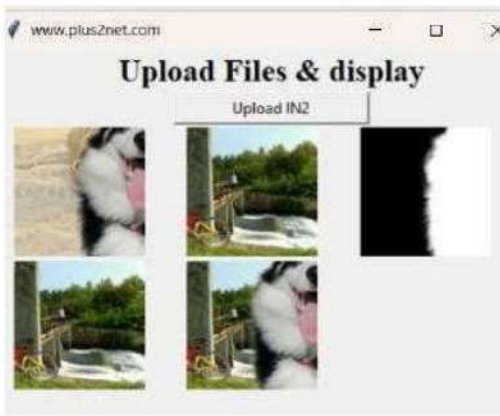


Fig.4 GUI REPRESENTATION

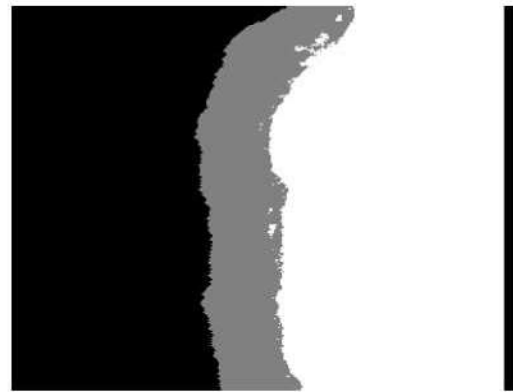


Fig.8 IMAGE TRIMAP



Fig.5 IMAGE_FG



Fig.9 IMAGE_OUT



Fig.6 IMAGE_BG



Fig.7 IMAGE_ALPHA



Fig.10 IMAGE_COMPOSED

5. ADVANTAGES:

Higher Accuracy: The deep image matting algorithm can achieve higher precision than traditional matting techniques. This is because deep learning models can learn to extract high-level features from images, allowing them to better distinguish between foreground and background pixels.

Automation: Traditional image matting requires manual annotation of trimaps which is time-consuming and error-prone. On the other hand, deep image matting is fully automated once the model has been trained.

Robustness: Deep image matting algorithms are generally more robust to changes in lighting, background, and other environmental factors.

Real-time performance deep image matting can be performed in real-time on modern GPUS, making it suitable for video editing and virtual reality applications.

Flexibility: Deep Image Matting can be applied to a variety of image and video editing tasks, including background removal, image compositing and color correction. This flexibility makes it an invaluable tool for a wide range of industries, including entertainment, advertising and e-commerce.

6. APPLICATIONS:

Image Editing: Deep Image matting makes extracting foreground objects from the background easy, making it an essential tool for image editing. With deep image matting, the background of an image can be easily removed or replaced with another background.

Augmented and Virtual Reality: Deep Image Matting can be used to separate the foreground and background of an image, allowing virtual objects to be seamlessly integrated into real scenes. The technology is used in applications such as augmented reality games and virtual fitting experiences.

Photography: Deep image matting can be used to create more natural portraits by separating foreground subjects from the background and applying a different effect or blur to each object.

Video Editing: Deep Image Matting can be used to separate the foreground and background of a video, allowing the background to be replaced or special effects to be added.

7. CONCLUSION

Overall, Deep Image Matting via vGG16 is a valuable technique for anyone working with images or video that need to be separate foreground and background. This provides a high level of precision which can help save time and effort during assembly.

8. REFERENCES:

- 1) Q. Chen ,D.Li, and C.K. Tng. knn matting. IEEE transactions on pattern analysis and machine intelligence,35(9):2175-218,2013.
- 2) H. Ding, X. Jiang, B. Shuai, A. Q. Liu, and G. Wang, "Semantic correlation promoted shape-variant context for segmentation," in Proc.IEEE/CVF Conf. Comput.Vis. Pattern Recognit. (CVPR), Jun. 2019,pp. 8885–8894.3
- 3) Q. Hou and F. Liu, "Context-aware image matting for simultaneous foreground and alpha estimation," in Proc. IEEE/CVF Int. Conf. Comput.Vis. (ICCV), Oct. 2019,pp. 4130–4139.
- 4) C. Szegedy et al., "Going deeper with convolutions," in Proc.IEEE Conf. Comput. Vis. Pattern Recognit. (CVPR), Jun. 2015, pp. 1 9.
- 5) H. Ding, X. Jiang, A. Q. Liu, N. M. Thalmann, and G. Wang, "Boundary-aware feature propagation for scene segmentation," in Proc. IEEE/CVF Int. Conf. Comput.Vis. (ICCV), Oct. 2019, pp. 6819–6829
- 6) T. Wei et al., "Improved image matting via real-time user clicks and uncertainty estimation," in Proc. IEEE/CVF Conf. Comput. Vis. PatternRecognit.(CVPR), Jun. 2021, pp. 15374–15383
- 7) Y. Li and H. Lu, "Natural image matting via guided_contextualattention,"2020arXiv:2001.04069.
- 8) Y. Zhang et al., "A late fusion CNN for digital matting," in Proc. IEEE/CVFConf. Comput. Vis. Pattern Recognit. (CVPR), Jun. 2019, pp. 7469–7478
- 9) S. Cai et al., "Disentangled image matting," in Proc. IEEE/CVF Int.Conf.Comput. Vis. (ICCV), Oct. 2019, pp. 8819–8828.
- 10) D.Cho, Y-W. Tai, I. Kweon, D.cho, Y-w. Tai, and I. kweon. Natural image matting using deep convolutional neural networks. In Proceedings of the European conference on computer vision 2016.

AIR CANVAS USING FINGER TRAJECTORY

Mr.K.Srinivasa Rao¹,Sarjil Ahmad²,R.Mallikarjuna³,T.Surya⁴,B.Avula Raju⁵

¹Assist Prof., ECE Department, ALIET, JNTUK, Vijayawada, Andhra Pradesh, India.

²Student, ECE Department, ALIET, JNTUK, Vijayawada, Andhra Pradesh, India.

³Student, ECE Department, ALIET, JNTUK, Vijayawada, Andhra Pradesh, India.

⁴Student, ECE Department, ALIET, JNTUK, Vijayawada, Andhra Pradesh, India.

⁵Student, ECE Department, ALIET, JNTUK, Vijayawada, Andhra Pradesh, India.

Abstract:

Drawing on a screen with Air Canvas is made possible by simply waving a finger in front of a camera. This project is built using OpenCV's computer vision algorithms. Python is popular because of its extensive libraries and simple syntax, but by grasping the fundamentals, it can be implemented in any language that supports OpenCV. The pointer finger is adjusted to map onto the screen using PyGame after a calibration screen to measure and record the color of the user's hand. The finger's direction is entirely controlled by open source OpenCV software. In the current work, raspberry pi and a camera is interfaced and OpenCV algorithm is used for mapping the coordinates of the user's pointer finger. The fundamental actions to do in order to complete the project. The first one involves looking for free, open-source software that uses Python and OpenCV to recognize hand gestures. The PyGame side of the project must now be independently developed. Integration of PyGame and OpenCV is the following stage. Implementing buttons and switching to the required size of display are the next steps. The project itself is an application of Air Canvas that will follow the finger's movement using computer vision. The created text can be used for a number of things, including sending emails and messages. This is going to powerful means of communication for especially abled people.

Keywords- Air canvas, OpenCV, Raspberry Pi, Python.

I. INTRODUCTION

One of the most intriguing and challenging fields of image processing and pattern recognition study has recently been writing in air. The incorporation of this technology benefits a wide spectrum of human-machine interactions. Numerous studies have looked into novel strategies and techniques for speeding up processing and increasing recognition accuracy. Object tracking is a critical component of the task in computer vision. Faster processors, more reasonably priced and higher quality video cameras, as well as the growing demand for automated video analysis have all contributed to the increased use of object tracking systems. Identification of the item, tracking of its movement from frame to frame, and behaviour analysis are the three main phases in video analysis. Object representation, feature selection for tracking, object identification, and tracking are the four considerations in object tracking. Numerous practical uses of object tracking algorithms exist, such as autonomous surveillance, vehicle navigation, and video indexing. This project focuses on motion-to-text converters for wearable devices with intelligence that can write in the air. This project acts as a time capsule for ephemeral movements. It will follow the finger's movement using computer vision. The created text could be used to send emails, messages, and other types of correspondence. The ability to converse will be greatly aided for those who are deaf. It's an effective method of speaking without writing.

A. Existing Model

In the current model, a brush is used to implement the project rather than a finger. The brush requires much more effort and is less accurate. The current research uses 1-D convolutional neural network, deep ensemble network, long and short term memory auto encoder, and silhouette-based tracking.

Drawbacks of the existing System:

It still needs to be greatly changed in terms of its edge, cameras, and usefulness. Just think about a regular-sized brush. System only monitors the presence of the brush handle. The genuine model does not replicate weather changes or overflows because it is unquestionably not an exact replica of the air and shade water liquids. A small amount of paint really seeps through the valve when a customer lightly squeezes the trigger while the paint liquid valve is still closed.

AR applications greatly deplete batteries. Re-localizing content that is displayed on the globe canvas can be done much more accurately. The program can be expanded to include volumetric training and classification of point cloud data.

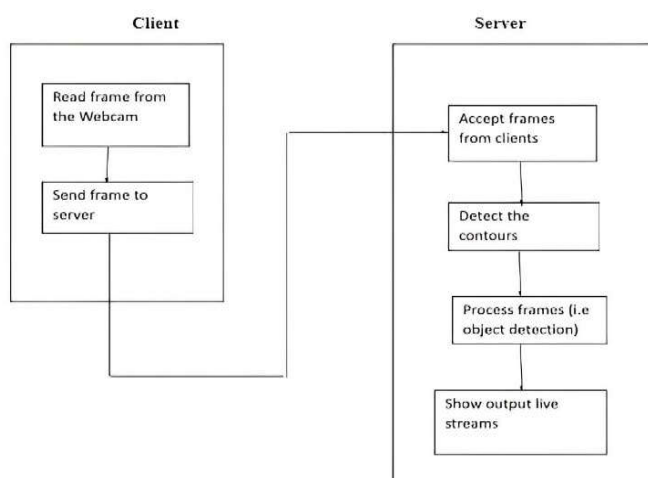


Fig 1. Block Diagram of Existing Model

B. Proposed Model

a) Hardware Required:

- Raspberry Pi 4 Model B
- Monitor/Laptop
- E-Camera FT-2251

b) Software Required:

- OpenCV Libraries
- Python

c) Tools Required:

- Python IDLE
- Visual Code Studio

In this proposed system, we are using a E-camera to detect the finger and track the trajectory of the finger and display whatever we drew in front of the camera on a laptop or monitor screen. This system uses various algorithms from opencv and displays the output on screen of laptop or monitor.

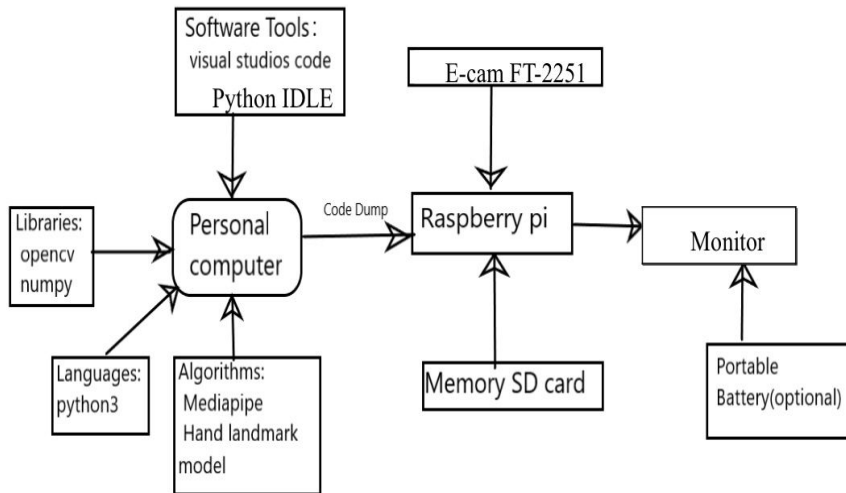


Fig 2. Block Diagram of Proposed Model

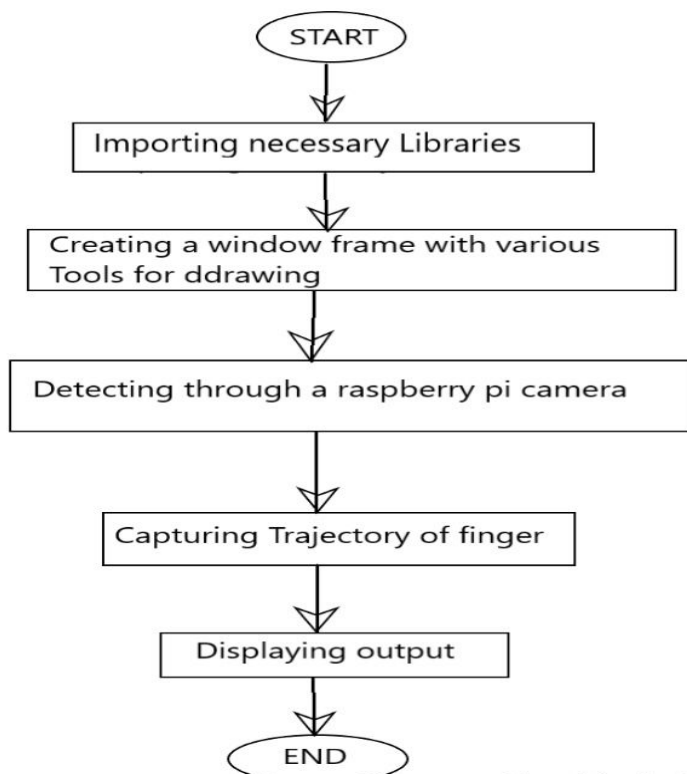


Fig 3. Flow Chart of Proposed Model

II. Working of Proposed Model

In this project, we are using a E-Camera to detect the finger and track the trajectory of the finger and display whatever we drew in front the camera on a laptop/monitor screen. This system uses various algorithms and displays the output on screen. There are 5 steps involved in the total process.

CAMERA USED FOR THE SYSTEM:

Here we are using a E-Camera FT-2251. The frames that are recorded by the e-camera are the foundation for the proposed system. The FT-2251 camera will begin recording video after the video capture object is created using python computer vision package(OpenCV). The pi board receives frames from the camera and processes them.



Fig 4. E-CAM FT-2251 camera

CAPTURING THE VIDEO AND PROCESSING:

The e-cam is used by the system and every frame is recorded up until the end of the application. As illustrated in the accompanying mode, the video frames are converted from BGR to RGB in order to find the hands in video frame by frame.

DETECTING WHICH FINGER IS UP:

Using the tip ID of the specific finger that we located using the mediapipe's HAND LANDMARK MODEL and corresponding co-ordinates of the finger that are up, we are able to determine which finger is up at this point. With that finger the specific font and colour is picked up.

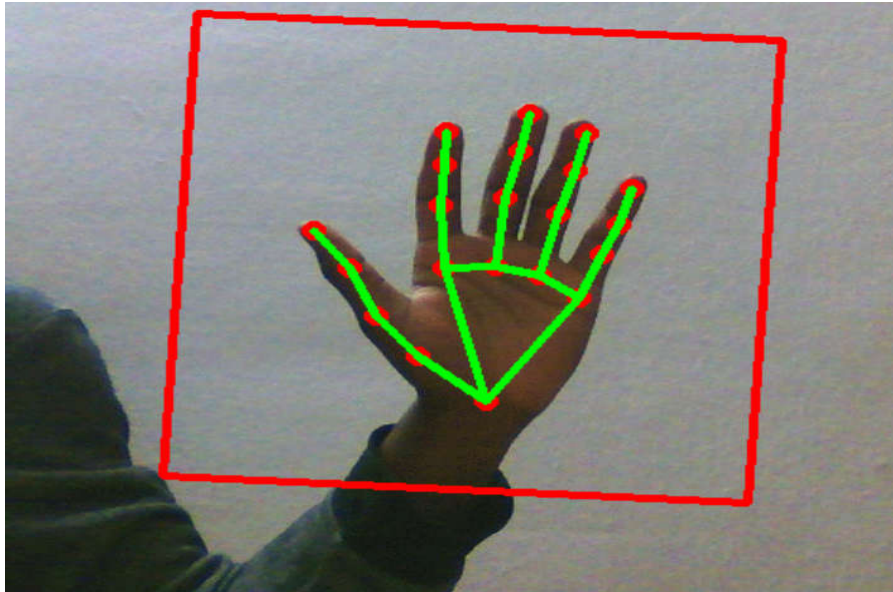


Fig 5. Detecting finger using hand landmark model

PERFORMING THE ACTION:

The trajectory of the finger according to its co-ordinates are captured with the e-camera. The frames are converted into the images and whatever is written with the finger is captured. We can write or draw whatever we want to in front of the camera. It will capture everything and finally displays the output.

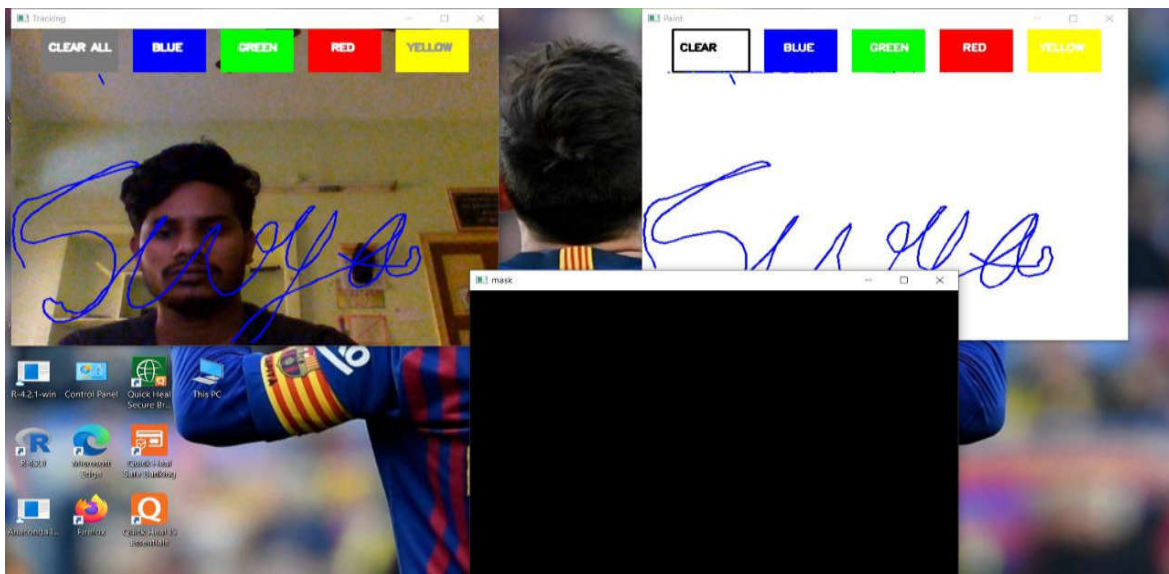


Fig 6. Performing the action in front of camera

DISPLAYING THE OUTPUT:

Finally whatever action we performed in front of the e-camera with the selected actions is displayed on the laptop/monitor screen.

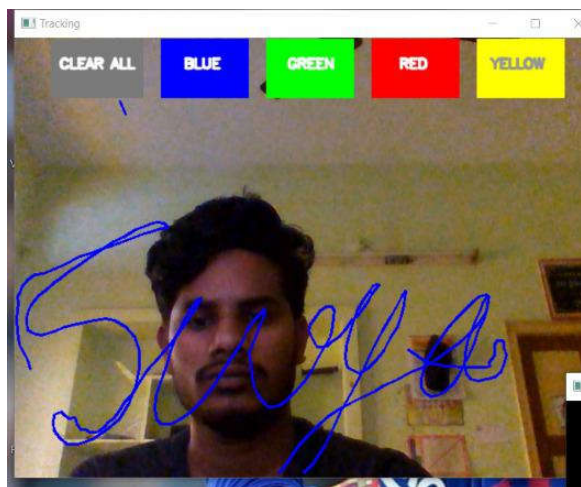


Fig 7. Displaying the Output

III. CONCLUSION

The programme has the ability to disrupt conventional writing techniques, to sum up. removes the need to carry a cell phone around in order to take notes and provides a convenient option to accomplish the same while on the road. It will once more serve a greater good by making communication simpler, especially for people who are familiar with them. The programme is simple enough to use for those who have trouble using the keyboard. Soon, this program's capability will allow for the control of IoT devices. You may also create air paintings. With the help of this programme, people will be able to interact with the digital world more effectively while wearing smart gear. The material may come alive by illustrating the unpopular reality of taxpayers. Wind-writing programmes should solely respond to their master's commands and not be swayed by outside influences. Following are several discovery algorithms that YOLO v3 may use to increase the speed and accuracy of fingerprint identification. The effectiveness of writing in the air will increase in the future as artificial intelligence research advances.

IV. REFERENCES

- [1] Sayli More, Prachi Mhstre, Shruthi Pakhare, Surekha Khot, " Air Canvas: Draw in Air" in ISO 9001:2008 Certified Journal(IRJET), Feb. 2022, pp. 2395-0056.
- [2] K. Kim et al., "Real Time Foreground-Background Segmentation Using Code Book Model," Real-Time Imaging, vol. 11, no.3, 2005, pp.172-185.
- [3] Kenji Oka, Yoichi Sato, and Hideki Koike, "Real-Time Fingertip Tracking and Gesture Recognition," IEEE Computer Graphics and Applications, 2002, pp.64-71.

- [4] Y. Huang, X. Liu, X. Zhang, and L. Jin, "A Pointing Gesture Based Egocentric Interaction System: Dataset, Approach, and Application," 2016 IEEE Conference on Computer Vision and Pattern Recognition Workshops (CVPRW), Las Vegas, NV, pp. 370-377, 2016.
- [5] Saira Beg, M. Fahad Khan and Faisal Baig, "Text Writing in Air," Journal of Information Display Volume 14, Issue 4, 2013 Y. Huang, X. Liu, X. Zhang, and L. Jin, "A Pointing Gesture Based Egocentric Interaction System: Dataset, Approach, and Application," 2016 IEEE Conference on Computer Vision and Pattern Recognition Workshops (CVPRW), Las Vegas, NV, pp. 370-377, 2016.
- [6] Alper Yilmaz, Omar Javed, Mubarak Shah, "Object Tracking: A Survey", ACM Computer Survey. Vol. 38, Issue. 4, Article 13, Pp. 1-45, 2006.
- [7] Yuan-Hsiang Chang, Chen-Ming Chang, "Automatic Hand-Pose Trajectory Tracking System Using Video Sequences", INTECH, pp. 132- 152, Croatia, 2010.
- [8] Yusuke Araga, Makoto Shirabayashi, Keishi Kaida, Hiroomi Hikawa, "Real Time Gesture Recognition System Using Posture Classifier and Jordan Recurrent NeuralNetwork", IEEE World Congress on Computational Intelligence, Brisbane, Australia, 2012.

REAL TIME HAND GESTURE RECOGNITION SYSTEM USING CNN

¹Mr. G. Ravi, ²M. Venkata Swetha, ³Ch. Keerthana, ⁴Ch. Kavitha, ⁵P. Jahnavi.

¹AssistProf., ECE Department, ALIET, JNTUK, Vijayawada, Andhra Pradesh, India.

²Student, ECE Department, ALIET, JNTUK, Vijayawada, Andhra Pradesh, India.

³Student, ECE Department, ALIET, JNTUK, Vijayawada, Andhra Pradesh, India.

⁴Student, ECE Department, ALIET, JNTUK, Vijayawada, Andhra Pradesh, India.

⁵Student, ECE Department, ALIET, JNTUK, Vijayawada, Andhra Pradesh, India.

ABSTRACT: Hand gesture recognition is an essential way of communication between the impaired people. Developing a simple channel to communicate with deaf and dumb people is crucial. To aid people with special needs it is important for everyone to understand sign language and it is necessary in case of any emergency. Here individuals communicate through hand signals or gestures. Signals are the actual activity performed by every individual to pass the important data. Hence people inculcate to know sign language to impart proficiently but this would be an issue for unpractised ones. The aim of this paper is to develop a Real Time Hand Gesture Recognition System using Convolutional Neural Networks (CNN). The focus of this work is to embrace capturing images of the hand gesture using web camera and the system shall predict and display the text corresponding to the image previously captured. Furthermore, the trained model recognizes the hand gesture and generates the speech from the text.

Keywords: CNN, Sign language, Hand Gesture, trained model, Real time, Image Processing.

1.INTRODUCTION:

Hand gestures are a natural and intuitive of communicating between the impaired people. With the increasing demand for efficient human-computer interaction systems. Hand gesture recognition has become an active research area in computer vision and pattern recognition. In recent years, Convolutional Neural Networks (CNNs) have achieved great success in various computer vision tasks including image classification, object detection and segmentation. In this paper, we propose a hand gesture recognition system using CNN. The proposed system consists of two main components: feature extraction and feature classification. The feature extraction component uses a pre-trained CNN architecture to extract high-level features

from hand gesture images, while the classification component employs a fully connected neural network to classify the gestures. The system is trained and tested on a large dataset of hand gesture images. We evaluate the performance of the system in terms of accuracy, robustness to different lighting conditions and camera angles and computational efficiency. CNN is a technology that enables machines to identify and understand human hand movements in real-time. This technology has a wide variety of applications from sign language recognition. The key to hand gesture recognition using CNN is to train a neural network to recognize specific patterns of hand movements. CNN is particularly suited for this task because it can automatically learn and extract features from images, such as the shape, orientation, and texture of objects, without requiring explicit feature engineering. This allows CNN to perform better than traditional machine learning methods for image recognition tasks. In hand gesture recognition, CNN can be trained to identify different hand gestures by analysing the shape, position, and motion of the hand in a video stream. Once the network is trained, it can be used to recognize hand gestures in real-time and trigger appropriate responses such as controlling a computer. Overall, Hand gesture recognition using CNN is a powerful technology that has the potential to revolutionize human-machine interaction and enable new applications in wide range of fields, from health care to entertainment.

2. PROPOSED SYSTEM

Hand gesture recognition system can be implemented using the SqueezeNet neural network architecture consisting of 18 layers, including 8 fire modules, convolutional, pooling layers. Here is a high-level overview of the steps involved in implementing HGR:

Data collection: The first step in building a hand gesture recognition system is to collect data. This involves capturing image of different hand gestures under various lighting conditions and backgrounds. The images here collected by using a web camera

Data pre-processing: After the data collected, it needs to be pre-processed. This includes resizing the images, normalizing pixel values, and removing background noise.

Data augmentation: To increase the size of dataset and improve the model performance, data augmentation techniques such as rotation, flipping and scaling can be used.

Model architecture: The next step is to design a CNN architecture. This involves selecting the number of layers, filters, and activation functions. The architecture can be customized based on the specific hand gesture recognized.

Training: The CNN model is trained using the pre-processed data. During training, the model learns to recognize hand gestures by adjusting the weights of filters.

Testing: After training, the model is tested using a separate set of images. This step helps to evaluate the accuracy of the model.

Deployment: Once the model has been trained and tested, it can deploy to recognize hand gestures in real-time. This involves capturing images of hand gestures using a web camera and passing them through the CNN model for recognition.

3. DEEP LEARNING:

Deep learning is a subset of machine learning that involves training complex neural networks with multiple layers of interconnected nodes. In hand gesture recognition, deep learning algorithms such as Convolutional Neural Networks (CNNs), have been shown to significantly improve the accuracy and robustness of the recognition system compared to traditional machine learning methods. The importance of deep learning in hand gesture recognition lies in its ability to automatically learn and extract features from raw data without the need for explicit feature engineering methods may not be able to capture all the relevant information.

In addition, deep learning models can be trained on large datasets of hand gesture images or videos, which allows them to learn and generalize patterns and features that are specific to different hand gestures. This enables them to accurately recognize and classify hand gestures in real-time, even in complex and dynamic environments.

Furthermore, deep learning algorithms can adopt and learn from new data, which means hand gesture recognition system can continue to improve time as more data is collected and added to the training set. In summary, deep learning is essential in hand gesture recognition because it enables the development of highly accurate and robust recognition systems that can learn and adapt to new data and environment.

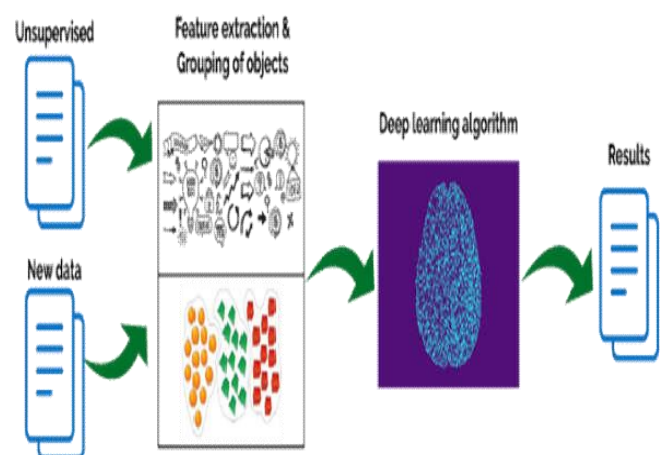


Fig1. Image of Deep learning.

4.OUTPUTS:

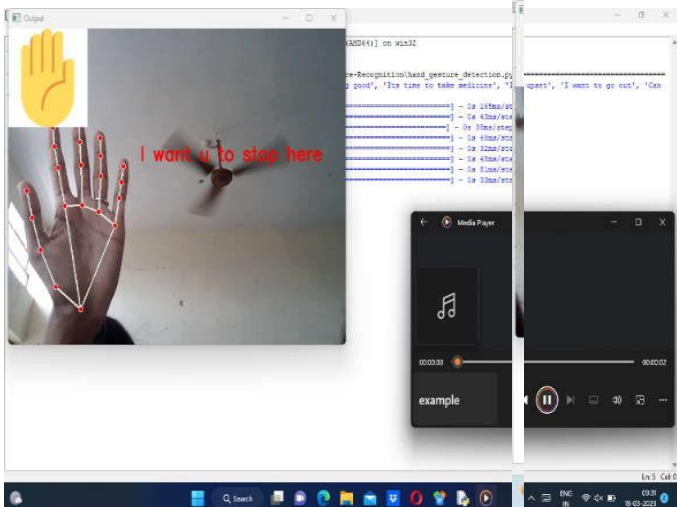


Fig.4 Displayed 1st Hand Gesture Image of "I WANT U TO STOP HERE"

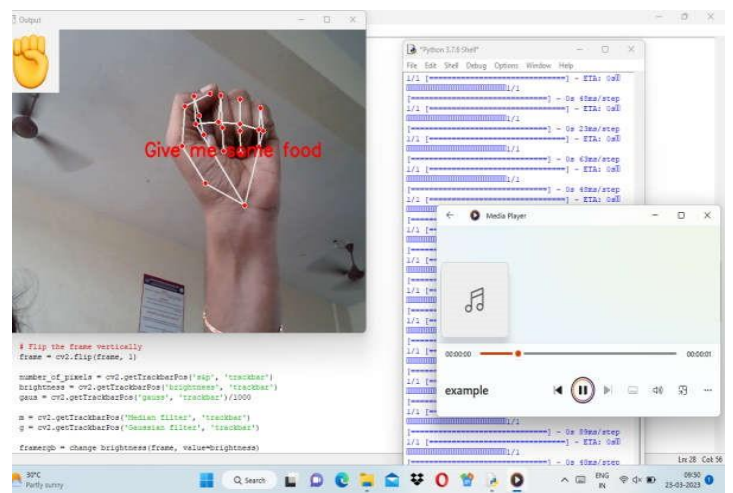


Fig.5 Displayed 2nd Hand Gesture Image "GIVE ME SOME FOOD"

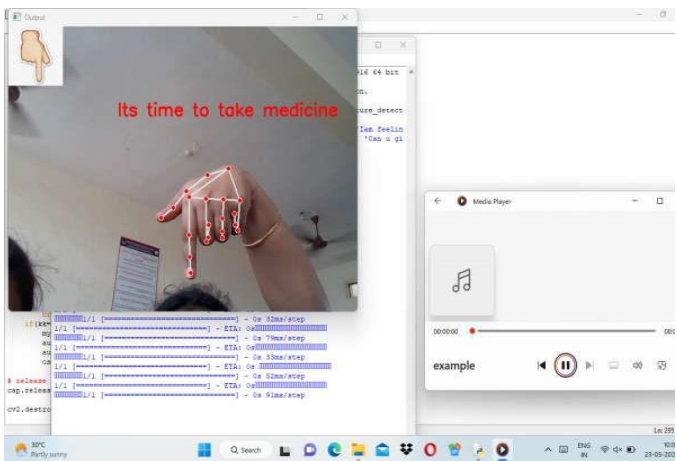


Fig.6 Displayed 3rd Hand Gesture Image of "IT'S TIME TO TAKE MEDICINES"

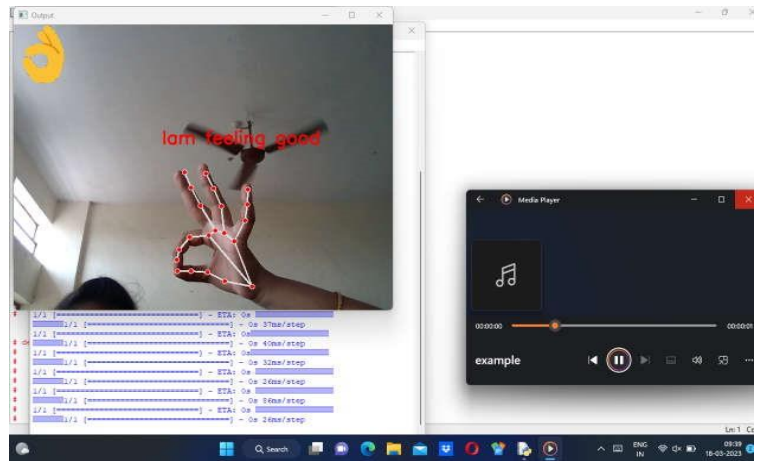


Fig.7 Displayed 4th Hand Gesture Image "I AM FEELING GOOD"

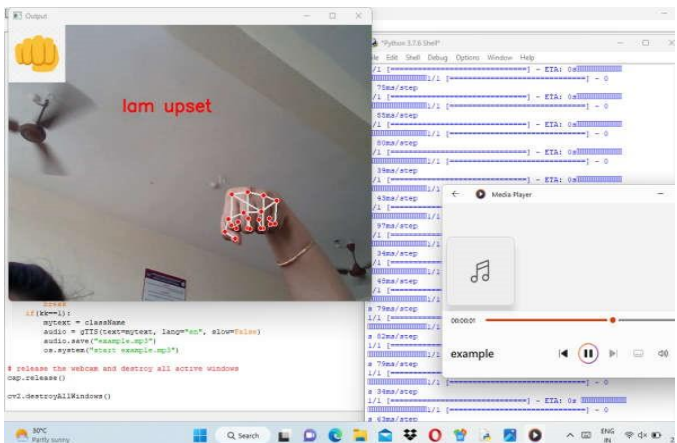


Fig.8 Displayed 5th Hand Gesture Image of "I AM UPSET"

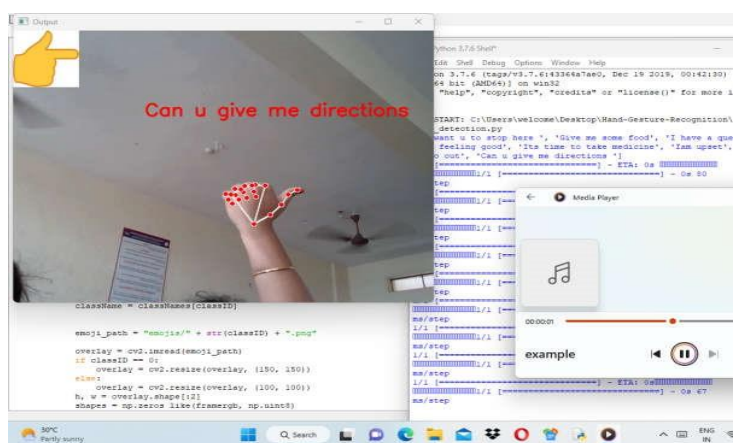


Fig.9 Displayed 6th Hand Gesture Image "CAN U GIVE ME DIRECTIONS?"

5. ADVANTAGES:

High Accuracy: CNNs are well-suited for recognizing patterns in images, which makes them highly accurate for recognizing hand gestures. This is especially true when the CNN is trained on a large dataset of hand gesture images, which can help the model learn the subtle differences between different gestures.

Robustness: CNN algorithms are generally more robust to changes in lighting, background, and other environmental factors that can affect hand gesture recognition. This is because the CNN is designed to extract features from images that are invariant to these types of changes.

Interpretability: CNNs can provide insights into which features are important for recognizing different hand gestures. This can be useful for improving the model's accuracy, as well as understanding the underlying mechanisms of hand gesture recognition. **Scalability:** CNNs can be trained on large datasets of hand gesture images, which makes them scalable to a wide range of hand gestures and applications. This allow the model to generalize well to new, unseen hand gestures, which is important for building robust and flexible hand gesture recognition systems. **Speed:** CNNs can be trained and used for inference quickly, which makes them well-suited for real-time hand gesture recognition applications. This is especially true when the CNN is optimized for hardware acceleration, such as running on a GPU. Hand gesture recognition can be performed in real-time making it suitable for wide range of applications from human interaction to robotics and virtual reality applications

6.APPLICATIONS:

Human Computer Interaction: Hand gesture recognition can be used as a natural interface for computer systems, allowing users to interact with computers using hand gestures instead of traditional input devices such as keyboards and mic. Applications include controlling media playback, navigating user interfaces and interacting with virtual environments.

Sign language translation: Hand gesture recognition can be used to translate sign language into text or speech, allowing deaf or hard-of-hearing individuals to communicate more easily with people who do not know sign language.

Robotics: Hand gesture recognition can be used to control robotic devices, allowing humans to interact with robots in a more intuitive way. Applications include controlling robotic arms and hands for industrial or medical purposes.

Security and Surveillance: Hand gesture recognition can be used for security and surveillance purposes, allowing for the identification of individuals.

7. CONCLUSION

Overall, a real-time sign language and hand gesture recognition system using Convolution Neural Network (CNNs) has shown promising results in accuracy recognizing a variety of hand gestures and signs in real-time. With further development and refinement, this technology has the potential to improve communication accessibility for the individuals with hearing or speech impairments and open up new avenues for human-computer interactions.

8. REFERENCES

- [1] Sign Language Recognition using multiple kernel Learning: A case of Pakistan sign language received April 7th2021, accepted April 24th 2021 date of publication May 4th 2021, date of current version M ay 12th 2021.Digital Object Identifier 10.1109/ACCESS.2021.3077386
- [2] Sign Language and Common Gesture Using CNN International Journal of Advanced Trends in Computer Science and Engineering volume 10, no: - 3 May-June 2021.
- [3] Nakul Nagpal, Dr. Arun Mitra, Dr. Pankaj Agrawal, Design Issue and Proposed Implementation of Communication Aid for Deaf & Dumb People, International Journal on Recent and Innovation Trends in Computing and Communication, Volume: 3 issues:5, pp-147 149.
- [4] IEEE TRANSACTIONS ON MOBILE COMPUTING, VOLUME 21, NO: -7, JULY 2022 Hear Sign Language: A Real-Time End-to-End Sign Language Recognition System
- [5] International Journal of Research Publication and Reviews, Vol 3, no: -4, pp 1554-1558, April 2022 International Journal of Research Publications and Reviews Journal homepage: www.ijrpr.com ISSN 2582-742.
- [6] V. Lopez-Ludena, R. San-Segundo, R. Martin, D. Sanchez and A. Garcia, "Evaluating a Speech Communication System for Deaf People," in IEEE Latin America Transactions, vol. 9, no. 4, pp. 565-570, July 2011, doi: 10.1109/TLA.2011.5993744.
- [7] I. Krak, I. Kryvonos and W. Wojcik, "Interactive systems for sign language learning," 2012 6th International Conference on Application of Information and Communication Technologies (AICT), Tbilisi, 2012, pp. 1- 3, doi: 10.1109/ICAICT.2012.6398523.
- [8] E. Abraham, A. Nayak and A. Iqbal, "Real-Time Translation of Indian Sign Language using LSTM," 2019 Global Conference for Advancement in Technology (GCAT), BANGALURU, India, 2019, pp. 1-5, doi: 10.1109/GCAT47503.2019.8978343.
- [9] Tolentino, Lean Karlo S. et al. "Static Sign Language Recognition Using Deep Learning." International Journal of Machine Learning and Computing 9 (2019): 821-827.

CNN Based Wildlife Intrusion Detection and Alert System

G. Ravi^{*1}, Sd. Afroz¹, K. Yamuna¹, Sd. Afsha¹

Abstract: Wildlife intrusion detection and alert systems are designed to detect and alert wildlife intrusion events, such as animals crossing highways, entering farms or protected areas, and approaching human settlements. This system often uses advanced technologies, such as cameras, sensors and machine learning algorithms, to detect and identify animal species and behaviors. Convolutional neural networks (CNNs) are a type of deep learning algorithm commonly used for image and video analysis tasks, including object detection and classification. CNNs can learn to extract features from images and videos automatically and accurately, making them well-suited for detecting animals in wildlife intrusion detection systems.

Keywords: CNN, Deep learning, Image -processing, Live capturing.

1. Introduction

The intrusion of wildlife into human habitats can pose a significant threat to both animals and people. To mitigate this problem, an efficient detection and alert system is necessary. In this regard, Convolutional Neural Networks (CNNs) and You Only Look Once (YOLO) object detection algorithms can be used to develop an automated system that can detect and alert wildlife intrusion in real time [1].

Article History

Received: 15-01-2023;

Revised: 20-03-2023;

Accepted: 30-03-2023

*Corresponding author: Department of Electronics and Communication Engineering, Andhra Loyola Institute of Engineering and Technology, Vijayawada -520008, India

E-mail: ravigorapudi234@gmail.com

Ph: +91 -9848794818

¹Department of Electronics and Communication Engineering, Andhra Loyola Institute of Engineering and Technology, Vijayawada-520008, India

E-Mail: afrozsyed.5302@gmail.com,
yamunakunche@gmail.com,
syedafsha234@gmail.com

This system typically uses cameras to monitor a specific area and then employs deep learning algorithms to analyze the images or data collected from these sensors. The CNN-based approach to this system involves the use of convolutional neural networks (CNNs), which are a class of deep-learning neural networks that are highly effective at image recognition and analysis. By training these networks on large datasets of images, the system can learn to identify specific types of wildlife, such as elephants or tigers, and distinguish them from other objects or backgrounds [2]. One of the key advantages of a CNN-based wildlife intrusion detection and alert system is its ability to operate in real-time, continuously analyzing incoming data and generating alerts when necessary [3]. This can help to mitigate potential conflicts between humans and wildlife, by enabling early detection of intrusions and allowing relevant authorities to take appropriate action.

2. Proposed system

The images captured are fed as input to the system and pass through the different layers of the convolution neural network. The animals will be detected by the webcam through live capturing if any animal is detected then it will identify the animal and gives an alert if it crosses or is near the borderline [4-5]. Each layer filters a possible outcome when it is compared with the images provided in the dataset finally the animal is identified.

3. Methodology

The CNN - based wildlife intrusion system comprises the following steps:

Step 1: Data collection

The first step in developing a CNN -based wildlife intrusion system is to collect a large amount of data. This data should include images of the local wildlife in different lighting conditions, angles, and backgrounds. The images should be labeled to indicate whether or not they contain wildlife. This labeled dataset will be used to train the CNN model.

Step 2: Data Preprocessing

The next step is to preprocess the data to improve its quality and consistency. This includes cropping the images to remove any unwanted background, resizing the images to a standard size, and converting the images to grayscale or RGB format. The data should also be split into training, validation, and testing sets.

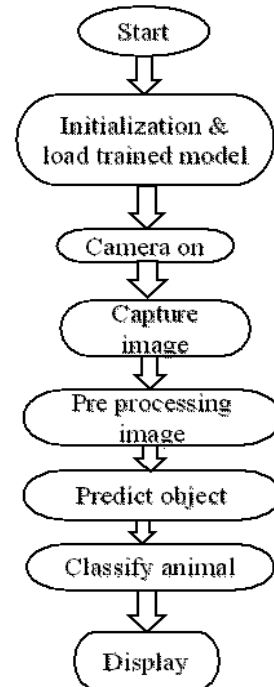


Fig.1: Flow chart of the proposed method

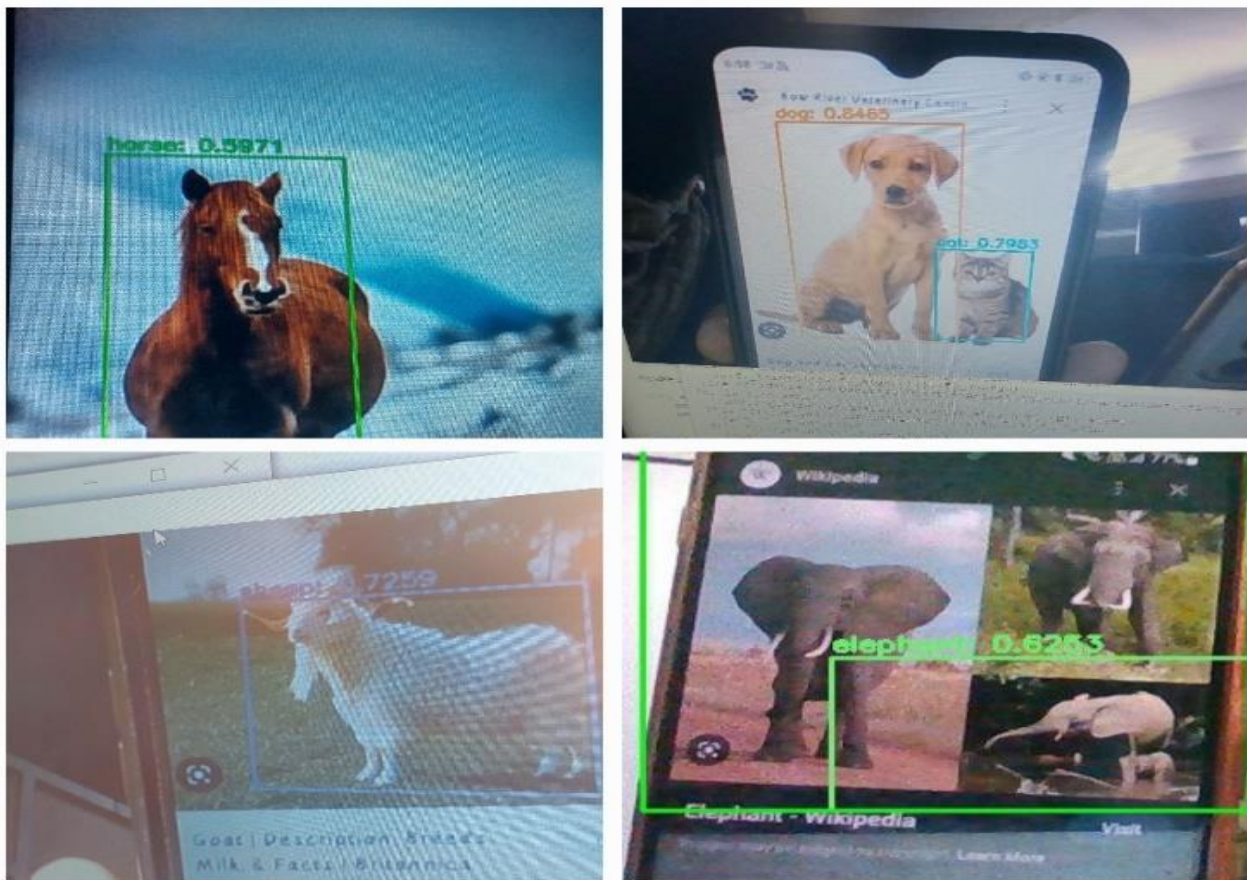


Fig.2: Domestic animal detection

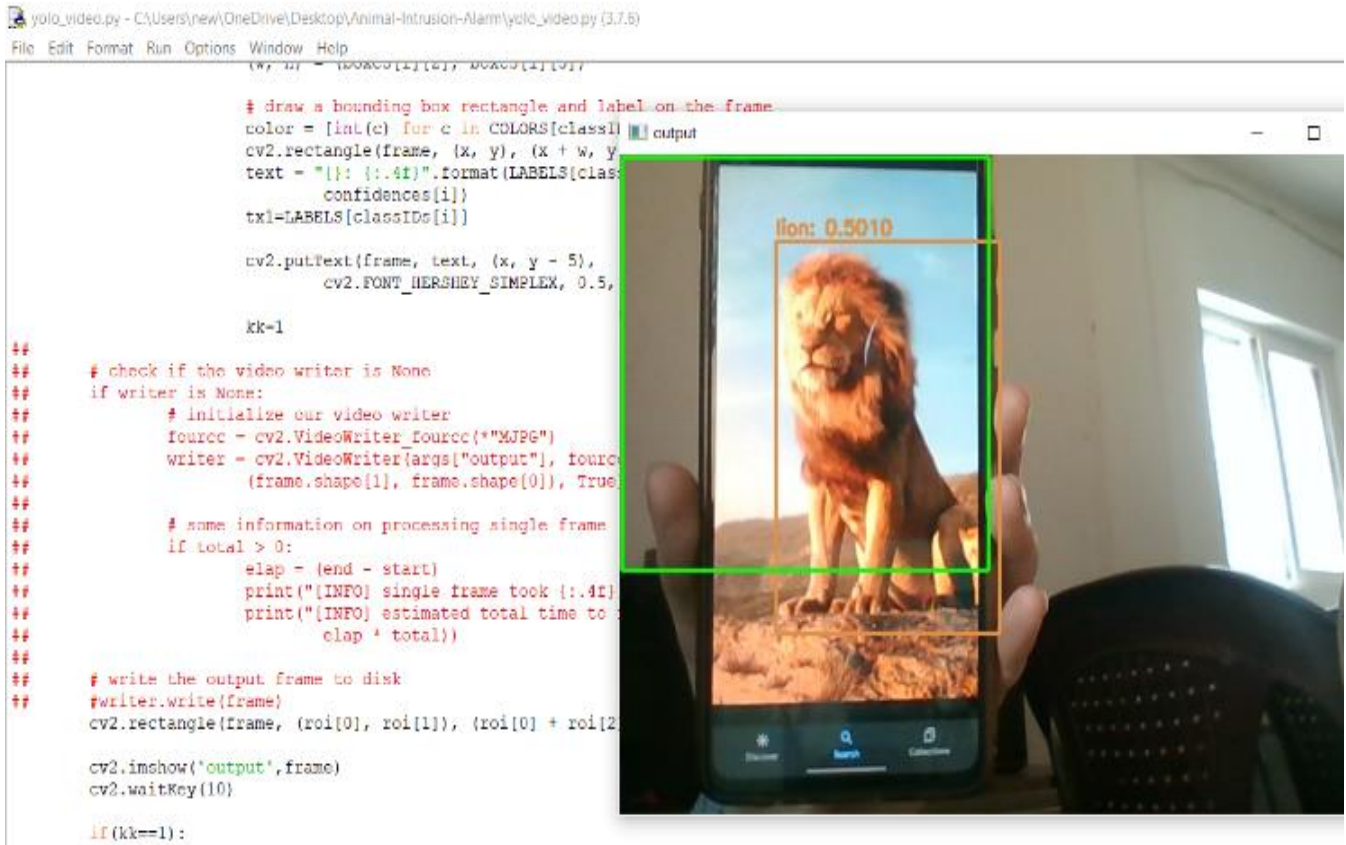


Fig.3: Lion

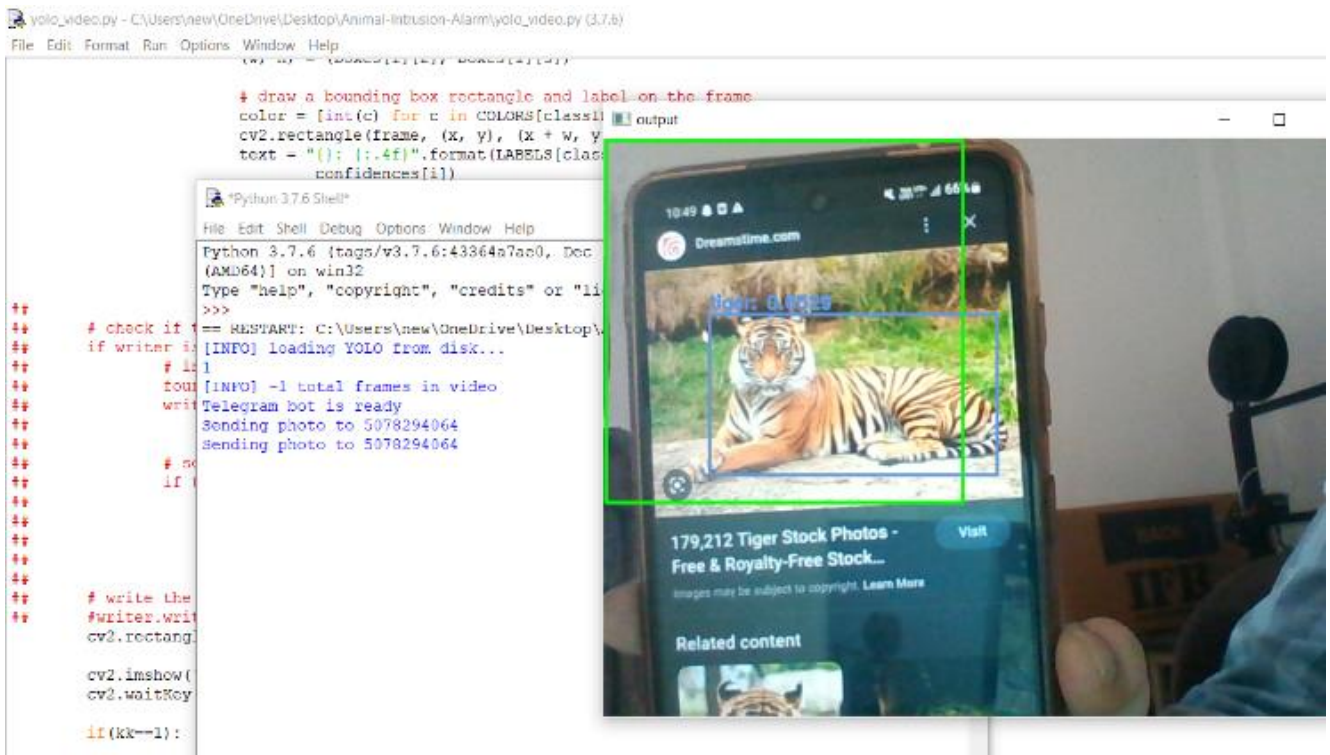


Fig.4: Tiger

Step 3: CNN Model Training

The third step is to train the CNN model using the preprocessed dataset [6]. The model architecture should include convolutional layers, pooling layers, and fully connected layers. The number of layers and neurons in each layer can be varied depending on the size and complexity of the dataset.

Step 4: Model Evaluation

Once the model is trained, it should be evaluated using the testing set. If the model's performance is not satisfactory, it can be fine-tuned by adjusting the model architecture or hyperparameters [7].

Step 5: Deployment

Once the model is trained and evaluated, it can be deployed to detect wildlife intrusion. When the system detects wildlife, it can alert the concerned authorities, who can take appropriate action.

4. Results and Discussion

CNN-based wildlife intrusion detection and alert systems have shown promising results and have the potential to be an effective tools for wildlife conservation and protection. It can be an effective tool to detect wildlife intrusion in rural and natural environments. By following the steps mentioned above, a reliable and accurate model can be developed which can help mitigate the problem of wildlife intrusion.

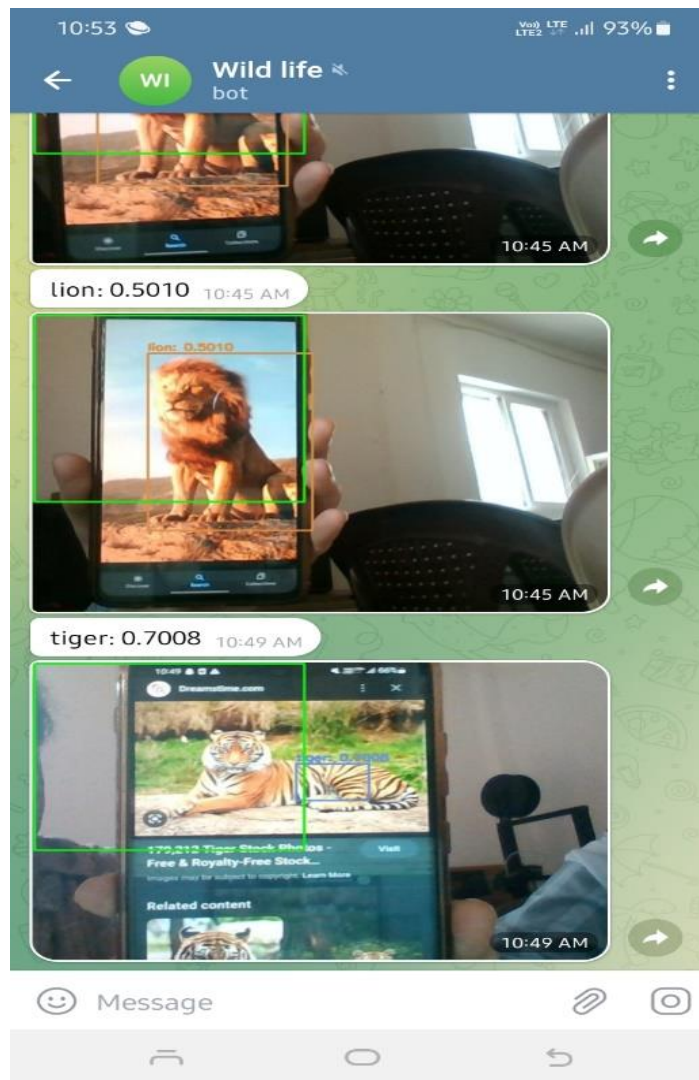


Fig.5: Alert message to telegram app

4.1 Wild animal detection

Animals are detected through live capturing, either an image or video is displayed in front of a webcam it detects the wild animal's name with accuracy and checks whether the wild animal is within the border, if the wild animal reaches out then an alert message is sent to the telegram app.

4.2 Notification

A Telegram Bot API is created in, order to send a notification to the users to make them alert about wild animals if they cross the border. The outputs are randomly taken and sent with the labels of the animal along with the confidence score.

5. Conclusion

A CNN-based wildlife intrusion detection and alert system can be an effective solution for monitoring and protecting wildlife habitats. By analyzing real-time footage using deep learning techniques, the system can accurately detect and classify potential threats, such as human intrusions or predator animals. With timely alerts, conservationists can take appropriate action to mitigate the risks and ensure the safety of wildlife. However, the success of such a system depends on several factors, including the quality of the data, the accuracy of the model, and the effectiveness of the alert mechanism. Additionally, ethical considerations must be taken into account, such as the potential impact on privacy and human rights.

Conflict of Interest

The authors declare no conflict of interest

References

[1] G. S. Rekha, A. H. Babu, S. Manjunath, K. K Bhat, and K. Prasad "Wildlife Monitoring Using Image

Processing," *International Journal of Science Technology and Engineering*, Vol. 7, No. 1, pp. 18-22, July 2020.

- [2] S. Kumar, M. Sushmitha, P. Sirisha, J. Shilpa and D. Roopashree, "Sound Activated Wildlife Capturing," *2018 3rd IEEE International Conference on Recent Trends in Electronics, Information & Communication Technology (RTEICT)*, Bangalore, India, pp. 2250-2253, 2018. doi: 10.1109/RTEICT42901.2018.9012357.
- [3] S. Vishwakarma, H. Ghosalkar, R. Benere and Y. Chavan, "Night Motion Detection and Alert System," *International Journal of Advanced Research in Science, Communication and Technology*, Vol. 7, No. 1, pp. 301-304, July 2021.
- [4] P. Sharma, C. K. Sirisha, S. Gururaj, C. Padmavathi "Neural Network Based Image Classification for Animal Intrusion Detection System," *International Journal of Progressive Research in Science and Engineering*, Vol. 1, No. 4, pp. 1-7, July, 2020.
- [5] C. K. Sreedevi, E. Saritha "Automated Wildlife Monitoring using Deep Learning," *International Conference in Sustainable Energy and Engineering* pp. 1-7, July 2019.
- [6] H. Archana, K. Poornima, V. Raksha, H. R. Shwetha and H. S. G. Supreeth "Artificial Neural Network Based Image Processing for Wild Animal Detection and Monitoring", *International Journal of Advanced Research in Computer Science and Software Engineering*, Vol. 7, No. 5, pp. 687-691, May 2017.
- [7] M. Vasile Ghiurcau, C. Rusu and R. Ciprian Bilc, "Wildlife intruder detection using sounds captured by acoustic sensors", *IEEE International Conference on Acoustics, Speech and Signal Processing*, Dallas, TX, USA, pp. 297-300, 2010. doi: 10.1109/ICASSP.2010.5495924.



Copyright: © 2023 by the authors, Licensee ITEECS, India. This article is an open-access article distributed under the terms and conditions of the Creative Commons Attribution (CC BY) license (<https://creativecommons.org/licenses/by/4.0/>).

Triple Band Dual Angular Ring Antenna for Wearable Applications

Mr. G.Vijaya Kumar¹, T.Anish², P.Yeshwanth Balaji³, G.Yaswanth⁴, N.Pratap⁵

¹ Assistant Professor, ^{2,3,4,5} UG Students

Department of ECE, Andhra Loyola Institute of Engineering and Technology, Vijayawada.

Abstract:

In this paper, a triple-band open-ring high-gain, high-efficiency antenna for wearable applications at 2.45, 3.0, and 3.45 GHz is presented. The proposed antenna runs at 3.0 GHz for military applications, 2.45 GHz for industrial specific, and medical (ISM), and 3.45 GHz for worldwide Microwave Access (WiMAX) application interoperability. For off-body communication, the suggested triple-band antenna offers great qualities, including a directional radiation pattern, high gain, high efficiency, low specific absorption rate (SAR), and wearer comfort. The antenna construction is made up of two substrates—a rigid substrate and a textile substrate—in order to achieve these features. The back of the textile substrate also has a square of conductive cloth attached to it. The inner open-ring of the open-ring radiator stimulates two resonant modes at high frequencies of 3.0 and 3.45 GHz, generating triple-band at 2.45, 3.0, and 3.45 GHz. A single resonant mode is excited by the outer open-ring at a low frequency of 2.45 GHz. In order to reduce the size of the antenna and yet preserve antenna stability, the outer annular ring is shorted to the ground plane via a shorting pin. The electromagnetic waves that are directed towards the human body are diminished by the conductive cloth, which acts as a full-ground plane or shield. As a result, the SARs are greatly reduced. The performance of the suggested antenna in free space and on phantom/human bodies is measured in order to confirm its suitability for off-body communication.

Keywords: Triple-band, Off Body communications, textile substrate, wearable antenna

I. INTRODUCTION

The demand for wearable communication devices has increased in recent years, and the development of efficient, comfortable, and reliable antennas for such devices has become increasingly important. In this paper, we present a triple-band dual annular ring high-gain high-efficiency antenna for 2.45/3.0/3.45 GHz wearable applications. The proposed antenna operates at 2.45 GHz for Industrial, Specific, and Medical (ISM) applications, 3.0 GHz for military applications, and 3.45 GHz for Worldwide Interoperability for Microwave Access (WiMAX) applications. The proposed triple-band antenna aims for excellent off-body communication, which has directional radiation pattern, high gain, high efficiency, low-specific absorption rate (SAR), and comfortability for wearers.

A. Design Considerations

To attain the desired features of the antenna, the antenna structure consists of two substrates, a rigid substrate and a textile substrate. Two open-ring radiators and a 1 by 2 power divider coaxial feeding network are printed on a low-loss rigid substrate. In addition, a square conductive textile is adhered on the backside of the textile substrate.

The open-ring radiator generates triple-band at 2.45, 3.0, and 3.45 GHz, in which the inner open-ring excites two resonant modes at high frequencies of 3.0 and 3.45 GHz.

Triple band Dual Angular Ring antenna for wearable applications

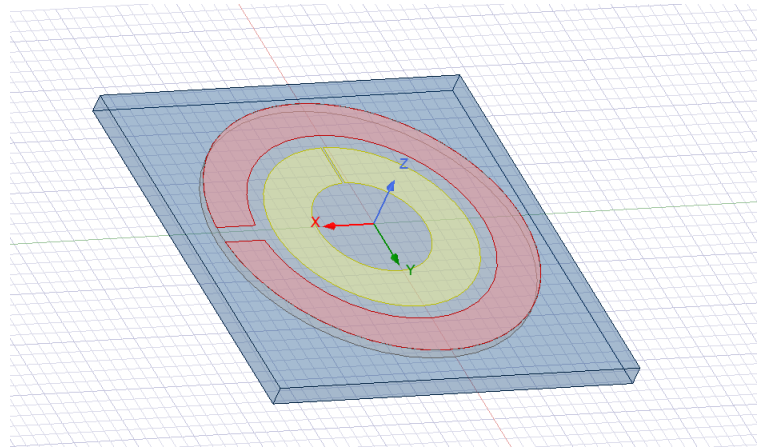


Fig 1. Rings Structure

The outer open-ring excites a single resonant mode at a low frequency of 2.45 GHz. The outer annular ring is connected to the ground plane by a conductive shorting pin to reduce the antenna size. The conductive textile works as a ground plane and acts as a protective shield to reduce the EM waves toward the wearer. Therefore, the SARs are significantly minimized.

B. Proposed Design

Fig 1. depicts the design of the wearable triple-band open ring antenna that is suggested for off-body communications. The two substrates that make up the suggested antenna structure are: a TLY-5 substrate and felt substrate are both used. A Taconic TLY-5 substrate with a dielectric constant of 2.2, a loss tangent of 0.0009, and a thickness of 1.52 mm is printed with two open-ring radiators.

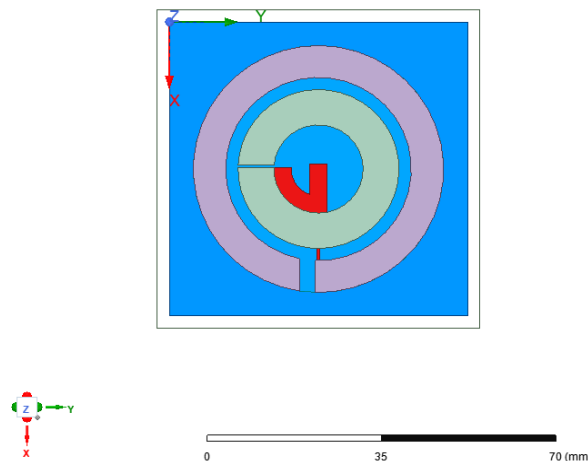


Fig 2. Top View of the antenna

The inner radius and width of the open-ring radiator, designated as IR, are r_1 and w_1 , respectively. The OR, or outer open-ring radiator, is designated by the letters r_2 and w_2 , which stand for its inner radius and width, respectively. G_1 , G_2 , and G_3 are the gaps on and between IR and OR.

According to **Fig 2.** the gap directions on IR and OR are parallel to one another. On the back of the TLY-5 substrate, a 1 2 feeding network is printed. A 50-ohm coaxial wire is soldered at the feeding network's input power.

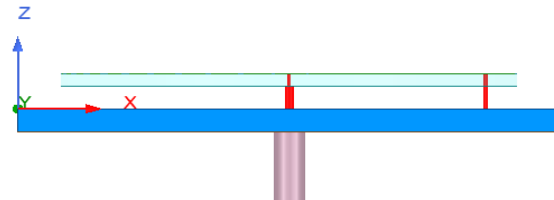


Fig 3. Side View of the antenna

The two vias, Via1 and Via2, provide the output powers to IR and OR, respectively. The inner radius and width of the feeding network sector are r_3 and w_3 , respectively. The two output strips have the following widths and lengths: w_4 , l_1 , and l_2 , as shown in Fig. The feeding network delivers balanced signals of equal magnitude to IR and OR. Additionally, it converts the IR and OR impedances to match the input signal's 50-ohm coaxial line. ShieldIt superconductive textile with a conductivity of 11800 S/m and a felt substrate with a thickness and width of 3 mm make up the ground plane. A 1 mm-radius shorting pin, designated as Via3, connects the OR to the ground plane. Additionally, Via3 functions as a supporter to keep the distance between the Taconic substrate and the felt substrate of h constant.

C. Design specifications

The antenna was designed using the ANSYS high-frequency structure simulator (HFSS). The dimensions used are listed as follows:
 $w_s = 60$, $r_1 = 9$, $w_1 = 7.2$, $r_2 = 18.7$, $w_2 = 6.5$, $g_1 = 0.4$, $g_2 = 3$, $g_3 = 2.5$, $r_3 = 5.5$, $w_3 = 3.5$, $l_1 = 13$, $l_2 = 3.6$, $w_4 = 0.5$, $h = 3$ (unit: mm).

Parameter	Dimensions (mm)
Ws	60
R1	9
W1	7.2
R2	18.7
W2	6.5
G1	0.4
G2	3
G3	2.5
R3	5.5
L1	3.5
L2	3.6
W4	0.5
H	3
W3	3.5

Table 1. Antenna dimensions

II. SIMULATION RESULTS

The compatibility of the proposed antenna for off-body communication is verified by measuring the antenna performance in free-space and on phantom/human bodies. The simulated and measured results show very good agreement. The proposed triple-band antenna has a directional radiation pattern, high gain, and high efficiency. The specific absorption rate (SAR) is low, which makes it suitable for wearable communication devices. The proposed antenna is comfortable for wearers, making it an ideal solution for off-body communication.

1.Return Loss: How much power is delivered from the source to a load is measured as a Return loss and given by S11 parameter. According to simulated result resonant frequencies are at 2.47 GHz , 3.0 GHz and 3.46 GHz with return loss of -13.7 dB , -22.7 dB and -14.15 dB respectively.

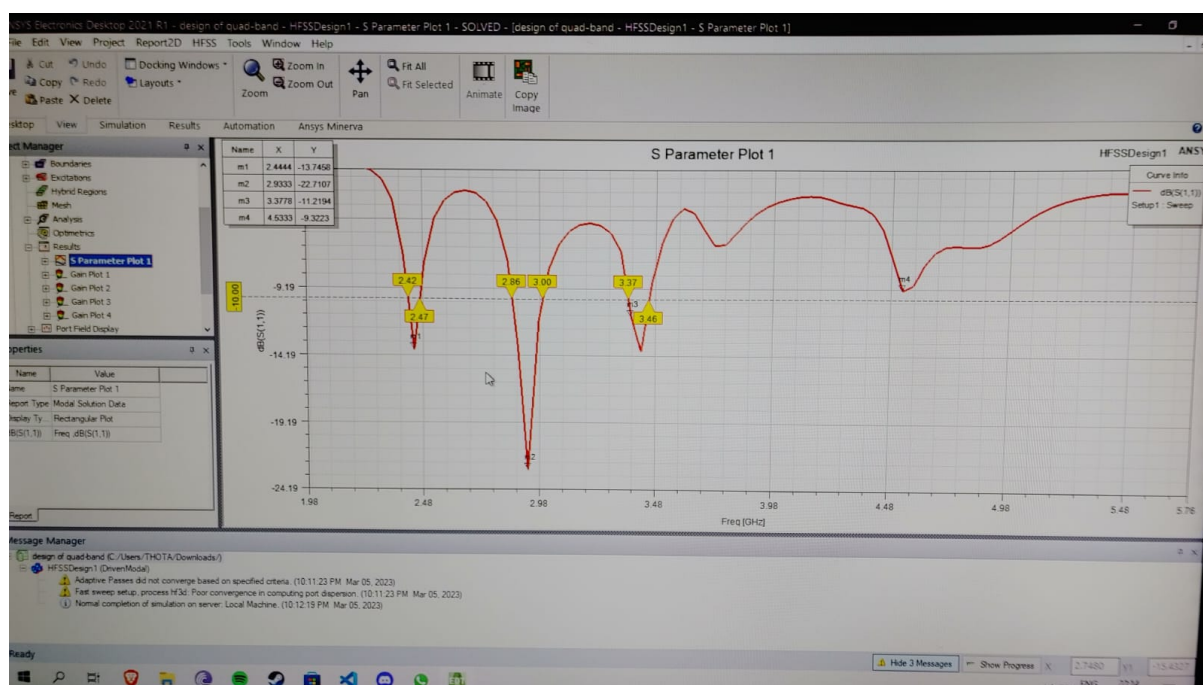


Fig 4. S-Parameter Plot (S11 Plot)

2.Radiation Patterns: It represents the energy radiated by an antenna. The gain of the designed antenna is shown below at different operating frequencies:

At 2.45 GHz simulation the maximum gain observed was at -85 degrees with a gain of >14dB, at 3.0 GHz the maximum radiation observed was 9.1dB at angles ranging from +85 degrees to + 115 degrees. At 3.45 GHz the maximum radiation observed was >15dB at angle 90 degrees. And 15dB at angles ranging from +85 degrees to +120 degrees.

The radiation patterns for the same are mentioned below.

Triple band Dual Angular Ring antenna for wearable applications

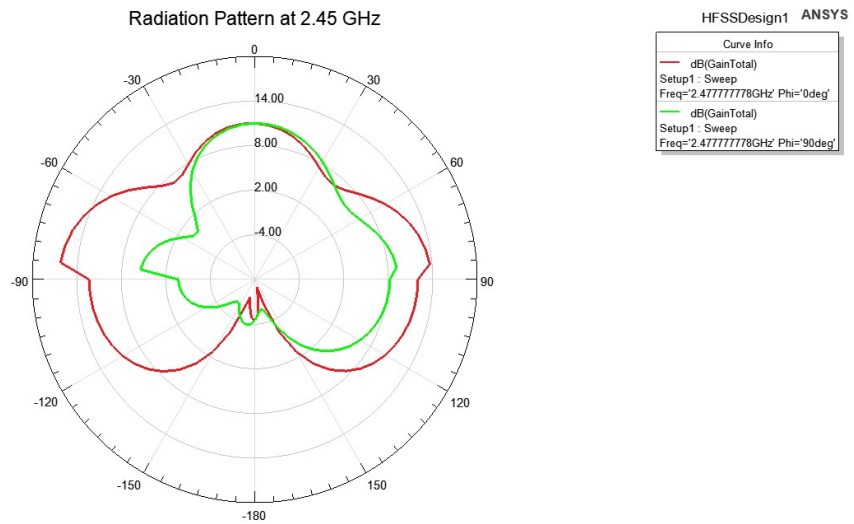


Fig 5. Radiation Pattern at 2.45 GHz

At 2.45 GHz simulation the maximum gain observed was at -85 degrees with a gain of >14dB, as shown in Fig 5.

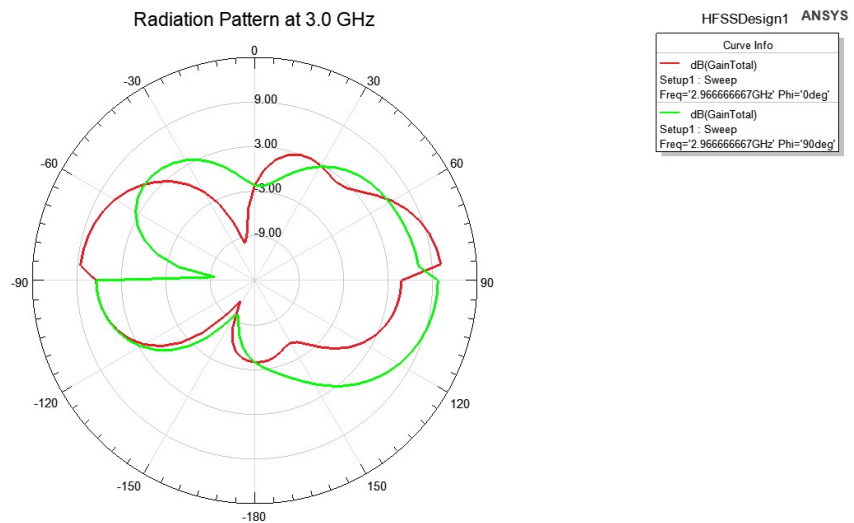


Fig 6. Radiation Pattern at 3.0 GHz

At 3.0 GHz the maximum radiation observed was 9.1dB at angles ranging from +85 degrees to + 115 degrees as shown in Fig 6.

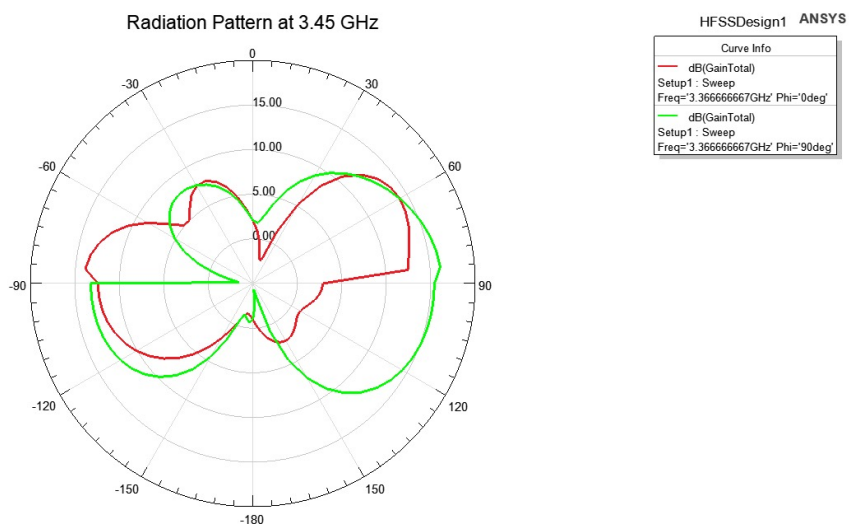


Fig 7. Radiation Pattern at 3.45 GHz

At 3.45 GHz the maximum radiation observed was >15dB at angle 90 degrees. And 15dB at angles ranging from +85 degrees to +120 degrees as shown in Fig 7.

3. Specific Absorption Rate (SAR): It is a measure of how RF transmitted energy is absorbed by the human tissue. The units of SAR are W/Kg, or equivalently, mW/g. The SAR limit in the US for mobile phones is 1.6 W/Kg , averaging over 1 gram of tissue.

In order to model a real-world scenario, the proposed antenna is simulated over a 160x160x27 mm three-layered human tissue sample, as shown in Fig 8. , with a 5 mm spacing between it and the human tissue. A 2 mm thick skin, a 5 mm thick layer of fat, and a 20 mm thick layer of muscle make up the three layers of tissue. Fig 9. contains information on relative permittivity, conductivity, and mass density. The SAR after simulation was satisfactory at 0.05 , 0.12 , 0.62 W/Kg at 2.45 , 3.0 and 3.45 GHz.

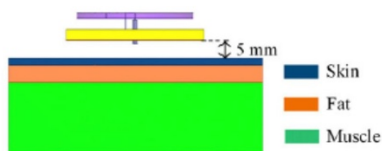


Fig 8. Human Tissue

Layer	Permittivity	Conductivity	Mass Density
Skin	35.11	3.72	1100
Fat	4.95	0.29	910
Muscle	48.48	4.96	1041

Fig 9. Properties of Human Tissue

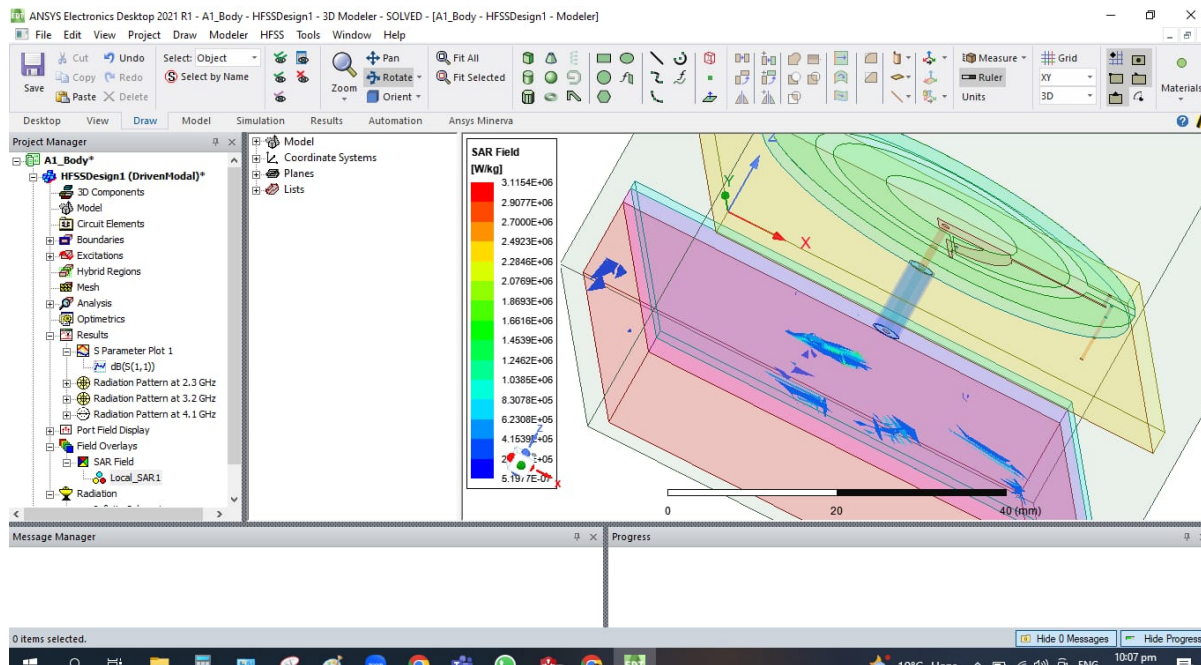
Triple band Dual Angular Ring antenna for wearable applications

Fig 10. SAR Simulation in HFSS

III. CONCLUSION

In conclusion, a triple-band dual annular ring high-gain high-efficiency antenna with three operating frequencies for wearable applications has been presented. The proposed antenna has excellent features for off-body communication, such as directional radiation pattern, high gain, high efficiency, low-SAR, and comfortability for wearers. The antenna structure consists of two substrates, a rigid substrate and a textile substrate, and a conductive textile is adhered on the backside of the textile substrate. The proposed antenna has been verified by measuring the antenna performance in free-space and on phantom/human bodies, and the results show very good agreement.

IV. REFERENCES

1. A Compact Circularly Polarized Antenna With Directional Pattern for Wearable Off-Body Communications.
2. Compact, Low-Profile and Robust Textile Antennas with Improved Bandwidth for Easy Garment Integration Idellyse Martinez¹, Member, IEEE, Chun Xu Mao^{1,2}, Member, IEEE, Dieff Vital³, Student Member, IEEE, Hasan Shahariar⁴, Douglas H. Werner¹, Fellow, IEEE, Jesse S. Jur⁴, and Shubhendu Bhardwaj³, Member, IEEE.
3. Design of Wearable Textile Patch Antenna Using Cshape Etching Slot for Wi-MAX and 5G Lower Band Applications M. Hasan Mahfuz, Md Rafiqul Islam, Nazmus Sakib, Mohamed Hadi Habaebi, Md Abu Tayab Sakib.
4. Dual-Band and Dual-polarization Microstrip Antennas Loaded with Split Ring Resonators; Bo Tao, Mingyan Jiang, Lei Zhang, Shijin Hu
5. Dual-Band Wearable Textile Antenna on an EBG Substrate. Authors: Shaozhen Zhu, Student Member, IEEE, and Richard Langley
6. A Wide Bandwidth Wearable All-textile PIFA with Dual Resonance Modes for 5-GHz WLAN Applications Guo-Ping Gao, Member, IEEE, Chen Yang, Student Member, IEEE, Bin Hu, Senior Member, IEEE, Rui-Feng Zhang, Student Member, IEEE, and Shao-Fei Wang, Student Member, IEEE

Triple band Dual Angular Ring antenna for wearable applications

7. Designing of Textile Antenna for on Body Communications. Authors: Prof. N.R. Ingale, Rasika Bhirud, Sapna Jadhav, Shivam Salunkhe
8. An Annular Ring Microstrip Patch antenna for multiband applications. Authors: Neha Gupta, Ramanjeet Singh.
9. Polarization Characteristics of Multiband Loaded Microstrip Annular Ring Antennas. Authors: Saeed I. Latif, Lotfollah Shafai.

Mutual coupling Reduction technique in a Dual-Band MIMO Antenna for WBAN Application

Mr. G. VIJAY KUMAR¹ V. RUCHITHA² R. SRAVANTHI³ K. JAHNAVI⁴

¹Assist Prof., ECE Department, ALIET, JNTUK, Vijayawada, Andhra Pradesh, India

²Student., ECE Department, ALIET, JNTUK, Vijayawada, Andhra Pradesh, India

³Student., ECE Department, ALIET, JNTUK, Vijayawada, Andhra Pradesh, India

⁴Student., ECE Department, ALIET, JNTUK, Vijayawada, Andhra Pradesh, India

Abstract: A MIMO(Multi-Input-Multi-output) antenna with 4 octagonal elements for the WBAN (wireless body area network) application is proposed in the paper. This antenna integrated with split-ring, bar slot and each patch separated by a meander line. The dimensions of this proposed antenna are 20*60*2mm. The substrate used in this antenna is an FELT substrate with a permittivity of 1.45 The operating frequency of this antenna is 2.45GHz and 3. 5GHz.All four octagonal elements are placed in an orthogonal manner with good isolation. Fed can be provided using co-axial. The proposed MIMO antenna achieved an impedance bandwidth($S_{11} < -10\text{dB}$) at both desired frequencies. In this antenna mutual coupling is also below -40dB .The performance parameter proposed MIMO antenna are relatively good. There is no need to concentrate on the isolation issue. The peak achieved is 5.8dB and radiation efficiency is 80%. The generated results, for proposed antenna four element MIMO antenna can be suggested as a suitable aspirant for WBAN application like health monitoring, sports, military applications.

Keywords: Orthogonal elements, multi input multi output (MIMO)Antenna, mutual coupling, Co-axial, Wireless body area network (WBAN).

1.Introduction

The transmission of data with higher data rates is a major consideration nowadays. Having this in mind MIMO (Multi Input Multi Output) came into the picture to solve this problem more efficiently. There are many other advantages of this MIMO like the low-cost and high performance. They are small in size and can be operated in the perfect band of frequency that the antenna is designed for. Over the past few years, MIMO s gave a greater edge for research and also for developing and designing new antennas for separate applications.

ISM bands are portions of the radio spectrum reserved internationally for industrial, scientific, and medical (ISM) purposes excluding applications in telecommunications. Medical applications like biotelemetry, industrial and commercial purposes. This antenna can be used for body-centric communication for various parameters. For scientific and industrial purposes like cordless phones, Microwave ovens, and baby monitoring which are operating in 2.4GHz frequency. For commercial purposes like wireless communication with long rang and moderate data rates and for short ranges, it is higher data rates.

Flexible electronics has gained a large amount of attention of the researchers in the recant years. This technology is widely used in the development of wearable devices such as wearable antennas and wearable sensors as the play a vital role in the field of military and medical applications. These wearable antennae can be integrated with clothing, attached with wearable such as shoes, wrist watch, health monitoring devices etc. The flexible wearable electronics has a lot of applications in health monitoring such as heart rate monitoring, ECG monitoring, motion detection, sweat monitoring etc. The most important requirement of such wearable flexible electronics are light weight, low cost, low maintenance and must with stand environmental effects.

Considerable published work has reported on the effects of mutual coupling in dual band antenna array. However, the alleviating the effects of coupling (S_{21} , S_{31} , S_{41}) for dual band MIMO antenna, operating at 2.45 and 3.5GHz is discussed. This research proposes a unique hybrid technique to suppress the mutual coupling of the 4x1 MIMO. In previous paper the author has proposed MIMO antenna array with dual bands for WBAN applications, with octagonal shape.

2. Antenna modelling

SINGLE ELEMENT

The antenna is designed with three layers the first is ground layer is placed upon which the substrate layer and finally patch is placed on it. The dimensions of antenna are 50*70*2mm. The substrate that we used here is FR4 Epoxy. We have introduced the slots in the patch.

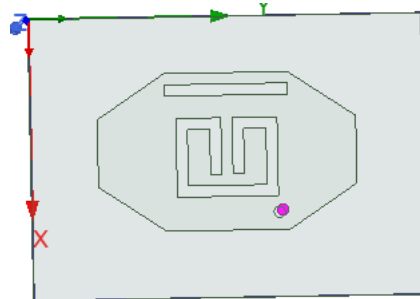
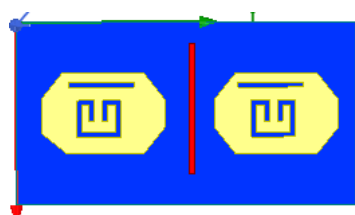


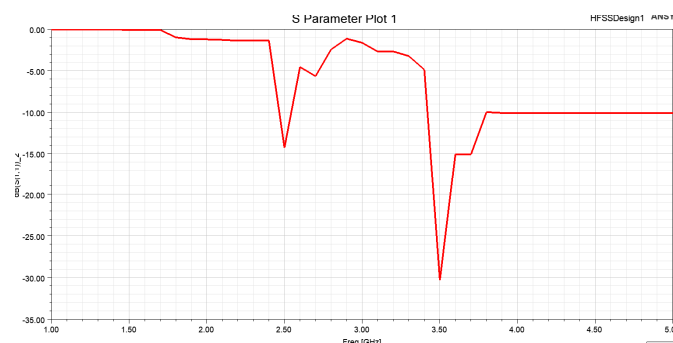
Fig: Single element with S11 characteristics

MIMO ANTENNA

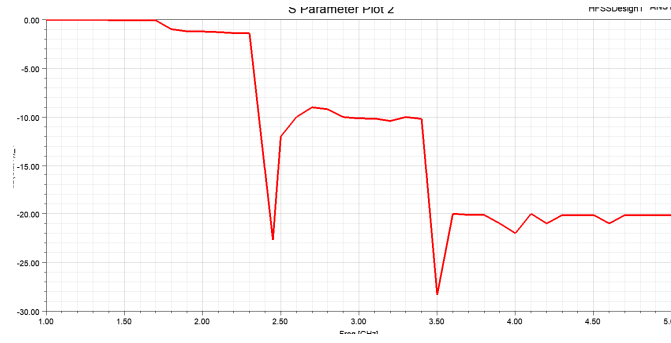
The MIMO antenna having a space of 4 mm between M1 and M2 elements. This antenna is prototyped on FR-4 substrate having 70*132.8*1.6mm. S-parameter characteristics of 2-element MIMO antenna are shown. Now s-parameters of port-1 and port-2 that is S11 and S12 are analyzed and calculated because the elements are analogous to each other. Coupling between two elements will be given by the parameter S21 and this coupling should be more than 10dB and its achieve a high degree of isolation.



(a)



(b)

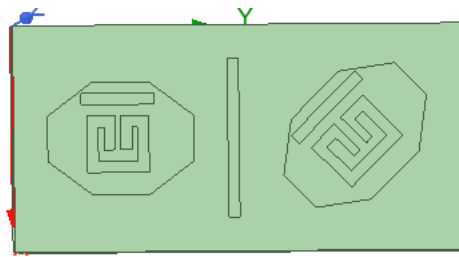


(c)

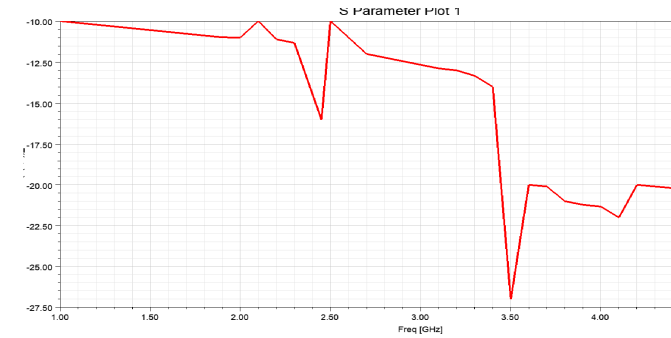
Fig: (a)Two-element MIMO antenna (b)(c) S-parameter characteristics of 2-element MIMO antenna

MIMO 45° ANTENNA

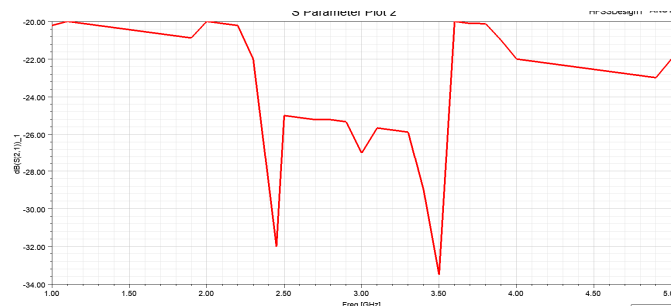
The geometrical view of MIMO antenna with 2-elements M1 and M2 elements are located in different directions. A space of 2mm between M1 and M2. The first patch is at 0° and second patch is rotated at an angle of 45°. This antenna is also prototyped on FELT substrate having dimension 20*40*2mm and these is operated at 2.45 and 3.5GHZ. In between the isolation between M1 and M2 is above 25dB. As, for a good isolation the dimensions and substrate has been changed and designed with different material.



(a)



(b)

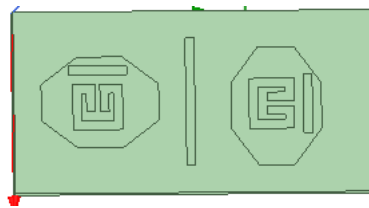


(c)

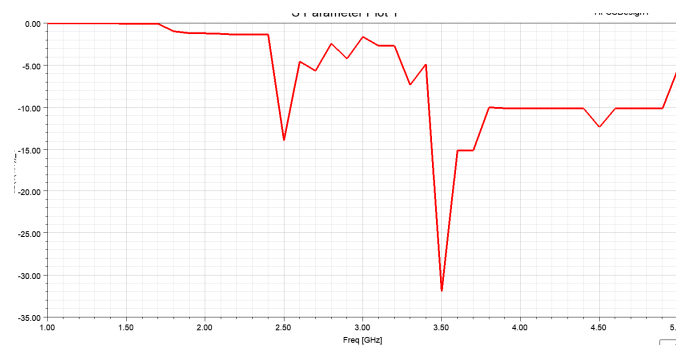
Fig: (a)Two-element MIMO antenna at 45 (b)(c) S-parameter characteristics of 2-element MIMO antenna

MIMO 90° ANTENNA

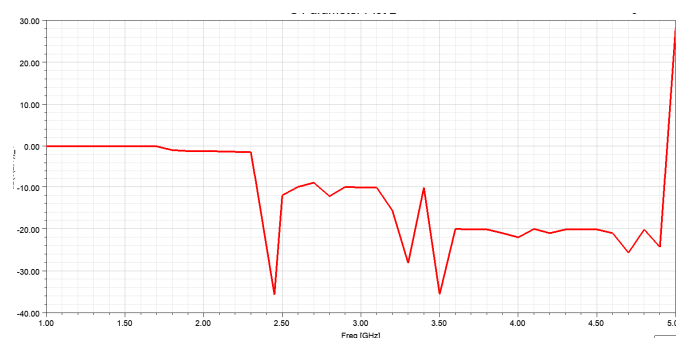
The MIMO antenna having a space of 2mm between M1 and M2. When M1 and M2 are placed orthogonal to each other (The first patch is placed at 0° and second patch is rotated at 90°) and substrate used is FELT and having dimensions 20*40*2mm and this antenna at dual band 2.45 and 3.5GHZ. The mutual coupling between M1 and M2 is more than -30dB. Finally, isolation has been decreased by arranging elements in 90° to each other.



(a)



(b)



(c)

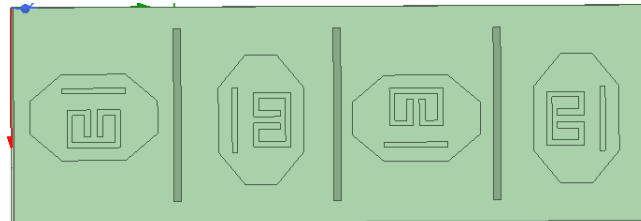
Fig: (a)Two-element MIMO antenna at 90 (b)(c) S-parameter characteristics of 2-element MIMO antenna

Summary of S11 and S21 at different rotation

Rotation (°)	Frequency (GHZ)	S11(dB)	S21(dB)
Single patch	2.45	-12.3	--
	3.5	-11.3	--
Both the patches are at 0°	2.45	-14.3	-22.7
	3.5	-30.3	-28.3

Patch 1 at 0° and patch 2 at 45°	2.45	-16.21	-32
	3.5	-27.10	-33.5
Patch 1 at 0° and patch 2 at 90°	2.45	-13.9	-35.62
	3.5	-31.95	-35.58

PROPOSED ORTHOGONAL MIMO ANTENNA

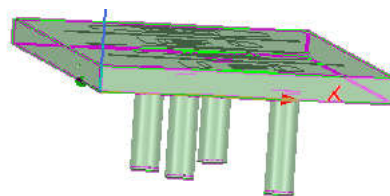


(a) Front view

The antenna proposed in this paper is designed with different slots on the patch. The antenna is designed with three layers the first layer is the ground is placed upon the substrate layer and then a patch is placed on it. The dimensions of the antenna are 20*60*2mm. The substrate that we use here is FELT. The measurement of this substrate are width is 20mm, length is 60mm and the thickness is 2mm. The ground plane is also same width and length.

Slots are placed in the patch which are called as bar-slots. The length of the upper slot is 8mm and the slots which are placed as a split -ring are having the dimensions of 4mm,6mm and 2mm.The width of the slot is 1mm.

Each element is separated with a mender line with a length of 16mm and each element are spaced with 2mm. Patch 1 is at 0° , Patch 2 is at 90°, Patch 3 is at 180° and patch 4 at 270°. The four elements are placed in the orthogonal manner.



(b) Side view

Theoretically, the values of the width and length of the patch can be calculated as mentioned in the formulae. ΔLp value and the ϵ_{eff} values are to be calculated first. In order to calculate this, we have to more formulae

$$\epsilon_{eff} = \frac{\epsilon_r + 1}{2} + \frac{\epsilon_r - 1}{2} \left(\frac{1}{\sqrt{1 + 12 \frac{hs}{W_p}}} \right)$$

$$\Delta Lp = 0.421hs \frac{(\epsilon_{eff} + 0.300) \left(\frac{W_p}{hs} + 0.264 \right)}{(\epsilon_{eff} - 0.258) \left(\frac{W_p}{hs} + 0.813 \right)}$$

- ΔLp = patch length change
- ϵ_{eff} = effective dielectric constant
- hs= height of the antenna z direction =2mm
- Lp= length of the patch
- Wp=width of the patch
- Co= λ_0 =velocity of light= 3×10^8 .

$$U = r^2 W_{rad} = B_0 F(\theta, \phi) \simeq \frac{r^2}{2\eta} \times [|E_\theta(r, \theta, \phi)|^2 + |E_\phi(r, \theta, \phi)|^2]$$

Directivity $D(\theta, \varphi)$
$$D = \frac{U}{U_0} = \frac{4\pi U}{P_{rad}} = \frac{4\pi}{\Omega_A}$$

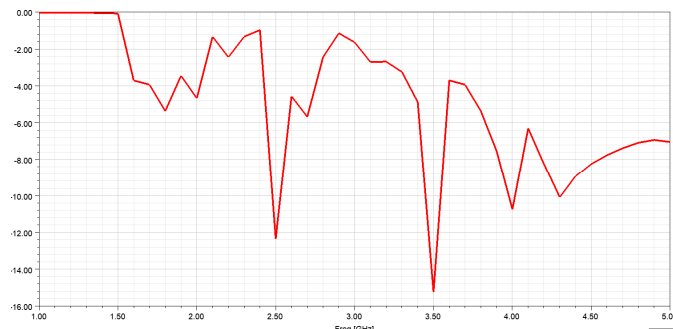
Maximum Directivity
$$D_{max} = D_0 = \frac{U_{max}}{U_0} = \frac{4\pi U_{max}}{P_{rad}}$$

Gain $G(\theta, \varphi)$
$$G = \frac{4\pi U(\theta, \phi)}{P_{in}}$$

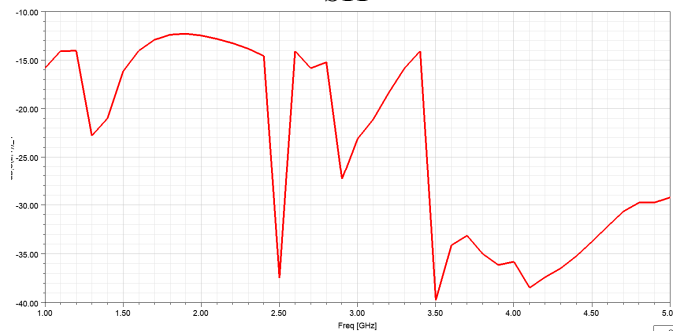
Total antenna efficiency $e_0 = e_r e_c e_d = e_r e_{cd} = (1 - |\Gamma|^2) e_{cd}$

Antenna Impedance $Z_A = R_A + jX_A = (R_r + R_L) + jX_A$

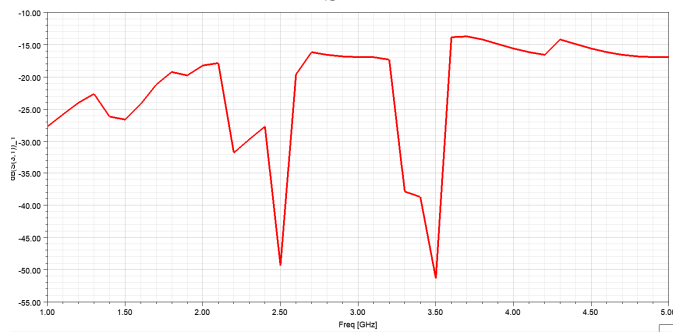
III. RESULTS



S11



S21



S31

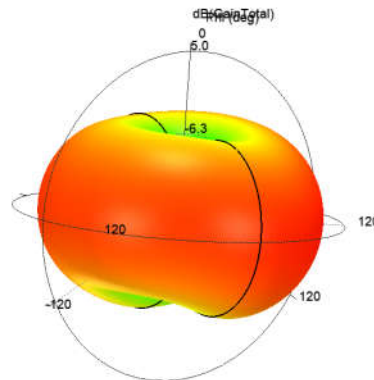
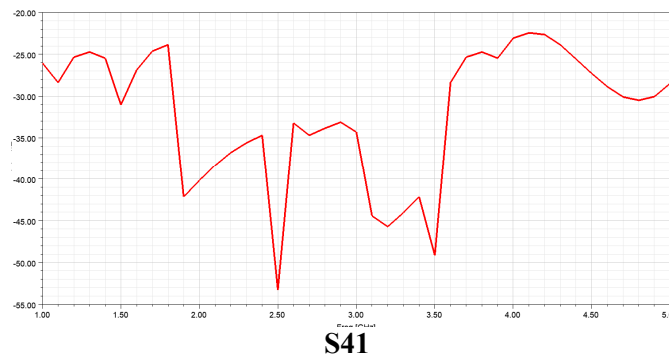


Fig: Gain plot of the antenna

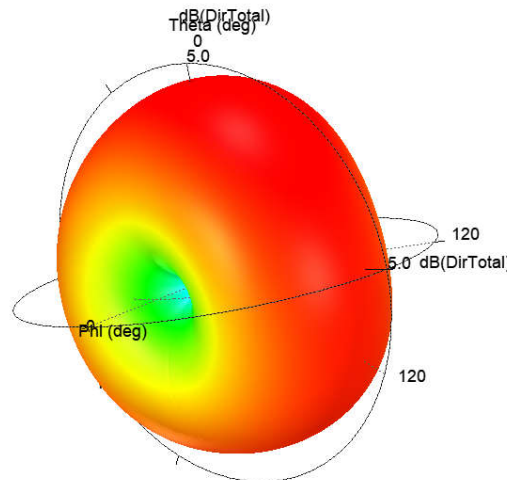


Fig: Directivity plot of the antenna

3.Application

This proposed antenna is being operated at two different frequencies that are at 2.45 and 3.5GHZ. So this antenna can be applicable in wireless communication and also this can be applicable in WBAN applications

4.Conclusion

This designed antenna can be preferred because of its high performance. An Orthogonal 4-element MIMO antenna is here proposed for WBAN application. Antenna parameters are achieved by incorporating the bar slots on the patch and a mender line between the patch. Simulated results are achieved at different frequencies. Some of the antenna parameters like s11, s21, s31, s41 and some far field radiation characteristics are discussed. The proposed MIMO antenna achieved an impedance bandwidth ($s_{11} < -10\text{dB}$) at the desired frequencies. Mutual coupling among the elements is also below -40dB . The proposed MIMO antenna has a good isolation and high diversity. Hence, proposed 4- element MIMO antenna is recommended as a good aspirant for WBAN applications and used at medical and non-medical applications.

REFERENCE

- [1] L. Liu, S. W. Cheung, and T. I. Yuk, "Compact MIMO antenna for portable devices in UWB applications," *IEEE Trans. Antennas Propag.*, vol. 61, no. 8, pp. 4257–4264, Aug. 2013.
- [2] J.-Y. Deng, L.-X. Guo and X.-L. Liu, "an ultra-wideband MIMO antenna with a high isolation," *IEEE Antennas Wireless Propag. Let.* vol. 15, pp. 182–185, 2016.
- [3] W. A. E. Ali and A. A. Ibrahim, "A compact double-sided MIMO antenna with an improved isolation for UWB applications," *AEU-Int. J. Electron Common.* vol. 82, pp. 7–13, Dec. 2017.
- [4] A. Iqbal, O. A. Saraereh, A. W. Ahmad, and S. Basher, "Mutual coupling reduction using F-shaped stubs in UWB-MIMO antenna," *IEEE Access*, vol. 6, pp. 2755–2799, 2018.
- [5] J.-F. Li, Q.-X. Chu, Z.-H. Li, and X.-X. Xia, "Compact dual band-notched UWB MIMO antenna with high isolation," *IEEE Trans. Antennas Propag.*, vol. 61, no. 9, pp. 4759–4766, Sep. 2013.
- [6] L. Liu, S. W. Cheung, and T. I. Yuk, "Compact MIMO antenna for portable devices in UWB applications," *IEEE Trans. Antennas Propag.*, vol. 61, no. 8, pp. 4257–4264, Aug. 2013.
- [7] J.-Y. Deng, L.-X. Guo and X.-L. Liu, "an ultra-wideband MIMO antenna with a high isolation," *IEEE Antennas Wireless Propag. Let.* vol. 15, pp. 182–185, 2016.
- [8] W. A. E. Ali and A. A. Ibrahim, "A compact double-sided MIMO antenna with an improved isolation for UWB applications," *AEU-Int. J. Electron Common.* vol. 82, pp. 7–13, Dec. 2017.
- [9] A. Iqbal, O. A. Saraereh, A. W. Ahmad, and S. Basher, "Mutual coupling reduction using F-shaped stubs in UWB-MIMO antenna," *IEEE Access*, vol. 6, pp. 2755–2799, 2018.
- [10] J.-F. Li, Q.-X. Chu, Z.-H. Li, and X.-X. Xia, "Compact dual band-notched UWB MIMO antenna with high isolation," *IEEE Trans. Antennas Propag.*, vol. 61, no. 9, pp. 4759–4766, Sep. 2013.



 Requires Authentication | Published online by [De Gruyter](#) | December 7, 2022

Single fiber grating profile multi scan parameters for the optimization of grating parameters by using OptiGrating simulation

Ahmed Nabih Zaki Rashed  , Baraa Riyadh Altahan, Thaticharla Manasavenna, P. Poorna Priya, M. Rama Krishna, SK Hasane Ahammad, Md. Amzad Hossain  and Salah Mohsen

From the journal [Journal of Optical Communications](#)

<https://doi.org/10.1515/joc-2022-0211>



Abstract

The paper reported the single fiber grating profile multi scan parameters for the optimization of the grating parameters by using OptiGrating program. The transmission/reflection spectrum of single grating fiber is reported versus variations of grating wavelength. Input–output pulse intensity of single grating fiber is clarified against the time span after the link length of 100 km. Fiber grating bandwidth, fiber grating side-lobes, fiber grating peak value and fiber grating pulse dispersion variations are clarified versus the scan parameter variations. The scan parameter can help the user in order to find the optimized grating parameters to meet the application requirements. As well as the optimized fiber grating amplitude/phase impulse response variations are outlined against the grating length variations.

Keywords: [dispersion parameter](#); [grating bandwidth](#); [grating spectrum](#); [scan parameter](#)

Corresponding authors: **Ahmed Nabih Zaki Rashed**, Electronics and Electrical Communications Engineering Department, Faculty of Electronic Engineering, Menoufia University, Menouf 32951, Egypt, E-mail: ahmed_733@yahoo.com; and **Md. Amzad Hossain**, Faculty of Electrical Engineering and Information Technology, Institute of Theoretical Electrical Engineering, Ruhr University Bochum, 44801 Bochum, Germany; and Department of Electrical and Electronic

Engineering, Jashore University of Science and Technology, Jashore, 7408,
Bangladesh, E-mail: mahossain.eee@gmail.com

Funding source: Al-Mustaqbal University College

Acknowledgment

The authors extend their appreciation and gratitude to Al-Mustaqbal University College in Iraq for funding this project.

Author contributions: All the authors have accepted responsibility for the entire content of this submitted manuscript and approved submission.

Research funding: This work is funded by Al-Mustaqbal University College in Iraq.

Conflict of interest statement: The authors declare no conflicts of interest regarding this article.

References

1. Miller, SE, Kaminow, IP, editors. *Optical fiber telecommunications II*. San Diego: Academic Press; 1988.
2. Adams, MJ. *An introduction to optical waveguides*. Boston: John Wiley & Sons; 1981.
3. Marcuse, D. *Principle of optical fiber measurements*. San Diego: Academic Press; 1981.
[10.1016/B978-0-12-470980-5.50008-7](https://doi.org/10.1016/B978-0-12-470980-5.50008-7) (<https://doi.org/10.1016/B978-0-12-470980-5.50008-7>)
4. Khan, SSA, Islam, MS. Determination of the best apodization function and grating length of linearly chirped fiber Bragg grating for dispersion compensation. *J Commun* 2012;7:840–6. <https://doi.org/10.4304/jcm.7.11.840-846> (<https://doi.org/10.4304/jcm.7.11.840-846>).
5. Rashed, ANZ, Tabbour, MSF. Suitable optical fiber communication channel for optical nonlinearity signal processing in high optical data rate systems. *Wirel Pers Commun* 2017;97:397–416.
[10.1007/s11277-017-4511-x](https://doi.org/10.1007/s11277-017-4511-x) (<https://doi.org/10.1007/s11277-017-4511-x>)
6. Rashed, ANZ, Tabour, MSF, El-Meadawy, S. Optimum flat gain with optical amplification technique based on both gain flattening filters and fiber Bragg grating methods. *J Nanoelectron Optoelectron* 2018;13:665–76.
<https://doi.org/10.1166/jno.2018.2168> (<https://doi.org/10.1166/jno.2018.2168>).
7. Mohamed, SEDN, Mohamed, AENA, El-Samie, FEA, Rashed, ANZ. Performance enhancement of IM/DD optical wireless systems. *Photonic Netw Commun* 2018;36:114–27.
<https://doi.org/10.1007/s11107-018-0761-0> (<https://doi.org/10.1007/s11107-018-0761-0>).

8. Rashed, ANZ, Tabbour, MSF. The trade off between different modulation schemes for maximum long reach high data transmission capacity optical orthogonal frequency division multiplexing (OOFDM). *Wireless Pers Commun* 2018;101:325–37. <https://doi.org/10.1007/s11277-018-5690-9> (<https://doi.org/10.1007/s11277-018-5690-9>).
9. Rashed, ANZ, Kader, HMA, Al-Awamry, AA, El-Aziz, IAA. Transmission performance simulation study evaluation for high speed radio over fiber communication systems. *Wireless Pers Commun* 2018;103:1765–79. <https://doi.org/10.1007/s11277-018-5879-y> (<https://doi.org/10.1007/s11277-018-5879-y>).
10. Rashed, ANZ, Tabbour, MSF. Best candidate integrated technology for low noise, high speed, and wide bandwidth based transimpedance amplifiers in optical computing systems and optical fiber applications. *Int J Commun Syst* 2018;31:e3801. <https://doi.org/10.1002/dac.3801> (<https://doi.org/10.1002/dac.3801>).
11. Rashed, ANZ, Tabbour, MSF, El-assar, M. 20 Gb/s hybrid CWDM/DWDM for extended reach fiber to the home network applications. *Proc Natl Acad Sci India Sect A (Phys Sci)* 2019;89:653–62. <https://doi.org/10.1007/s40010-018-0526-2> (<https://doi.org/10.1007/s40010-018-0526-2>).
12. Boopathi, CS, Kumar, VK, Sheebarani, S, Selvakumar, K, Rashed, ANZ, Yupapin, P. Design of human blood sensor using symmetric dual core photonic crystal fiber. *Results Phys* 2018;11:964–5. <https://doi.org/10.1016/j.rinp.2018.10.065> (<https://doi.org/10.1016/j.rinp.2018.10.065>).
13. Vigneswaran, D, Rajan, MSM, Aly, MH, Rashed, ANZ. Few-mode ring core fiber characteristics: temperature impact. *Photonic Netw Commun* 2019;37:131–8. [10.1007/s11107-018-0804-6](https://doi.org/10.1007/s11107-018-0804-6) (<https://doi.org/10.1007/s11107-018-0804-6>).
14. Chakkavarthy, SP, Arthi, V, Karthikumar, S, Rashed, ANZ, Yupapin, P, Amiri, IS. Ultra high transmission capacity based on optical first order soliton propagation systems. *Results Phys* 2019;12:512–3. <https://doi.org/10.1016/j.rinp.2018.12.002> (<https://doi.org/10.1016/j.rinp.2018.12.002>).
15. Rashed, ANZ, Kumar, KV, Prithi, S, Maheswar, R, Tabbour, MSF. Transmittivity/reflectivity, bandwidth, and ripple factor level measurement for different refractive index fiber grating shape profiles. *J Opt Commun* 2019. <https://doi.org/10.1515/joc-2018-0233> (<https://doi.org/10.1515/joc-2018-0233>) [Epub ahead of print].
16. Rashed, ANZ, Kumar, KV, Kumar, VP, Mohamed, AENA, Tabbour, MS, El-Assar, M. DWDM channel spacing effects on the signal quality for DWDM/CWDM FTTx network. *J Opt Commun* 2019. <https://doi.org/10.1515/joc-2019-0012> (<https://doi.org/10.1515/joc-2019-0012>) [Epub ahead of print].
17. Rashed, ANZ, Tabbour, MSF, Vijayakumari, P. Numerical analysis of optical properties using octagonal shaped photonic crystal fiber. *J Opt Commun* 2019. <https://doi.org/10.1515/joc-2019-0013> (<https://doi.org/10.1515/joc-2019-0013>) [Epub ahead of print].

18. Rashed, ANZ, Kumar, SS, Tabbour, MSF, Sundararajan, TVP, Maheswar, R. Different graded refractive index fiber profiles design for the control of losses and dispersion effects. *J Opt Commun* 2019. <https://doi.org/10.1515/joc-2019-0036> (<https://doi.org/10.1515/joc-2019-0036>) [Epub ahead of print].
19. Rashed, ANZ. Comparison between NRZ/RZ modulation techniques for upgrading long haul optical wireless communication systems. *J Opt Commun* 2019. <https://doi.org/10.1515/joc-2019-0038> (<https://doi.org/10.1515/joc-2019-0038>) [Epub ahead of print].
20. Rashed, ANZ, Kumar, KV, Tabbour, MSF, Sundararajan, TVP. Nonlinear characteristics of semiconductor optical amplifiers for optical switching control realization of logic gates. *J Opt Commun* 2019. <https://doi.org/10.1515/joc-2019-0027> (<https://doi.org/10.1515/joc-2019-0027>) [Epub ahead of print].
21. Ahmed, K, Paula, BK, Vasudevan, B, Rashed, ANZ, Maheswar, R, Amiri, IS, et al.. Design of D-shaped elliptical core photonic crystal fiber for blood plasma cell sensing application. *Results Phys* 2019;12:2021–5. <https://doi.org/10.1016/j.rinp.2019.02.026> (<https://doi.org/10.1016/j.rinp.2019.02.026>) .
22. Ramana, TV, Pandian, A, Ellammal, C, Jarin, T, Rashed, ANZ, Sampathkumar, A. Numerical analysis of circularly polarized modes in coreless photonic crystal fiber. *Results Phys* 2019;13:102140. <https://doi.org/10.1016/j.rinp.2019.02.076> (<https://doi.org/10.1016/j.rinp.2019.02.076>) .
23. Rashed, ANZ, Mohammed, AENA, Zaky, WF, Amiri, IS, Yupapin, P. The switching of optoelectronics to full optical computing operations based on nonlinear metamaterials. *Results Phys* 2019;13:102152. <https://doi.org/10.1016/j.rinp.2019.02.088> (<https://doi.org/10.1016/j.rinp.2019.02.088>) .
24. Ranathive, S, Kumar, KV, Rashed, ANZ, Tabbour, MSF, Sundararajan, TVP. Performance signature of optical fiber communications dispersion compensation techniques for the control of dispersion management. *J Opt Commun* 2019;76:1265–77. <https://doi.org/10.1515/joc-2019-0021> (<https://doi.org/10.1515/joc-2019-0021>) .
25. Amiri, IS, Rashed, ANZ, Yupapin, P. Interaction between optical sources and optical modulators for high-speed optical communication networks. *J Opt Commun* 2019. <https://doi.org/10.1515/joc-2019-0041> (<https://doi.org/10.1515/joc-2019-0041>) — .
26. Amiri, IS, Rashed, ANZ, Yupapin, P. Effects of order super Gaussian pulses on the performance of high data rate optical fiber channel in the presence of self phase modulation. *J Opt Commun* 2019. <https://doi.org/10.1515/joc-2019-0039> (<https://doi.org/10.1515/joc-2019-0039>) [Epub ahead of print].
27. Amiri, IS, Rashed, ANZ, Yupapin, P. Mathematical model analysis of dispersion and loss in photonic crystal fibers. *J Opt Commun* 2019. <https://doi.org/10.1515/joc-2019-0052> (<https://doi.org/10.1515/joc-2019-0052>) [Epub ahead of print].

28. Amiri, IS, Rashed, ANZ, Yupapin, P. Basic functions of fiber Bragg grating effects on the optical fiber systems performance efficiency. *J Opt Commun* 2019. <https://doi.org/10.1515/joc-2019-0042> (<https://doi.org/10.1515/joc-2019-0042>) [Epub ahead of print].
29. Amiri, IS, Rashed, ANZ, Mohammed, AENA, Aboelazm, MB, Yupapin, P. Nonlinear effects with semiconductor optical amplifiers. *J Opt Commun* 2019. <https://doi.org/10.1515/joc-2019-0053> (<https://doi.org/10.1515/joc-2019-0053>) [Epub ahead of print].
30. Amiri, IS, Rashed, ANZ, Yupapin, P. High-speed light sources in high-speed optical passive local area communication networks. *J Opt Commun* 2019. <https://doi.org/10.1515/joc-2019-0070> (<https://doi.org/10.1515/joc-2019-0070>) [Epub ahead of print].
31. Rashed, ANZ, Tabbour, MSF, Natarajan, K. Performance enhancement of overall LEO/MEO intersatellite optical wireless communication systems. *Int J Satell Commun Netw* 2019;38:31–40. <https://doi.org/10.1002/sat.1306.Jan./Feb.2020> (<https://doi.org/10.1002/sat.1306.Jan./Feb.2020>) .
32. Amiri, IS, Rashed, ANZ, Mohammed, AEA, El-Din, ES, Yupapin, P. Spatial continuous wave laser and spatiotemporal VCSEL for high-speed long Haul optical wireless communication channels. *J Opt Commun* 2019. <https://doi.org/10.1515/joc-2019-0061> (<https://doi.org/10.1515/joc-2019-0061>) [Epub ahead of print].
33. Amiri, IS, Rashed, ANZ, Yupapin, P. Average power model of optical Raman amplifiers based on frequency spacing and amplifier section stage optimization. *J Opt Commun* 2019. <https://doi.org/10.1515/joc-2019-0081> (<https://doi.org/10.1515/joc-2019-0081>) [Epub ahead of print].
34. Amiri, IS, Houssien, FMAM, Rashed, ANZ, Mohammed, AENA. Temperature effects on characteristics and performance of near-infrared wide bandwidth for different avalanche photodiodes structures. *Results Phys* 2019;14:102399. <https://doi.org/10.1016/j.rinp.2019.102399> (<https://doi.org/10.1016/j.rinp.2019.102399>) .
35. Amiri, IS, Rashed, ANZ. Simulative study of simple ring resonator-based brewster plate for power system operation stability. *Indones J Electr Eng Comput Sci* 2019;16:1070–6. <https://doi.org/10.11591/ijeecs.v16.i2.pp1070-1076> (<https://doi.org/10.11591/ijeecs.v16.i2.pp1070-1076>) .
36. Amiri, IS, Rashed, ANZ. Different photonic crystal fibers configurations with the key solutions for the optimization of data rates transmission. *J Opt Commun* 2019. <https://doi.org/10.1515/joc-2019-0100> (<https://doi.org/10.1515/joc-2019-0100>) [Epub ahead of print].
37. Amiri, IS, Rashed, ANZ, Ramya, KC, Kumar, KV, Maheswar, R. The physical parameters of EDFA and SOA optical amplifiers and bit sequence variations based optical pulse generators impact on the performance of soliton transmission systems. *J Opt*

Commun 2019. <https://doi.org/10.1515/joc-2019-0156> (<https://doi.org/10.1515/joc-2019-0156>) [Epub ahead of print].

38. Amiri, IS, Houssien, FMAM, Rashed, ANZ, Mohammed, AENA. Optical networks performance optimization based on hybrid configurations of optical fiber amplifiers and optical receivers. *J Opt Commun* 2019. <https://doi.org/10.1515/joc-2019-0153> (<https://doi.org/10.1515/joc-2019-0153>) [Epub ahead of print].

39. Amiri, IS, Rashed, ANZ, Sarker, K, Paul, BK, Ahmed, K. Chirped large mode area photonic crystal modal fibers and its resonance modes based on finite element technique. *J Opt Commun* 2019. <https://doi.org/10.1515/joc-2019-0146> (<https://doi.org/10.1515/joc-2019-0146>) [Epub ahead of print].

40. Amiri, IS, Houssien, FMAM, Rashed, ANZ, Mohammed, AENA. Comparative simulation of thermal noise effects for photodetectors on performance of long-haul DWDM optical networks. *J Opt Commun* 2019. <https://doi.org/10.1515/joc-2019-0152> (<https://doi.org/10.1515/joc-2019-0152>) [Epub ahead of print].

41. Amiri, IS, Rashed, ANZ, Mohammed, AEA, Aboelazm, MB. Single wide band traveling wave semiconductor optical amplifiers for all optical bidirectional wavelength conversion. *J Opt Commun* 2019. <https://doi.org/10.1515/joc-2019-0168> (<https://doi.org/10.1515/joc-2019-0168>) [Epub ahead of print].

42. Amiri, IS, Rashed, ANZ, Mohammed, AENA, Zaky, WF. Influence of loading, regeneration and recalling elements processes on the system behavior of all optical data bus line system random access memory. *J Opt Commun* 2019. <https://doi.org/10.1515/joc-2019-0163> (<https://doi.org/10.1515/joc-2019-0163>) [Epub ahead of print].

43. Malathy, S, Kumar, KV, Rashed, ANZ, Vigneswaran, D, Eeldien, ES. Upgrading superior operation performance efficiency of submarine transceiver optical communication systems toward multi tera bit per second. *J Comput Commun* 2019;14:6:192–200. <https://doi.org/10.1016/j.comcom.2019.08.009> (<https://doi.org/10.1016/j.comcom.2019.08.009>).

44. Amiri, IS, Rashed, ANZ. Numerical investigation of V shaped three elements resonator for optical closed loop system. *Indones J Electr Eng Comput Sci* 2019;16:1392–7. <https://doi.org/10.11591/ijeecs.v16.i3.pp1392-1397> (<https://doi.org/10.11591/ijeecs.v16.i3.pp1392-1397>).

45. Rashed, ANZ, Tabbour, MSF. The engagement of hybrid dispersion compensation schemes performance signature for ultra wide bandwidth and ultra long Haul optical transmission systems. *Wireless Pers Commun* 2020. <https://doi.org/10.1007/s11277-019-06687-2> (<https://doi.org/10.1007/s11277-019-06687-2>).

46. Rashed, ANZ, Tabbour, MSF, El-Meadawy, S, Anwar, T, Sarlan, A, Yupapin, P, et al.. The effect of using different materials on erbium-doped fiber amplifiers for indoor applications. *Results Phys* 2019;15:102650. <https://doi.org/10.1016/j.rinp.2019.102650> (<https://doi.org/10.1016/j.rinp.2019.102650>).

47. Amiri, IS, Rashed, ANZ. Power enhancement of the U-shape cavity microring resonator through gap and material characterizations. *J Opt Commun* 2019. <https://doi.org/10.1515/joc-2019-0108> (<https://doi.org/10.1515/joc-2019-0108>) [Epub ahead of print].
48. Amiri, IS, Kuppusamy, PG, Rashed, ANZ, Jayarajan, P, Thiyagupriyadharsan, MR, Yupapin, P. The engagement of hybrid ultra high space division multiplexing with maximum time division multiplexing techniques for high-speed single-mode fiber cable systems. *J Opt Commun* 2019. <https://doi.org/10.1515/joc-2019-0205> (<https://doi.org/10.1515/joc-2019-0205>) [Epub ahead of print].
49. Amiri, IS, Rashed, ANZ, Jahan, S, Paul, BK, Ahmed, K. Polar polarization mode and average radical flux intensity measurements based on all optical spatial communication systems. *J Opt Commun* 2019. <https://doi.org/10.1515/joc-2019-0159> (<https://doi.org/10.1515/joc-2019-0159>) [Epub ahead of print].
50. Sivaranjani, S, Sampathkumar, A, Rashed, ANZ, Sundararajan, TVP, Amiri, IS. Performance evaluation of bidirectional wavelength division multiple access broadband optical passive elastic networks operation efficiency. *J Opt Commun* 2019. <https://doi.org/10.1515/joc-2019-0175> (<https://doi.org/10.1515/joc-2019-0175>) [Epub ahead of print].
51. Amiri, IS, Rashed, ANZ, Yupapin, P. High-speed transmission circuits signaling in optical communication systems. *J Opt Commun* 2019. <https://doi.org/10.1515/joc-2019-0197> (<https://doi.org/10.1515/joc-2019-0197>) [Epub ahead of print].
52. Amiri, IS, Rashed, ANZ, Jahan, S, Paul, BK, Ahmed, K, Yupapin, P. Technical specifications of the submarine fiber optic channel bandwidth/capacity in optical fiber transmission systems. *J Opt Commun* 2019. <https://doi.org/10.1515/joc-2019-0226> (<https://doi.org/10.1515/joc-2019-0226>) [Epub ahead of print].
53. Amiri, IS, Rashed, ANZ. Signal processing criteria based on electro-optic filters for fiber optic access transceiver systems. *J Opt Commun* 2019. <https://doi.org/10.1515/joc-2019-0116> (<https://doi.org/10.1515/joc-2019-0116>) [Epub ahead of print].
54. Amiri, IS, Rashed, ANZ, Yupapin, P. Pump laser automatic signal control for erbium-doped fiber amplifier gain, noise figure, and output spectral power. *J Opt Commun* 2019. <https://doi.org/10.1515/joc-2019-0203> (<https://doi.org/10.1515/joc-2019-0203>) [Epub ahead of print].
55. Amiri, IS, Rashed, ANZ, Parvez, AHMS, Paul, BK, Ahmed, K. Performance enhancement of fiber optic and optical wireless communication channels by using forward error correction codes. *J Opt Commun* 2019. <https://doi.org/10.1515/joc-2019-0191> (<https://doi.org/10.1515/joc-2019-0191>) [Epub ahead of print].
56. Amiri, IS, Rashed, ANZ, Yupapin, P. Z Shaped like resonator with crystal in the presence of flat mirror based standing wave ratio for optical antenna systems. *Indones J Electr Eng Comput Sci* 2020;17:1405–9. <https://doi.org/10.11591/ijeecs.v17.i3.pp1405-1409> (<https://doi.org/10.11591/ijeecs.v17.i3.pp1405-1409>) .

57. Amiri, IS, Rashed, ANZ, Yupapin, P. Influence of device to device interconnection elements on the system behavior and stability. *Indones J Electr Eng Comput Sci* 2020;18:843–7. <https://doi.org/10.11591/ijeecs.v18.i2.pp843-847> (<https://doi.org/10.11591/ijeecs.v18.i2.pp843-847>).
58. Eid, MMA, Amiri, IS, Rashed, ANZ, Yupapin, P. Dental lasers applications in visible wavelength operational band. *Indones J Electr Eng Comput Sci* 2020;18:890–5. <https://doi.org/10.11591/ijeecs.v18.i2.pp890-895> (<https://doi.org/10.11591/ijeecs.v18.i2.pp890-895>).
59. Amiri, IS, Rashed, ANZ, Yupapin, P. Comparative simulation study of multi stage hybrid all optical fiber amplifiers in optical communications. *J Opt Commun* 2020. <https://doi.org/10.1515/joc-2019-0132> (<https://doi.org/10.1515/joc-2019-0132>) [Epub ahead of print].
60. Amiri, IS, Rashed, ANZ, Kader, HMA, Al-Awamry, AA, El-Aziz, IAA, Yupapin, P, et al.. Optical communication transmission systems improvement based on chromatic and polarization mode dispersion compensation simulation management. *Optik* 2020;207:163853. <https://doi.org/10.1016/j.ijleo.2019.163853> (<https://doi.org/10.1016/j.ijleo.2019.163853>).
61. Samanta, D, Sivaram, M, Rashed, ANZ, Boopathi, CS, Amiri, IS, Yupapin, P. Distributed feedback laser (DFB) for signal power amplitude level improvement in long spectral band. *J Opt Commun* 2020. <https://doi.org/10.1515/joc-2019-0252> (<https://doi.org/10.1515/joc-2019-0252>) [Epub ahead of print].
62. Amiri, IS, Rashed, ANZ, Yupapin, P. Analytical model analysis of reflection/transmission characteristics of long-period fiber Bragg grating (LPFBG) by using coupled mode theory. *J Opt Commun* 2020. <https://doi.org/10.1515/joc-2019-0187> (<https://doi.org/10.1515/joc-2019-0187>) [Epub ahead of print].
63. Amiri, IS, Rashed, ANZ, Rahman, Z, Paul, BK, Ahmed, K. Conventional/phase shift dual drive mach–zehnder modulation measured type based radio over fiber systems. *J Opt Commun* 2020. <https://doi.org/10.1515/joc-2019-0312> (<https://doi.org/10.1515/joc-2019-0312>) [Epub ahead of print].
64. Alatwi, AM, Rashed, ANZ, El-Eraki, AM, Amiri, IS. Best candidate routing algorithms integrated with minimum processing time and low blocking probability for modern parallel computing systems. *Indones J Electr Eng Comput Sci* 2020;19:847–54. <https://doi.org/10.11591/ijeecs.v19.i2.pp847-854> (<https://doi.org/10.11591/ijeecs.v19.i2.pp847-854>).
65. El-Hageen, HM, Alatwi, AM, Rashed, ANZ. Silicon-Germanium dioxide and aluminum indium gallium arsenide-based acoustic optic modulators. *Open Eng J* 2020;10:506–11. <https://doi.org/10.1515/eng-2020-0065> (<https://doi.org/10.1515/eng-2020-0065>).
66. El-Hageen, HM, Alatwi, AM, Rashed, ANZ. RZ line coding scheme with direct laser modulation for upgrading optical transmission systems. *Open Eng J* 2020;10:546–51. <https://doi.org/10.1515/eng-2020-0066> (<https://doi.org/10.1515/eng-2020-0066>).

67. Alatwi, AM, Rashed, ANZ, El-Gammal, EM. Wavelength division multiplexing techniques based on multi transceiver in low earth orbit intersatellite systems. *J Opt Commun* 2020. <https://doi.org/10.1515/joc-2019-0171> (<https://doi.org/10.1515/joc-2019-0171>) [Epub ahead of print].
68. El-Hageen, HM, Kuppusamy, PG, Alatwi, AM, Sivaram, M, Yasar, ZA, Rashed, ANZ. Different modulation schemes for direct and external modulators based on various laser sources. *J Opt Commun* 2020. <https://doi.org/10.1515/joc-2020-0029> (<https://doi.org/10.1515/joc-2020-0029>) [Epub ahead of print].
69. El-Hageen, HM, Alatwi, AM, Rashed, ANZ. High-speed signal processing and wide band optical semiconductor amplifier in the optical communication systems. *J Opt Commun* 2020. <https://doi.org/10.1515/joc-2020-0070> (<https://doi.org/10.1515/joc-2020-0070>) [Epub ahead of print].
70. El-Hageen, HM, Alatwi, AM, Rashed, ANZ. Laser measured rate equations with various transmission coders for optimum of data transmission error rates. *Indones J Electr Eng Comput Sci* 2020;20:1406–12. <https://doi.org/10.11591/ijeecs.v20.i3.pp1406-1412> (<https://doi.org/10.11591/ijeecs.v20.i3.pp1406-1412>) .
71. Eid, MMA, Habib, MA, Anower, MS, Rashed, ANZ. Highly sensitive nonlinear photonic crystal fiber based sensor for chemical sensing applications. *Microsyst Technol* 2020;55:134–45. [10.1007/s00542-020-05019-w](https://doi.org/10.1007/s00542-020-05019-w) (<https://doi.org/10.1007/s00542-020-05019-w>)
72. Eid, MMA, Rashed, ANZ, Shafkat, A, Ahmed, K. Fabry perot laser properties with high pump lasers for upgrading fiber optic transceiver systems. *J Opt Commun* 2020. <https://doi.org/10.1515/joc-2020-0146> (<https://doi.org/10.1515/joc-2020-0146>) [Epub ahead of print].
73. Eid, MMA, Rashed, ANZ, Hosen, MS, Paul, BK, Ahmed, K. Spatial optical transceiver system-based key solution for high data rates in measured index multimode optical fibers for indoor applications. *J Opt Commun* 2020. <https://doi.org/10.1515/joc-2020-0117> (<https://doi.org/10.1515/joc-2020-0117>) [Epub ahead of print].
74. Eid, MMA, Rashed, ANZ, El-Meadawy, S, Ahmed, K. Simulation study of signal gain optimization based on hybrid composition techniques for high speed optically dense multiplexed systems. *J Opt Commun* 2020. <https://doi.org/10.1515/joc-2020-0150> (<https://doi.org/10.1515/joc-2020-0150>) [Epub ahead of print].
75. Alatwi, AM, Rashed, ANZ. Hybrid CPFSK/OQPSK modulation transmission techniques' performance efficiency with RZ line coding-based fiber systems in passive optical networks. *Indones J Electr Eng Comput Sci* 2021;21:263–70. <https://doi.org/10.11591/ijeecs.v21.i1.pp263-270> (<https://doi.org/10.11591/ijeecs.v21.i1.pp263-270>) .
76. Alatwi, AM, Rashed, ANZ. An analytical method with numerical results to be used in the design of optical slab waveguides for optical communication system applications. *Indones J Electr Eng Comput Sci* 2021;21:278–86, <https://doi.org/10.11591/ijeecs.v21.i1.pp278-286> (<https://doi.org/10.11591/ijeecs.v21.i1.pp278-286>) .

77. Alatwi, AM, Rashed, ANZ. Conventional doped silica/fluoride glass fibers for low loss and minimum dispersion effects. *Indones J Electr Eng Comput Sci* 2021;21:287–95. <https://doi.org/10.11591/ijeecs.v21.i1.pp287-295> (<https://doi.org/10.11591/ijeecs.v21.i1.pp287-295>).
78. El-Hageen, HM, Alatwi, AM, Rashed, ANZ. Spatial optical transmitter based on on/off keying line coding modulation scheme for optimum performance of telecommunication systems. *Indones J Electr Eng Comput Sci* 2021;21:305–12. <https://doi.org/10.11591/ijeecs.v21.i1.pp305-312> (<https://doi.org/10.11591/ijeecs.v21.i1.pp305-312>).
79. Eid, MMA, Rashed, AANZ, Kurmendra. High speed optical switching gain based EDFA model with 30 Gb/s NRZ modulation code in optical systems. *J Opt Commun* 2020. <https://doi.org/10.1515/joc-2020-0223> (<https://doi.org/10.1515/joc-2020-0223>) [Epub ahead of print].
80. Eid, MMA, Rashed, ANZ, Amiri, IS. Fast speed switching response and high modulation signal processing bandwidth through LiNbO₃ electro-optic modulators. *J Opt Commun* 2020. <https://doi.org/10.1515/joc-2020-0012> (<https://doi.org/10.1515/joc-2020-0012>) [Epub ahead of print].
81. Eid, MMA, Houssien, FMAM, Rashed, ANZ, Mohammed, AENA. Performance enhancement of transceiver system based inter satellite optical wireless channel (IS-OWC) for ultra long distances. *J Opt Commun* 2020;1–19. <https://doi.org/10.1515/joc-2020-0216> (<https://doi.org/10.1515/joc-2020-0216>).
82. Eid, MMA, Rashed, ANZ, El-din, ES. Simulation performance signature evolution of optical inter satellite links based booster EDFA and receiver preamplifiers. *J Opt Commun* 2020. <https://doi.org/10.1515/joc-2020-0190> (<https://doi.org/10.1515/joc-2020-0190>) [Epub ahead of print].
83. Eid, MMA, Rashed, ANZ, El-gammal, EM. Influence of dense wavelength division multiplexing (DWDM) technique on the low earth orbit intersatellite systems performance. *J Opt Commun* 2020. <https://doi.org/10.1515/joc-2020-0188> (<https://doi.org/10.1515/joc-2020-0188>) [Epub ahead of print].
84. Eid, MMA, Rashed, ANZ, Bulbul, AAM, Podder, E. Mono rectangular core photonic crystal fiber (MRC-PCF) for skin and blood cancer detection. *Plasmonics* 2020. <https://doi.org/10.1007/s11468-020-01334-0> (<https://doi.org/10.1007/s11468-020-01334-0>) [Epub ahead of print].
85. Eid, MMA, Seliem, AS, Rashed, ANZ, Mohammed, AENA, Ali, MY, Abaza, SS. High speed pulse generators with electro-optic modulators based on different bit sequence for the digital fiber optic communication links. *Indones J Electr Eng Comput Sci* 2021;21:957–67. <https://doi.org/10.11591/ijeecs.v21.i2.pp957-967> (<https://doi.org/10.11591/ijeecs.v21.i2.pp957-967>).
86. Eid, MMA, Seliem, AS, Rashed, ANZ, Mohammed, AENA, Ali, MY, Abaza, SS. The key management of direct/external modulation semiconductor laser response systems for relative intensity noise control. *Indones J Electr Eng Comput Sci* 2021;21:968–77. <https://doi.org/10.11591/ijeecs.v21.i2.pp968-977> (<https://doi.org/10.11591/ijeecs.v21.i2.pp968-977>).

87. Eid, MMA, Seliem, AS, Rashed, ANZ, Mohammed, AENA, Ali, MY, Abaza, SS. Duobinary modulation/predistortion techniques effects on high bit rate radio over fiber systems. *Indones J Electr Eng Comput Sci* 2021;21:978–86. <https://doi.org/10.11591/ijeecs.v21.i2.pp978-986> (<https://doi.org/10.11591/ijeecs.v21.i2.pp978-986>).
88. Alatwi, AM, Rashed, ANZ. A pulse amplitude modulation scheme based on in-line semiconductor optical amplifiers (SOAs) for optical soliton systems. *Indones J Electr Eng Comput Sci* 2021;21:1014–21. <https://doi.org/10.11591/ijeecs.v21.i2.pp1014-1021> (<https://doi.org/10.11591/ijeecs.v21.i2.pp1014-1021>).
89. Eid, MMA, Rashed, ANZ, El-Meadawy, S, Habib, MA. Best selected optical fibers with wavelength multiplexing techniques for minimum bit error rates. *J Opt Commun* 2020. <https://doi.org/10.1515/joc-2020-0239> (<https://doi.org/10.1515/joc-2020-0239>) [Epub ahead of print].
90. Alatwi, AM, Rashed, ANZ, El-Aziz, IAA. High speed modulated wavelength division optical fiber transmission systems performance signature. *Telkomnika* 2021;19:380–9. <https://doi.org/10.12928/TELKOMNIKA.v19i2.16871> (<https://doi.org/10.12928/TELKOMNIKA.v19i2.16871>).
91. Eid, MMA, Rashed, ANZ, El-gammal, EM, Delwar, TS, Ryu, JY. The influence of electrical filters with sequence generators on optical ISL performance evolution with suitable data rates. *J Opt Commun* 2020. <https://doi.org/10.1515/joc-2020-0257> (<https://doi.org/10.1515/joc-2020-0257>) [Epub ahead of print].
92. Alatwi, AM, Rashed, ANZ, Parvez, AHMS, Paul, BK, Ahmed, K. Beam divergence and operating wavelength bands effects on free space optics communication channels in local access networks. *J Opt Commun* 2020. <https://doi.org/10.1515/joc-2019-0276> (<https://doi.org/10.1515/joc-2019-0276>) [Epub ahead of print].
93. Shafkat, A, Rashed, ANZ, El-Hageen, HM, Alatwi, AM. The effects of adding different adhesive layers with a microstructure fiber sensor based on surface plasmon resonance: a numerical study. *Plasmonics* 2021;55:167–78. [10.1007/s11468-020-01352-y](https://doi.org/10.1007/s11468-020-01352-y) (<https://doi.org/10.1007/s11468-020-01352-y>).
94. Eid, MMA, Rashed, ANZ. Fiber optic propagation problems and signal bandwidth measurements under high temperature and high dopant germanium ratios. *J Opt Commun* 2020. <https://doi.org/10.1515/joc-2020-0278> (<https://doi.org/10.1515/joc-2020-0278>) [Epub ahead of print].
95. Eid, MMA, Rashed, ANZ. Simulative and analytical methods of bidirectional EDFA amplifiers in optical communication links in the optimum case. *J Opt Commun* 2020. <https://doi.org/10.1515/joc-2020-0193> (<https://doi.org/10.1515/joc-2020-0193>) [Epub ahead of print].
96. Eid, MMA, Shehata, E, Rashed, ANZ. Cascaded stages of parametric optical fiber amplifiers with Raman fiber amplifiers for upgrading of telecommunication networks through optical wireless communication channel. *J Opt Commun* 2020.

- <https://doi.org/10.1515/joc-2020-0279> (<https://doi.org/10.1515/joc-2020-0279>) [Epub ahead of print].
97. Eid, MMA, Mohammed, AENA, Rashed, ANZ. Simulative study on the cascaded stages of traveling wave semiconductor optical amplifiers based multiplexing schemes for fiber optic systems improvement. *J Opt Commun* 2020. <https://doi.org/10.1515/joc-2020-0281> (<https://doi.org/10.1515/joc-2020-0281>) [Epub ahead of print].
98. Parvin, T, Ahmed, K, Alatwi, AM, Rashed, ANZ. Differential optical absorption spectroscopy based refractive index sensor for cancer cell detection. *Opt Rev* 2021;67:564–73. [10.1007/s10043-021-00644-w](https://doi.org/10.1007/s10043-021-00644-w) (<https://doi.org/10.1007/s10043-021-00644-w>)
99. Eid, MMA, Said, SM, Rashed, ANZ. Gain/noise figure spectra of average power model Raman optical amplifiers in coarse wavelength multiplexed systems. *J Opt Commun* 2020. <https://doi.org/10.1515/joc-2020-0289> (<https://doi.org/10.1515/joc-2020-0289>) [Epub ahead of print].
100. Eid, MMA, Rashed, ANZ, Ahammad, MS, Paul, BK, Ahmed, K. The effects of Tx./Rx. pointing errors on the performance efficiency of local area optical wireless communication networks. *J Opt Commun* 2020. <https://doi.org/10.1515/joc-2019-0256> (<https://doi.org/10.1515/joc-2019-0256>) [Epub ahead of print].
101. Eid, MMA, El-Hamid, HSA, Rashed, ANZ. High-speed fiber system capacity with bidirectional Er-Yb CDFs based on differential phase shift keying (DPSK) modulation technique. *J Opt Commun* 2020. <https://doi.org/10.1515/joc-2021-0001> (<https://doi.org/10.1515/joc-2021-0001>) [Epub ahead of print].
102. Eid, MMA, Ibrahim, A, Rashed, ANZ. In line and post erbium-doped fiber amplifiers with ideal dispersion compensation fiber Bragg grating for upgrading optical access networks. *J Opt Commun* 2020. <https://doi.org/10.1515/joc-2020-0306> (<https://doi.org/10.1515/joc-2020-0306>) [Epub ahead of print].
103. Tahhan, SR, Taha, RM. Mercedes benz logo based plasmon resonance PCF sensor. *Sens Bio-Sens Res* 2022;35:100468. <https://doi.org/10.1016/j.sbsr.2021.100468> (<https://doi.org/10.1016/j.sbsr.2021.100468>) .
104. Tahhan, SR, Atieh, A, Hasan, M, Hall, T. Characterization and experimental verification of actively mode-locked erbium doped fiber laser utilizing ring cavity. *TM – Tech Mess* 2020;87:535–41. <https://doi.org/10.1515/teme-2020-0003> (<https://doi.org/10.1515/teme-2020-0003>) .
105. Tahhan, SR, Abass, AK, Ali, MH. Characteristics of chirped fiber Bragg grating dispersion compensator utilizing two apodization profiles. *J Commun* 2018;13:108–13. <https://doi.org/10.12720/jcm.13.3.108-113> (<https://doi.org/10.12720/jcm.13.3.108-113>) .
106. Tahhan, SR, Atieh, A, Ali, MH, Hasan, M, Abass, AK, Hall, T. Characteristics of actively mode-locked erbium doped fiber laser utilizing ring cavity. In: *2019 IEEE jordan international joint conference on electrical engineering and information technology*

(JEEIT). Amman, Jordan; 2019:840–4 pp.

[10.1109/JEEIT.2019.8717483](https://doi.org/10.1109/JEEIT.2019.8717483) (<https://doi.org/10.1109/JEEIT.2019.8717483>)

107. Fadil, EA, Abass, AK, Tahhan, SR. Secure WDM-free space optical communication system based optical chaotic. *Opt Quant Electron* 2022;54:477.

<https://doi.org/10.1007/s11082-022-03870-x> (<https://doi.org/10.1007/s11082-022-03870-x>).

108. Tahhan, SR, Mohammed, MF, Moosa, AA, Atieh, A. WDM ROF OFDM/QAM system for wireless PON. In: *2021 IEEE jordan international joint conference on electrical engineering and information technology (JEEIT)*. Amman, Jordan; 2021:164–9 pp.

[10.1109/JEEIT53412.2021.9634158](https://doi.org/10.1109/JEEIT53412.2021.9634158) (<https://doi.org/10.1109/JEEIT53412.2021.9634158>)

109. Tahhan, SR, Ghazai, AJ, Alwan, IM, Ali, MH. Investigation of the characteristics of high-resistivity silica based hybrid porous core photonic crystal fiber for terahertz wave guidance. *Digest J Nanomater Biostruct* 2019;14:831–41.

110. Singh, M, Malhotra, J. Performance comparison of different modulation schemes in high-speed MDM based radio over FSO transmission link under the effect of atmospheric turbulence using aperture averaging. *Wireless Pers Commun* 2020;111:825–42.

<https://doi.org/10.1007/s11277-019-06886-x> (<https://doi.org/10.1007/s11277-019-06886-x>).

111. Singh, M, Malhotra, J. Modeling and performance analysis of 400 gbps CO-OFDM based inter-satellite optical wireless communication (IsOWC) system incorporating polarization division multiplexing with enhanced detection. *Wireless Pers Commun* 2020;111:495–511.

<https://doi.org/10.1007/s11277-019-06870-5> (<https://doi.org/10.1007/s11277-019-06870-5>).

112. Singh, M, Malhotra, J. Performance comparison of 2×20 gbps-40 GHz OFDM based RoFSO transmission link incorporating MDM of hermite Gaussian modes using different modulation schemes. *Wireless Pers Commun* 2020;110:699–711.

<https://doi.org/10.1007/s11277-019-06750-y> (<https://doi.org/10.1007/s11277-019-06750-y>).

113. Singh, M, Malhotra, J. Performance investigation of high-speed FSO transmission system under the influence of different atmospheric conditions incorporating 3-D orthogonal modulation scheme. *Opt Quant Electron* 2019;51:285,

<https://doi.org/10.1007/s11082-019-1998-2> (<https://doi.org/10.1007/s11082-019-1998-2>).

114. Singh, M, Malhotra, J. 4×20 Gbit/s-40 GHz OFDM based radio over FSO transmission link incorporating hybrid wavelength division multiplexing-mode division multiplexing of LG and HG modes with enhanced detection. *Optoelectron Adv Mater Rapid Commun* 2020;14:233–43.

115. Singh, M, Malhotra, J. 40 Gbit/s-80 GHz hybrid MDM-OFDM-Multibeam based RoFSO transmission link under the effect of adverse weather conditions with enhanced detection. *Optoelectron Adv Mater Rapid Commun* 2019;14:146–53.

116. Al-Khaffaf, DAJ, Hujijo, HSR. High data rate optical wireless communication system using millimeter wave and optical phase modulation. *ARPN J Eng Appl Sci* 2018;13:9086–92.

117. Al-Khaffaf, DAJ, Alshimaysawe, IA. Miniaturised tri-band microstrip patch antenna design for radio and millimetre waves of 5G devices. *Indones J Electr Eng Comput Sci* 2021;21:1594–601. <https://doi.org/10.11591/ijeecs.v21.i3.pp1594-1601> (https://doi.org/10.11591/ijeecs.v21.i3.pp1594-1601) .
118. Al-Khaffaf, DAJ, Alsahlany, AM. A cloud VLC access point design for 5G and beyond. *Opt Quant Electron* 2021;53:472–81. <https://doi.org/10.1007/s11082-021-03132-2> (https://doi.org/10.1007/s11082-021-03132-2) .
119. Rashed, ANZ. High reliability optical interconnections for short range applications in high speed optical communication systems. *Opt Laser Technol* 2013;48:302–8. <https://doi.org/10.1016/j.optlastec.2012.10.038> (https://doi.org/10.1016/j.optlastec.2012.10.038) .
120. Rashed, ANZ. High performance photonic devices for multiplexing/demultiplexing applications in multi band operating regions. *J Comput Theor Nanosci* 2012;9:522–31. <https://doi.org/10.1166/jctn.2012.2055> (https://doi.org/10.1166/jctn.2012.2055) .
121. Rashed, ANZ, Sharshar, HA. Analysis of transmission line feed method for transparent conductor oxide materials based optical microstrip patch antennas design. *Optoelectron Adv Mater Rapid Commun* 2012;6:980–7.
122. Rashed, ANZ, Metwae'e, MA. Operation performance characteristics of vertical cavity surface emitting lasers (VCSELs) under high thermal neutrons irradiated fields. *J Russ Laser Res* 2013;34:1–8. <https://doi.org/10.1007/s10946-013-9317-z> (https://doi.org/10.1007/s10946-013-9317-z) .
123. Rashed, ANZ. Optical fiber communication cables systems performance under harmful gamma irradiation and thermal environment effects. *IET Commun* 2013;7:448–55. <https://doi.org/10.1049/iet-com.2012.0313> (https://doi.org/10.1049/iet-com.2012.0313) .
124. Rashed, ANZ, MohamedEl-halawany, ME. Transmission characteristics evaluation under bad weather conditions in optical wireless links with different optical transmission windows. *Wireless Pers Commun* 2013;71:1577–95. <https://doi.org/10.1007/s11277-012-0893-y> (https://doi.org/10.1007/s11277-012-0893-y) .
125. Smirani, LK, Ahammad, SKH, Daher, MG, Hossain, MA, Rashed, ANZ, Abdelhamid, HS. Optical transceiver communication systems performance evaluation based on nonlinear cross gain modulation effects. *J Opt Commun* 2022. <https://doi.org/10.1515/joc-2022-0134> (https://doi.org/10.1515/joc-2022-0134) [Epub ahead of print].
126. Smirani, LK, El-Aziz, IAA, Ahammad, SKH, Hossain, MA, Daher, MG, Rashed, ANZ. Low loss flexibility and high efficiency of radio per fiber system for modern wireless communication system. *J Opt Commun* 2022. <https://doi.org/10.1515/joc-2022-0145> (https://doi.org/10.1515/joc-2022-0145) [Epub ahead of print].
127. Rashed, ANZ, Sharshar, H. Performance evaluation of short range underwater optical wireless communications for different ocean water types. *Wireless Pers Commun* 2013;72:693–708. [10.1007/s11277-013-1037-8](https://doi.org/10.1007/s11277-013-1037-8) (https://doi.org/10.1007/s11277-013-1037-8)

128. Daher, MG, Jaroszewicz, Z, Zyoud, SH, Panda, A, Ahammad, SKH, Abd-Elnaby, M, et al.. Design of a novel detector based on photonic crystal nanostructure for ultra high performance detection of cells with diabetes. *Opt Quant Electron* 2022;54:701. <https://doi.org/10.1007/s11082-022-04093-w> (<https://doi.org/10.1007/s11082-022-04093-w>).

129. Smirani, LK, Rashed, ANZ, Ahammad, SKH, Hossain, MA, Daher, MG, Fahmy, E. Conventional/linear/Lorentzian material gain semiconductor optical amplifiers performance signature with four wave mixing (FWM) nonlinearity in optical fiber communication systems. *J Opt Commun* 2022. <https://doi.org/10.1515/joc-2022-0147> (<https://doi.org/10.1515/joc-2022-0147>) [Epub ahead of print].

130. Lassaad, KS, Kumari, M, Ahammad, SKH, Hossain, MA, Daher, MG, Rashed, ANZ, et al.. Signal quality enhancement in multiplexed communication systems based on the simulation model of the optimum technical specifications of Raman fiber optical amplifiers. *J Opt Commun* 2022. <https://doi.org/10.1515/joc-2022-0129> (<https://doi.org/10.1515/joc-2022-0129>) [Epub ahead of print].

Received: 2022-08-22

Accepted: 2022-11-08

Published Online: 2022-12-07

© 2022 Walter de Gruyter GmbH, Berlin/Boston

— or —

PDF 30,00 €

From the journal



Journal of Optical Communications

Downloaded on 8.12.2023 from

<https://www.degruyter.com/document/doi/10.1515/joc-2022-0211/html?lang=en>



Requires Authentication | Published online by [De Gruyter](#) | November 28, 2022

Design and analysis of high-speed data optical fiber communication system through EDFA amplifier system

Ahmed Nabih Zaki Rashed  , Baraa Riyadh Altahan, Thaticharla Manasavenna, S. K. Hasane Ahammad, P. Poorna Priya, M. Rama Krishna, Md. Amzad Hossain , Lassaad K. Smirani and Ashraf Ali Nabil

From the journal [Journal of Optical Communications](#)

<https://doi.org/10.1515/joc-2022-0164>

Abstract

This study presented design and analysis of high-speed data optical fiber communication system through EDFA amplifier system. The design with practical data for parameters to maximize the transmission bit-rate is clarified. The bit rate distance product can be optimized for the improvement of performance of high-speed long haul repeater spacing with amplification technique. The basic amplification system for optical fiber communication system is clarified. Transmitter/receiver components with the circuit connections and the operation are also indicated in details. The practical circuit model of the transmitter and receiver are designed clearly in this work. The design of distribution maps to measure the Q factor and minimum bit error rate and many different simulation models for applied to achieve high-speed data optical fiber communication system.

Keywords: [channel](#); [EDFA amplifier](#); [fiber system](#); [Rx. system](#); [Tx. system](#)

Corresponding authors: **Ahmed Nabih Zaki Rashed**, Electronics and Electrical Communications Engineering Department, Faculty of Electronic Engineering, Menoufia University, Menouf 32951, Egypt, E-mail: ahmed_733@yahoo.com; and **Md. Amzad Hossain**, Faculty of Electrical Engineering and Information Technology, Institute of Theoretical Electrical Engineering, Ruhr University Bochum, 44801 Bochum, Germany; and Department of Electrical and Electronic

Engineering, Jashore University of Science and Technology, Jashore 7408,
Bangladesh, E-mail: mahossain.eee@gmail.com

Funding source: Al-Mustaqbal University College in Iraq

Award Identifier / Grant number: 22UQU4340560DSR08

Acknowledgment

The authors extend their appreciation and gratitude to Al-Mustaqbal University College in Iraq for funding this project.

Author contribution: All the authors have accepted responsibility for the entire content of this submitted manuscript and approved submission.

Research funding: This work was funded by the Deanship of Scientific Research at Umm Al-Qura University for supporting this work by Grant Code: (22UQU4340560DSR08).

Conflict of interest statement: The authors declare no conflicts of interest regarding this article.

References

1. Habib, A, Rashed, ANZ, El-Hageen, HM, Alatwi, AM. Extremely sensitive photonic crystal fiber-based cancer cell detector in the terahertz regime. *Plasmonics* 2020;21–35. <https://doi.org/10.1007/s11468-021-01409-6> (<https://doi.org/10.1007/s11468-021-01409-6>).
2. Shafkat, A, Rashed, ANZ, El-Hageen, HM, Alatwi, AM. Design and analysis of a single elliptical channel photonic crystal fiber sensor for potential malaria detection. *J Sol Gel Sci Technol* 2020;97–106. <https://doi.org/10.1007/s10971-021-05490-5> (<https://doi.org/10.1007/s10971-021-05490-5>).
3. Eid, MMA, Rashed, ANZ. Fixed scattering section length with variable scattering section dispersion based optical fibers for polarization mode dispersion penalties. *Indones J Electr Eng Comput Sci* 2021;21:1540–7. <https://doi.org/10.11591/ijeecs.v21.i3.pp1540-1547> (<https://doi.org/10.11591/ijeecs.v21.i3.pp1540-1547>).
4. Eid, MMA, Seliem, AS, Rashed, ANZ, Mohammed, AE-NA, Ali, MY, Abaza, SS. High sensitivity sapphire FBG temperature sensors for the signal processing of data communications technology. *Indones J Electr Eng Comput Sci* 2021;21:1567–74. <https://doi.org/10.11591/ijeecs.v21.i3.pp1567-1574> (<https://doi.org/10.11591/ijeecs.v21.i3.pp1567-1574>).
5. Eid, MMA, Seliem, AS, Rashed, ANZ, Mohammed, AE-NA, Ali, MY, Abaza, SS. High modulated soliton power propagation interaction with optical fiber and optical wireless communication channels. *Indones J Electr Eng Comput Sci* 2021;21:1575–83.

<https://doi.org/10.11591/ijeecs.v21.i3.pp1575-1583> (<https://doi.org/10.11591/ijeecs.v21.i3.pp1575-1583>) .

6. MahmoudEid, MA, Rashed, ANZ, Delwar, TS, Siddique, A, Ryu, JY. Linear/cubic measured pulse numerically with electrical jitter amplitude variations for the impact on fiber communication systems. *J Opt Commun* 2021;1–14. <https://doi.org/10.1515/joc-2020-0301> (<https://doi.org/10.1515/joc-2020-0301>) .
 7. Eid, MMA, El-Meadawy, S, Mohammed, AE-NA, Rashed, ANZ. Wavelength division multiplexing developed with optimum length-based EDFA in the presence of dispersion-compensated fiber system. *J Opt Commun* 2021;1–20. <https://doi.org/10.1515/joc-2020-0302> (<https://doi.org/10.1515/joc-2020-0302>) .
 8. Eid, MMA, Sorathiya, V, Lavadiya, S, Habib, MA, Helmy, A, Rashed, ANZ. Dispersion compensation FBG with optical quadrature phase shift keying (OQPSK) modulation scheme for high system capacity. *J Opt Commun* 2021;1–22. <https://doi.org/10.1515/joc-2021-0022> (<https://doi.org/10.1515/joc-2021-0022>) .
 9. Eid, MMA, Sorathiya, V, Lavadiya, S, Shehata, E, Rashed, ANZ. Free space and wired optics communication systems performance improvement for short-range applications with the signal power optimization. *J Opt Commun* 2021;1–18. <https://doi.org/10.1515/joc-2020-0304> (<https://doi.org/10.1515/joc-2020-0304>) .
 10. Eid, MMA, Rashed, ANZ. Numerical simulation of long-period grating sensors (LPGS) transmission spectrum behavior under strain and temperature effects. *Sens Rev* 2021;1–19. <https://doi.org/10.1108/SR-10-2020-0248> (<https://doi.org/10.1108/SR-10-2020-0248>) .
 11. Eid, MMA, Rashed, ANZ. Basic FBG apodization functions effects on the filtered optical acoustic signal. *Indones J Electr Eng Comput Sci* 2021;22:287–96. <https://doi.org/10.11591/ijeecs.v22.i1.pp287-296> (<https://doi.org/10.11591/ijeecs.v22.i1.pp287-296>) .
 12. Eid, MMA, El-Meadawy, S, Mohammed, AE-NA, Rashed, ANZ. High data rates in optic fiber systems based on the gain optimization techniques. *J Opt Commun* 2021;1–18. <https://doi.org/10.1515/joc-2021-0017> (<https://doi.org/10.1515/joc-2021-0017>) .
 13. Ahmed, K, AlZain, MA, Abdullah, H, Luo, Y, Vigneswaran, D, Faragallah, OS, et al.. Highly sensitive twin resonance coupling refractive index sensor based on gold- and MgF₂-coated nano metal films. *Biosensors* 2021;11:110–24. <https://doi.org/10.3390/bios11040104> (<https://doi.org/10.3390/bios11040104>) .
- [PubMed](https://pubmed.ncbi.nlm.nih.gov/33918524/) (<https://pubmed.ncbi.nlm.nih.gov/33918524/>)
[PubMed Central](https://www.ncbi.nlm.nih.gov/pmc/articles/PMC8066326/) (<https://www.ncbi.nlm.nih.gov/pmc/articles/PMC8066326/>)
14. Delwar, TS, Siddique, A, Biswal, MR, Rashed, ANZ, Jee, AJ, Ryu, Y. Novel multi-user MC-CSK modulation technique in visible light communication. *Opt Quant Electron* 2021;1–17. <https://doi.org/10.1007/s11082-021-02784-4> (<https://doi.org/10.1007/s11082-021-02784-4>) .
 15. Eid, MMA, Habib, MA, Anower, MS, Rashed, ANZ. Hollow core photonic crystal fiber (PCF)-Based optical sensor for blood component detection in terahertz spectrum. *Braz J Phys* 2021;1–13. <https://doi.org/10.1007/s13538-021-00906-7> (<https://doi.org/10.1007/s13538-021-00906-7>) .

00906-7).

16. Eid, MMA, Sorathiya, V, Lavadiya, S, Abd El-Hamid, HS, Rashed, ANZ. Wide band fiber systems and long transmission applications based on optimum optical fiber amplifiers lengths. *J Opt Commun* 2021;1–17. <https://doi.org/10.1515/joc-2021-0020> (<https://doi.org/10.1515/joc-2021-0020>).
17. Eid, MMA, Sorathiya, V, Lavadiya, S, Shehata, E, Rashed, ANZ. Optical switches based semiconductor optical amplifiers (SOAs) for performance characteristics enhancement by using various electrical pulse generators. *J Opt Commun* 2021;1–0. <https://doi.org/10.1515/joc-2021-0066> (<https://doi.org/10.1515/joc-2021-0066>).
18. Eid, MMA, Rashed, ANZ, Sorathiya, V, Lavadiya, S, Habib, MA, Amiri, IS. GaAs electro-optic absorption modulators performance evaluation, under high-temperature variations. *J Opt Commun* 2021;1–19. <https://doi.org/10.1515/joc-2020-0011> (<https://doi.org/10.1515/joc-2020-0011>).
19. Abdullaha, H, Ahmed, K, Alama, MS, Rashed, ANZ, Mitua, SA, Al-Zahranid, FA, et al.. High sensitivity refractive index sensor based on triple layer MgF₂-gold-MgF₂ coated nano metal films photonic crystal fiber. *Optik* 2021;241:166950. <https://doi.org/10.1016/j.ijleo.2021.166950> (<https://doi.org/10.1016/j.ijleo.2021.166950>).
20. Eid, MMA, Sorathiya, V, Lavadiya, S, Abd El-Aziz, IA, Rashed, ANZ. Free space optics communication channel with amplitude/frequency shift keying modulation technique based raised cosine line coding. *J Opt Commun* 2021;1–12. <https://doi.org/10.1515/joc-2021-0037> (<https://doi.org/10.1515/joc-2021-0037>).
21. Eid, MMA, Rashed, ANZ, Rajagopal, M, Parimanam, J, Abhay, V. Integrated role between VCSEL diodes and Gaussian pulse generators with ideal EDFA for self phase modulation instability management. *J Opt Commun* 2021;1–10. <https://doi.org/10.1515/joc-2020-0251> (<https://doi.org/10.1515/joc-2020-0251>).
22. Eid, MMA, Sorathiya, V, Lavadiya, S, Helmy, A, Rashed, ANZ. Technical specifications and spectral performance characteristics of dispersion flattened fiber (DFF) in optical fiber systems. *J Opt Commun* 2021;1–14. <https://doi.org/10.1515/joc-2021-0063> (<https://doi.org/10.1515/joc-2021-0063>).
23. Eid, MMA, Rashed, ANZ. Hybrid NRZ/RZ line coding scheme based hybrid FSO/FO dual channel communication systems. *Indones J Electr Eng Comput Sci* 2021;22:866–73. <https://doi.org/10.11591/ijeecs.v22.i2.pp866-873> (<https://doi.org/10.11591/ijeecs.v22.i2.pp866-873>).
24. Al-Mamun Bulbul, A, Rashed, ANZ, El-Hageen, HM, Alatwi, AM. Design and numerical analysis of an extremely sensitive PCF-based sensor for detecting kerosene adulteration in petrol and diesel. *Alex Eng J* 2021;60:5419–30. <https://doi.org/10.1016/j.aej.2021.04.041> (<https://doi.org/10.1016/j.aej.2021.04.041>).
25. Eid, MMA, Sorathiya, V, Lavadiya, S, Abd El-Aziz, IA, Asaduzzaman, S, Rehana, H, et al.. ROF systems performance efficiency based on continuous phase frequency shift keying phase modulation scheme. *J Opt Commun* 2021;1–17. <https://doi.org/10.1515/joc-2021-0061> (<https://doi.org/10.1515/joc-2021-0061>).

26. Ahasan Habib, M, Shamim Anower, M, AlGhamdi, A, Faragallah, OS, Eid, MMA, Rashed, ANZ. Efficient way for detection of alcohols using hollow core photonic crystal fiber sensor. *Opt Rev* 2021;1–19. <https://doi.org/10.1007/s10043-021-00672-6>
(<https://doi.org/10.1007/s10043-021-00672-6>).
27. Eid, MMA, Sorathiya, V, Lavadiya, S, Parmar, J, Patel, SK, Ahmed Ali, S, et al.. CWDM communication system based inline erbium-doped fiber amplifiers with the linear geometrical polarization model. *J Opt Commun* 2021;1–14. <https://doi.org/10.1515/joc-2021-0033> (<https://doi.org/10.1515/joc-2021-0033>).
28. Sorathiya, V, Lavadiya, S, AlGhamdi, A, Faragallah, OS, El-sayed, HS, Eid, MMA, et al.. A comparative study of broadband solar absorbers with different gold metasurfaces and MgF2 on tungsten substrates. *J Comput Electron* 2021;1–16.
<https://doi.org/10.1007/s10825-021-01746-z> (<https://doi.org/10.1007/s10825-021-01746-z>).
29. Lavadiya, SP, Sorathiya, V, Kanzariya, S, Chavda, B, Faragallah, OS, Eid, MMA, et al.. Design and verification of novel low profile miniaturized pattern and frequency tunable microstrip patch antenna using two PIN diodes. *Braz J Phys* 2021;1–18.
<https://doi.org/10.1007/s13538-021-00951-2> (<https://doi.org/10.1007/s13538-021-00951-2>).
30. Eid, MMA, Urooj, S, Alwadai, NM, Rashed, ANZ. AlGaInP optical source integrated with fiber links and silicon avalanche photo detectors in fiber optic systems. *Indones J Electr Eng Comput Sci* 2021;23:847–54. <https://doi.org/10.11591/ijeecs.v23.i2.pp847-854>
(<https://doi.org/10.11591/ijeecs.v23.i2.pp847-854>).
31. Urooj, S, Alwadai, NM, Ibrahim, A, Rashed, ANZ. Simulative study of raised cosine impulse function with Hamming grating profile based Chirp Bragg grating fiber. *J Opt Commun* 2021;1–17. <https://doi.org/10.1515/joc-2021-0062> (<https://doi.org/10.1515/joc-2021-0062>).
32. Jibon, RH, Al-Mamun Bulbul, A, Nahid, A-A, Faragallah, OS, Baz, M, Eid, MMA, et al.. Design and numerical analysis of a photonic crystal fiber (PCF)-based flattened dispersion THz waveguide. *Opt Rev* 2021;1–20. <https://doi.org/10.1007/s10043-021-00698-w>
(<https://doi.org/10.1007/s10043-021-00698-w>).
33. Eid, MMA, Mohammed, AE-NA, Rashed, ANZ. Different soliton pulse order effects on the fiber communication systems performance evaluation. *Indones J Electr Eng Comput Sci* 2021;23:1485–92. <https://doi.org/10.11591/ijeecs.v23.i3.pp1485-1492>
(<https://doi.org/10.11591/ijeecs.v23.i3.pp1485-1492>).
34. Urooj, S, Alwadai, NM, Sorathiya, V, Lavadiya, S, Parmar, J, Patel, SK, et al.. Differential coding scheme based FSO channel for optical coherent DP-16 QAM transceiver systems. *J Opt Commun* 2021;1–19. <https://doi.org/10.1515/joc-2021-0118>
(<https://doi.org/10.1515/joc-2021-0118>).
35. Rashed, ANZ, Zaky, WF, Eid, MMA, Faragallah, OS. Dynamic response based on non-linear material for electrical and optical analogy of full optical oscillator. *Opt Quant Electron* 2021;53:658. <https://doi.org/10.1007/s11082-021-03301-3>
(<https://doi.org/10.1007/s11082-021-03301-3>).

36. Rashed, ANZ, Zaky, WF, HazemEl-Hageen, M, Alatwi, AM. Technical specifications for an all-optical switch for information storage and processing systems. *Eur Phys J Plus* 2021;136:1100. <https://doi.org/10.1140/epjp/s13360-021-01841-x>
(<https://doi.org/10.1140/epjp/s13360-021-01841-x>).
37. Sorathiya, V, Lavadiya, S, Parmar, B, Das, S, Krishna, M, Faragallah, OS, et al.. Numerical investigation of the tunable polarizer using gold array and graphene metamaterial structure for an infrared frequency range. *Appl Phys B* 2022;128:13. <https://doi.org/10.1007/s00340-021-07731-5> (<https://doi.org/10.1007/s00340-021-07731-5>).
38. Delwar, TS, Siddique, A, Biswal, MR, Behera, P, Rashed, ANZ, Choi, Y, et al.. A novel dual mode configurable and tunable high-gain, high-efficient CMOS power amplifier for 5G applications. *Integrat VLSI J* 2022;83:77–87. <https://doi.org/10.1016/j.vlsi.2021.12.004>
(<https://doi.org/10.1016/j.vlsi.2021.12.004>).
39. Eid, MMA, Arunachalam, R, Sorathiya, V, Lavadiya, S, Patel, SK, Parmar, J, et al.. QAM receiver based on light amplifiers measured with effective role of optical coherent duobinary transmitter. *J Opt Commun* 2022;1–15. <https://doi.org/10.1515/joc-2021-0205>
(<https://doi.org/10.1515/joc-2021-0205>).
40. Sorathiya, V, Lavadiya, S, Ahmed, AG, Faragallah, OS, El-Sayed, HS, Parmar, B, et al.. Hilbert resonator based multiband tunable graphene metasurface polarizer for lower THz frequency. *J Comput Electron* 2022;1–10. <https://doi.org/10.1007/s10825-021-01848-8>
(<https://doi.org/10.1007/s10825-021-01848-8>).
41. Mohammad, A, Alzaidi, MS, MahmoudEid, MA, Sorathiya, V, Lavadiya, S, Patel, SK, et al.. First order surface grating fiber coupler under the period chirp and apodization functions variations effects. *Indones J Electr Eng Comput Sci* 2022;25:1020–9. <https://doi.org/10.11591/ijeecs.v25.i2.pp1020-1029> (<https://doi.org/10.11591/ijeecs.v25.i2.pp1020-1029>).
42. Mohammad, A, Alzaidi, MS, Eid, MMA, Sorathiya, V, Lavadiya, S, Patel, SK, et al.. Free space optical communication system for indoor applications based on printed circuit board design. *Indones J Electr Eng Comput Sci* 2022;25:1030–7. <https://doi.org/10.11591/ijeecs.v25.i2.pp1030-1037> (<https://doi.org/10.11591/ijeecs.v25.i2.pp1030-1037>).
43. Sorathiya, V, Lavadiya, S, Singh Parmar, B, Baxi, S, Taher Dhankot, Faragallah, OS, et al.. Tunable squared patch based graphene metasurface infrared polarizer. *Appl Phys B* 2022;1–16. <https://doi.org/10.1007/s00340-022-07765-3> (<https://doi.org/10.1007/s00340-022-07765-3>).
44. Lavadiya, S, Sorathiya, V, Faragallah, OS, El-Sayed, HS, Eid, MMA, Rashed, ANZ. Infrared graphene assisted multi-band tunable absorber. *Opt Quant Electron* 2022;54:134. <https://doi.org/10.1007/s11082-022-03523-z> (<https://doi.org/10.1007/s11082-022-03523-z>).
45. Jibon, RH, Ahmed, M, Abd-Elnaby, M, Rashed, ANZ, Eid, MMA. Design mechanism and performance evaluation of photonic crystal fiber (PCF) based sensor in the THz regime for sensing noxious chemical substrates of poultry feed. *Appl Phys A* 2022;128:169. <https://doi.org/10.1007/s00339-022-05302-9> (<https://doi.org/10.1007/s00339-022-05302-9>).

46. Sorathiya, V, Lavadiya, S, Thomas, L, Abd-Elnaby, M, Rashed, ANZ, Eid, MMA. Graphene based tunable short band absorber for infrared wavelength. *Appl Phys B* 2022;128:40. <https://doi.org/10.1007/s00340-022-07763-5> (<https://doi.org/10.1007/s00340-022-07763-5>).
47. Dutta, N, Patel, SK, Faragallah, OS, Baz, M, Rashed, ANZ. Caching scheme for information-centric networks with balanced content distribution. *Int J Commun Syst* 2022;1–10. <https://doi.org/10.1002/dac.5104> (<https://doi.org/10.1002/dac.5104>).
48. Lavadiya, SP, Sorathiya, V, Kanzariya, S, Chavda, B, Naweed, A, Faragallah, OS, et al.. Low profile multiband microstrip patch antenna with frequency reconfigurable feature using PIN diode for S, C, X, and Ku band applications. *Int J Commun Syst* 2022;1–13. <https://doi.org/10.1002/dac.5141> (<https://doi.org/10.1002/dac.5141>).
49. Asaduzzaman, S, Rehana, H, Aziz, T, Faragallah, OS, Baz, M, Eid, MMA, et al.. Key performance parameters estimation with Epsilon near zero (ENZ) for Kagome photonic crystal fiber in THz system. *Opt Quant Electron* 2022;54:202. <https://doi.org/10.1007/s11082-022-03588-w> (<https://doi.org/10.1007/s11082-022-03588-w>).
50. Patel, SK, Solanki, N, Charola, S, Parmar, J, Zakaria, R, Faragallah, OS, et al.. Graphene based highly sensitive refractive index sensor using double split ring resonator metasurface. *Opt Quant Electron* 2022;54:203. <https://doi.org/10.1007/s11082-022-03600-3> (<https://doi.org/10.1007/s11082-022-03600-3>).
51. Sorathiya, V, Lavadiya, S, Faragallah, OS, Eid, MMA, Rashed, ANZ. D shaped dual core photonics crystal based refractive index sensor using graphene–titanium–silver materials for infrared frequency spectrum. *Opt Quant Electron* 2022;54:290. <https://doi.org/10.1007/s11082-022-03700-0> (<https://doi.org/10.1007/s11082-022-03700-0>).
52. Hossain, E, Shazzad Hossain, M, Selim Hossain, M, Jannat, SA, Huda, M, Alsharif, S, et al.. Brain tumor auto-segmentation on multimodal imaging modalities using deep neural network. *Comput Mater Continua (CMC)* 2022;72:4509–23. <https://doi.org/10.32604/cmc.2022.025977> (<https://doi.org/10.32604/cmc.2022.025977>).
53. Asaduzzaman, S, Rehana, H, Chakma, R, Faragallah, OS, El-Sayed, HS, Eid, MMA, et al.. Hexa sector square photonic crystal fiber for blood serum and plasma sensing with ultralow confinement loss. *Appl Phys A* 2022;128:467. <https://doi.org/10.1007/s00339-022-05621-x> (<https://doi.org/10.1007/s00339-022-05621-x>).
54. Nyangaresi, VO, Abd-Elnaby, M, Eid, MMA, Rashed, ANZ. Trusted authority based session key agreement and authentication algorithm for smart grid networks. *Trans Emerg Telecommun Technol* 2022;33:e4528. <https://doi.org/10.1002/ett.4528> (<https://doi.org/10.1002/ett.4528>).
55. Sunitha, G, Arunachalam, R, Abd-Elnaby, M, Eid, MMA, Rashed, ANZ. A comparative analysis of deep neural network on acoustic cough features. *Int J Imag Syst Technol* 2022;1–14. <https://doi.org/10.1002/ima.22749> (<https://doi.org/10.1002/ima.22749>).

PubMed (<https://pubmed.ncbi.nlm.nih.gov/35941929/>)

PubMed Central (<https://www.ncbi.nlm.nih.gov/pmc/articles/PMC9348187/>)

56. Sorathiya, V, Faragallah, OS, El-Sayed, HS, Eid, MMA, Rashed, ANZ. Nanofocusing of optical wave using staircase tapered plasmonic waveguide. *Appl Phys B* 2022;128:104. <https://doi.org/10.1007/s00340-022-07828-5> (<https://doi.org/10.1007/s00340-022-07828-5>).
57. Rashed, ANZ, Hasane Ahammad, SK, Daher, MG, Sorathiya, V, Siddique, A, Asaduzzaman, S, et al.. Spatial single mode laser source interaction with measured pulse based parabolic index multimode fiber. *J Opt Commun* 2022;1–11. <https://doi.org/10.1515/joc-2021-0214> (<https://doi.org/10.1515/joc-2021-0214>).
58. Soundararajan, R, Prabu, AV, Routray, S, Malla, PP, Kumar Ray, A, Palai, G, et al.. Deeply trained real-time body sensor networks for analyzing the symptoms of Parkinson's disease. *IEEE Access* 2022;10:63403–21. <https://doi.org/10.1109/ACCESS.2022.3181985> (<https://doi.org/10.1109/ACCESS.2022.3181985>).
59. Rashed, ANZ, Hasane Ahammad, SK, Daher, MG, Sorathiya, V, Siddique, A, Asaduzzaman, S, et al.. Signal propagation parameters estimation through designed multi layer fibre with higher dominant modes using OptiFibre simulation. *J Opt Commun* 2022;1–12. <https://doi.org/10.1515/joc-2021-0213> (<https://doi.org/10.1515/joc-2021-0213>).
60. Dave1, K, Sorathiya, V, Lavadiya, SP, Patel, SK, Dhankecha, U, Swain, D, et al.. Graphene based double loaded complementary split ring resonator (CSRR) slotted MIMO patch antenna for spectroscopy and imaging THz applications. *Appl Phys A* 2022;128:656. <https://doi.org/10.1007/s00339-022-05820-6> (<https://doi.org/10.1007/s00339-022-05820-6>).
61. Rashed, ANZ, Daher, MG, Hasane Ahammad, SK, Montalbo, FJP, Sorathiya, V, Sayed Asaduzzaman, et al.. Non return to zero line coding with suppressed carrier in FSO transceiver systems under light rain conditions. *J Opt Commun* 2022;1–13. <https://doi.org/10.1515/joc-2022-0039> (<https://doi.org/10.1515/joc-2022-0039>).
62. Rashed, ANZ, Hasane Ahammad, SK, Daher, MG, Zyoud, SH, Sorathiya, V, Montalbo, FJP, et al.. Various transmission codes for the control of bit error rate in both optical wired and wireless communication channels. *J Opt Commun* 2022;1–17. <https://doi.org/10.1515/joc-2022-0044> (<https://doi.org/10.1515/joc-2022-0044>).
63. Asaduzzaman, S, Rehana, H, Bhuiyan, T, Sarma, D, Faragallah, OS, MahmoudEid, MA, et al.. Extremely high birefringent slotted core umbrella-shaped photonic crystal fiber in terahertz regime. *Appl Phys B* 2022;128:148. <https://doi.org/10.1007/s00340-022-07868-x> (<https://doi.org/10.1007/s00340-022-07868-x>).
64. Sorathiya, V, Lavadiya, S, Parmar, B, Baxi, S, Taher Dhankot, Faragallah, OS, et al.. Tunable frequency selective surface using crossed shaped graphene metasurface geometry for far infrared frequency spectrum. *Appl Phys B* 2022;128:169. <https://doi.org/10.1007/s00340-022-07886-9> (<https://doi.org/10.1007/s00340-022-07886-9>).

65. Zuhayer, A, Abd-Elnaby, M, Ahammad, SH, Eid, MMA, Sorathiya, V, Rashed, ANZ. A gold plated twin core D-formed photonic crystal fiber (PCF) for ultrahigh sensitive applications based on surface plasmon resonance (SPR) approach. *Plasmonics* 2022;1–19. <https://doi.org/10.1007/s11468-022-01700-0> (<https://doi.org/10.1007/s11468-022-01700-0>).
66. Tahhan, SR, Taha, RM. Mercedes Benz logo based plasmon resonance PCF sensor. *Sens Bio-Sens Res* 2022;35:100468. <https://doi.org/10.1016/j.sbsr.2021.100468> (<https://doi.org/10.1016/j.sbsr.2021.100468>).
67. Singh, M, Malhotra, J. A high-speed long-haul wavelength division multiplexing-based inter-satellite optical wireless communication link using spectral-efficient 2-D orthogonal modulation scheme. *Int J Commun Syst* 2020;33:e4293. <https://doi.org/10.1002/dac.4293> (<https://doi.org/10.1002/dac.4293>).
68. Al-Khaffaf, DAJ, Rashid Hujjo, HS. High data rate optical wireless communication system using millimeter wave and optical phase modulation. *ARPJ Eng Appl Sci* 2018;13:9086–92.
69. Al-Khaffaf, DAJ, Alshimaysawe, IA. Miniaturised tri-band microstrip patch antenna design for radio and millimetre waves of 5G devices. *Indones J Electr Eng Comput Sci* 2021;21:1594–601. <https://doi.org/10.11591/ijeecs.v21.i3.pp1594-1601> (<https://doi.org/10.11591/ijeecs.v21.i3.pp1594-1601>).
70. Al-Khaffaf, DAJ, Alsahlany, AM. 60 GHz millimetre wave/10 gbps transmission for super broadband wi-fi network. *J Commun* 2019;14:261–6. <https://doi.org/10.12720/jcm.14.4.261-266> (<https://doi.org/10.12720/jcm.14.4.261-266>).
71. Tahhan, SR, Atieh, A, Hasan, M, Hall, T. Characterization and experimental verification of actively mode-locked erbium doped fiber laser utilizing ring cavity. *TM - Tech Mess* 2020;87:535–41. <https://doi.org/10.1515/teme-2020-0003> (<https://doi.org/10.1515/teme-2020-0003>).
72. Tahhan, SR, Abass, AK, Ali, MH. Characteristics of chirped fiber bragg grating dispersion compensator utilizing two apodization profiles. *J Commun* 2018;13:108–13. <https://doi.org/10.12720/jcm.13.3.108-113> (<https://doi.org/10.12720/jcm.13.3.108-113>).
73. Tahhan, SR, Atieh, A, Ali, MH, Hasan, M, Abass, AK, Hall, T. Characteristics of actively mode-locked erbium doped fiber laser utilizing ring cavity. In: *2019 IEEE Jordan international joint conference on electrical engineering and information technology (JEEIT)*. Amman, Jordan; 2019:840–4 pp. [10.1109/JEEIT.2019.8717483](https://doi.org/10.1109/JEEIT.2019.8717483) (<https://doi.org/10.1109/JEEIT.2019.8717483>).
74. Fadil, EA, Abass, AK, Tahhan, SR. Secure WDM-free space optical communication system based optical chaotic. *Opt Quant Electron* 2022;54:477. <https://doi.org/10.1007/s11082-022-03870-x> (<https://doi.org/10.1007/s11082-022-03870-x>).
75. Tahhan, SR, Mohammed, MF, Moosa, AA, Atieh, A. WDM ROF OFDM/QAM system for wireless PON. In: *2021 IEEE Jordan international joint conference on electrical engineering and information technology (JEEIT)*. Amman, Jordan; 2021:164–9 pp.

<https://doi.org/10.1109/JEIT53412.2021.9634158> (<https://doi.org/10.1109/JEIT53412.2021.9634158>) .
[10.1109/JEIT53412.2021.9634158](https://doi.org/10.1109/JEIT53412.2021.9634158) (<https://doi.org/10.1109/JEIT53412.2021.9634158>)

76. Tahhan, SR, Ghazai, AJ, Alwan, IM, Ali, MH. Investigation of the characteristics of high-resistivity silica based hybrid porous core photonic crystal fiber for terahertz wave guidance. *Dig J Nanomater Biostruct* 2019;14:831–41.

77. Rashed, ANZ. High reliability optical interconnections for short range applications in high speed optical communication systems. *J Opt Laser Technol* 2013;48:302–8. <https://doi.org/10.1016/j.optlastec.2012.10.038> (<https://doi.org/10.1016/j.optlastec.2012.10.038>) .

78. Rashed, ANZ. High performance photonic devices for multiplexing/demultiplexing applications in multi band operating regions. *J Comput Theor Nanosci* 2012;9:522–31. <https://doi.org/10.1166/jctn.2012.2055> (<https://doi.org/10.1166/jctn.2012.2055>) .

79. Rashed, ANZ, Sharshar, HA. Analysis of transmission line feed method for transparent conductor oxide materials based optical microstrip patch antennas design. *Optoelectron Adv Mater Rapid Commun* 2012;6:980–7.

80. Rashed, ANZ, Metwae'e, MA. Operation performance characteristics of vertical cavity surface emitting lasers (VCSELs) under high thermal neutrons irradiated fields. *J Russ Laser Res* 2013;34:1–8. <https://doi.org/10.1007/s10946-013-9317-z> (<https://doi.org/10.1007/s10946-013-9317-z>) .

81. Rashed, ANZ. Optical fiber communication cables systems performance under harmful gamma irradiation and thermal environment effects. *IET Commun* 2013;7:448–55. <https://doi.org/10.1049/iet-com.2012.0313> (<https://doi.org/10.1049/iet-com.2012.0313>) .

82. Rashed, ANZ, El-halawany, MME. Transmission characteristics evaluation under bad weather conditions in optical wireless links with different optical transmission windows. *Wireless Pers Commun* 2013;71:1577–95. <https://doi.org/10.1007/s11277-012-0893-y> (<https://doi.org/10.1007/s11277-012-0893-y>) .

83. Rashed, ANZ, Sharshar, H. Performance evaluation of short range underwater optical wireless communications for different ocean water types. *Wireless Pers Commun* 2013;72:693–708. <https://doi.org/10.1007/s11277-013-1037-8> (<https://doi.org/10.1007/s11277-013-1037-8>) .

84. Rashed, ANZ. Performance signature and optical signal processing of high speed electro-optic modulators. *Opt Commun* 2013;294:49–58. <https://doi.org/10.1016/j.optcom.2012.12.041> (<https://doi.org/10.1016/j.optcom.2012.12.041>) .

85. Rashed, ANZ, Metwae'e, MA. Maximization of repeater spacing in ultra wide-wavelength-division multiplexing optical communication systems based on multi pumped laser diodes. *J Russ Laser Res* 2013;34:255–61. <https://doi.org/10.1007/s10946-013-9349-4> (<https://doi.org/10.1007/s10946-013-9349-4>) .

86. Rashed, ANZ. High efficiency wireless optical links in high transmission speed wireless optical communication networks. *Int J Commun Syst* 2014;27:3416–27. [10.1002/dac.2550](https://doi.org/10.1002/dac.2550) (<https://doi.org/10.1002/dac.2550>)

87. Rashed, ANZ, Saad, AE-FA. Different electro-optical modulators for high transmission-data rates and signal-quality enhancement. *J Russ Laser Res* 2013;34:336–45. <https://doi.org/10.1007/s10946-013-9359-2> (<https://doi.org/10.1007/s10946-013-9359-2>).
88. Rashed, ANZ. High efficiency laser power transmission with all optical amplification for high transmission capacity submarine cables. *J Russ Laser Res* 2013;34:603–13. <https://doi.org/10.1007/s10946-013-9393-0> (<https://doi.org/10.1007/s10946-013-9393-0>).
89. Rashed, ANZ. Submarine fiber cable network systems cost planning considerations with achieved high transmission capacity and signal quality enhancement. *Opt Commun* 2014;311:44–54. <https://doi.org/10.1016/j.optcom.2013.08.025> (<https://doi.org/10.1016/j.optcom.2013.08.025>).
90. Rashed, ANZ, Mohamed, AE-NA, Metawe'e, MA. New trends of transmission capacity evaluation of submarine fiber cable systems with different ultra-high multiplexing, amplification and propagation techniques. *Arabian J Sci Eng* 2014;39:945–56. <https://doi.org/10.1007/s13369-013-0645-7> (<https://doi.org/10.1007/s13369-013-0645-7>).
91. Rashed, ANZ. Optical network management and its performance evaluation for both future cost planning and triple play solutions. *Wireless Pers Commun* 2014;75:2005–20. <https://doi.org/10.1007/s11277-013-1450-z> (<https://doi.org/10.1007/s11277-013-1450-z>).
92. Rashed, ANZ, Metawe'e, MA. Optical filters dimensions and thermal operation conditions impact on its transmission considerations in near infrared (NIR) optical spectrum transmission region. *Optoelectron Adv Mater J Rapid Commun* 2014;8:175–84.
93. Rashed, ANZ, Mohammed, A-EA, Dardeer, OMA. Performance evaluation of a WDM/OCDM based hybrid optical switch utilizing efficient resource allocation. *Chin Opt Lett* 2014;12:050602. <https://doi.org/10.3788/col201412.050602> (<https://doi.org/10.3788/col201412.050602>).
94. Rashed, ANZ. Optical wireless communication systems operation performance efficiency evaluation in the presence of different fog density levels and noise impact. *Wireless Pers Commun* 2015;81:427–44. <https://doi.org/10.1007/s11277-014-2137-9> (<https://doi.org/10.1007/s11277-014-2137-9>).
95. Boopathi, CS, Vinoth Kumar, K, Sheebarani, S, Selvakumar, K, Rashed, ANZ, Yupapin, P. Design of human blood sensor using symmetric dual core photonic crystal fiber. *Results Phys* 2018;11:964–5. <https://doi.org/10.1016/j.rinp.2018.10.065> (<https://doi.org/10.1016/j.rinp.2018.10.065>).
96. Vigneswaran, D, Mani Rajan, MS, Aly, MH, Rashed, ANZ. Few-mode ring core fiber characteristics: temperature impact. *Photonic Netw Commun* 2019;1–16. <https://doi.org/10.1007/s11107-018-0804-6> (<https://doi.org/10.1007/s11107-018-0804-6>).
97. Chakkravarthy, SP, Arthi, V, Karthikumar, S, Rashed, ANZ, Yupapin, P, Amiri, IS. Ultra high transmission capacity based on optical first order soliton propagation systems. *Results Phys* 2019;12:512–3. <https://doi.org/10.1016/j.rinp.2018.12.002>

(<https://doi.org/10.1016/j.rinp.2018.12.002>).

Received: 2022-07-25

Accepted: 2022-11-08

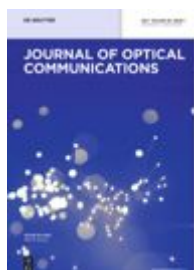
Published Online: 2022-11-28

© 2022 Walter de Gruyter GmbH, Berlin/Boston

— or —

PDF 30,00 €

From the journal



Journal of Optical Communications

Downloaded on 8.12.2023 from

<https://www.degruyter.com/document/doi/10.1515/joc-2022-0164/html?lang=en>



Requires Authentication | Published online by [De Gruyter](#) | December 8, 2022

Multi-mode step graded index fibers performance parameters (attenuation/dispersion/mode field) measurements by using OptiFiber simulation

Ahmed Nabih Zaki Rashed  , Baraa Riyadh Altahan, Thaticharla Manasavenna, P. Poorna Priya, M. Rama Krishna, S.K. Hasane Ahammad, Md. Amzad Hossain  and Marwa Hamed Amin

From the journal [Journal of Optical Communications](#)

<https://doi.org/10.1515/joc-2022-0217>

 Citations  7

Abstract

This paper has clarified the positive and negative effects of 3.1% germania and 1% fluorine DS fibers in multi-mode silica profile. The group delay and the total fiber dispersion against operating wavelength for PS and various doped silica (DS) fibers are demonstrated and assured by using OptiFiber simulation. The material, waveguide and total fiber dispersions are demonstrated against wavelength for the PS fiber, 3.1% germania DS (GDS) fiber and 1% fluorine DS (FDS) fiber. Besides the mode field diameter, fiber material loss, fiber bending loss and the dispersion group delay are simulated and clarified against the operating wavelength for PS and different DS fibers. The study gives the effects of the dopant ratio of germania and fluorine on the zero dispersion wavelength shift and DS.

Keywords: [composite materials](#); [dopant ratio](#); [fluorine material](#); [Germania material](#); [silica-doped](#)

Corresponding authors: **Ahmed Nabih Zaki Rashed**, Electronics and Electrical Communications Engineering Department, Faculty of Electronic Engineering, Menoufia University, Menouf 32951, Egypt, E-mail: ahmed_733@yahoo.com; and **Md. Amzad Hossain**, Faculty of Electrical Engineering and Information

Technology, Institute of Theoretical Electrical Engineering, Ruhr University Bochum, 44801 Bochum, Germany; and Department of Electrical and Electronic Engineering, Jashore University of Science and Technology, Jashore, 7408, Bangladesh, E-mail: mahossain.eee@gmail.com

Funding source: Al-Mustaqbal University College

Acknowledgment

The authors extend their appreciation and gratitude to Al-Mustaqbal University College in Iraq for funding this project.

Author contributions: All the authors have accepted responsibility for the entire content of this submitted manuscript and approved submission.

Research funding: This work is funded by the Al-Mustaqbal University College in Iraq.

Conflict of interest statement: The authors declare no conflicts of interest regarding this article.

References

1. Oglah, MH. Estimate the attenuation and simulation of dispersion Gaussian pulses propagation in a single mode optical fiber. *Tikrit J Pure Sci* 2017;22:108–14.
2. Adams, MJ. *An introduction to optical waveguides*. Boston: John Wiley & Sons; 1981.
3. Rashed, ANZ, Mohamed, AENAEG, Hanafy, SAERS, Aly, MH. A comparative study of the performance of graded index perfluorinated plastic and alumino silicate optical fibers in internal optical interconnections. *Optik J* 2016;127:9259–63.
<https://doi.org/10.1016/j.ijleo.2016.07.002> (<https://doi.org/10.1016/j.ijleo.2016.07.002>).
4. Rashed, ANZ, Mohamed, AENA, Mostafa, S, Abd El-Samie, FE. Performance evaluation of SAC-OCDMA system in free space optics and optical fiber system based on different types of codes. *Wirel Pers Commun J* 2017;96:2843–61.
<https://doi.org/10.1007/s11277-017-4327-8> (<https://doi.org/10.1007/s11277-017-4327-8>).
5. Rashed, ANZ, Tabbour, MSF. Suitable optical fiber communication channel for optical nonlinearity signal processing in high optical data rate systems. *Wirel Pers Commun J* 2017;97:397–416. <https://doi.org/10.1007/s11277-017-4511-x> (<https://doi.org/10.1007/s11277-017-4511-x>).
6. Rashed, ANZ, Tabbour, MSF, El-Meadawy, S. Optimum flat gain with optical amplification technique based on both gain flattening filters and fiber bragg grating methods. *J Nanoelectron Optoelectron* 2018;13:665–76.

<https://doi.org/10.1166/jno.2018.2168> (<https://doi.org/10.1166/jno.2018.2168>) .

7. Mohamed, SEDN, Mohamed, AENA, Abd El-Samie, FE, Rashed, ANZ. Performance enhancement of IM/DD optical wireless systems. *Photonic Netw Commun J* 2018;36:114–27. <https://doi.org/10.1007/s11107-018-0761-0> (<https://doi.org/10.1007/s11107-018-0761-0>) .
8. Rashed, ANZ, Tabbour, MSF. The trade off between different modulation schemes for maximum long reach high data transmission capacity optical orthogonal frequency division multiplexing (OOFDM). *Wirel Pers Commun J* 2018;101:325–37. <https://doi.org/10.1007/s11277-018-5690-9> (<https://doi.org/10.1007/s11277-018-5690-9>) .
9. Rashed, ANZ, Abdel Kader, HM, Al-Awamry, AA, Abd El-Aziz, IA. Transmission performance simulation study evaluation for high speed radio over fiber communication systems. *Wirel Pers Commun J* 2018;103:1765–79. <https://doi.org/10.1007/s11277-018-5879-y> (<https://doi.org/10.1007/s11277-018-5879-y>) .
10. Rashed, ANZ, Tabbour, MSF. Best candidate integrated technology for low noise, high speed, and wide bandwidth based transimpedance amplifiers in optical computing systems and optical fiber applications. *Int J Commun Syst* 2018;31:e3801. <https://doi.org/10.1002/dac.3801> (<https://doi.org/10.1002/dac.3801>) .
11. Rashed, ANZ, Tabbour, MSF, El-assar, M. 20 Gb/s hybrid CWDM/DWDM for extended reach fiber to the home network applications. *Proc Natl Acad Sci, India, Sect A* 2019;89:653–62. <https://doi.org/10.1007/s40010-018-0526-2> (<https://doi.org/10.1007/s40010-018-0526-2>) .
12. Boopathi, CS, Vinoth Kumar, K, Sheebarani, S, Selvakumar, K, Rashed, ANZ, Yupapin, P. Design of human blood sensor using symmetric dual core photonic crystal fiber. *Results Phys* 2018;11:964–5. <https://doi.org/10.1016/j.rinp.2018.10.065> (<https://doi.org/10.1016/j.rinp.2018.10.065>) .
13. Vigneswaran, D, Rajan, MSM, Aly, MH, Rashed, ANZ. Few-mode ring core fiber characteristics: temperature impact. *Photonic Netw Commun J* 2018;54:165–75. <https://doi.org/10.1007/s11107-018-0804-6> (<https://doi.org/10.1007/s11107-018-0804-6>) .
14. Chakkravarthy, SP, Arthi, V, Karthikumar, S, Rashed, ANZ, Yupapin, P, Amiri, IS. Ultra high transmission capacity based on optical first order soliton propagation systems. *Results Phys* 2019;12:512–3. <https://doi.org/10.1016/j.rinp.2018.12.002> (<https://doi.org/10.1016/j.rinp.2018.12.002>) .
15. Rashed, ANZ, Kumar, KV, Prithi, S, Maheswar, R, Tabbour, MSF. Transmittivity/reflectivity, bandwidth, and ripple factor level measurement for different refractive index fiber grating shape profiles. *J Opt Commun* 2019. <https://doi.org/10.1515/joc-2018-0233> (<https://doi.org/10.1515/joc-2018-0233>) [Epub ahead of print].
16. Rashed, ANZ, Kumar, KV, Kumar, PV, Mohamed, AENA, Tabbour, MS, El-Assar, M. DWDM channel spacing effects on the signal quality for DWDM/CWDM FTTx network. *J Opt Commun* 2019. <https://doi.org/10.1515/joc-2019-0012> (<https://doi.org/10.1515/joc-2019-0012>) [Epub ahead of print].

17. Rashed, ANZ, Tabbour, MSF, Vijayakumari, P. Numerical analysis of optical properties using octagonal shaped photonic crystal fiber. *J Opt Commun* 2019. <https://doi.org/10.1515/joc-2019-0013> (<https://doi.org/10.1515/joc-2019-0013>) [Epub ahead of print].
18. Rashed, ANZ, Kumar, SS, Tabbour, MSF, Sundararajan, TVP, Maheswar, R. Different graded refractive index fiber profiles design for the control of losses and dispersion effects. *J Opt Commun* 2019. <https://doi.org/10.1515/joc-2019-0036> (<https://doi.org/10.1515/joc-2019-0036>) [Epub ahead of print].
19. Rashed, ANZ. Comparison between NRZ/RZ modulation techniques for upgrading long haul optical wireless communication systems. *J Opt Commun* 2019. <https://doi.org/10.1515/joc-2019-0038> (<https://doi.org/10.1515/joc-2019-0038>) [Epub ahead of print].
20. Rashed, ANZ, Kumar, KV, Tabbour, MSF, Sundararajan, TVP. Nonlinear characteristics of semiconductor optical amplifiers for optical switching control realization of logic gates. *J Opt Commun* 2019. <https://doi.org/10.1515/joc-2019-0027> (<https://doi.org/10.1515/joc-2019-0027>) [Epub ahead of print].
21. Ahmed, K, Paula, BK, Vasudevan, B, Rashed, ANZ, Maheswar, R, Amiri, IS, et al. Design of D-shaped elliptical core photonic crystal fiber for blood plasma cell sensing application. *Results Phys* 2019;12:2021–5. <https://doi.org/10.1016/j.rinp.2019.02.026> (<https://doi.org/10.1016/j.rinp.2019.02.026>) .
22. Ramana, TV, Pandian, A, Ellammal, C, Jarin, T, Rashed, ANZ, Sampathkumar, A. Numerical analysis of circularly polarized modes in coreless photonic crystal fiber. *Results Phys* 2019;13:102140. <https://doi.org/10.1016/j.rinp.2019.02.076> (<https://doi.org/10.1016/j.rinp.2019.02.076>) .
23. Rashed, ANZ, Mohammed, AENA, Zaky, WF, Amiri, IS, Yupapin, P. The switching of optoelectronics to full optical computing operations based on nonlinear metamaterials. *Results Phys* 2019;13:102152. <https://doi.org/10.1016/j.rinp.2019.02.088> (<https://doi.org/10.1016/j.rinp.2019.02.088>) .
24. Ranathive, S, Kumar, KV, Rashed, ANZ, Tabbour, MSF, Sundararajan, TVP. Performance signature of optical fiber communications dispersion compensation techniques for the control of dispersion management. *J Opt Commun* 2019. <https://doi.org/10.1515/joc-2019-0021> (<https://doi.org/10.1515/joc-2019-0021>) [Epub ahead of print].
25. Amiri, IS, Rashed, ANZ, Yupapin, P. Interaction between optical sources and optical modulators for high-speed optical communication networks. *J Opt Commun* 2019. <https://doi.org/10.1515/joc-2019-0041> (<https://doi.org/10.1515/joc-2019-0041>) [Epub ahead of print].
26. Amiri, IS, Rashed, ANZ, Yupapin, P. Effects of order super Gaussian pulses on the performance of high data rate optical fiber channel in the presence of self phase modulation. *J Opt Commun* 2019. <https://doi.org/10.1515/joc-2019-0039> (<https://doi.org/10.1515/joc-2019-0039>) [Epub ahead of print].

27. Amiri, IS, Rashed, ANZ, Yupapin, P. Mathematical model analysis of dispersion and loss in photonic crystal fibers. *J Opt Commun* 2019. <https://doi.org/10.1515/joc-2019-0052> (<https://doi.org/10.1515/joc-2019-0052>) [Epub ahead of print].
28. Amiri, IS, Rashed, ANZ, Yupapin, P. Basic functions of fiber bragg grating effects on the optical fiber systems performance efficiency. *J Opt Commun* 2019. <https://doi.org/10.1515/joc-2019-0042> (<https://doi.org/10.1515/joc-2019-0042>) [Epub ahead of print].
29. Amiri, IS, Mohammed, ANZRAENA, Aboelazm, MB, Yupapin, P. Nonlinear effects with semiconductor optical amplifiers. *J Opt Commun* 2019. <https://doi.org/10.1515/joc-2019-0053> (<https://doi.org/10.1515/joc-2019-0053>) [Epub ahead of print].
30. Amiri, IS, Rashed, ANZ, Yupapin, P. High-Speed light sources in high-speed optical passive local area communication networks. *J Opt Commun* 2019. <https://doi.org/10.1515/joc-2019-0070> (<https://doi.org/10.1515/joc-2019-0070>) [Epub ahead of print].
31. Rashed, ANZ, Tabbour, MSF, Natarajan, K. Performance enhancement of overall LEO/MEO intersatellite optical wireless communication systems. *Int J Satell Commun Netw* 2020;38:31–40. <https://doi.org/10.1002/sat.1306> (<https://doi.org/10.1002/sat.1306>) .
32. Amiri, IS, Rashed, ANZ, Mohammed, AEA, Salah El-Din, E, Yupapin, P. Spatial continuous wave laser and spatiotemporal VCSEL for high-speed long haul optical wireless communication channels. *J Opt Commun* 2019. <https://doi.org/10.1515/joc-2019-0061> (<https://doi.org/10.1515/joc-2019-0061>) [Epub ahead of print].
33. Amiri, IS, Rashed, ANZ, Yupapin, P. Average power model of optical Raman amplifiers based on frequency spacing and amplifier section stage optimization. *J Opt Commun* 2019. <https://doi.org/10.1515/joc-2019-0081> (<https://doi.org/10.1515/joc-2019-0081>) [Epub ahead of print].
34. Amiri, IS, Houssien, FMAM, Rashed, ANZ, Mohammed, AE-NA. Temperature effects on characteristics and performance of near-infrared wide bandwidth for different avalanche photodiodes structures. *Results Phys* 2019;14:102399. <https://doi.org/10.1016/j.rinp.2019.102399> (<https://doi.org/10.1016/j.rinp.2019.102399>) .
35. Amiri, IS, Rashed, ANZ. Simulative study of simple ring resonator-based brewster plate for power system operation stability. *Indones J Electr Eng Comput Sci* 2019;16:1070–6. <https://doi.org/10.11591/ijeecs.v16.i2.pp1070-1076> (<https://doi.org/10.11591/ijeecs.v16.i2.pp1070-1076>) .
36. Amiri, IS, Rashed, ANZ. Different photonic crystal fibers configurations with the key solutions for the optimization of data rates transmission. *J Opt Commun* 2019. <https://doi.org/10.1515/joc-2019-0100> (<https://doi.org/10.1515/joc-2019-0100>) [Epub ahead of print].
37. Amiri, IS, Rashed, ANZ, Ramya, KC, Kumar, KV, Maheswar, R. The physical Parameters of EDFA and SOA optical amplifiers and bit sequence variations based optical pulse generators impact on the performance of soliton transmission systems. *J Opt*

Commun 2019. <https://doi.org/10.1515/joc-2019-0156> (<https://doi.org/10.1515/joc-2019-0156>).

38. Amiri, IS, Houssien, FMAM, Rashed, ANZ, Mohammed, AENA. Optical networks performance optimization based on hybrid configurations of optical fiber amplifiers and optical receivers. *J Opt Commun* 2019. <https://doi.org/10.1515/joc-2019-0153>

(<https://doi.org/10.1515/joc-2019-0153>) [Epub ahead of print].

39. Amiri, IS, Rashed, ANZ, Sarker, K, Paul, BK, Ahmed, K. Chirped large mode area photonic crystal modal fibers and its resonance modes based on finite element technique. *J Opt Commun* 2019. <https://doi.org/10.1515/joc-2019-0146> (<https://doi.org/10.1515/joc-2019-0146>)

[Epub ahead of print].

40. Amiri, IS, Houssien, FMAM, Rashed, ANZ, Mohammed, AENA. Comparative simulation of thermal noise effects for photodetectors on performance of long-haul DWDM optical networks. *J Opt Commun* 2019. <https://doi.org/10.1515/joc-2019-0152>

(<https://doi.org/10.1515/joc-2019-0152>) [Epub ahead of print].

41. Amiri, IS, Rashed, ANZ, Mohammed, AEA, Aboelazm, MB. Single wide band traveling wave semiconductor optical amplifiers for all optical bidirectional wavelength conversion. *J Opt Commun* 2019. <https://doi.org/10.1515/joc-2019-0168>

(<https://doi.org/10.1515/joc-2019-0168>) [Epub ahead of print].

42. Amiri, IS, Rashed, ANZ, Mohammed, AENA, Zaky, WF. Influence of loading, regeneration and recalling elements processes on the system behavior of all optical data bus line system random access memory. *J Opt Commun* 2019. <https://doi.org/10.1515/joc-2019-0163>

(<https://doi.org/10.1515/joc-2019-0163>) [Epub ahead of print].

43. Malathy, S, Kumar, KV, Rashed, ANZ, Vigneswaran, D, Eeldien, ES. Upgrading superior operation performance efficiency of submarine transceiver optical communication systems toward multi tera bit per second. *Comput Commun J*

2019;146:192–200. <https://doi.org/10.1016/j.comcom.2019.08.009>

(<https://doi.org/10.1016/j.comcom.2019.08.009>).

44. Amiri, IS, Rashed, ANZ. Numerical investigation of V shaped three elements resonator for optical closed loop system. *Indones J Electr Eng Comput Sci* 2019;16:1392–7.

<https://doi.org/10.11591/ijeecs.v16.i3.pp1392-1397> (<https://doi.org/10.11591/ijeecs.v16.i3.pp1392-1397>).

45. Rashed, ANZ, Tabbour, MSF. The engagement of hybrid dispersion compensation schemes performance signature for ultra wide bandwidth and ultra long haul optical transmission systems. *Wirel Pers Commun J* 2020;67:354–66.

<https://doi.org/10.1007/s11277-019-06687-2> (<https://doi.org/10.1007/s11277-019-06687-2>).

46. Rashed, ANZ, Tabbour, MSF, El-Meadawy, S, Anwar, T, Sarlan, A, Yupapin, P, et al.. The effect of using different materials on erbium-doped fiber amplifiers for indoor applications. *Results Phys* 2019;15:102650. <https://doi.org/10.1016/j.rinp.2019.102650>

(<https://doi.org/10.1016/j.rinp.2019.102650>).

47. Amiri, IS, Rashed, ANZ. Power enhancement of the U-shape cavity microring resonator through gap and material characterizations. *J Opt Commun* 2019. <https://doi.org/10.1515/joc-2019-0108> (<https://doi.org/10.1515/joc-2019-0108>) [Epub ahead of print].
48. Amiri, IS, Kuppusamy, PG, Rashed, ANZ, Jayarajan, P, Thiyagupriyadharsan, MR, Yupapin, P. The engagement of hybrid ultra high space division multiplexing with maximum time division multiplexing techniques for high-speed single-mode fiber cable systems. *J Opt Commun* 2019. <https://doi.org/10.1515/joc-2019-0205> (<https://doi.org/10.1515/joc-2019-0205>) [Epub ahead of print].
49. Amiri, IS, Rashed, ANZ, Jahan, S, Paul, BK, Ahmed, K. Polar polarization mode and average radical flux intensity measurements based on all optical spatial communication systems. *J Opt Commun* 2019;55:134–45. <https://doi.org/10.1515/joc-2019-0159> (<https://doi.org/10.1515/joc-2019-0159>) .
50. Sivaranjani, S, Sampathkumar, A, Rashed, ANZ, Sundararajan, TVP, Amiri, IS. Performance evaluation of bidirectional wavelength division multiple access broadband optical passive elastic networks operation efficiency. *J Opt Commun* 2019. <https://doi.org/10.1515/joc-2019-0175> (<https://doi.org/10.1515/joc-2019-0175>) [Epub ahead of print].
51. Amiri, IS, Rashed, ANZ, Yupapin, P. High-Speed transmission circuits signaling in optical communication systems. *J Opt Commun* 2019. <https://doi.org/10.1515/joc-2019-0197> (<https://doi.org/10.1515/joc-2019-0197>) [Epub ahead of print].
52. Amiri, IS, Rashed, ANZ, Jahan, S, Paul, BK, Ahmed, K, Yupapin, P. Technical specifications of the submarine fiber optic channel bandwidth/capacity in optical fiber transmission systems. *J Opt Commun* 2019. <https://doi.org/10.1515/joc-2019-0226> (<https://doi.org/10.1515/joc-2019-0226>) [Epub ahead of print].
53. Amiri, IS, Rashed, ANZ. Signal processing criteria based on electro-optic filters for fiber optic access transceiver systems. *J Opt Commun* 2019. <https://doi.org/10.1515/joc-2019-0116> (<https://doi.org/10.1515/joc-2019-0116>) [Epub ahead of print].
54. Amiri, IS, Rashed, ANZ, Yupapin, P. Pump laser automatic signal control for erbium-doped fiber amplifier gain, noise figure, and output spectral power. *J Opt Commun* 2019. <https://doi.org/10.1515/joc-2019-0203> (<https://doi.org/10.1515/joc-2019-0203>) [Epub ahead of print].
55. Amiri, IS, Rashed, ANZ, Parvez, AHMS, Paul, BK, Ahmed, K. Performance enhancement of fiber optic and optical wireless communication channels by using forward error correction codes. *J Opt Commun* 2019. <https://doi.org/10.1515/joc-2019-0191> (<https://doi.org/10.1515/joc-2019-0191>) [Epub ahead of print].
56. Amiri, IS, Rashed, ANZ, Yupapin, P. Z Shaped like resonator with crystal in the presence of flat mirror based standing wave ratio for optical antenna systems. *Indones J Electr Eng Comput Sci* 2020;17:1405–9. <https://doi.org/10.11591/ijeecs.v17.i3.pp1405-1409> (<https://doi.org/10.11591/ijeecs.v17.i3.pp1405-1409>) .

57. Amiri, IS, Rashed, ANZ, Yupapin, P. Influence of device to device interconnection elements on the system behavior and stability. *Indones J Electr Eng Comput Sci* 2020;18:843–7. <https://doi.org/10.11591/ijeecs.v18.i2.pp843-847> (<https://doi.org/10.11591/ijeecs.v18.i2.pp843-847>).
58. Eid, MMA, Amiri, IS, Rashed, ANZ, Yupapin, P. Dental lasers applications in visible wavelength operational band. *Indones J Electr Eng Comput Sci* 2020;18:890–5. <https://doi.org/10.11591/ijeecs.v18.i2.pp890-895> (<https://doi.org/10.11591/ijeecs.v18.i2.pp890-895>).
59. Amiri, IS, Rashed, ANZ, Yupapin, P. Comparative simulation study of multi stage hybrid all optical fiber amplifiers in optical communications. *J Opt Commun* 2020. <https://doi.org/10.1515/joc-2019-0132> (<https://doi.org/10.1515/joc-2019-0132>) [Epub ahead of print].
60. Amiri, IS, Rashed, ANZ, Abdel Kader, HM, Al-Awamry, AA, Abd El-Aziz, IA, Yupapin, P, et al.. Optical communication transmission systems improvement based on chromatic and polarization mode dispersion compensation simulation management. *Optik J* 2020;207:163853. <https://doi.org/10.1016/j.ijleo.2019.163853> (<https://doi.org/10.1016/j.ijleo.2019.163853>).
61. Samanta, D, Sivaram, M, Rashed, ANZ, Boopathi, CS, Amiri, IS, Yupapin, P. Distributed feedback laser (DFB) for signal power amplitude level improvement in long spectral band. *J Opt Commun* 2020. <https://doi.org/10.1515/joc-2019-0252> (<https://doi.org/10.1515/joc-2019-0252>) [Epub ahead of print].
62. Amiri, IS, Rashed, ANZ, Yupapin, P. Analytical model analysis of reflection/transmission characteristics of long-period fiber bragg grating (LPFBG) by using coupled mode theory. *J Opt Commun* 2020. <https://doi.org/10.1515/joc-2019-0187> (<https://doi.org/10.1515/joc-2019-0187>) [Epub ahead of print].
63. Amiri, IS, Rashed, ANZ, Rahman, Z, Paul, BK, Ahmed, K. Conventional/Phase shift dual drive mach–zehnder modulation measured type based radio over fiber systems. *J Opt Commun* 2020. <https://doi.org/10.1515/joc-2019-0312> (<https://doi.org/10.1515/joc-2019-0312>) [Epub ahead of print].
64. Alatwi, AM, Rashed, ANZ, El-Eraki, AM, Amiri, IS. Best candidate routing algorithms integrated with minimum processing time and low blocking probability for modern parallel computing systems. *Indones J Electr Eng Comput Sci* 2020;19:847–54. <https://doi.org/10.11591/ijeecs.v19.i2.pp847-854> (<https://doi.org/10.11591/ijeecs.v19.i2.pp847-854>).
65. El-Hageen, HM, Alatwi, AM, Rashed, ANZ. Silicon-Germanium dioxide and aluminum indium gallium arsenide-based acoustic optic modulators. *Open Eng J* 2020;10:506–11. <https://doi.org/10.1515/eng-2020-0065> (<https://doi.org/10.1515/eng-2020-0065>).
66. El-Hageen, HM, Alatwi, AM, Rashed, ANZ. RZ line coding scheme with direct laser modulation for upgrading optical transmission systems. *Open Eng J* 2020;10:546–51. <https://doi.org/10.1515/eng-2020-0066> (<https://doi.org/10.1515/eng-2020-0066>).

67. Alatwi, AM, Rashed, ANZ, El-Gammal, EM. Wavelength division multiplexing techniques based on multi transceiver in low earth orbit intersatellite systems. *J Opt Commun* 2020. <https://doi.org/10.1515/joc-2019-0171> (<https://doi.org/10.1515/joc-2019-0171>) [Epub ahead of print].
68. El-Hageen, HM, Kuppusamy, PG, Alatwi, AM, Sivaram, M, Yasar, ZA, Rashed, ANZ. Different modulation schemes for direct and external modulators based on various laser sources. *J Opt Commun* 2020. <https://doi.org/10.1515/joc-2020-0029> (<https://doi.org/10.1515/joc-2020-0029>) [Epub ahead of print].
69. El-Hageen, HM, Alatwi, AM, Rashed, ANZ. High-speed signal processing and wide band optical semiconductor amplifier in the optical communication systems. *J Opt Commun* 2020. <https://doi.org/10.1515/joc-2020-0070> (<https://doi.org/10.1515/joc-2020-0070>) [Epub ahead of print].
70. El-Hageen, HM, Alatwi, AM, Rashed, ANZ. Laser measured rate equations with various transmission coders for optimum of data transmission error rates. *Indones J Electr Eng Comput Sci* 2020;20:1406–12. <https://doi.org/10.11591/ijeecs.v20.i3.pp1406-1412> (<https://doi.org/10.11591/ijeecs.v20.i3.pp1406-1412>) .
71. Eid, MMA, Habib, MA, Anower, MS, Rashed, ANZ. Highly sensitive nonlinear photonic crystal fiber based sensor for chemical sensing applications. *Microsyst Technol J* 2020;34:657–70. <https://doi.org/10.1007/s00542-020-05019-w> (<https://doi.org/10.1007/s00542-020-05019-w>) .
72. Eid, MMA, Rashed, ANZ, Shafkat, A, Ahmed, K. Fabry Perot laser properties with high pump lasers for upgrading fiber optic transceiver systems. *J Opt Commun* 2020. <https://doi.org/10.1515/joc-2020-0146> (<https://doi.org/10.1515/joc-2020-0146>) [Epub ahead of print].
73. Eid, MMA, Rashed, ANZ, Hosen, MS, Paul, BK, Ahmed, K. Spatial optical transceiver system-based key solution for high data rates in measured index multimode optical fibers for indoor applications. *J Opt Commun* 2020. <https://doi.org/10.1515/joc-2020-0117> (<https://doi.org/10.1515/joc-2020-0117>) [Epub ahead of print].
74. Eid, MMA, Rashed, ANZ, El-Meadawy, S, Ahmed, K. Simulation study of signal gain optimization based on hybrid composition techniques for high speed optically dense multiplexed systems. *J Opt Commun* 2020;55:167–78. <https://doi.org/10.1515/joc-2020-0150> (<https://doi.org/10.1515/joc-2020-0150>) .
75. Alatwi, AM, Rashed, ANZ. Hybrid CPFSK/OQPSK modulation transmission techniques' performance efficiency with RZ line coding-based fiber systems in passive optical networks. *Indones J Electr Eng Comput Sci* 2021;21:263–70. <https://doi.org/10.11591/ijeecs.v21.i1> (<https://doi.org/10.11591/ijeecs.v21.i1>) .
76. Alatwi, AM, Rashed, ANZ. An analytical method with numerical results to be used in the design of optical slab waveguides for optical communication system applications. *Indones J Electr Eng Comput Sci* 2021;21:278–86. <https://doi.org/10.11591/ijeecs.v21.i1.pp278-286> (<https://doi.org/10.11591/ijeecs.v21.i1.pp278-286>) .

77. Alatwi, AM, Rashed, ANZ. Conventional doped silica/fluoride glass fibers for low loss and minimum dispersion effects. *Indones J Electr Eng Comput Sci* 2021;21:287–95. <https://doi.org/10.11591/ijeecs.v21.i1.pp287-295> (<https://doi.org/10.11591/ijeecs.v21.i1.pp287-295>).
78. El-Hageen, HM, Alatwi, AM, Rashed, ANZ. Spatial optical transmitter based on on/off keying line coding modulation scheme for optimum performance of telecommunication systems. *Indones J Electr Eng Comput Sci* 2021;21:305–12. <https://doi.org/10.11591/ijeecs.v21.i1.pp305-312> (<https://doi.org/10.11591/ijeecs.v21.i1.pp305-312>).
79. Eid, MMA, Rashed, AANZ, Kurmendra. High speed optical switching gain based EDFA model with 30 Gb/s NRZ modulation code in optical systems. *J Opt Commun* 2020. <https://doi.org/10.1515/joc-2020-0223> (<https://doi.org/10.1515/joc-2020-0223>) [Epub ahead of print].
80. Eid, MMA, Rashed, ANZ, Amiri, IS. Fast speed switching response and high modulation signal processing bandwidth through LiNbO₃ electro-optic modulators. *J Opt Commun* 2020. <https://doi.org/10.1515/joc-2020-0012> (<https://doi.org/10.1515/joc-2020-0012>) [Epub ahead of print].
81. Eid, MMA, Houssien, FMAM, Rashed, ANZ, Mohammed, AE-NA. Performance enhancement of transceiver system based inter satellite optical wireless channel (IS-OWC) for ultra long distances. *J Opt Commun* 2020. <https://doi.org/10.1515/joc-2020-0216> (<https://doi.org/10.1515/joc-2020-0216>) [Epub ahead of print].
82. Eid, MMA, Rashed, ANZ, El-din, ES. Simulation performance signature evolution of optical inter satellite links based booster EDFA and receiver preamplifiers. *J Opt Commun* 2020;67:564–73. <https://doi.org/10.1515/joc-2020-0190> (<https://doi.org/10.1515/joc-2020-0190>).
83. Eid, MMA, Rashed, ANZ, El-gammal, EM. Influence of dense wavelength division multiplexing (DWDM) technique on the low earth orbit intersatellite systems performance. *J Opt Commun* 2020. <https://doi.org/10.1515/joc-2020-0188> (<https://doi.org/10.1515/joc-2020-0188>) [Epub ahead of print].
84. Eid, MMA, Rashed, ANZ, Bulbul, AAM, Podder, E. Mono rectangular core photonic crystal fiber (MRC-PCF) for skin and blood cancer detection. *Plasmonics J* 2020. <https://doi.org/10.1007/s11468-020-01334-0> (<https://doi.org/10.1007/s11468-020-01334-0>) [Epub ahead of print].
85. Eid, MMA, Seliem, AS, Rashed, ANZ, Mohammed, AENA, Ali, MY, Abaza, SS. High speed pulse generators with electro-optic modulators based on different bit sequence for the digital fiber optic communication links. *Indones J Electr Eng Comput Sci* 2021;21:957–67. <https://doi.org/10.11591/ijeecs.v21.i2.pp957-967> (<https://doi.org/10.11591/ijeecs.v21.i2.pp957-967>).
86. Eid, MMA, Seliem, AS, Rashed, ANZ, Mohammed, AENA, Ali, MY, Abaza, SS. The key management of direct/external modulation semiconductor laser response systems for relative intensity noise control. *Indones J Electr Eng Comput Sci* 2021;21:968–77. <https://doi.org/10.11591/ijeecs.v21.i2.pp968-977> (<https://doi.org/10.11591/ijeecs.v21.i2.pp968-977>).

87. Eid, MMA, Seliem, AS, Rashed, ANZ, Mohammed, AENA, Ali, MY, Abaza, SS. Duobinary modulation/predistortion techniques effects on high bit rate radio over fiber systems. *Indones J Electr Eng Comput Sci* 2021;21:978–86. <https://doi.org/10.11591/ijeecs.v21.i2.pp978-986> (<https://doi.org/10.11591/ijeecs.v21.i2.pp978-986>).
88. Alatwi, AM, Rashed, ANZ. A pulse amplitude modulation scheme based on in-line semiconductor optical amplifiers (SOAs) for optical soliton systems. *Indones J Electr Eng Comput Sci* 2021;21:1014–21. <https://doi.org/10.11591/ijeecs.v21.i2.pp1014-1021> (<https://doi.org/10.11591/ijeecs.v21.i2.pp1014-1021>).
89. Eid, MMA, Rashed, ANZ, El-Meadawy, S, Habib, MA. Best selected optical fibers with wavelength multiplexing techniques for minimum bit error rates. *J Opt Commun* 2020. <https://doi.org/10.1515/joc-2020-0239> (<https://doi.org/10.1515/joc-2020-0239>) [Epub ahead of print].
90. Alatwi, AM, Rashed, ANZ, Abd El-Aziz, IA. High speed modulated wavelength division optical fiber transmission systems performance signature. *TELKOMNIKA* 2021;19:380–9. <https://doi.org/10.12928/TELKOMNIKA.v19i2.16871> (<https://doi.org/10.12928/TELKOMNIKA.v19i2.16871>).
91. Eid, MMA, Rashed, ANZ, El-gammal, EM, Delwar, TS, Ryu, JY. The influence of electrical filters with sequence generators on optical ISL performance evolution with suitable data rates. *J Opt Commun* 2020. <https://doi.org/10.1515/joc-2020-0257> (<https://doi.org/10.1515/joc-2020-0257>) [Epub ahead of print].
92. Alatwi, AM, Rashed, ANZ, Parvez, AHMS, Paul, BK, Ahmed, K. Beam divergence and operating wavelength bands effects on free space optics communication channels in local access networks. *J Opt Commun* 2020. <https://doi.org/10.1515/joc-2019-0276> (<https://doi.org/10.1515/joc-2019-0276>) [Epub ahead of print].
93. Shafkat, A, Rashed, ANZ, El-Hageen, HM, Alatwi, AM. The effects of adding different adhesive layers with a microstructure fiber sensor based on surface plasmon resonance: a numerical study. *Plasmonics J* 2021. <https://doi.org/10.1007/s11468-020-01352-y> (<https://doi.org/10.1007/s11468-020-01352-y>) [Epub ahead of print].
94. Eid, MMA, Rashed, ANZ. Fiber optic propagation problems and signal bandwidth measurements under high temperature and high dopant germanium ratios. *J Opt Commun* 2020;54:165–75. <https://doi.org/10.1515/joc-2020-0278> (<https://doi.org/10.1515/joc-2020-0278>).
95. Eid, MMA, Rashed, ANZ. Simulative and analytical methods of bidirectional EDFA amplifiers in optical communication links in the optimum case. *J Opt Commun* 2020. <https://doi.org/10.1515/joc-2020-0193> (<https://doi.org/10.1515/joc-2020-0193>) [Epub ahead of print].
96. Eid, MMA, Shehata, E, Rashed, ANZ. Cascaded stages of parametric optical fiber amplifiers with Raman fiber amplifiers for upgrading of telecommunication networks through optical wireless communication channel. *J Opt Commun* 2020. <https://doi.org/10.1515/joc-2020-0279> (<https://doi.org/10.1515/joc-2020-0279>) [Epub ahead of print].

97. Eid, MMA, Mohammed, AENA, Rashed, ANZ. Simulative study on the cascaded stages of traveling wave semiconductor optical amplifiers based multiplexing schemes for fiber optic systems improvement. *J Opt Commun* 2020. <https://doi.org/10.1515/joc-2020-0281> (<https://doi.org/10.1515/joc-2020-0281>) [Epub ahead of print].
98. Parvin, T, Ahmed, K, Alatwi, AM, Rashed, ANZ. Differential optical absorption spectroscopy based refractive index sensor for cancer cell detection. *Opt Rev* 2021;32:1120–35. <https://doi.org/10.1007/s10043-021-00644-w> (<https://doi.org/10.1007/s10043-021-00644-w>).
99. Eid, MMA, Said, SM, Rashed, ANZ. Gain/noise figure spectra of average power model Raman optical amplifiers in coarse wavelength multiplexed systems. *J Opt Commun* 2020;45:765–77. <https://doi.org/10.1515/joc-2020-0289> (<https://doi.org/10.1515/joc-2020-0289>).
100. Eid, MMA, Rashed, ANZ, Ahammad, MS, Paul, BK, Ahmed, K. The effects of Tx./Rx. pointing errors on the performance efficiency of local area optical wireless communication networks. *J Opt Commun* 2020. <https://doi.org/10.1515/joc-2019-0256> (<https://doi.org/10.1515/joc-2019-0256>).
101. Eid, MMA, El-Hamid, HSA, Rashed, ANZ. High-speed fiber system capacity with bidirectional Er-Yb CDFs based on differential phase shift keying (DPSK) modulation technique. *J Opt Commun* 2020. <https://doi.org/10.1515/joc-2021-0001> (<https://doi.org/10.1515/joc-2021-0001>).
102. Eid, MMA, Ibrahim, A, Rashed, ANZ. In line and post erbium-doped fiber amplifiers with ideal dispersion compensation fiber Bragg grating for upgrading optical access networks. *J Opt Commun* 2020. <https://doi.org/10.1515/joc-2020-0306> (<https://doi.org/10.1515/joc-2020-0306>).
103. Tahhan, SR, Taha, RM. Mercedes Benz logo based plasmon resonance PCF sensor. *Sens Bio-Sens Res* 2022;35:100468. <https://doi.org/10.1016/j.sbsr.2021.100468> (<https://doi.org/10.1016/j.sbsr.2021.100468>).
104. Tahhan, SR, Atieh, A, Hasan, M, Hall, T. Characterization and experimental verification of actively mode-locked erbium doped fiber laser utilizing ring cavity. *TM – Tech Mess* 2020;87:535–41. <https://doi.org/10.1515/teme-2020-0003> (<https://doi.org/10.1515/teme-2020-0003>).
105. Tahhan, SR, Abass, AK, Ali, MH. Characteristics of chirped fiber bragg grating dispersion compensator utilizing two apodization profiles. *J Commun* 2018;13:108–13. <https://doi.org/10.12720/jcm.13.3.108-113> (<https://doi.org/10.12720/jcm.13.3.108-113>).
106. Tahhan, SR, Atieh, A, Ali, MH, Hasan, M, Abass, AK, Hall, T. Characteristics of actively mode-locked erbium doped fiber laser utilizing ring cavity. In: *2019 IEEE Jordan International Joint Conference on Electrical Engineering and Information Technology (JEEIT)*. Amman, Jordan; 2019:840–4 pp. [10.1109/JEEIT.2019.8717483](https://doi.org/10.1109/JEEIT.2019.8717483) (<https://doi.org/10.1109/JEEIT.2019.8717483>)

107. Fadil, EA, Abass, AK, Tahhan, SR. Secure WDM-free space optical communication system based optical chaotic. *Opt Quant Electron* 2022;54:477. <https://doi.org/10.1007/s11082-022-03870-x> (<https://doi.org/10.1007/s11082-022-03870-x>).
108. Tahhan, SR, Mohammed, MF, Moosa, AA, Atieh, A. WDM ROF OFDM/QAM system for wireless PON. In: *2021 ieee jordan international joint conference on electrical engineering and information technology (JEEIT)*. Amman, Jordan; 2021:164–9 pp. [10.1109/JEEIT53412.2021.9634158](https://doi.org/10.1109/JEEIT53412.2021.9634158) (<https://doi.org/10.1109/JEEIT53412.2021.9634158>)
109. Tahhan, SR, Ghazai, AJ, Alwan, IM, Ali, MH. Investigation of the characteristics of high-resistivity silica based hybrid porous core photonic crystal fiber for terahertz wave guidance. *Dig J Nanomater Biostructures* 2019;14:831–41.
110. Singh, M, Malhotra, J. Performance comparison of different modulation schemes in high-speed MDM based radio over FSO transmission link under the effect of atmospheric turbulence using aperture averaging. *Wireless Pers Commun* 2020;111:825–42. <https://doi.org/10.1007/s11277-019-06886-x> (<https://doi.org/10.1007/s11277-019-06886-x>).
111. Singh, M, Malhotra, J. Modeling and performance analysis of 400 gbps CO-OFDM based inter-satellite optical wireless communication (IsOWC) system incorporating polarization division multiplexing with enhanced detection. *Wireless Pers Commun* 2020;111:495–511. <https://doi.org/10.1007/s11277-019-06870-5> (<https://doi.org/10.1007/s11277-019-06870-5>).
112. Singh, M, Malhotra, J. Performance comparison of 2×20 gbps-40 GHz OFDM based RoFSO transmission link incorporating MDM of hermite Gaussian modes using different modulation schemes. *Wireless Pers Commun* 2020;110:699–711. <https://doi.org/10.1007/s11277-019-06750-y> (<https://doi.org/10.1007/s11277-019-06750-y>).
113. Singh, M, Malhotra, J. Performance investigation of high-speed FSO transmission system under the influence of different atmospheric conditions incorporating 3-D orthogonal modulation scheme. *Opt Quant Electron* 2019;51:285. <https://doi.org/10.1007/s11082-019-1998-2> (<https://doi.org/10.1007/s11082-019-1998-2>).
114. Singh, M, Malhotra, J. 4×20 Gbit/s-40 GHz OFDM based Radio over FSO transmission link incorporating hybrid wavelength division multiplexing-mode division multiplexing of LG and HG modes with enhanced detection. *Optoelectron Adv Mater Rapid Commun* 2020;14:233–43.
115. Singh, M, Malhotra, J. 40 Gbit/s-80 GHz hybrid MDM-OFDM-Multibeam based RoFSO transmission link under the effect of adverse weather conditions with enhanced detection. *Optoelectron Adv Mater Rapid Commun* 2019;14:146–53.
116. Al-Khaffaf, DAJ, Hujjjo, HSR. High data rate optical wireless communication system using millimeter wave and optical phase modulation. *ARPJ Eng Appl Sci* 2018;13:9086–92.
117. Al-Khaffaf, DAJ, Alshimaysawe, IA. Miniaturised tri-band microstrip patch antenna design for radio and millimetre waves of 5G devices. *Indones J Electr Eng Comput Sci* 2021;21:1594–601. <https://doi.org/10.11591/ijeecs.v21.i3.pp1594-1601>

(<https://doi.org/10.11591/ijeecs.v21.i3.pp1594-1601>) .

118. Al-Khaffaf, DAJ, Alsahlany, AM. A cloud VLC access point design for 5G and beyond. *Opt Quant Electron* 2021;53:472–81. <https://doi.org/10.1007/s11082-021-03132-2>

(<https://doi.org/10.1007/s11082-021-03132-2>) .

119. Rashed, ANZ. High reliability optical interconnections for short range applications in high speed optical communication systems. *J Opt Laser Technol* 2013;48:302–8.

<https://doi.org/10.1016/j.optlastec.2012.10.038> (<https://doi.org/10.1016/j.optlastec.2012.10.038>) .

120. Rashed, ANZ. High performance photonic devices for multiplexing/demultiplexing applications in multi band operating regions. *J Comput Theor Nanosci* 2012;9:522–31.

<https://doi.org/10.1166/jctn.2012.2055> (<https://doi.org/10.1166/jctn.2012.2055>) .

121. Rashed, ANZ, Sharshar, HA. Analysis of transmission line feed method for transparent conductor oxide materials based optical microstrip patch antennas design.

Optoelectron Adv Mater, Rapid Commun 2012;6:980–7.

122. Rashed, ANZ, Metwae'e, MA. Operation performance characteristics of vertical cavity surface emitting lasers (VCSELs) under high thermal neutrons irradiated fields. *J Russ Laser Res* 2013;34:1–8.

<https://doi.org/10.1007/s10946-013-9317-z>

(<https://doi.org/10.1007/s10946-013-9317-z>) .

123. Rashed, ANZ. Optical fiber communication cables systems performance under harmful gamma irradiation and thermal environment effects. *IET Commun* 2013;7:448–

55. <https://doi.org/10.1049/iet-com.2012.0313> (<https://doi.org/10.1049/iet-com.2012.0313>) .

124. Rashed, ANZ, Sharshar, H. Performance evaluation of short range underwater optical wireless communications for different ocean water types. *Wirel Pers Commun J*

2013;72:693–708. <https://doi.org/10.1007/s11277-013-1037-8> ([https://doi.org/10.1007/s11277-013-](https://doi.org/10.1007/s11277-013-1037-8)

1037-8) .

125. Daher, MG, Jaroszewicz, Z, Zyoud, SH, Panda, A, Ahammad, SKH, Abd-Elnaby, M, et al.. Design of a novel detector based on photonic crystal nanostructure for ultra high performance detection of cells with diabetes. *Opt Quant Electron* 2022;54:701.

<https://doi.org/10.1007/s11082-022-04093-w> (<https://doi.org/10.1007/s11082-022-04093-w>) .

126. Rashed, ANZ, El-halawany, MME. Transmission characteristics evaluation under bad weather conditions in optical wireless links with different optical transmission

windows. *Wireless Pers Commun* 2013;71:1577–95. [https://doi.org/10.1007/s11277-012-](https://doi.org/10.1007/s11277-012-0893-y)

[0893-y](https://doi.org/10.1007/s11277-012-0893-y) (<https://doi.org/10.1007/s11277-012-0893-y>) .

Received: 2022-08-26

Accepted: 2022-11-08

Published Online: 2022-12-08

© 2022 Walter de Gruyter GmbH, Berlin/Boston

— or —

PDF 30,00 €

From the journal



Journal of Optical Communications

Downloaded on 8.12.2023 from

<https://www.degruyter.com/document/doi/10.1515/joc-2022-0217/html?lang=en>



INTERNATIONAL JOURNAL OF CREATIVE RESEARCH THOUGHTS (IJCRT)

An International Open Access, Peer-reviewed, Refereed Journal

Intelligent Accident Prevention And Detection System

Abdul Azeem¹, M. Ramesh², P. Leela Krishna³, N. Srinivas Reddy⁴, Sk. Sameer Sai⁵

¹Assistant Professor, ^{2,3,4,5} UG Students

Department of ECE, Andhra Loyola Institute of Engineering and Technology, Vijayawada

Abstract: The usage of vehicles has greatly increased in modern times. Since more people are driving, there is more traffic, which has led to an increase in traffic accidents. Accidents are occurring more frequently now. Every hour, there are about 17 accidents. Due to the lack of immediate preventive measures and immediate preventive and safety facilities, this damages the property and results in human life loss.

Our project's primary goal is to prevent accidents that result from driver intoxication, sudden sleepiness, Rash driving, and engine overheating. However, even in the unlikely event that an accident results from a different cause, the used electronic devices will be able to communicate a victim's precise location to emergency personnel and send out spontaneous messages. Many car accidents are caused by driving too fast, driving while intoxicated or fatigued, driving recklessly or rashly, and breaking the law.

While cars greatly reduce the amount of time we spend traveling, they also raise the possibility of an accident occurring. To reduce this risk, we can apply extra sophisticated technologies. We are using sensors, electronic modules, and a microcontroller unit in our project. This supports us in providing accident prevention, recognizes the accident if it happens despite the precautions, and alerts the ambulance service.

Keywords: Accelerometer, GSM Module, GPS module, Ultrasonic sensor.

I. INTRODUCTION

These hypothetical situations are probably going to become reality within the next couple of years because technological advancements have occurred so quickly. A microcontroller or application-specific integrated circuit is a component of embedded systems or electronic systems that are used to run a particular, dedicated application. It works along with the other parts of the system to accomplish a general function. This project is implemented with the aid of such an embedded processor, which primarily contributes to preventing the loss of human lives as a result of accidents. There are various reasons why accidents happen, but one of the main causes is driver irresponsibility. This project's major goal is to lessen traffic-related injuries by doing more to avoid accidents. The sufferer should always be saved and treated as quickly as possible after an accident.

II. LITERATURE SURVEY

Although there are many research works on online/intelligent accident prevention and detection system, here in this chapter we have critically analyzed and summarized several research works and projects, which are more recent and relevant, and similar to the project. This literature survey will logically explain the system.

1. Accident-Avoidance System Using IR Transmitter

This method is said to try to prevent accidents by determining the driver's state, or whether the driver is feeling drowsy or not in a fit state to operate a vehicle. This technology offers a very effective means of reducing such incidences because tiredness is a significant contributor to accidents. Even though the system offers a means of preventing accidents brought on by tiredness, there may be other causes that are not identified, and since the system does not offer damage detection and notification of emergency contacts, this could be a significant disadvantage.

2. Accident Detection & Alert System

In this paper, a system with an HDy Copilot, an Android app with integrated multimodal warning dissemination for accident detection, was proposed. A DENM alert, as well as SMS and audio calls to the emergency number, are sent to all adjacent vehicles when an accident is detected. But, the main issue remained the same: smartphone breakage or signal loss, which renders the system useless.

3. Accident Alert System using Face Recognition

According to this paper, the major causes of road accidents are inattention, drowsiness, and drunk driving. The system will give a false alarm if the driver has a medical condition or blinks at an abnormal rate despite not being drowsy. In the worst-case scenario, the driver is involved in an accident, and the system fails to detect the impact and notify the appropriate authorities. Finally, because the system constantly monitors the driver, it consumes power and drains the power supply. As a result of not being able to identify the actual accident scenario, we rejected the idea of incorporating face recognition into our system because it would be costly, power-consuming, and inefficient.

4. An efficient vehicle accident detection using sensor technology

They have demonstrated a system in this that uses MEMS sensors to identify accidents and send the information as input to the controller for processing. To examine journey time and traffic flow for various time frames, this calculation can be kept. This study suggests a method that would be effective and simple to use, but it doesn't offer a switch or other device to guard against a false alarm.

5. Smart Vehicle Accident Detection and Alarming System Using a Smartphone

They claim that smartphones are now a need of modern life, and this study consequently suggests a gadget that uses a smartphone to detect whether a mishap involving a smartphone's sensors has taken place. For this device to function properly, there must always be an internet connection. With cell phones, which are now an everyday requirement in modern life, the approach utilized in this study can provide systematic results and protect the driver's safety. As the smartphone's sensors occasionally potentially offer inaccurate information, this system also includes a switch that the driver could deploy in the event of inaccurate readings. This system's functional downside may be that it requires a constant internet connection, which may not be viable in remote locations. The system might malfunction in such a circumstance.

6. Accident Detection and Alert System

They suggested a system in which car accidents are one of the most common causes of fatalities. the time interval between an accident and the dispatch the availability of emergency medical care at the scene of the accident is essential to accident survival rates. The vehicle will have an accident detection and messaging system installed, which will be useful in the event of an accident because hospitals, police, and emergency contacts may be notified right away. The system operates with the aid of GSM and GPS. They proposed a system in which one of the most frequent causes of fatalities is automobile accidents. the period between a crash and a dispatch For accident survival rates to be high, emergency medical care must be accessible at the location of the event. The car will be equipped with an accident detection and messaging system, which will be helpful in the event of an accident because it might alert the hospital, police, and other emergency contacts immediately away. The use of GSM and GPS allows the system to function

II. PROBLEM STATEMENT

Based on the distance between the vehicles, the existing model used an Infrared sensor for prevention. In this model, when the distance between the cars is very close, the threshold levels automatically increase and the infrared rays are transformed into electrical signals. which will recognize the occurrence of the accident and notify the public by sending SMS messages over GSM to certain phone numbers and sharing its location via GPS. The IR sensor was the sole preventive discussed in this paper. These IR sensors have many drawbacks, including the inability to function in sunlight due to the infrared rays and also it does not provide any preventive methods for the prevention of accidents.

III. PROPOSED MODEL

By utilizing an alcohol sensor, an eye blink sensor, an ultrasonic sensor, a seat belt sensor, a DHT11 sensor, and an ADXL 335 accelerometer for detection, we have added five preventative measures to the model. We use an MQ3 alcohol sensor, and if the driver is drunk means that we apply some quantity of alcohol to the sensor then the threshold value goes high, it will automatically shut off the engine and Seat belt sensor, it acts as a switch when we press the seatbelt sensor the engine will start otherwise it does not allow to start the engine. DHT11 sensor is used to identify heat in the engine as a prototype we checked the room temperature, if the temperature is high it gives a warning to the driver. Eye blink sensor for determining whether the driver is sleepy. If the eye is closed for longer than 4 seconds, an automatic warning will sound., and an ADXL 335 accelerometer is used to determine the accidents. When an accident has occurred send it will automatically SMS messages to nearby hospitals and family members, sharing the location of the event.

IV. SYSTEM ARCHITECTURE

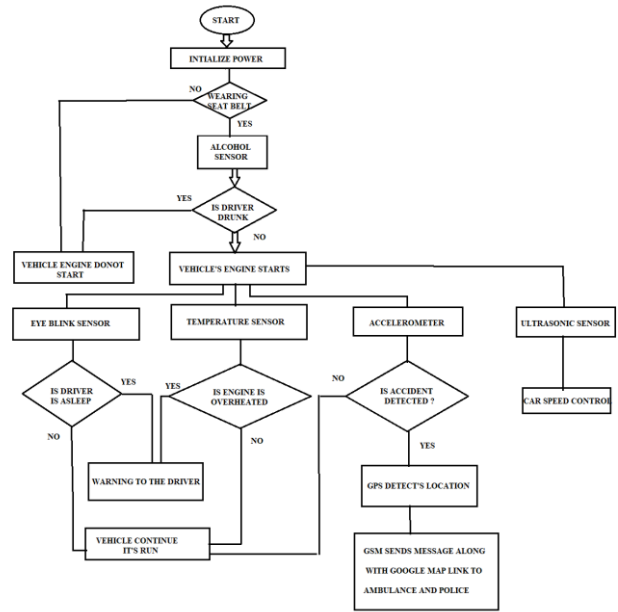


FIG 1: ARCHITECTURE

V. BLOCK DIAGRAM

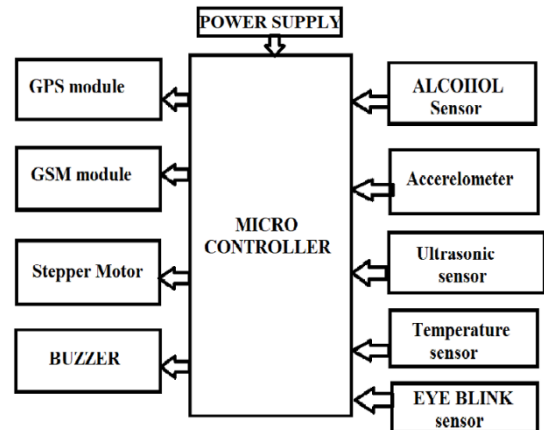


FIG 2: BLOCK DIAGRAM

VI. ALGORITHM

1. Start
2. The system is initially powered by the appropriate amount of power supply.
3. .Later, the system checks to see if the driver is wearing a seatbelt; if so, the engine will turn on; otherwise, the engine will never start.
4. The alcohol sensor in the car determines if the driver is intoxicated or not when the engine starts. When a driver is too intoxicated, the device issues a warning and the car's engine shuts off.
5. If no alcohol was detected, the vehicle starts or continues to run normally.
6. Eye blink sensors detect whether the driver is drowsy or not. If the driver falls asleep, the system alerts him with an alarm and a red light alert. A continuous temperature sensor detects engine heat and, if the engine is overheated, the driver receives a red light alert or continues to drive.
7. As a prototype engine, we used a stepper motor. We also proposed vehicle-to-vehicle communication using an ultrasonic sensor. If the car is very close to the system, the engine will automatically slow down.
8. If an accident occurs, the accelerometer detects it and sends the signal to the microcontroller for further processing.
9. The GPS module determines the location, and the GSM module sends a message with the latitude, longitude, and a link to Google Maps to ambulance and police emergency numbers.
10. When the system is activated, an AT mega processor is used to conduct all of the prevention, detection, and reporting functions.

VII. Hardware Setup

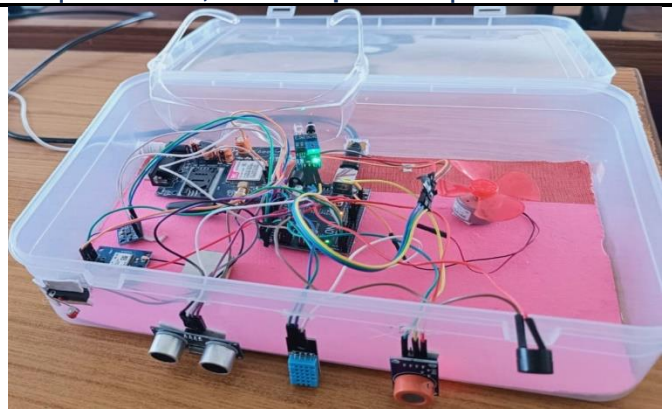
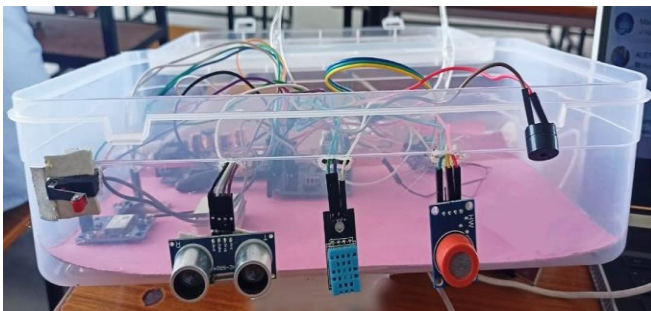


FIG.3: -HARDWARE KITS

VIII. RESULTS

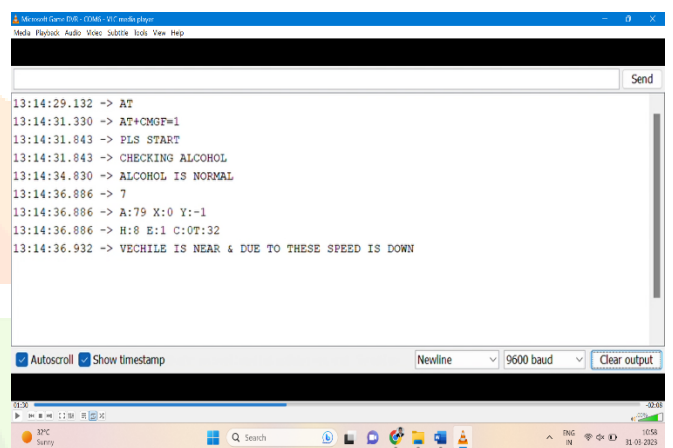


Fig 4: Results recorded in Serial Monitor

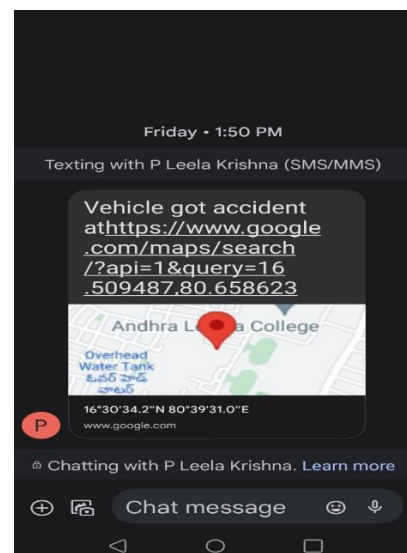


Fig 5: Message sent when the accident is detected

IX. CONCLUSION

The primary goal of our project is to prevent accidents caused by drunk driving, falling asleep suddenly (drowsy), Rash driving, and overheating engines. Vehicle to vehicle communication we are using ultrasonic sensor if the vehicle is very near it will automatically slowdowns the engine, if an accident occurs due to another cause, an accelerometer will be used to detect the collision and a customized GSM module will be used to send out spontaneous messages and GPS, for example.

X. REFERENCES

1. Miss. Priyanka M. Sankpal, Prof. P. P. More "Accident-Avoidance System Using IR Transmitter ", IJRASET, Volume 5 Issue IV, April 2017 v
2. Prashant Kapi, Shubham Patane, Arul Shalom A, "Accident Detection & Alert System", IEEE, 2018 Bruno Fernandes, Vitor Gomes, Joaquim Ferreira, and Arnaldo Oliveira, "Mobile Application for Automatic Accident Detection and Multimodal Alert", IEEE, 2015
3. Mr. Sikaianan, Mr. Karthala, Dr. Kartheeban, R.M.Priyadarshani, K. Anithadevi, "Accident Alert System using Face Recognition", IEEE, 2019
4. P. Kaliuga Lakshmi, Tithingman, "An efficient vehicle accident detection using sensor technology", 2016
5. Adnan Bin Faiz, Ahmed Imtiaz, Maphumulo Chowdhury, "Smart Vehicle Accident Detection and Alarming System Using a Smartphone", International Conference on Computer & Information Engineering, 2015
6. T Kalyani, S Monika, B Naresh, Mahindra Nucha, "Accident Detection and Alert System", 2019
7. Naji Taaib Said Al Wadhahi, Shaik Mazhar-Hussain, Kamaluddin Mohammad Yosof, Shaik Ashfaq Hussain, Ajay Vikram Singh "Accidents Detection and Prevention System to reduce Traffic Hazards using IR Sensors", IEEE 2018.





INTERNATIONAL JOURNAL OF CREATIVE RESEARCH THOUGHTS (IJCRT)

An International Open Access, Peer-reviewed, Refereed Journal

Iot Based Smart City Monitoring System

Abdul Azeem¹, N Hima vardhini², B.S.N.S.Jahnavi³, K.Supriya⁴

¹Professor, ^{2,3,4,5} UG Students

Department of ECE, Andhra Loyola Institute of Engineering and Technology, Vijayawada

Abstract: A Smart city is the future goal to have cleaner and better amenities for the safety and security purpose of society. Here network-level performance analysis and implementation of the smart city using Internet of Things. The world is about to witness revolution in the communication and technology after internet in the form of IoT. They will be used to create smart environment for people globally. IoT has become one of those things that has slowly made its way into almost all aspects of all sectors and made more suited for the changing world. Almost anything can be made better with the wonders of IoT and many of times at relatively lower prices. The use of IoT products will be the great advantage to boost the mission of setting up the smart cities in the India. The paper focuses on the aspects of applying IoT Products of various smart solutions to set up the smart cities in the India. Some of the domains have been discussed in the paper. Also, the projected solutions that can be implemented is showcased. The key to set up the smart cities successfully is depend upon how the technology has been integrated to solve the complex problems being faced by the society at large.

Our project's primary goal is to provide a solution to the problem in a smart way using Internet of Things. In smart city there are lot of parameters that are very challenged to solve, Here the considered parameters are Air quality, weather monitoring, waste management, parking slots. This paper mainly helps the people with smart solutions.

Keywords: Esp32s microcontroller, IoT Technology, servo motors, Blynk platform, Wi-Fi mode user.

I. INTRODUCTION

A smart city is a technologically modern urban area that uses different types of electronic methods and sensors to collect specific data. Information gained from that data is used to manage assets, resources and services efficiently, in return, that data is used to improve operations across the city. This smart environment is created by connecting devices to the internet and making them interact. The intended smart city IoT system can monitor the principle parameters and provides the solution to cope up with urban challenges and to improve the quality of life of citizens.

II. LITERATURE SURVEY

Although there are many research works on smart city monitoring system, here in this chapter we have critically analyzed and summarized several research works and projects, which are more recent and relevant and similar to project. This literature survey will logically explain the system.

1. Application of IoT products in smart cities of India

This paper focuses on the aspects of applying IoT products for various smart solutions for setting up smart cities in india. Some of the domains have been discussed in the paper. Also, the projected solutions that can be implemented have been showcased. The key to set up smart city successfully depends upon how the technology has been integrated to solve the complex problems being faced by the society at large.

2. A smart IoT platform for Air Quality Monitoring

In this paper it mainly concentrates on the Air quality monitoring. The AirQ platform is a smart and cost effective solution for air quality monitoring. The AirQ device is portable, low-cost and provides real-time and location-specific air quality data. It supports wireless data communication technologies including WIFI,4G,Bluetooth, LoRa, etc. Here they have developed an ontology based backend to support data management and the implementation of smart data analytics algorithms.

3. Research on the Application of Face Recognition Technology in public service of smart city

This paper proposes a novel application method of face recognition technology. This method is based on a variety of information science and technology, big data technology and so on, Which improves the accuracy of traditional face recognition technology. The research results show that this method can not only effectively give full play to the application of face recognition technology in all aspects of smart city public service, but also improve the modernization and intelligence of smart city public service.

4. IoT and Mobility in Smart Cities

This article refers to the smart sensors technologies in IoT mobility and their implementations. The challenges encountered in citizens privacy and protection of their personal data as well as the possibility of IoT use for the prevention of pedestrians accidents. The installation of smart sensors and cameras provide specialists with a p[le]ntiful of data. The results of their usage can be studied and bring conclusions regarding a more appropriate architecture of public transport networks, control of traffic violations and vehicle tracking through platforms that could observe traffic using the consolidation of information selected by smart sensors.

5. Monitoring of Electric Buses within an Urban Smart City Environment

A practical experience on monitoring the data generated by electric buses is presented, focusing on energy consumption, charge and state of the batteries. The work is carried out in the framework of a global smart city strategy developed by the H2020 smart city Lighthouse STARDUST project. The crucial role of the data collections and transmission from electric buses has become evident in this work, so the adopted solutions are covered in detail. various key factors for the practical implementation of the necessary communication infrastructure together with the monitoring system architecture are also discussed.

6. Research on the Application of Electronic Technology of Internet of Things in Smart City

In order to realize the ap[cityplication of the electronic technology of the Internet of things in the smart city, this paper puts forward a novel application method of the electronic technology of the Internet of things, Which integrates a variety of advanced science and technology, wireless radio frequency technology and cloud computing technology, and can accurately analyze the construction process of smart city. The research results show that this method can fundamentally realize the application of the electronic technology of the Internet of Things in the smart city, give full play to the advantages of the electronic technology of the Internet of things, and promote the construction process of the smart city.

II. PROBLEM STATEMENT

In a city when we explore the things we can observe many parameters that have some problems. Those are eradicated with the help of Internet of things which monitors the data continuously and uploads the data at user friendly. For the considered parameters there are certain solutions with the help of Internet of things. The pollution is very high that it should be monitored and when it comes to waste management the level of the bin is filled every time it creates health issues to people and animals near by. Due to heavy traffic there is a parking problems. These few issues are overcome with the help of advanced technology into its complex infrastructure.

III. MOTIVATION

When we discuss Internet of Things, we refer to smart devices that are connected to one other or the internet usually collecting and sending data over the internet. The main goal of a smart city is to optimize city functions and promote economic growth while also improving the quality of life for citizens by using smart technologies and data analysis. The value lies in how these technology is used rather than simply how much technology is available. The creation of this smart environment is when the devices that are connected to the internet interact with other connected devices. This smart environment is created by connecting devices to the internet and making them interact. The rapid growth of urban populations has given rise to concerns about the effective management of the city. Notable concerns arising from rapid urbanization include: waste management, human health concerns, traffic congestion, inappropriate infrastructure and similar public safety issues. The survey estimates that half of the world's population lives in cities, and to avoid a resultant crisis, new ways of managing and operating the city are necessary. This has given rise to discussions of the smart city, especially as this trend is expected to continue for years.

We embed sophisticated sensors and chips in devices to make them smarter, these devices in turn start transmitting data out of which we extract the data that may be valuable in knowing how these things or devices work together. Simply stating the what we talked about till now, the data that is collected from the sensors is sent to the cloud. So, the cloud we talk about here is a huge, interconnected network of powerful servers that performs services for businesses

and for people Almost anything can be made better with the wonders of IoT and many a times at relatively lower prices.

IV. SYSTEM ARCHITECTURE

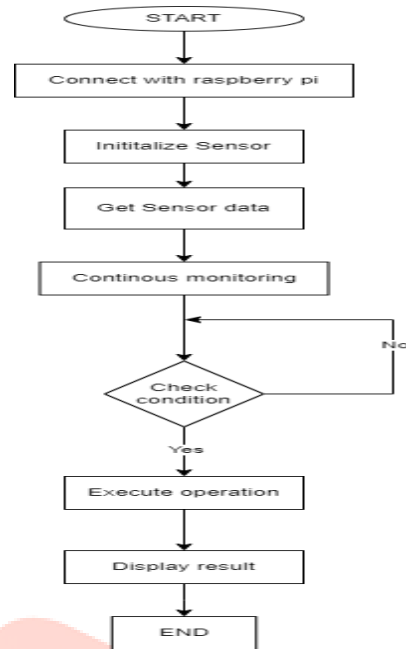


FIG 1: ARCHITECTURE

V. BLOCK DIAGRAM

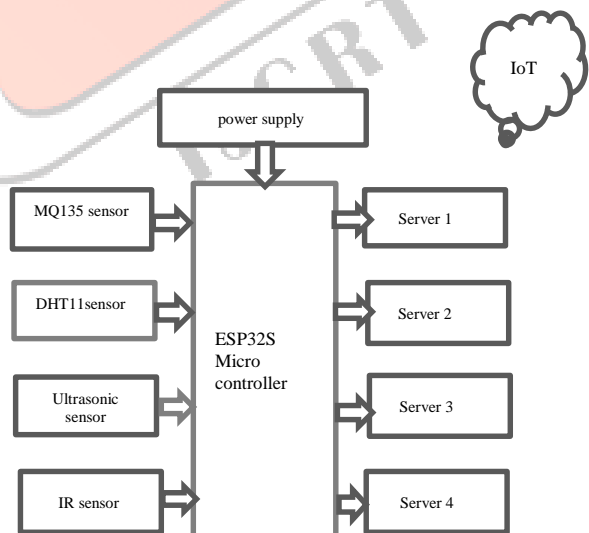


FIG 2: BLOCK DIAGRAM

VII. CONCLUSION

VI. ALGORITHM

1. Start
2. INITIALLY, the system is powered with the proper amount of power supply.
3. Here the buck converter is used to supply the equal amount of power among the all sensors.
4. When we place the system in the public polluted content then we can monitor the harmful content present in the air at IoT platform.
5. Like wise we can monitor the weather conditions on blynk platform.
6. when it comes to waste management, when the bin level is full then it notifies to the municipal authorities to registered account.
7. The parking slots are observed to park the vehicle and when it times of payment the gates are opened according to their payment actions.
8. The gates are opened only if the payment is made properly with correct amount. Here servo motors are taken as gates.
9. Once the system is on, it continuously checks all the sensors by the help of microcontroller (Esp32s) in order to perform all the monitoring, detection and report .

Hardware system

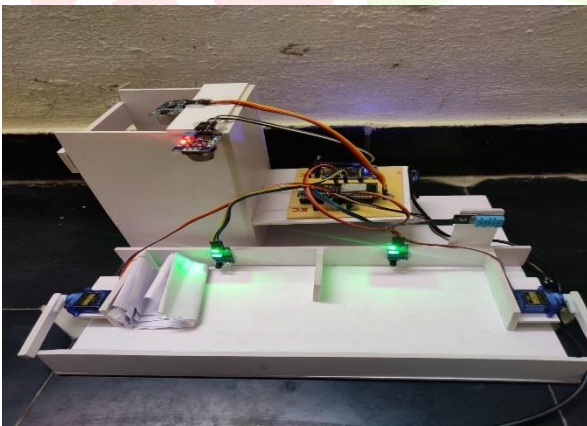


FIG.3:-HARDWARE KITS

The primary goal of our project is to monitor and detect the problem causing and to overcome malpractices with help of the sensors and advanced IoT technology. In addition to using different sensors and methodologies there is a chance to solve the problems in a smarter way. There is also a huge chance to extend this type of projects to further higher levels.

VIII. REFERENCES

1. Mohammad N, Muhammad S, Bashar A, Khan MA (2019) Formal analysis of human assisted smart city emergency services. IEEE Access
2. Zhao L, Sun W, Shi Y, Liu J (2018) Optimal placement of cloudlets for access delay minimization in SDN-based internet of things networks. IEEE Internet Things J 5(2):1334–1344
3. Li W, Song H, Zeng F (2017) Policy-based secure and trustworthy sensing for internet of things in smart cities. IEEE Internet Things J 5(2):716–723
4. Ullah R, Faheem Y, Kim BS (2017) Energy and congestion aware routing metric for smart grid AMI networks in smart city. IEEE Access 5:13799–13810
5. Deebak BD, Al-Turjman F, Aloqaily M, Alfandi O (2019) An authentic-based privacy preservation protocol for smart e-healthcare systems in IoT. IEEE Access 7:135632–135649
6. Tahir Y, Yang S, McCann J (2017) BRPL: backpressure rpl for high-throughput and mobile IoTs. IEEE Trans Mob Comput 17(1):29–43
7. Benayache A, Bilami A, Barkat S, Lorenz P, Taleb H (2019) MsM: A microservice middleware for smart WSN-based IoT application. J NetWComputAppl 144:138–154
8. Farooq MS, Riaz S, Abid A, Abid K, Naeem MA (2019) A survey on the role of IoT in agriculture for the implementation of smart farming. IEEE Access 7:156237–156271
9. Ray PP, Thapa N, Dash D (2019) Implementation and performance analysis of interoperable and heterogeneous IoT-edge gateway for pervasive wellness care. IEEE Trans Consumer Electron 65(4)
10. Rajpoot SC, Pandey C, Rajpoot PS et al (2021) A dynamic SUGPDS model for faults detection and isolation of underground power cable based on detection and isolation algorithm and smart sensors. J Electr Eng Technol 16:1799–1819



Downl FDF

Browse My Settings Help

Access provided by: Andhra Loyola Institute of Engineering-VIJAYAWADA

Sign Out

Access provided by: Andhra Loyola Institute of Engineering-VIJAYAWADA

Sign Out

All



ADVANCED SEARCH

Conferences > 2022 International Conference... ?

Hardware Implementation of Forest Fire Detection System using Deep Learning Architectures

Publisher: IEEE

Cite This

PDF

Mohammad Baig Mohammad ; N. Bhuvaneswari ; Ch. Pooja Koteswari ; V Bhavani Priya All Authors



49 Full Text Views

Alerts

Manage Content Alerts Add to Citation Alerts

Abstract

Abstract: Forests being called as lungs of earth play a very important role in maintaining a sustainable climate on the earth. They are instrumental in maintaining a quality eco-sy... [View more](#)

Document Sections

- 1. Introduction
- 2. Literature Survey
- 3. Proposed Method
- 4. Experimental Analysis
- 5. Conclusion

Show Full Outline

Authors

Figures

References

Keywords

Metrics

More Like This

Metadata

Abstract:

Forests being called as lungs of earth play a very important role in maintaining a sustainable climate on the earth. They are instrumental in maintaining a quality eco-system by filtering the air, preventing soil erosion and help to maintain diverse life on the earth. Forest fires are a matter of concern in terms of economic growth and ecological damage and damage to animals and human life. Forest fires contribute to global warming and imbalances the climate on the earth making the lives harder. Early detection of forest fire can prevent the damage by a great extent. Sensor based and Image processing-based methods have been widely used followed by machine learning techniques to process the sensor data and detect the occurrence of forest fires. These methods are costly and difficult to install at different locations in the forest. As the dimensions of the forest area increases, the complexity of the system also increases. Deep Learning techniques such as variations of convolutional neural networks process image data and can provide an early warning about the occurrence of the fire. In the proposed system different pre trained deep neural network architectures such as Resnet 50, InceptionV3, GoogleNet, AlexNet, MobileNet have been employed using transfer learning approaches on two very important datasets namely Mendely dataset and Kaggle Datasets. The best performing architecture i.e Alexnet has been deployed on to Raspberry PI embedded hardware to work as a standalone module. The trained models have demonstrated a good accuracy of 99.45% on Mendely and 99.42 on Kaggle Datasets for Fire detection.

Published in: 2022 International Conference on Edge Computing and Applications (ICECAA)

Date of Conference: 13-15 October 2022

INSPEC Accession Number: 22240160

Date Added to IEEE Xplore: 08 November 2022

DOI: 10.1109/ICECAA55415.2022.9936371

ISBN Information:

Publisher: IEEE

IEEE websites place cookies on your device to give you the best user experience. By using our websites, you agree to the placement of these cookies. To learn more, read our [Privacy Policy](#).

Conference Location: Tamilnadu, India [Accept & Close](#)



Downl

PDF

Contents

1. Introduction

Forests being our lifeline; mankind relies on them for survival, clean air, medicines, food, and a range of environmental resources. A forest is a heavily vegetated area or a complex ecosystem that is rich in biodiversity and supports a diverse range of living organisms. They sustain the ground by avoiding soil erosion. The trees assist to keep the environment clean, which supports the forest's vegetation and animals. They are an important component of the ecosystem because they clean the air, cool it during the day, and act as excellent sound absorbers. A forest fire is indeed an uncontrolled fire as a result of combustion and heat from surface and ground fires. A large forest fire quickly spread through the upper branches of the trees before involving the shrubbery or the forest floor. As a result, violent blow-ups in forest fires are common, and they might start taking on the characteristics of a fire storm. Plant and animal extinctions, wildlife habitat devastation, depletion and loss of natural regeneration and reduction of forest cover are only a few of the major losses caused by forest fires. Warmer temperatures and drier conditions can aid in the spread of fires and make them more difficult to extinguish. Warmer, drier weather can aid in the spread of the mountain pine beetle and other insects that can weaken or kill trees, contributing to the accumulation of fuels in a forest. Increased drought and a longer fire season are boosting these increases in wildfire risk. An average annual 1 degree C temperature increase would increase the median burned area per year as much as 600 percent [11]. Sensor based approach for the early detection of forest fires is very popular. These systems require very accurate sensors to avoid false positives. Fire can be detected by using the amount of smoke. This smoke sensor readings used to measure the amount of smoke from the fire, and it could be compared with a threshold value and if it is beyond that value, it is considered as fire scenario. Using image processing, fire can also be detected. Fixing the CCTV camera in the vast forest field to detect the occurrence of fire by processing of these acquired images is not a cost effective solution. Machine learning and deep learning techniques are developed to aid signal processing tasks, with the added benefit of being generalizable to different problems. The signal processing way of solving a problem is optimum but it lacks generalizability. Machine learning techniques focus on the manual extraction of relevant features from the data, rank the features for better suitability and then applied to either regression or classification problem. Manual extraction of features is cumbersome and a tedious process. Deep learning architectures which are mainly modification of convolutional neural network are prepared with intermediate layers for automatic extraction of relevant features. Machine learning and deep learning techniques are used for variety of applications that involves prediction of events. Coupled with Computer vision, deep learning can be used for the early detection of forest fires. In this paper it is proposed to build an efficient deep neural network to detect the forest fires and deploy the high performance deep neural network on to Raspberry PI embedded hardware to make it act as a standalone module. Different pertained model architectures such as Resnet50, InceptionV3, GoogleNet, Alexnet etc., have been studied and best model has been deployed on the Raspberry PI hardware to act as a standalone module.

Authors	▼
Figures	▼
References	▼
Keywords	▼
Metrics	▼



Downl
PDF

More Like This

A Novel Fire Detection Method Based on Deep Neural Network and Image Processing
2022 2nd International Conference on Networking Systems of AI (INSAI)
Published: 2022

Fire Detection Using Image Processing Techniques with Convolutional Neural Networks
2019 International Seminar on Research of Information Technology and Intelligent Systems (ISRITI)
Published: 2019

Show More

IEEE Personal Account

CHANGE
USERNAME/PASSWORD

Purchase Details

PAYMENT OPTIONS
VIEW PURCHASED
DOCUMENTS

Profile Information

COMMUNICATIONS
PREFERENCES
PROFESSION AND
EDUCATION
TECHNICAL INTERESTS

Need Help?

US & CANADA: +1 800
678 4333
WORLDWIDE: +1 732
981 0060
CONTACT & SUPPORT

Follow



Accept & Close

A not-for-profit organization, IEEE is the world's largest technical professional organization dedicated to advancing technology for the benefit of humanity.



Downl

© Copyright 2023 IEEE - All rights reserved.

IEEE Account

- » Change Username/Password
- » Update Address

Purchase Details

- » Payment Options
- » Order History
- » View Purchased Documents

Profile Information

- » Communications Preferences
- » Profession and Education
- » Technical Interests

Need Help?

- » **US & Canada:** +1 800 678 4333
- » **Worldwide:** +1 732 981 0060
- » Contact & Support

[About IEEE Xplore](#) | [Contact Us](#) | [Help](#) | [Accessibility](#) | [Terms of Use](#) | [Nondiscrimination Policy](#) | [Sitemap](#) | [Privacy & Opting Out of Cookies](#)

A not-for-profit organization, IEEE is the world's largest technical professional organization dedicated to advancing technology for the benefit of humanity.

© Copyright 2023 IEEE - All rights reserved. Use of this web site signifies your agreement to the terms and conditions.

IEEE websites place cookies on your device to give you the best user experience. By using our websites, you agree to the placement of these cookies. To learn more, read our [Privacy Policy](#).

Accept & Close

Article

Experimental Investigation and Performance Characteristics of Francis Turbine with Different Guide Vane Openings in Hydro Distributed Generation Power Plants

Megavath Vijay Kumar ^{1,*}, T. Subba Reddy ², P. Sarala ³, P. Srinivasa Varma ⁴, Obbu Chandra Sekhar ⁵, Abdulrahman Babqi ⁶, Yasser Alharbi ⁶, Basem Alamri ^{6,*} and Ch. Rami Reddy ^{3,5}

¹ Department of Mechanical Engineering, Malla Reddy Engineering College, Maisammaguda, Secunderabad 500100, India

² Department of Mechanical Engineering, Andhra Loyola Institute of Engineering and Technology, Vijayawada 520008, India

³ Department of Electrical and Electronics Engineering, Malla Reddy Engineering College, Secunderabad 500100, India

⁴ Department of Electrical and Electronics Engineering, Koneru Lakshmaiah Education Foundation, Vaddeswaram 522502, India

⁵ Department of Electrical Engineering, National Institute of Technology, Srinagar 190006, India

⁶ Department of Electrical Engineering, College of Engineering, Taif University, P.O. Box 11099, Taif 21944, Saudi Arabia

* Correspondence: vijaykumar.084@mrec.ac.in (M.V.K.); b.alamri@tu.edu.sa (B.A.)



Citation: Vijay Kumar, M.; Reddy, T.S.; Sarala, P.; Varma, P.S.; Chandra Sekhar, O.; Babqi, A.; Alharbi, Y.; Alamri, B.; Reddy, C.R. Experimental Investigation and Performance Characteristics of Francis Turbine with Different Guide Vane Openings in Hydro Distributed Generation Power Plants. *Energies* **2022**, *15*, 6798. <https://doi.org/10.3390/en15186798>

Academic Editor: Chirag Trivedi

Received: 28 July 2022

Accepted: 10 September 2022

Published: 17 September 2022

Publisher's Note: MDPI stays neutral with regard to jurisdictional claims in published maps and institutional affiliations.



Copyright: © 2022 by the authors. Licensee MDPI, Basel, Switzerland. This article is an open access article distributed under the terms and conditions of the Creative Commons Attribution (CC BY) license (<https://creativecommons.org/licenses/by/4.0/>).

Abstract: This article presents a study on the performance characteristics of a Francis turbine operating with various guide vane openings to determine the best operating point based on unit quantities. The guide vane openings were specified based on the width between the vanes at their exit, i.e., 10 mm, 13 mm, 16 mm, and 19 mm. The performance characteristic curves of the Francis turbine—head versus speed, torque versus speed, discharge versus speed, and efficiency versus speed—were obtained at various input power and guide vane openings. From these data, unit curves were plotted and the corresponding best efficiency points were obtained. The highest efficiency of 50.25% was obtained at a guide vane opening of 19 mm. The values of head, discharge, speed, and output power at BEP were 7.84 m, 13.55 lps, 1250 rpm, and 524 W, respectively.

Keywords: renewable energy; Francis turbine; guide vane opening; performances & unit quantities

1. Introduction

The motive energy found in water is known as hydropower. By using hydroelectric power plants, it can be transformed into electrical energy. All that is needed is a constant inflow of water and a height difference between the location where the water is found and the location where it can be released. The potential for hydropower is impressive. It is a free resource that is perpetually renewable and nonpolluting. Hydropower plays a significant role in the multipurpose use of water resources in many situations. The destructive forces of flood flows and the energy of normal flows are harnessed by hydropower projects to provide useful electrical energy. The economy of different power sources is reflected in the cost of electricity. Countries that have a large proportion of hydropower in their systems have the lowest tariffs. Upgrading existing hydropower plants is frequently more economical than building new ones. High initial investment-prone hydropower plants hold the substantial potential of uprating at the time of renovation, thereby making upgrading proposals cost-effective [1]. Due to the rising demand for electricity, hydropower plants are now more necessary than ever. Therefore, modernizing hydroelectric facilities is crucial to meeting public demand.

1.1. Selection of Turbines

The head under which a turbine is going to be operated gives guidance for the selection of the type of turbine. The range of operation of each type is shown concerning the head (H) and specific speed (ns) [2]. The total power to be installed must be known and the number of machines then are chosen by economic consideration of load factor, the extent of water storage, if any, cost of powerhouse, the convenience of operation, and maintenance. Once the output per machine has been decided, information must be obtained concerning the suitable speeds for which the generator can be constructed economically. From these data, the coupling power, effective head, and speed of the turbine are known. Hence, the specific speed is calculated. From the previous table, the suitable turbine is selected. Since the speed of the generator can generally be selected from several suitable numbers of pairs of poles, the appropriate specific speed is not limited to one value. In many cases, the overlap is considerably extended and the problem arises of selecting from two types of turbines, either of which could be used [3]. Here, knowledge of the advantages and disadvantages of each type will assist, especially concerning efficiency when running at part load. If the machine is required to operate for long periods of part loads, the Pelton turbine would be preferred to the Francis turbine. Similarly, if the choice lay between two Francis turbines, that with the lower specific speed would be more suitable, whereas if the choice lay between a Kaplan turbine or a propeller turbine or a Francis turbine with a high specific speed, the Kaplan turbine would be preferred. This is because of the flattest efficiency curve being obtained from the Kaplan turbine, followed by the Pelton turbine, the low-specific-speed Francis turbine, the high-specific-speed Francis turbine, and finally the propeller turbine, which has the most peaked form of the efficiency curve. It must not be assumed that the highest possible specific speed is always desirable [4,5].

1.2. Francis Turbine

Francis turbines can be built to handle a wide range of head and flow rates. This, combined with their high efficiency, has resulted in them being the most widely used turbine in the world. The Francis-type units have a head range of 20 m to 700 m, a specific speed of 60 to 400 rpm, and an output power ranging from a few kilowatts to one gigaton. Large Francis turbines are custom-built for each location to achieve the highest possible efficiency, typically exceeding 90% [6]. The water initially needs to enter the scroll (volute), which is an annular channel that surrounds the runner, and then flows between the stationary vanes and adjustable guide vanes, which provide the water with the best flow direction. It then enters the completely submerged runner, altering the momentum of the water and causing a reaction in the turbine. Water flows in a radial direction towards the center. The water is impinged upon by curved vanes on the runner. The guide vanes are configured in such a way that the energy of the water is largely converted into rotary motion, rather than being consumed by eddies and other undesirable flow phenomena that cause energy losses. The guide vanes are typically adjustable to provide some adaptability to variations in the water flow rate and turbine load. The Francis turbine's guide vanes are the elements that direct the flow of water [7]. The authors investigated flow parameters, such as flow angles at the runner's inlet and outlet, flow velocities, and guide vane angles, to derive flow characteristics. The goal was to analyze the pressure distribution and flow behavior to achieve the level of accuracy required for the concept design of a revitalized turbine. The obtained results are in good agreement with the on-site experiments, particularly for the characteristic curve [8].

For three different specific speed turbines, the authors predicted the accuracy and compared it to the model test results. It was demonstrated that the numerical model test presented in this investigation could predict important characteristics of the Francis turbine with high accuracy not only quantitatively but also qualitatively by comparing simulation results with model test results for pressure-fluctuation characteristics, efficiency characteristics, and cavitation characteristics. As a result, it was determined that numerical model testing would be a more realistic estimation tool for Francis turbine hydraulic

performance, contributing to cost reduction in the development of the Francis turbine [9]. The authors investigated Francis turbine guide vanes with pivoted support and an external control mechanism for converting pressure to kinetic energy and directing it to runner vanes. It has been discovered that increasing the clearance gap of the guide vane opening increases leakage, lowering energy conversion and turbine efficiency and resulting in a larger secondary vortex [10].

Many simulated results on hydroturbines have been conducted using various turbulence models to identify their performance parameters [11]. Three distinct turbulence models were explored in this work to measure the sensitivity of the model for the derivation of Francis hydroturbine performance characteristics. To evaluate the performance of the turbine, three different operating circumstances were chosen: part load, overload, and best efficiency point. The highest velocity fluctuation inside the Francis runner was anticipated by the model. The turbulence model can be used to capture the vortex rope that appears at the runner's output [12]. The influence of blade thickness on hydraulic performance was investigated numerically using six types of impellers with varied blade thicknesses that were integrated into the same pump to compare head and efficiency under design point [13]. The effect of clearance on the performance of a Francis turbine was investigated, and it was discovered that as transverse flow and loss increased, efficiency decreased significantly. When considering a specific degree of erosion, the pressure on both sides of the blade and at the outflow of the blade was precisely proportional to the erosion state [14–16]. The flow conditions in the runner inlet of a low-speed-number Francis turbine are found to be identical when a cascade with one guide vane between two flow channels is optimized [17].

Guide vane (GV) clearance gaps grow larger due to abrasive wear, which worsens the flow and reduces efficiency. In order to reduce potential consequences of an eroded guide vane on the performance of the turbine, this research evaluates several guide vane profiles. It is discovered that the pressure differential between the neighboring sides causes the clearance gap to create a leakage flow. A vortex filament is created when the leaky flow combines with the main flow and is forced within the runner [18]. The authors offer a methodology for the design, optimization, and additive manufacture of turbine blade rows and other components of highly stressed turbomachinery. The technique subsequently produces final geometries that have been suitably represented for additive manufacturing. A few aluminum prototypes of the newly improved turbine blade have been produced in order to undergo mechanical and fatigue testing [19]. The mechanical power turbine's torque varies with its size. With a peak value of 3249.7 Nm at pitch angle 17°, significant torque was obtained in the pitch angle range of 15–20°. As turbines grow in size and their pitch angle range increases, they will produce more power, reaching a maximum of 124,987.1 W or 125 kW [20]. The findings demonstrated that in operating conditions involving substantial flow rates, severe sand abrasion might be seen close to the blade head and outlet. In working conditions with low flow rates, there may be very minor abrasion found close to the blade flange. The runner is severely abraded and its effectiveness is lowered in proportion to the sediment concentration and sand diameter [21]. While the flow separation on the suction side close to the blade tip merges, the flow characteristics on the blade pressure side are often stable. The flow-separation phenomenon manifests itself more visibly with larger tip clearance. The tip leakage vortex, which is also a spatial three-dimensional spiral structure created by the entrainment effect of the tip leakage flow and main flow, becomes more pronounced as the tip clearance rises [22].

After detailed review of the literature, it was apparent that lots of research has been carried out on hydroturbines, but few studies have made an attempt at different guide vane openings and no literature was found on best operating point based on unit quantities. As such, the present work focuses the best operating point based on unit quantities by studying the performance characteristics of the Francis turbine at various input powers and guide vane openings.

2. Experimental Setup

2.1. Experimental Setup of Francis Turbine

The model Francis turbine available at Hydro Turbo Machines Lab was designed and built by Nilavalagan (1973) and was used for these experiments, as shown in Figures 1 and 2.

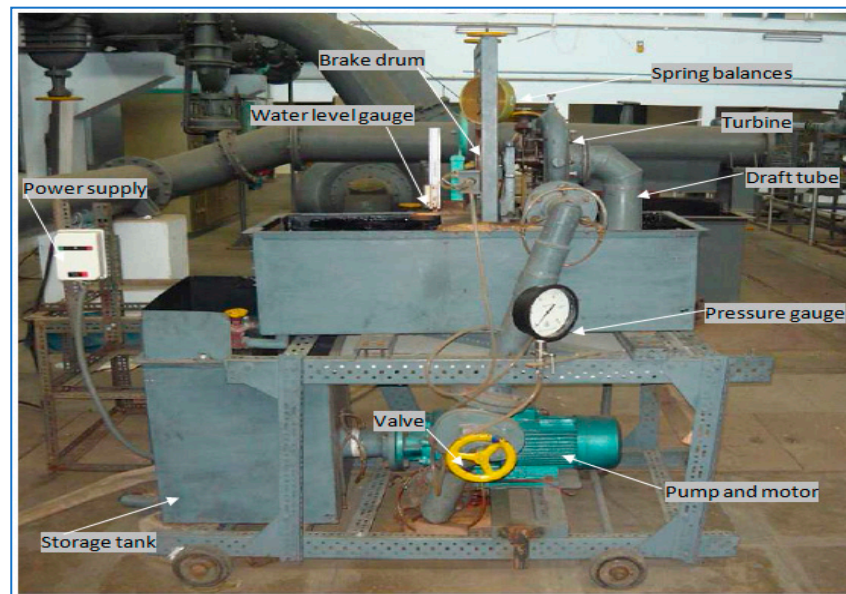


Figure 1. The Francis turbine test setup.

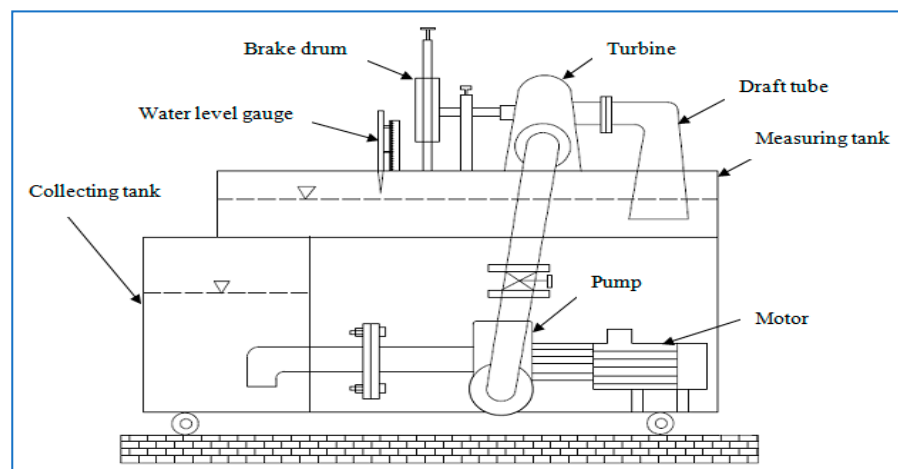


Figure 2. Schematic of Francis turbine test setup.

The Francis turbine is a machine that uses the energy of water and converts it into mechanical energy. Thus, it becomes the prime mover to run the electrical generators to produce electricity. The head is generated using a pump that draws water from the storage tank and supplies it to the inlet of the turbine. The torque generated by the turbine is measured using a brake drum. The water outlet flow of the turbine is sent to the measuring tank through the draft tube. The excess water from the measuring tank flows to the storage tank.

Four pressure tapings made near the inlet of the turbine were made to form a piezoring and were connected to a pressure gauge (range 0–2.5 kg/cm²). The tachometer was used to measure the speed (N) of the turbine. The turbine was loaded with the help of a brake drum connected to a loading belt. The tension in the belt on both sides of the brake drum was measured with spring balances. The load on the turbines was altered with the help of hand wheels connected to balances. The diameter of the brake drum was 225 mm

and the thickness of the belt 5 mm. At the back of the turbine casing, there is a guiding vane mechanism. The distance between the two successive guide vanes can be altered by rotating a hand wheel. The maximum distance between one guide vane's tip to another was measured using a vernier caliper. It was found to be 19 mm maximum.

2.2. Specification of the Instruments Required for Measuring

(a) Discharge

The discharge measurement in this experiment was done using a rectangular notch, shown in Figure 3, fitted in the measuring tank. The discharge formula found by the Indian Standard (IS: 9108-1979) was used and is discussed below.

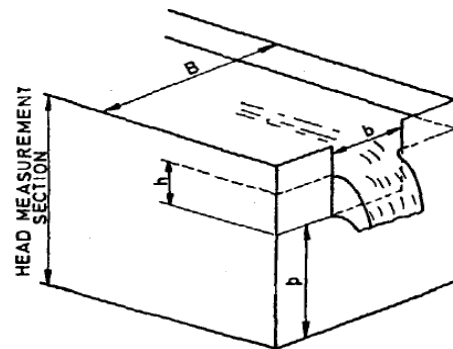


Figure 3. Rectangular notch.

The Kindsvater–Carter rectangular weir formula is

$$Q = C_e \frac{2}{3} \sqrt{2g} b_e h_e^{3/2} \quad (1)$$

where,

Q = discharge, m^3/sec

C_e = coefficient of discharge,

b_e = effective width, in mm, and

h_e = effective head in mm.

The coefficient of discharge was determined by experiment as a function of two variables from the formula:

$$C_e = f\left(\frac{b}{B}, \frac{h}{p}\right) \quad (2)$$

The effective width and head are defined by the equations:

$$b_e = b + k_b = b + 3.6 \quad (3)$$

$$h_e = h + k_h = h + 0.0012 \quad (4)$$

Which are experimentally determined quantities, in meters, which compensates for the combined effects of viscosity and surface tension.

From the value of b/B , formula for C_e can be written as

$$(b/B = 0.6): = 0.593 + 0.018 \quad (5)$$

The water-level gauge was used to measure the height of the water level in a rectangular notch. This water-level gauge was fixed with the scale. This gauge mechanism has a rotating device for making adjustments.

(b) Speed

The digital tachometer was used to measure the speed of the turbine. Its range is 0–5000 rpm. This tachometer is kept at the back of the brake drum to find the speed of the turbine.

(c) *Pressure*

A Bourdon tube pressure gauge was used to find the pressure at the inlet of the turbine. The pressure gauge range was 0 to 2.5 kg/cm².

(d) *Load*

The spring balance was used to find the loads applied on the brake drum. The spring-balance range was 10 kg × 50 gm and 20 kg × 100 gm.

2.3. Experimental Methodology

- Connect the supply-pump motor unit to 3 ph, 440 V, 30 A, electrical supply, with neutral and earth connection and ensure the correct direction of pump motor unit. Keep the gate closed before the pump is on. Later, press the green button of the supply-pump starter and then release. The guide vane distance is maintained at 19 mm initially for fully open guide vane position and altered to 16 mm, 13 mm, and 10 mm distance with the help of a hand wheel. For each of the above guide vane openings, the speed of the turbine is maintained initially at 1000, 1500, 2000, and 2500 rpm by adjusting the pump outlet valve. Later, the load is applied in steps of 250 g till the lowest possible speed at which the turbine can run continuously. For each corresponding set of readings, the pressure at the inlet of the turbine, speed, load on the brake drum, and head over notch are noted. Then, the gate valve is closed and the supply-water pump switched off.
- The performances of the turbine were calculated, i.e., discharge, head, torque, input power, output, efficiency, and unit quantities. Later, the performance characteristics of the turbine were plotted.

3. Results and Discussion

The best efficiency point of the Francis laboratory scale was found by operating the water pump at different guide vane openings. The performance characteristics were plotted for these conditions. For each water supply, the reading was obtained and respective characteristics curves plotted for four different guide vane openings. The guide vane openings were specified based on the width between the vanes at their exit, i.e., 10 mm, 13 mm, 16 mm, and 19 mm. For each water supply and respective guide vane opening, an experiment was conducted as per the procedure indicated in Section 2.3. Each experiment was repeated and performance curves for discharge versus speed, head versus speed, torque versus speed, and efficiency versus speed were plotted.

A polynomial curve fit was done for the two individual sets of readings that were repeated for the same experimental condition to check repeatability. Then, the two individual experimental results were merged as one single set and fitted as a polynomial curve. The correlation coefficient was found to be not less than 0.98. The respective polynomial equation for each of torque, discharge, and head with speed were substituted in the efficiency formula and corresponding efficiency was calculated.

3.1. Performance Characteristics of Francis Turbine

The performance characteristics of discharge versus speed, head versus speed, torque versus speed, and efficiency versus speed for 10 mm guide vane opening are shown in Figures 4–11. At lower input power, few points could be obtained. The turbine came to a halt at higher loads, but starting the turbine at higher power enables taking a large number of readings. The discharge appears to be less at high speeds compared to low speeds; this may be because the machine is vibrating and fluctuating while it is functioning.

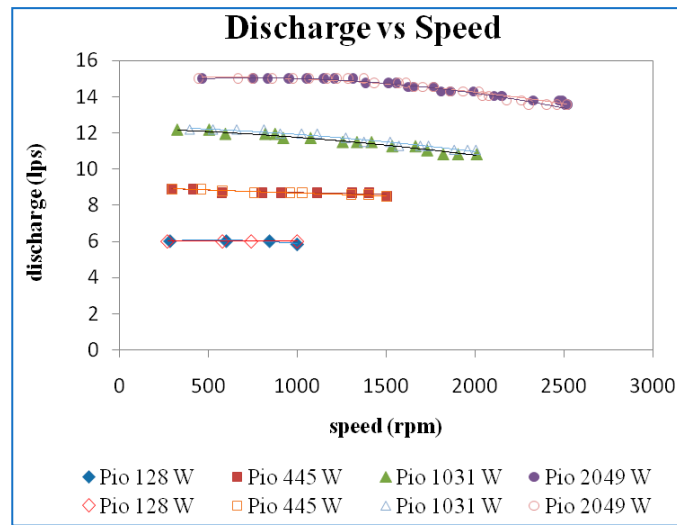


Figure 4. Discharge vs. speed at a guide vane opening of 10 mm.

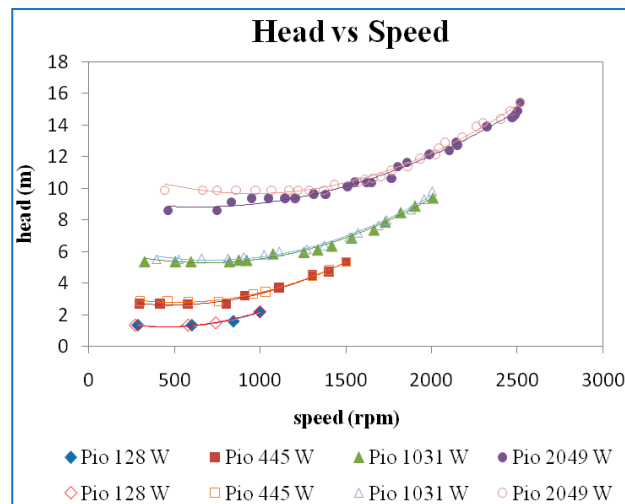


Figure 5. Head vs. speed at a guide vane opening of 10 mm.

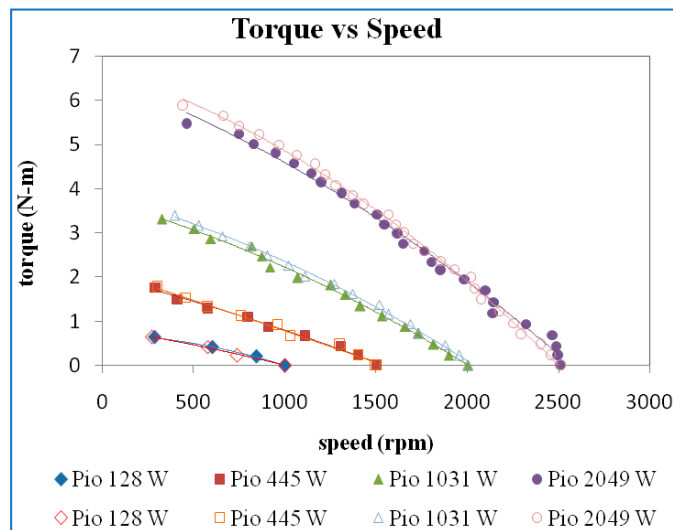


Figure 6. Torque vs. speed at a guide vane opening of 10 mm.

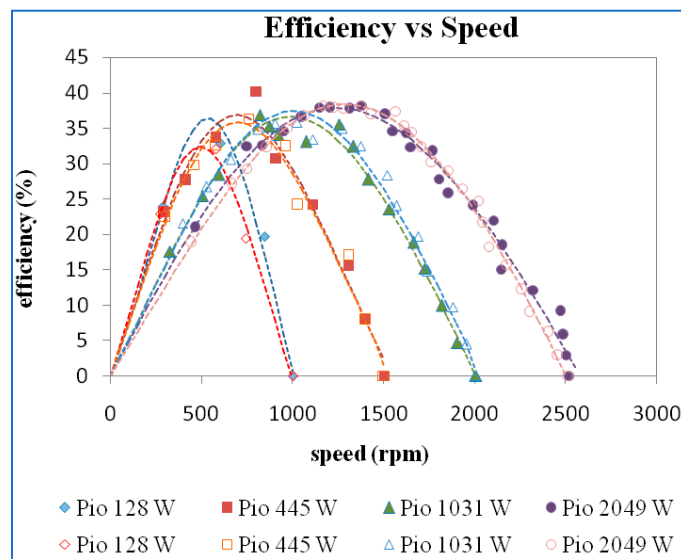


Figure 7. Efficiency vs. speed at a guide vane opening of 10 mm.

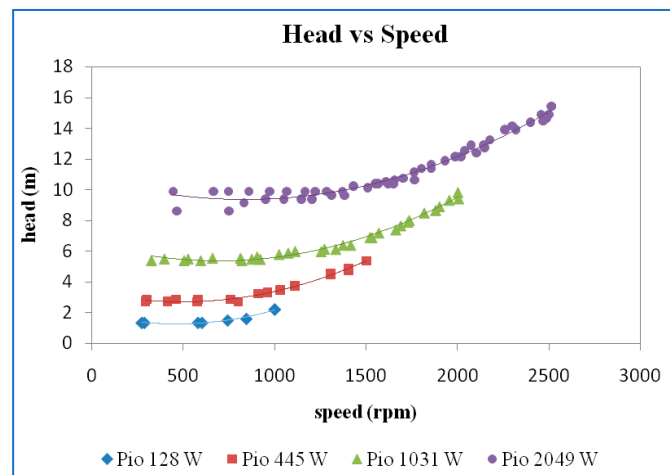


Figure 8. Head vs. speed at a guide vane opening of 10 mm.

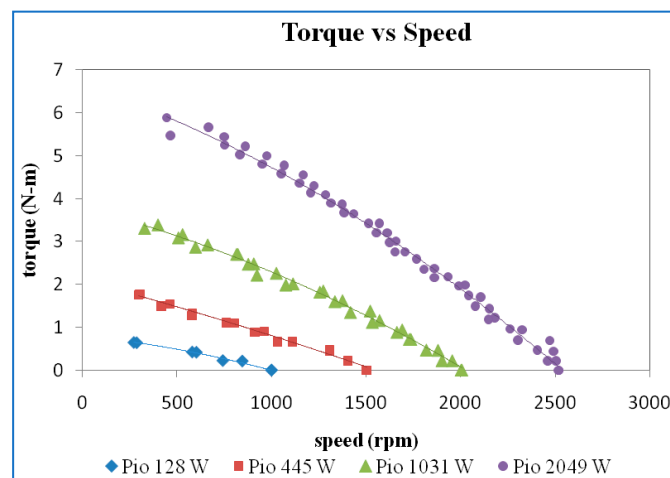


Figure 9. Torque vs. speed at a guide vane opening of 10 mm.

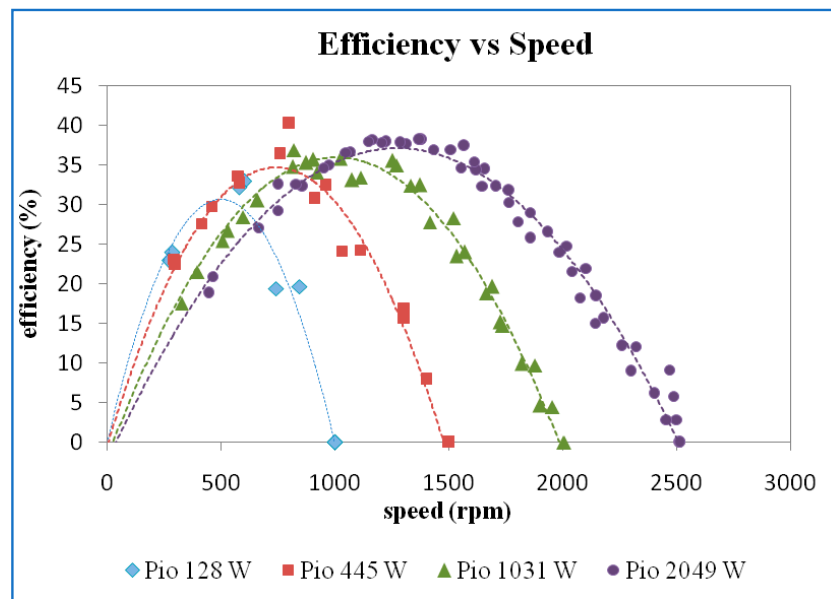


Figure 10. Efficiency vs. speed at a guide vane opening of 10 mm.

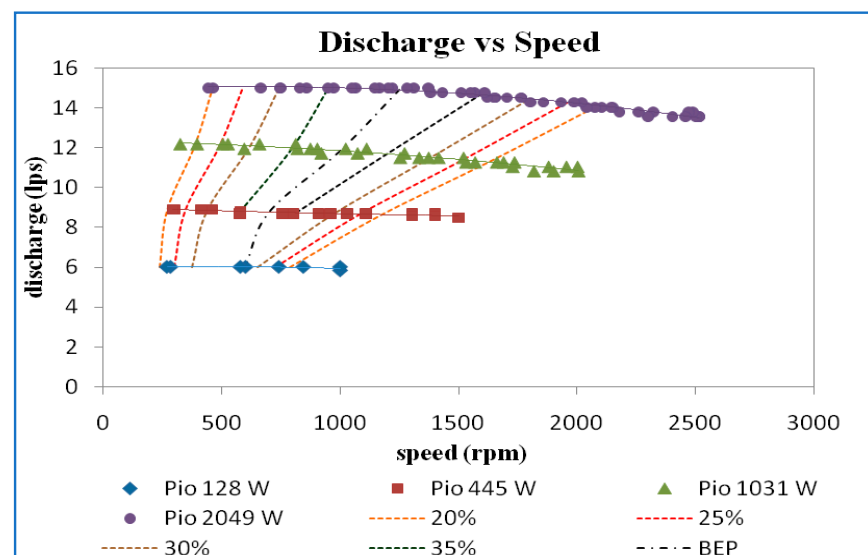


Figure 11. Discharge vs. speed and iso-efficiency line at 10 GVO.

Figure 5 shows the plot of the variation of the head concerning the speed for different power inputs. The head increases with an increase in the power inputs. The head is almost constant at lower speeds and then increases with speed. There is a slight increase in the head curves even during the lower speeds for the power input of 2049 (W). In this plot also, it may be observed that the repeatability of the readings is good.

A study of Figure 6 showing the plot of torque versus speed shows that at no load conditions, the speed of the turbine is about 2500 rpm for the power input of 2049 (W). This is the maximum speed that was achieved for the highest possible power input. The speed at no load came down to 2000 rpm, 1500 rpm, and 1000 rpm, respectively, as the input power was decreased. In fact, during the experiments, the input valve that changes the power input to the turbine was fixed based on the speed in the no-load condition. When a load is applied, the torque rises, increasing the frictional forces acting between the brake drum and the belt. This causes heat to be released, reducing speed. The repeatability of the readings can also be seen in the two sets plotted in Figure 6.

Efficiency versus speed for different power inputs is shown in Figure 7. It may be seen that higher maximum efficiency was obtained for higher inputs and efficiency increased

to a maximum then decreased as speed increased. This is because the output power is contributed by the torque and speed. The speed decreases with increases in torque; thereby, the overall output power increases, reaches a maximum, and then decreases. One can argue that the effect of input power may also contribute to the variation in efficiency. This is true, but only at higher speeds. The discharge and the head were almost constant at lower speeds, so the variation of input power becomes insignificant. That is the reason that the efficiency curves show the increasing and decreasing trend.

The two sets of points in Figures 4–7 indicate clearly that the results are repeatable and hence they were considered together and a single curve fitted for every value of input power.

Figure 8 shows the plot of the variation of the head concerning the speed for different power inputs. Trial 1 and trial 2 were combined and plotted as a single curve. It can be seen that head decreases with a decrease in the power inputs.

Figure 9 shows that when the load is applied, the torque increases the frictional forces acting between the brake drum and the belt increase and dissipate the energy in the form of heat; therefore, the speed comes down. The torque is increased by decreasing the speed.

The efficiency versus speed for different power inputs is shown in Figure 10. The higher maximum efficiency was obtained for higher input power. However, there is only a slight variation of maximum efficiency at 445 W, 1031 W, and 2049 W input power.

The iso-efficiency lines plotted on discharge versus speed curves are shown in Figure 11. From the efficiency curves, horizontal lines corresponding to efficiencies of 20%, 25%, 30%, 35%, and best efficiency point (BEP) were drawn and the speed and the discharge corresponding to the point where the efficiency curves intersect the horizontal iso-efficiency lines were noted and plotted, as shown in the above figure. It may be noted that the value of discharge and speed at maximum efficiency is 32%, 36%, 37%, and 38% at input power of 77 W, 243 W, 647 W, and 1414 W for guide vane opening of 10 mm.

The head versus speed curve shown in Figure 12 was obtained at a guide vane opening of 13 mm. The head is decreasing with decreasing the speed. When input power is more, the head seems to be more.

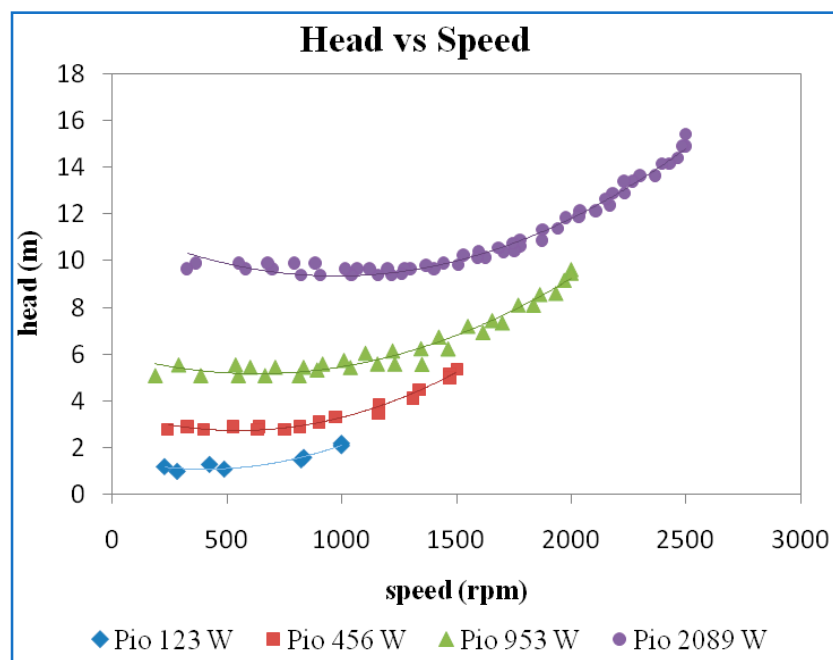


Figure 12. Head vs. speed at a guide vane opening of 13 mm.

From Figure 13, it may be seen that as speed decreases, the torque starts to increase when the load is applied to the brake drum. There is not much variation in these curves between guide vane openings of 13 mm and 10 mm, as seen in Figures 9 and 13.

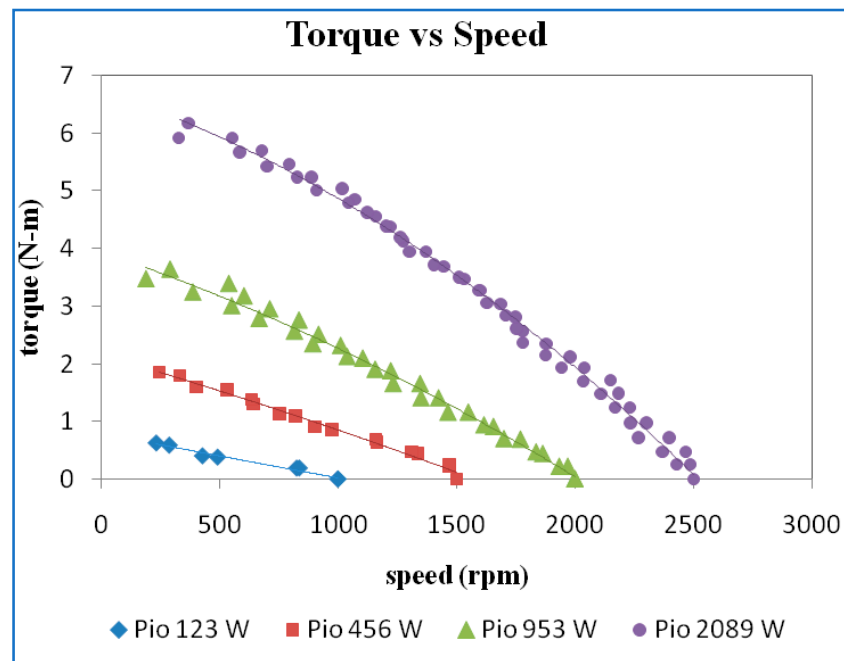


Figure 13. Torque vs. speed at a guide vane opening of 13 mm.

The maximum efficiency was observed at a power input of 953 W for a guide vane opening of 13 mm, as seen in Figure 14. At input power of 123 W, 456 W, and 953 W the maximum efficiency increases gradually, but at power input 2089 W it is decreased slightly due to the vibration, which leads to cavitations within the turbine.

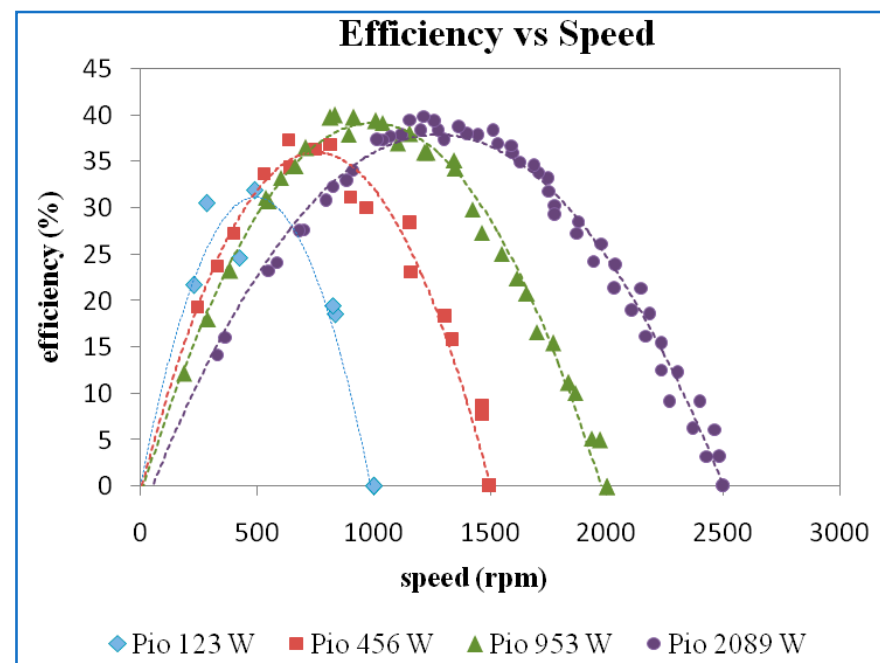


Figure 14. Efficiency vs. speed at a guide vane opening of 13 mm.

Figure 15 shows that the discharge is more or less constant at different input power. The iso-efficiency plot seems not much different between the guide vane openings of 10 mm and 13 mm. The values at best efficiency points are 33%, 37%, 40%, and 39%.

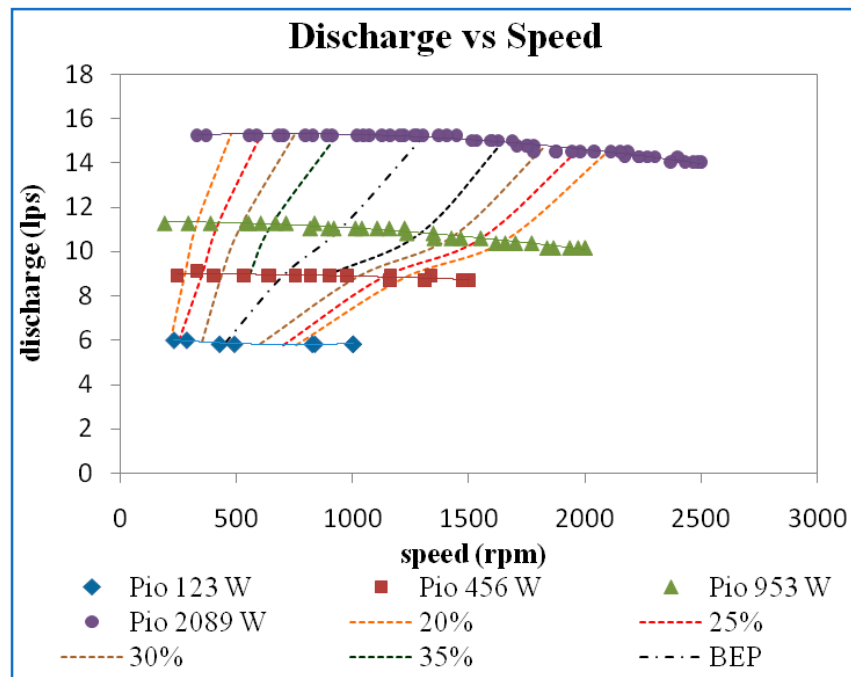


Figure 15. Discharge vs. speed and iso-efficiency line at 13 GVO.

The plot of the variation between the head and speed for different power input at 16 mm GVO is shown in Figure 16. The head decreases with decreasing power input. A notable variation may be observed at higher speeds.

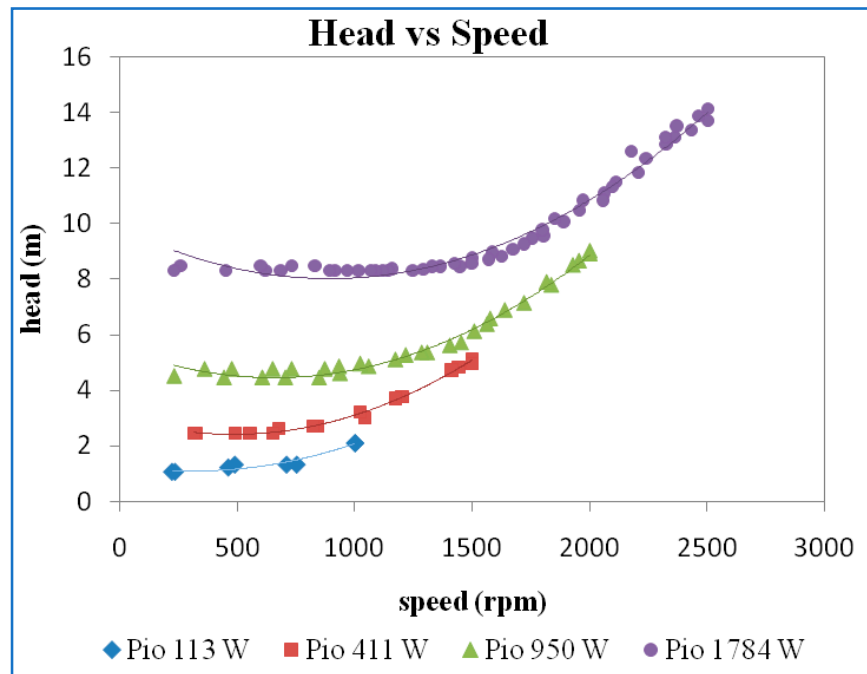


Figure 16. Head vs. speed at a guide vane opening of 16 mm.

From Figure 17, it may be concluded that at a GVO of 16 mm, when the torque increases the speed starts decreasing when the load is applied on the brake drum. There is not much variation from guide vane openings of 16 mm, 13 mm, and 10 mm.

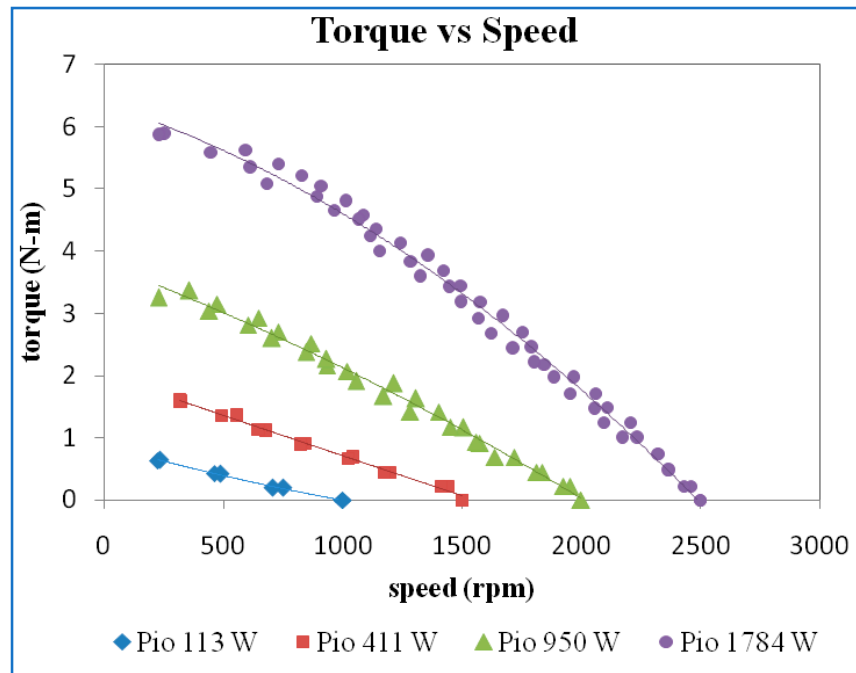


Figure 17. Torque vs. speed at a guide vane opening of 16 mm.

From Figure 18, it is observed that the maximum efficiency at 16 mm GVO was seen at a power input of 1784 W. The maximum efficiency decreases as input power is decreased. As there is an increase in guide vane opening, the efficiency improves compared to the low guide vane opening due to there being no impediment or vibration.

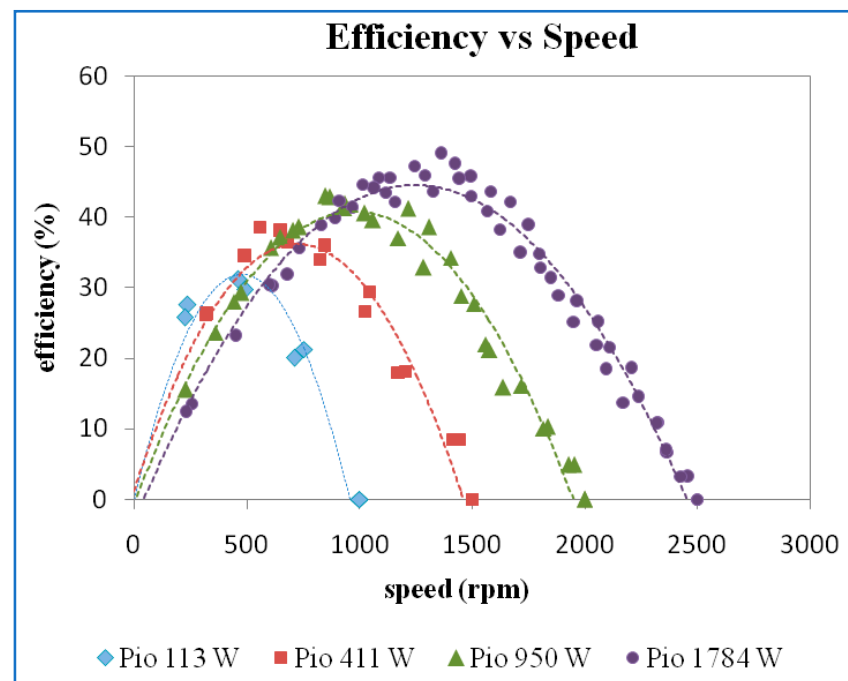


Figure 18. Efficiency vs. speed at a guide vane opening of 16 mm.

From Figure 19, it is seen that at 113 W power input, the discharge was constant. At other input power, the discharge was slightly decreased as speed increased at 16 mm GVO. The iso-efficiency lines plotted seem to be a straight line with different slopes. The discharge versus speed at BEP is 32%, 38%, 42%, and 46%.

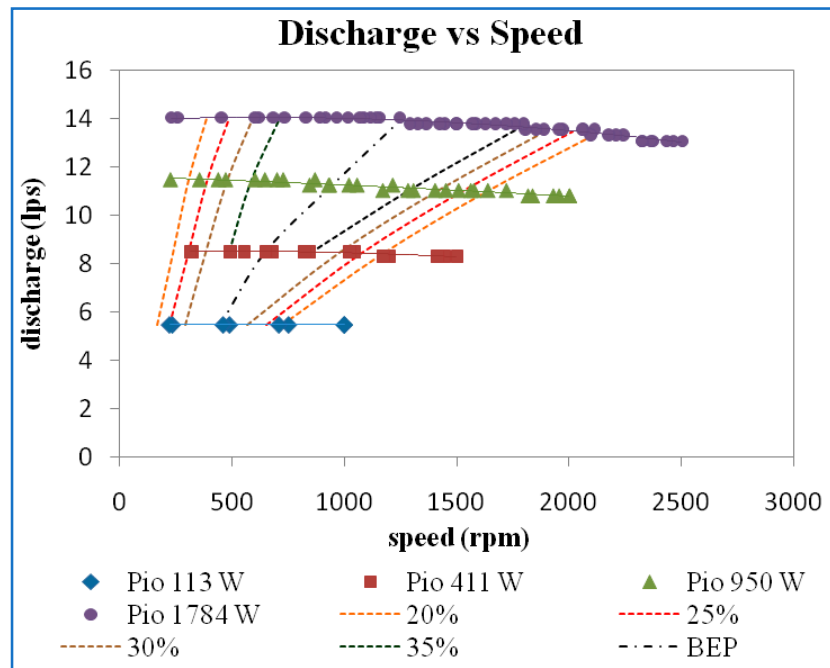


Figure 19. Discharge vs. speed and iso-efficiency line at 16 GVO.

Figure 20 shows the plot of the variation of head with respect to the speed for different power input at a GVO of 19 mm. The head increases with increase in the power input. There is a variation in the head curves at higher speed for all the four power inputs.

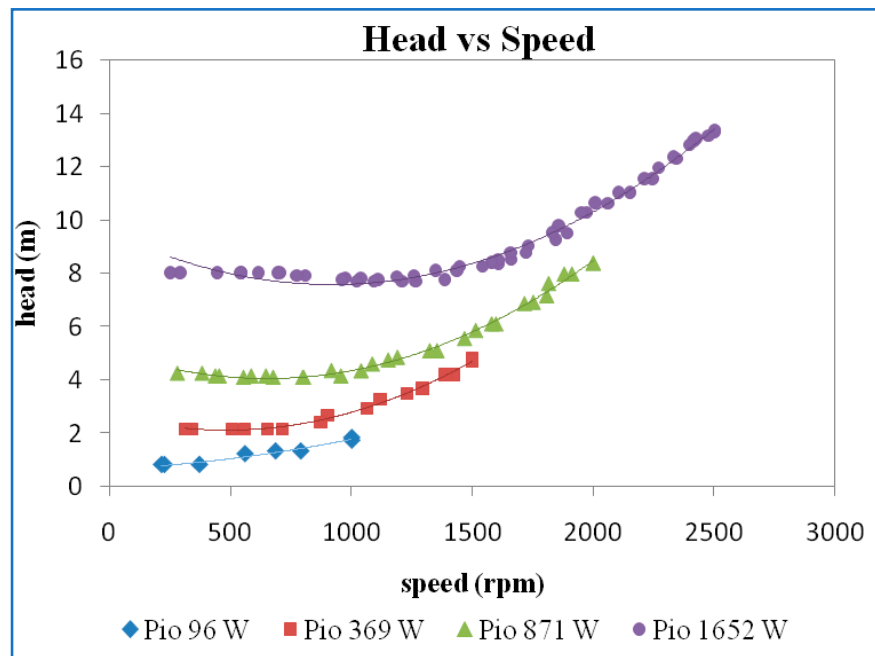


Figure 20. Head vs. speed at a guide vane opening of 19 mm.

According to Figure 21, when the load is applied the torque increases the frictional forces acting between the brake drum and the belt increases and dissipates the energy in the form of heat, and thus the speed comes down. The torque is increased with increased input power. There is a large variation in torque at 1652 W power input compared to other lower input power.

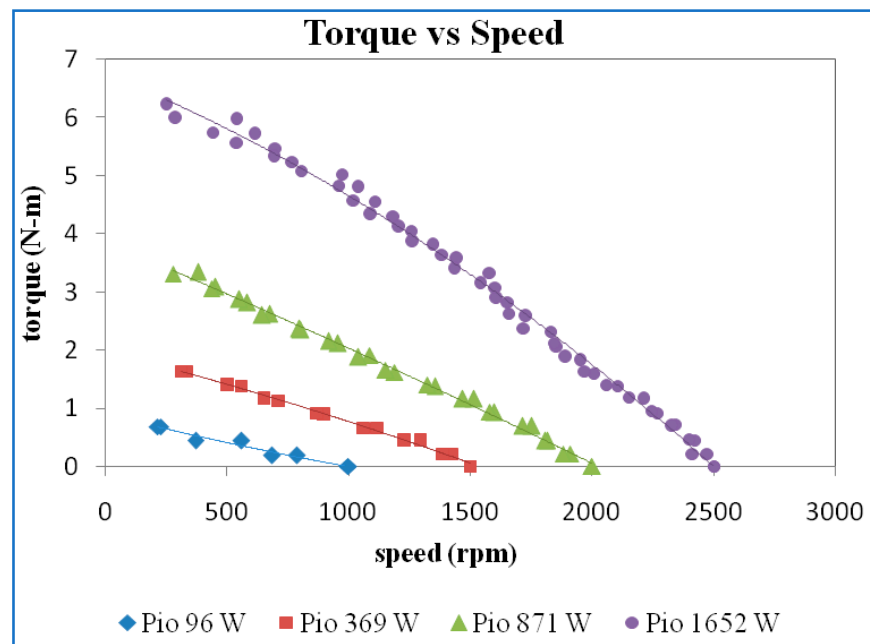


Figure 21. Torque vs. speed at a guide vane opening of 19 mm.

From Figure 22, maximum efficiency is observed at 1652 W. Maximum efficiency observed at 871 W was higher compared to the 96 W and 369 W power inputs. Compared to all other guide vane openings, the 19 mm guide vane opening showed the best efficiency due to no obstruction and vibration compared to low guide vane openings. As per the standard of this turbine, it could not achieve more efficiency at 19 mm guide vane opening due to some of the drawbacks, such as leakages between the blades and the casing and vibrations of the turbine.

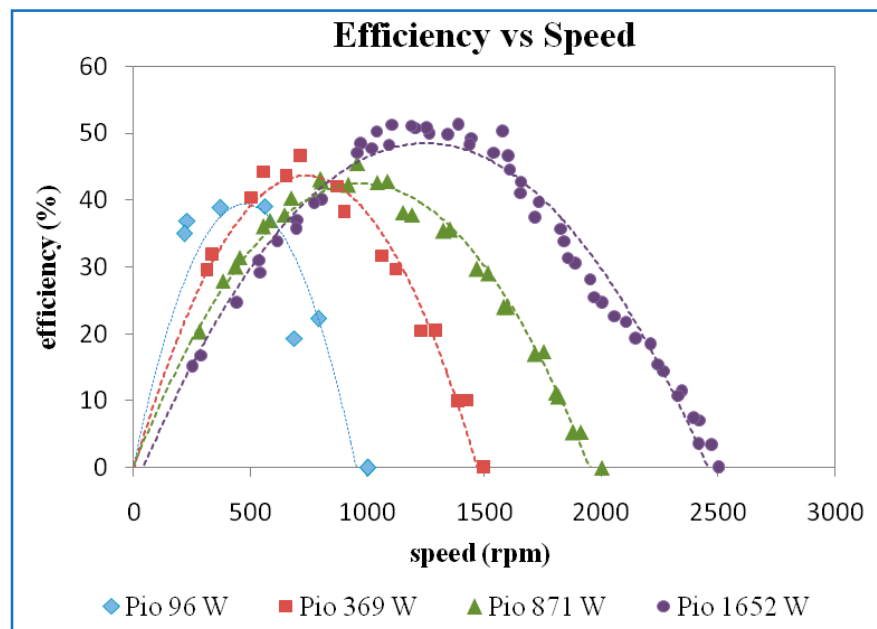


Figure 22. Efficiency vs. speed at a guide vane opening of 19 mm.

Discharge was found to be constant as speed was varied at different input powers, as shown in Figure 23 at a GVO of 19 mm. The iso-efficiency was plotted and seems not much different between guide vane openings of 10 mm, 13 mm, 16 mm and 19 mm. The bp values are 41%, 46%, 47% and 50%.

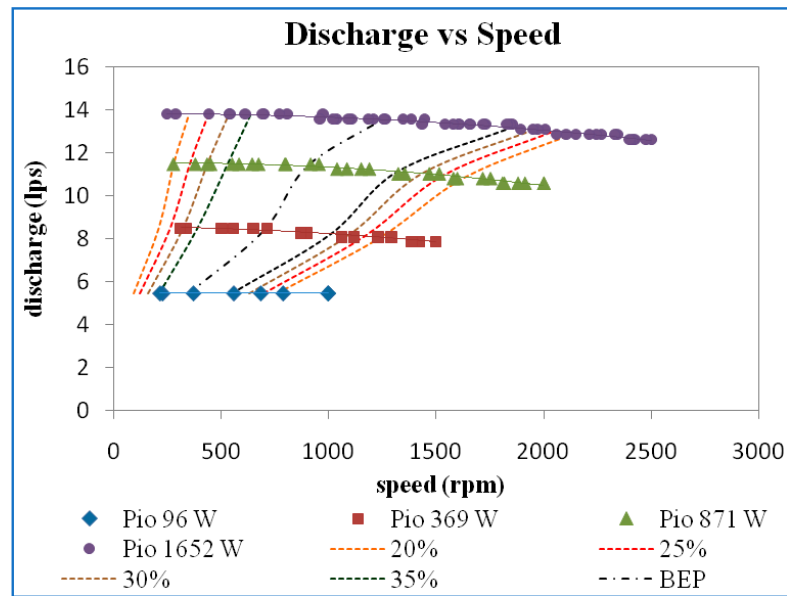


Figure 23. Discharge vs. speed and iso-efficiency line at 19 GVO.

3.2. Best Efficiency Point Curves

Figure 24 shows that all the best efficiency points with different guide vane openings are plotted in 10 mm guide vane opening. The four best efficiency points combined are intersecting at 930 speed and 11 discharge. They all split at higher discharge and lower discharge. All the discharge curves seem to be constant. As the guide vane opening was varied, there was a variation in the line of best efficiency, as shown in Figure 10. This plot indicates that all these lines merge at speed of 920 rpm.

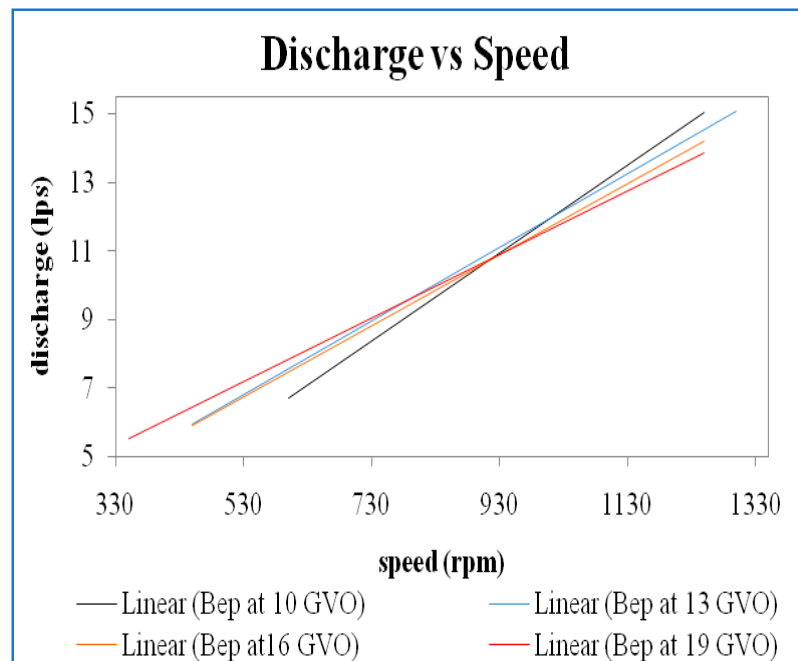


Figure 24. Discharge vs. speed for best efficiency point at 10 mm GVO.

3.3. Unit Curves

The unit discharge versus unit speed curve is shown in Figure 25. For all trial 1 and trial 2 readings at various input power, the points seem to coalesce, so one universal trend line was drawn for all the data indicating the variation of the unit discharge with respect to

unit speed. Compared to characteristic curves of discharge versus speed, the unit discharge decreases with increase in unit speed.

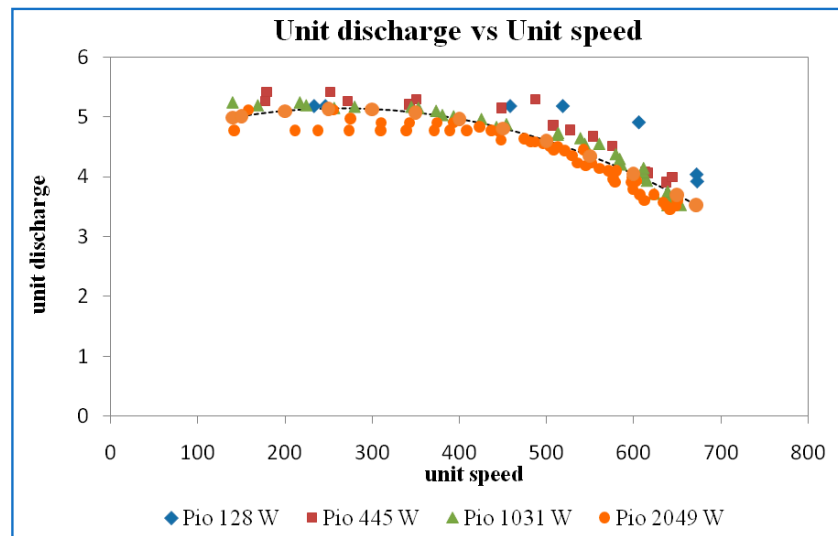


Figure 25. Unit discharge vs. unit speed at a guide vane opening of 10 mm.

The variation of output power versus unit speed operating at different power inputs is shown in Figure 26. These points form a second-order polynomial curve fit with correlation coefficients near one. The maximum unit output power is found at a unit speed of 396 rpm.

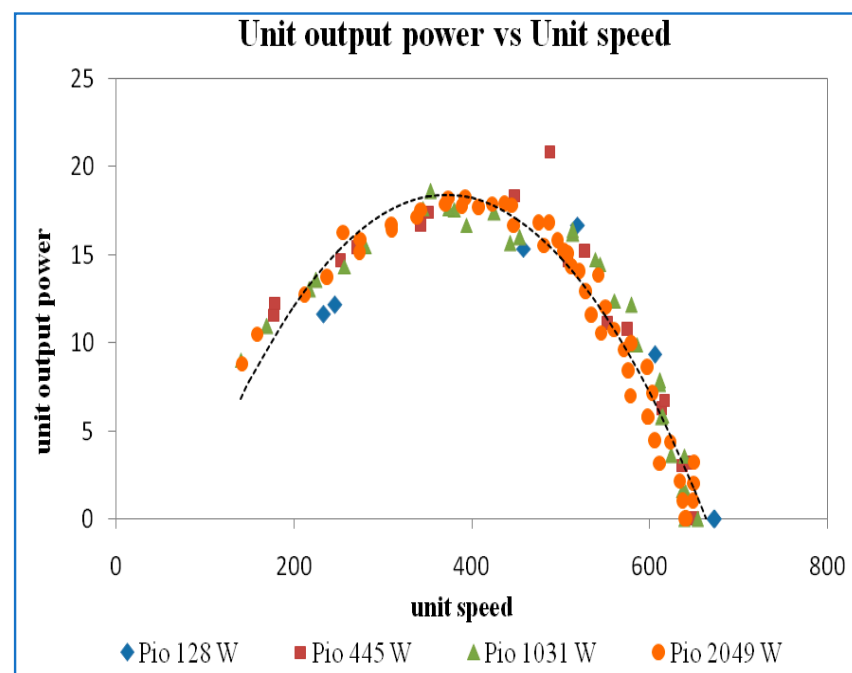


Figure 26. Unit output power vs. unit speed at a guide vane opening of 10 mm.

For the 10 mm guide vane opening, the maximum efficiency is obtained for unit speed of 400, as shown in Figure 27. The highest efficiency is about 38%.

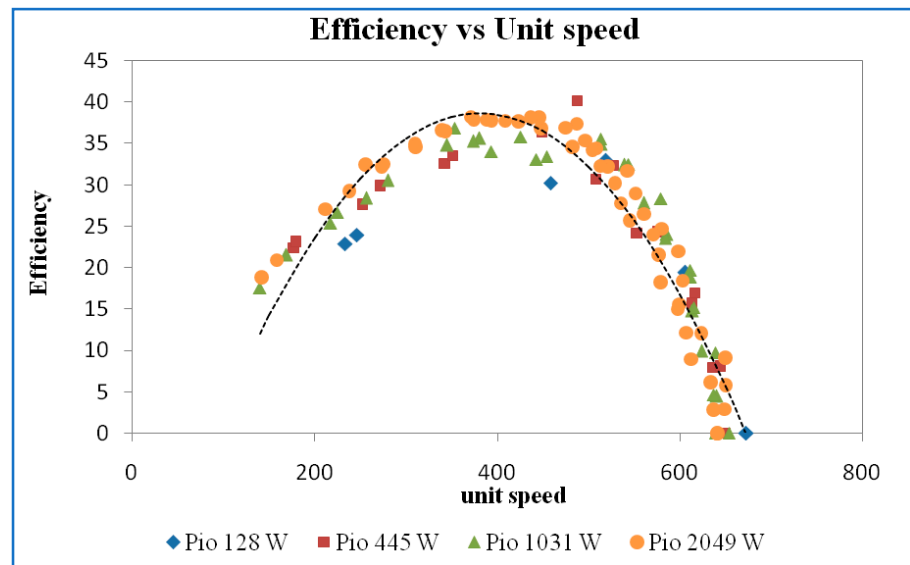


Figure 27. Efficiency vs. unit speed at a guide vane opening of 10 mm.

For a guide vane opening of 13 mm, the unit discharge versus unit speed curve is shown in Figure 28. The unit discharge decreases with increase in unit speed at this guide vane opening also. When compared to that for 10 mm, the unit discharge increases and decreases with increasing speed.

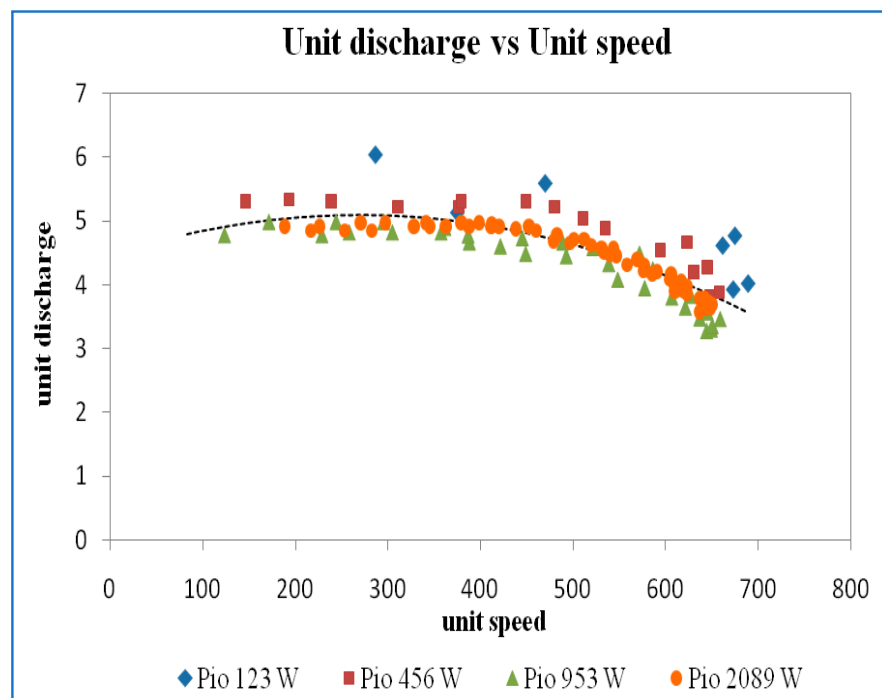


Figure 28. Unit discharge vs. unit Speed at a guide vane opening of 13 mm.

The variation in unit output power versus unit speed operating at different power inputs is shown in Figure 29. The maximum output power is found at a unit speed of 396 rpm, the same as that at a GVO of 10 mm.

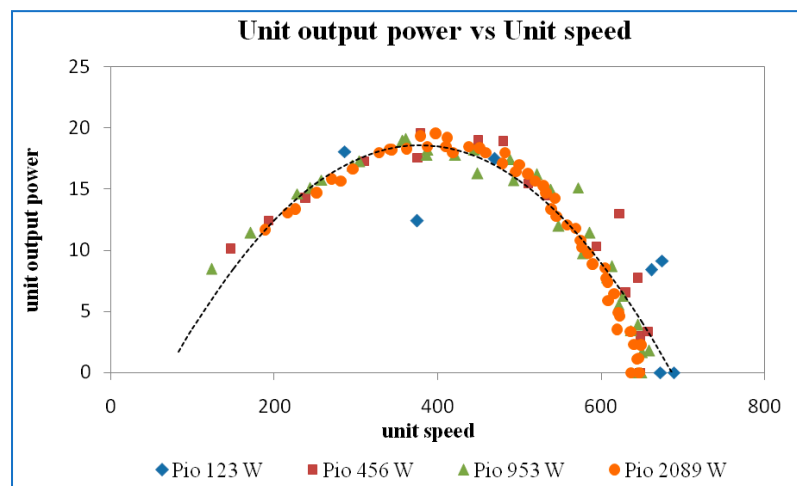


Figure 29. Unit output power vs. unit speed at a guide vane opening of 13 mm.

Variation in efficiency versus unit speed is shown in Figure 30. The efficiency gradually increases and decreases. The maximum efficiency is attained at a unit speed of 400 rpm.

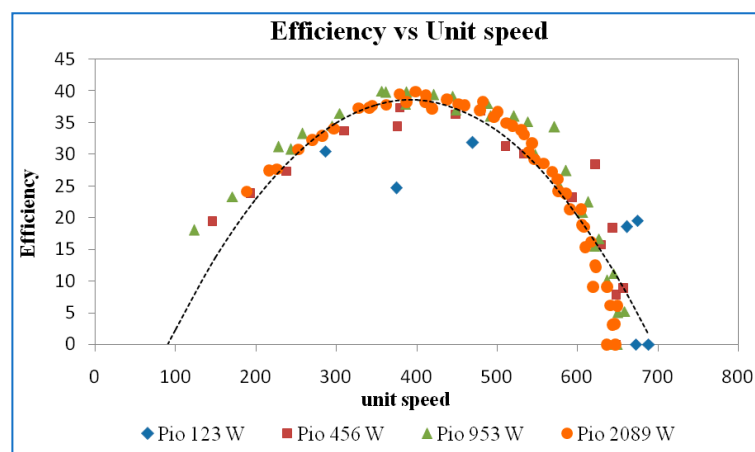


Figure 30. Efficiency vs. unit speed at a guide vane opening of 13 mm.

For a guide vane opening of 16 mm, the unit discharge versus unit speed curve is shown in Figure 31. The unit discharge decreases with an increase in unit speed.

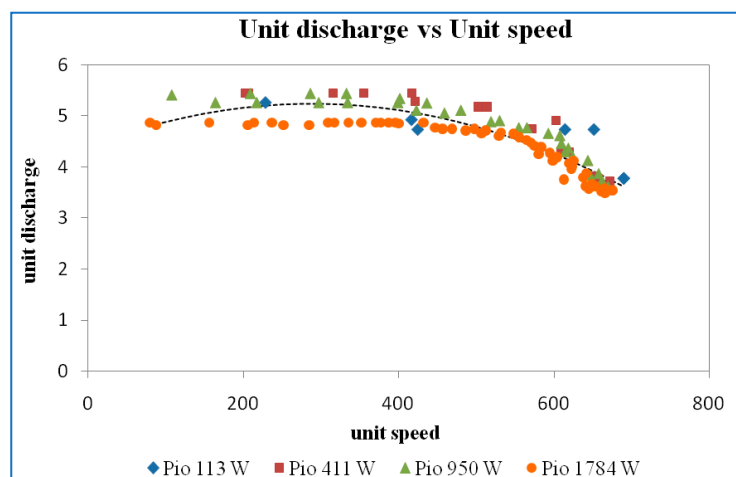


Figure 31. Unit discharge vs. unit speed at a guide vane opening of 16 mm.

The variation in unit output power versus unit speed operating at different power inputs is shown in Figure 32. The maximum output power is found at a unit speed of 396 rpm, the same as that at a GVO of 10 mm and 13 mm.

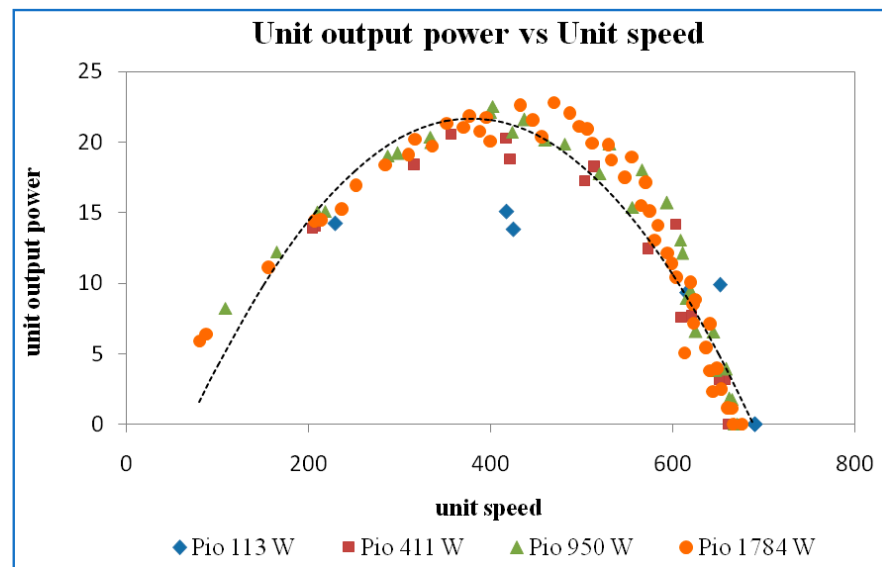


Figure 32. Unit output power vs. unit speed at a guide vane opening of 16 mm.

Figure 33 shows that a higher maximum efficiency is obtained at 45% with a guide vane opening of 16 mm. This curve at a unit speed value of 400 rpm attained maximum efficiency.

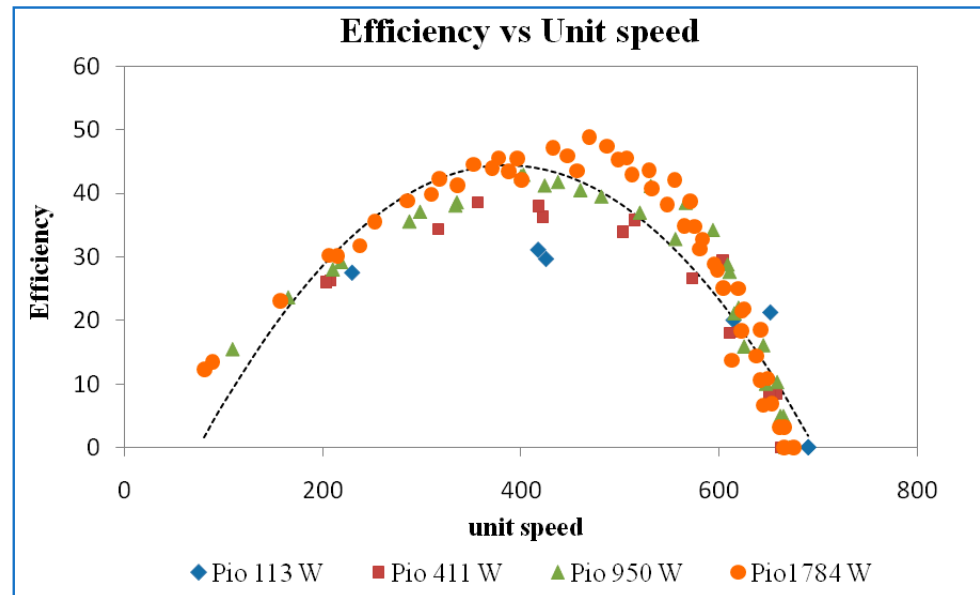


Figure 33. Efficiency vs. unit speed at a guide vane opening of 16 mm.

The unit discharge versus unit speed curve is shown in Figure 34. The unit discharge decreases with increasing unit speed. The unit discharge decreases with increasing unit speed. The unit discharge curve looks similar to GVO of 13 mm, 16 mm, and 19 mm.

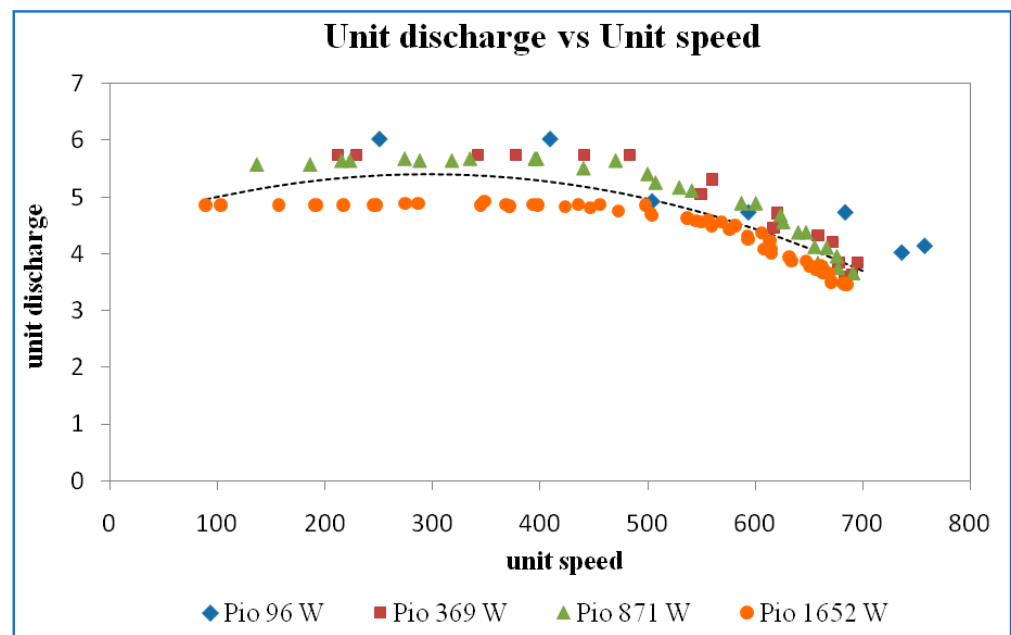


Figure 34. Unit discharge vs. unit speed at a guide vane opening of 19 mm.

The variation in unit output power versus unit speed operating at different power inputs is shown in Figure 35. The maximum output power is found at a unit speed of 400 rpm, the same as that at a GVO of 10 mm, 13 mm, and 19 mm.

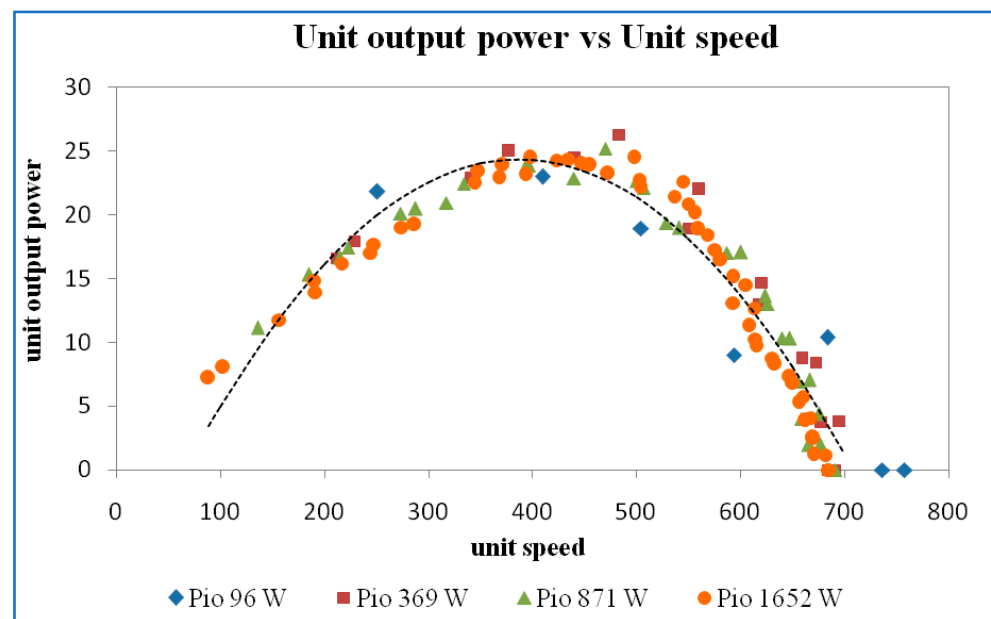


Figure 35. Unit output power vs. unit speed at a guide vane opening of 19 mm.

Figure 36 shows the variation in efficiency with unit speed for GVO of 19 mm. It shows that the unit speed at BEP is 400 rpm.

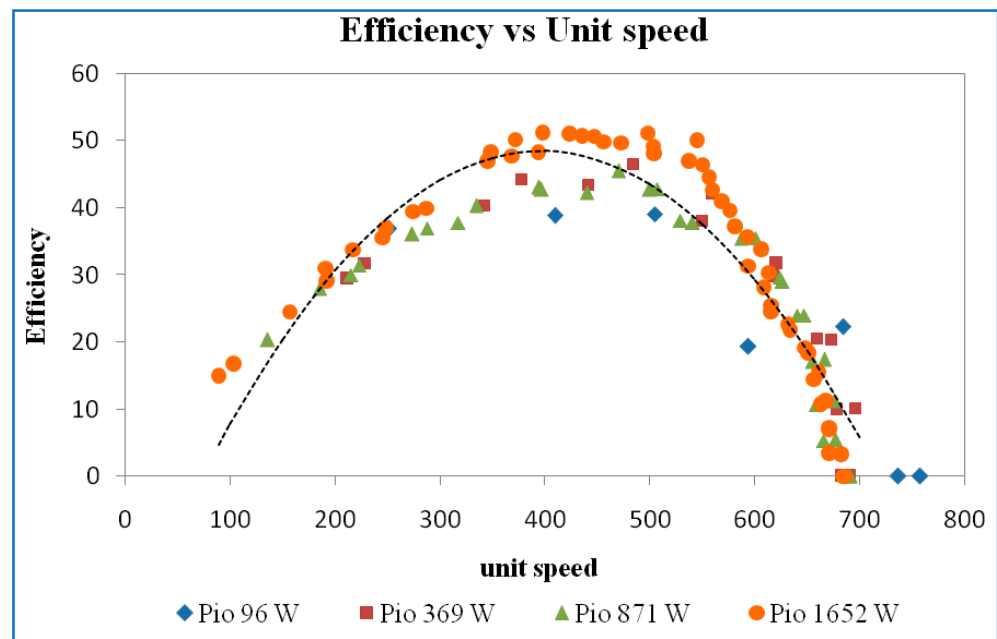


Figure 36. Efficiency vs. unit speed at a guide vane opening of 19 mm.

Using results obtained for other GVOs, as mentioned in Table 1, variations of unit quantities at the best efficiency point were plotted concerning GVO. The results presented in Figure 37 show the values to be more or less constant for all guide vane openings.

Table 1. Best efficiency points from characteristics of Francis turbine.

S. No	Guide Vane Opening GVO (mm)	Speed N (rpm)	Discharge Q (lps)	Head Given to Turbine H (m)	Brake Output Power (W)	Power Input to the Turbine (W)	Efficiency (%)
1	10	600	6.02	1.31	25.08	77.44	32.39
2		700	8.77	2.82	88.15	242.86	36.30
3		1000	11.83	5.58	239.34	647.33	36.97
4		1250	14.89	9.68	537.68	1414.14	38.02
5	13	450	5.86	1.09	20.90	62.89	33.24
6		700	8.92	2.81	92.36	245.79	37.58
7		950	11.06	5.39	236.09	584.55	40.39
8		1300	15.14	9.61	558.15	1427.69	39.09
9	16	450	5.47	1.14	20.57	61.33	33.54
10		650	8.49	2.47	78.64	205.51	38.27
11		950	11.29	4.67	220.64	517.26	42.66
12		1250	13.94	8.29	522.94	1134.04	46.11
13	19	350	5.47	0.91	19.99	48.89	40.88
14		700	8.40	2.25	85.26	185.57	45.94
15		900	11.38	4.19	209.13	468.15	44.67
16		1250	13.55	7.84	524.00	1042.79	50.25

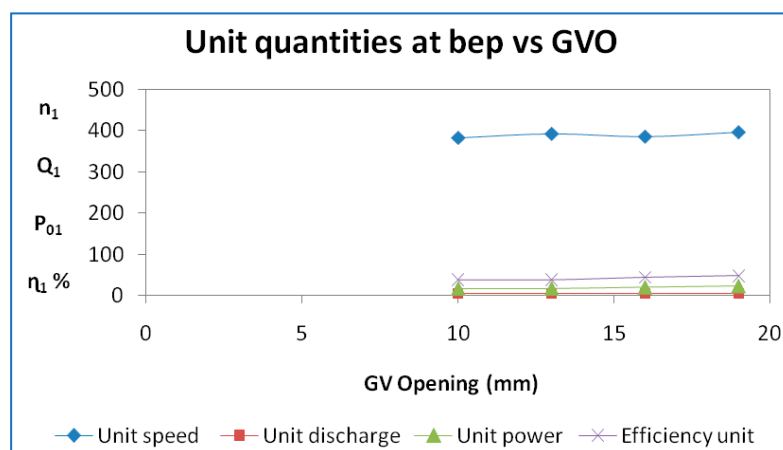


Figure 37. BEP unit quantities vs. GVO.

4. Conclusions

In the current work on the best operating point based on unit quantities by studying the performance characteristics of the Francis turbine at various input powers and guide vane openings, the important conclusions are revealed below.

The performance characteristic curves were plotted within the available range of variation of guide vane openings (10 mm to 19 mm) and input power (96 W to 2089 W). From these available data, unit curves were plotted and corresponding best efficiency points obtained. The highest efficiency of 50.25% was obtained at a guide vane opening of 19 mm. The values of head, discharge, speed, and output power at BEP were 7.84 m, 13.55 lps, 1250 rpm, and 524 W, respectively. As per the condition of this Francis turbine, the main reason for not obtaining more than the higher efficiency of 50.25% was leakage flow that passed through the clearance gap between the guide vanes' high-pressure and low-pressure sides. To determine how much leakage flow there is, finding the velocity vectors inside the gap can be used.

Author Contributions: Conceptualization, M.V.K., T.S.R. and P.S.; methodology, C.R.R., P.S.V. and O.C.S.; software, B.A., Y.A. and A.B.; validation, M.V.K., P.S.V. and C.R.R.; formal analysis, B.A. and Y.A.; investigation M.V.K. and A.B.; resources, M.V.K.; data curation, T.S.R.; writing—original draft preparation, M.V.K. and C.R.R.; writing—review and editing, M.V.K., T.S.R., C.R.R., P.S., P.S.V. and O.C.S.; visualization, Y.A.; supervision, C.R.R.; project administration, C.R.R.; funding acquisition, B.A. All authors have read and agreed to the published version of the manuscript.

Funding: The authors would like to acknowledge the financial support received from the Taif University Researchers Supporting Project (TURSP-2020/278), Taif University, Taif, Saudi Arabia.

Institutional Review Board Statement: Not applicable.

Informed Consent Statement: Not applicable.

Data Availability Statement: Not applicable.

Conflicts of Interest: The authors declare no conflict of interest.

References

1. Logan, E., Jr. *Turbomachinery: Basic Theory and Applications*; CRC Press: Boca Raton, FL, USA, 1993. Available online: <https://books.google.co.in/books?hl=en&lr=&id=s4Qfa1AWGGkC&oi=fnd&pg=PR5&dq=1.%09Logan+Jr,+Earl.+Turbomachinery:+Basic+theory+and+applications> (accessed on 25 June 2022).
2. Yannopoulos, S.I.; Lyberatos, G.; Theodossiou, N.; Li, W.; Valipour, M.; Tamburrino, A.; Angelakis, A.N. Evolution of Water Lifting Devices (Pumps) over the Centuries Worldwide. *Water* **2015**, *7*, 5031–5060. [[CrossRef](#)]
3. Reynolds, T.S. *Stronger than a Hundred Men: A History of the Vertical Water Wheel*; No. 7; JHU Press: Baltimore, MD, USA, 1983.
4. Pang, J.; Liu, H.; Liu, X.; Yang, H.; Peng, Y.; Zeng, Y.; Yu, Z. Study on sediment erosion of high head Francis turbine runner in Minjiang River basin. *Renew. Energy* **2022**, *192*, 849–858. [[CrossRef](#)]

5. Zhang, W.; Zhu, B.; Yu, Z.; Yang, C. Numerical study of pressure fluctuation in the whole flow passage of a low specific speed mixed-flow pump. *Adv. Mech. Eng.* **2017**, *9*, 1687814017707651. [[CrossRef](#)]
6. Gatte, M.T.; Rasim, A.K. Hydro Power. *Energy Conserv.* **2012**, *9*, 95–124. Available online: <https://books.google.co.in/books?hl=en&lr=&id=DASaDwAAQBAJ&oi=fnd&pg=PA95&dq=Gatte,+Mohammed+Taih,+and+Rasim+Azeez+Kadhim.+%22Hydro+power> (accessed on 30 June 2022).
7. Norquest, P.E. Ambient Pressure Water Turbine. U.S. Patent No. 4,416,584, 22 November 1983. Available online: <https://patents.google.com/patent/US4416584A/en> (accessed on 7 July 2022).
8. Choi, H.-J.; Zullah, M.A.; Roh, H.-W.; Ha, P.-S.; Oh, S.-Y.; Lee, Y.-H. CFD validation of performance improvement of a 500 kW Francis turbine. *Renew. Energy* **2013**, *54*, 111–123. [[CrossRef](#)]
9. Kurosawa, S.; Lim, S.M.; Enomoto, Y. Virtual model test for a Francis turbine. In *IOP Conference Series: Earth and Environmental Science*; IOP Publishing: Bristol, UK, 2010; Volume 12.
10. Sahu, R.K.; Gandhi, B.K. Erosive flow field investigation on guide vanes of Francis turbine—A systematic review. *Sustain. Energy Technol. Assess.* **2022**, *53*, 102491.
11. Li, G.; Ma, F.; Guo, J.; Zhao, H. Case Study of Roadway Deformation Failure Mechanisms: Field Investigation and Numerical Simulation. *Energies* **2021**, *14*, 1032. [[CrossRef](#)]
12. Kamal, M.; Abbas, A.; Prasad, V.; Kumar, R. A numerical study on the performance characteristics of low head Francis turbine with different turbulence models. *Mater. Today Proc.* **2021**, *49*, 349–353. [[CrossRef](#)]
13. Shigemitsu, T.; Fukutomi, J.; Kaji, K. Influence of Blade Outlet Angle and Blade Thickness on Performance and Internal Flow Conditions of Mini Centrifugal Pump. *Int. J. Fluid Mach. Syst.* **2011**, *4*, 317–323. [[CrossRef](#)]
14. Koirala, R.; Zhu, B.; Neopane, H.P. Effect of Guide Vane Clearance Gap on Francis Turbine Performance. *Energies* **2016**, *9*, 275. [[CrossRef](#)]
15. Koirala, R.; Thapa, B.; Neopane, H.P.; Zhu, B.; Chhetry, B. Sediment erosion in guide vanes of Francis turbine: A case study of Kaligandaki Hydropower Plant, Nepal. *Wear* **2016**, *362–363*, 53–60. [[CrossRef](#)]
16. Koirala, R.; Neopane, H.P.; Zhu, B.; Thapa, B. Effect of sediment erosion on flow around guide vanes of Francis turbine. *Renew. Energy* **2019**, *136*, 1022–1027. [[CrossRef](#)]
17. Thapa, B.S.; Trivedi, C.; Dahlhaug, O.G. Design and development of guide vane cascade for a low speed number Francis turbine. *J. Hydrodyn.* **2016**, *28*, 676–689. [[CrossRef](#)]
18. Chitrakar, S.; Dahlhaug, O.G.; Neopane, H.P. Numerical investigation of the effect of leakage flow through erosion-induced clearance gaps of guide vanes on the performance of Francis turbines. *Eng. Appl. Comput. Fluid Mech.* **2018**, *12*, 662–678. [[CrossRef](#)]
19. Amedei, A.; Meli, E.; Rindi, A.; Romani, B.; Pinelli, L.; Vanti, F.; Arnone, A.; Benvenuti, G.; Fabbrini, M.; Morganti, N. Innovative design, structural optimization and additive manufacturing of new-generation turbine blades. Turbo Expo: Power for Land, Sea, and Air. *Am. Soc. Mech. Eng.* **2020**, *84089*, V02CT35A004. [[CrossRef](#)]
20. Sosilo, A.K.; Hadi, H.; Soehartanto, T. Design of Hydro Power by Using Turbines Kaplan on The Discharge Channel Paiton 1 and 2. *E3S Web Conf.* **2018**, *42*, 01008. [[CrossRef](#)]
21. Weili, L.; Jinling, L.; Xingqi, L.; Yuan, L. Research on the cavitation characteristic of Kaplan turbine under sediment flow condition. *IOP Conf. Ser. Earth Environ. Sci.* **2010**, *12*, 012022. [[CrossRef](#)]
22. Ma, Y.; Qian, B.; Feng, Z.; Wang, X.; Shi, G.; Liu, Z.; Liu, X. Flow behaviors in a Kaplan turbine runner with different tip clearances. *Adv. Mech. Eng.* **2021**, *13*, 16878140211015879. [[CrossRef](#)]

VOLUME 46 • SPECIAL ISSUE • MAY, 2023

ISSN 0971-3034

THE INDIAN JOURNAL OF TECHNICAL EDUCATION

Published by
INDIAN SOCIETY FOR TECHNICAL EDUCATION
Near Katwaria Sarai, Shasheed Jeet Singh Marg,
New Delhi - 110 016



FABRICATION AND INVESTIGATION OF MECHANICAL PROPERTIES FOR MAGNESIUM ALLOYS BY STIR CASTING

T. SUBBA REDDY, B. SRINU, S. K. AMEER
BASHA, T. DHANESH BABU, K. LEELA
SIVA KRISHNA

Department of Mechanical Engineering, Andhra Loyola
Institute of Engineering and Technology, Vijayawada

ABSTRACT

Magnesium alloys have numerous applications due to their high strength-to-weight ratio in comparison to aluminium alloys. Although these alloys cannot be used at high temperatures due to their susceptibility to burning, they play a crucial role in the production of electric vehicles, particularly in components such as wheels, the motor casing, frame, and body. The utilization of magnesium alloys in these parts reduces the weight of electric vehicles. In this study, we conducted four castings of magnesium alloys (Al40Z1, Mg60Al40, Al25Z1, Al15Z1) using stir casting equipment to investigate their mechanical properties. We conducted a series of tests including wear testing, Vickers micro hardness testing, Porosity and density testing. We also examined the microstructure of the alloys using an optical microscope. Our results revealed that the magnesium alloys became more brittle with an increase in aluminium percentage, and the hardness was higher for alloys with a higher percentage of aluminium. We also found that Al15Z1 had a lower density than the other castings. This study contributes to the understanding of the properties of magnesium alloys and provides valuable information for the development of new electric vehicle components.

KEYWORDS : *Magnesium alloy, Stir casting, Hardness, Porosity, Wear.*

1. INTRODUCTION

Magnesium alloys have emerged as a promising material for the construction of electric vehicles (EVs) due to their exceptional strength to weight ratio. This makes them ideal for building lightweight vehicle components like the body, frame, and wheels, as they can reduce the weight of an EV without sacrificing strength or safety. Magnesium alloys are roughly two thirds less dense than aluminium alloys and one fourth less dense than steel. However, magnesium is a highly reactive metal and can easily ignite when exposed to air at high temperatures. To avoid combustion, magnesium alloys should be handled carefully and

stored in cool, dry areas away from any heat sources. Magnesium alloys have high thermal conductivity, which is essential for dissipating the heat generated by the EV's power train and battery pack. This property is critical for maintaining the performance and durability of these components. Magnesium alloys are also relatively cheap and widely available, making them a cost-effective alternative to other materials like carbon fibre and titanium. Nonetheless, the manufacturing process for magnesium alloys is complex, and this can add to the cost of production. Despite these obstacles, researchers and manufacturers continue to investigate the potential of magnesium alloys in the EV industry.

As a result, it's predicted that the use of magnesium alloys in EV construction will continue to expand in the coming years.

2. LITERATURE SURVEY

The latest research on magnesium alloys and their applications are discussed in this section.

The study conducted by Aathisugan and Razal Rose [1] on fabricated magnesium composites using stir casting is an important contribution to the field of materials science. Their findings demonstrate that the use of stir casting results in composites that exhibit improved mechanical properties compared to traditional alloys, making them ideal for use in various applications. In addition, the historical overview provided by Alan A. Luo [2] sheds light on the development of magnesium casting and its structural uses, which has played a significant role in the advancement of many industries. This knowledge can be useful for researchers and engineers who are working on the development of new magnesium-based materials and alloys. Anil Kumar et al. [3] study on the casting of magnesium composites using flux provides valuable insights into the most suitable processes for fabricating these materials. Their findings highlight the importance of vacuum-assisted stir casting, and the need to carefully consider the ductility and ultimate tensile strength of composites when designing materials for specific applications. Jiangfeng Song et al. [4] research on the physical and chemical properties of magnesium and its alloys further emphasizes the potential of these materials for use in a wide range of applications. Their work underscores the need for continued research and development in this field, as magnesium-based materials can play a key role in the aerospace, transportation, electronic 3C, biomedical, and energy sectors. The study by S V Satya Prasad et al. [5] highlights the importance of considering the drawbacks of magnesium, such as its poor corrosion resistance, when designing materials for specific applications. By alloying magnesium with other elements, researchers can improve its properties and make it more suitable for use in a wider range of applications. Tian Li, et al., [6] conducted experiment on defects formed in AZ91 alloy. And they found there are two types of oxide layers are there that is single layered and multi layered. According to their experimental results and theoretical thermodynamic calculations, it was observed that fluorides present in the trapped

gas were depleted before the consumption of sulphur. Finally, the overview provided by Arun Kumar Sharma et al. [7] on the fabrication process of magnesium-based materials using stir casting is a valuable resource for researchers and engineers. Their insights into the factors that affect the fabrication process can help to improve the quality and consistency of these materials, leading to more reliable and effective products. In summary, these studies provide important contributions to the field of materials science and highlight the potential of magnesium-based materials for use in various industries. Continued research and development in this field can lead to the development of new and improved materials that can address important challenges in areas such as transportation, energy, and healthcare.

3. EXPERIMENTAL WORK

3.1 Preparation of Materials

In this research, we used magnesium, aluminium, and zinc as our materials. The aluminium grade was 6061, and its composition is listed in Table 1. We cut the raw materials into small pieces to fit the furnace chamber, as shown in Figure 1. Stir casting equipment, shown in Figure 2, was used in the process. Composition alloy samples, shown in Table 2, were prepared for the experiment. The die was cleaned and graphite paste was applied to the surface of the mould cavity. The die was preheated to 400°C, while the furnace was heated to 750°C and argon gas supplied to avoid burning of magnesium by reacting with oxygen. Once the material was melted, the molten liquid was mixed with a stirrer at a rotational speed of 250 RPM. The die was placed in front of the outlet valve of the furnace pot, and the die input valve was straight aligned with it. The molten liquid flowed quickly into the mould cavity as the furnace outlet valve was opened by computer signal. The casting process was repeated for the other three composition alloys. After this we switch off machine and cools the die in open atmosphere. After cooled we open the die and taken out moulded samples. The final samples underwent a heat treatment process for 2 days at 350°C and were tested for mechanical properties, including hardness, wear, microscopic, density, and porosity tests. The A15Z1 composition alloy was found to have the best mechanical properties and was considered the most suitable for applications that require less weight and more strength, with lower density and higher strength compared to other alloys.



Fig.1. (a) Magnesium



Fig.1. (b) Aluminium 6061

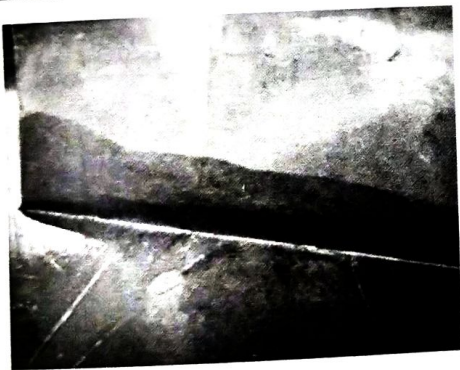


Fig.1. (c) Zinc powder

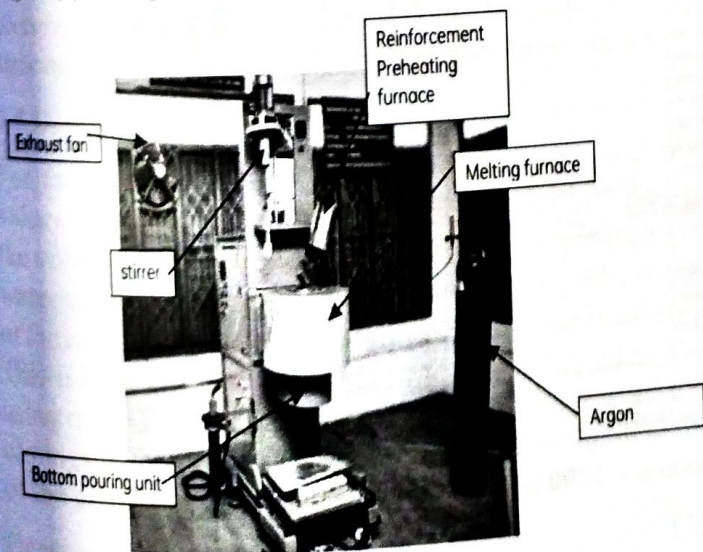


Figure 2. Stir casting machine

Table 1. Aluminium 6061

Element	Amount(wt%)
Aluminium	96.85
Magnesium	0.9
Silicon	0.7
Iron	0.6
Copper	0.25
Zinc	0.20
Titanium	0.10
Manganese	0.05
Others	0.05

Table 2. Composition of magnesium alloys

S.no	Name	Magnesium (%)	Aluminium (%)	Zinc (%)
1	A15Z1	15	84	1
2	A25Z1	25	74	1
3	A40Z1	40	59	1
4	M60A40	40	60	0

3.2 Hardness Test

We performed hardness test in Vickers micro hardness equipment by using diamond pointer indenter. And applying a load of 500KN the indentation made on the specimen. Then the micro image of the indentation is captured on the screen and by marking the indentation area hardness values are obtained. The values are shown in Table 3.

Table 3. Hardness values

S.no	Sample	Hardness value
1	A15Z1	136
2	A25Z1	216

3.3 Wear test

We performed Wear test on Disc wear testing machine, we had taken A15Z1 specimen for test of diameter 9mm and length 40mm round bar and the track diameter is considered as 70mm. Here we applied load 10N with constant Disc speed and by varying distance and time. We run 3 passes and the wear, coefficient of friction results is obtained in below Table 4 and graph are obtained. The process parameters at various levels are shown in below Table 4.

Table 4. Process parameters at various levels

Sl.no	Load (N)	Velocity (m/sec)	Distance (m)	Disc Speed (rpm)	Time of Travel (min)	Wear (μm)	Coefficient of Friction
1	10	0.5	500	137	16.67	61	0.445
2	10	0.5	1000	137	33.33	74	0.508
3	10	0.5	1500	137	50	89	0.576

The wear performance of alloys is determined using an ASTM G99 standard pattern pin-on-disc wear tester.

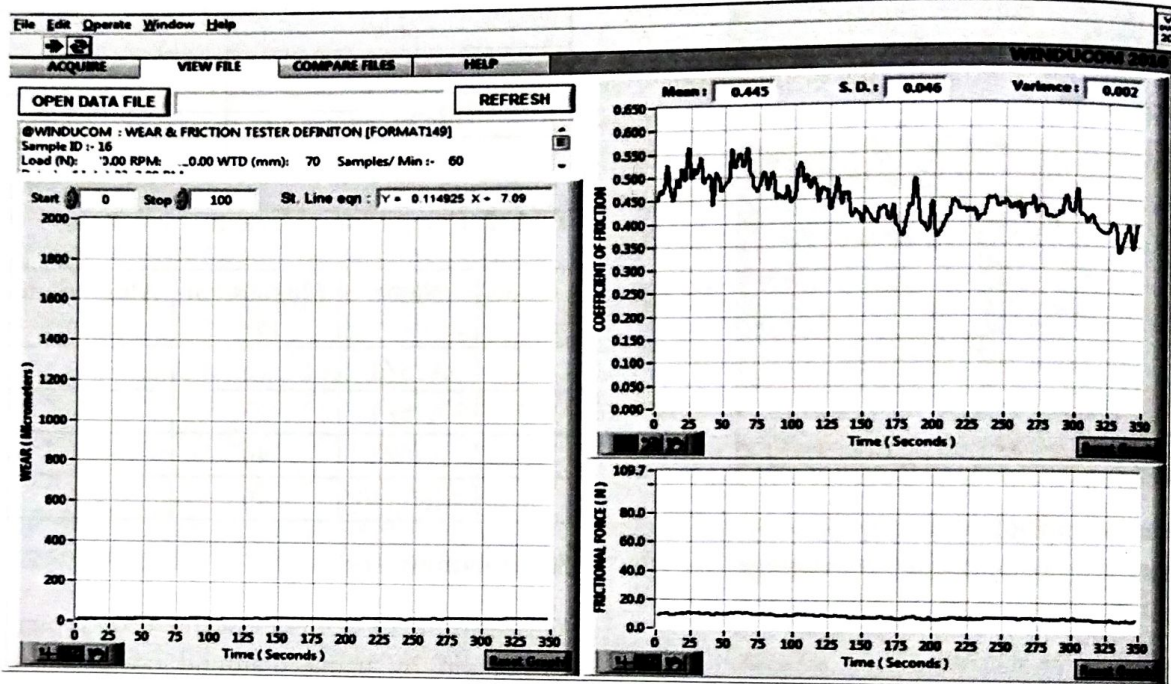


Fig.3. (a)Wear graph at Load = 10N, velocity =0.5m/s and distance = 500

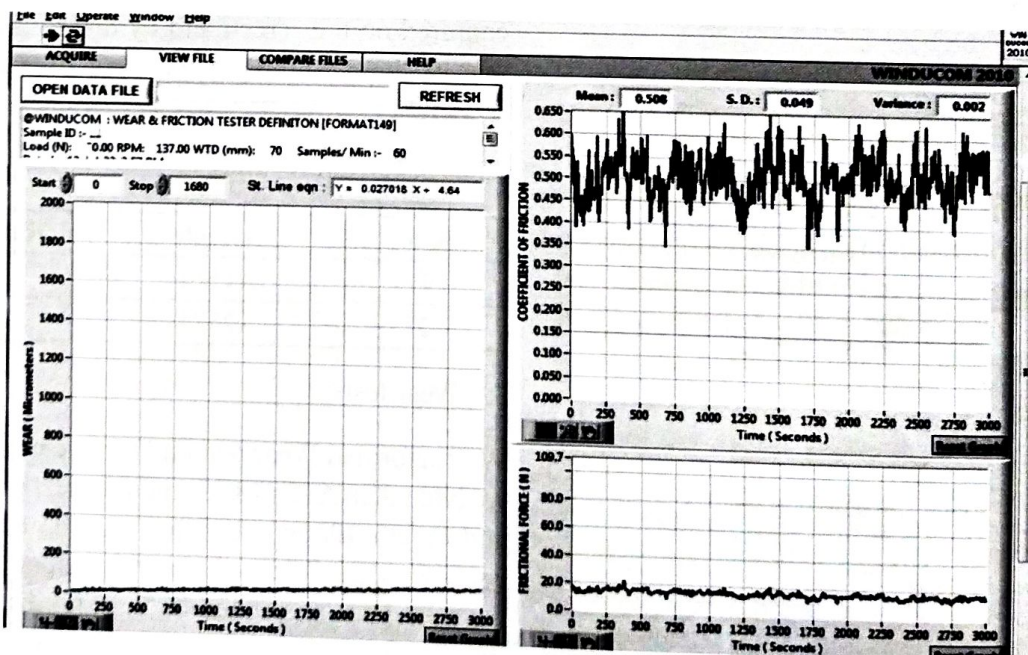


Fig.3. (b)Wear graph at Load = 10N, velocity =0.5m/s and distance = 1000 m

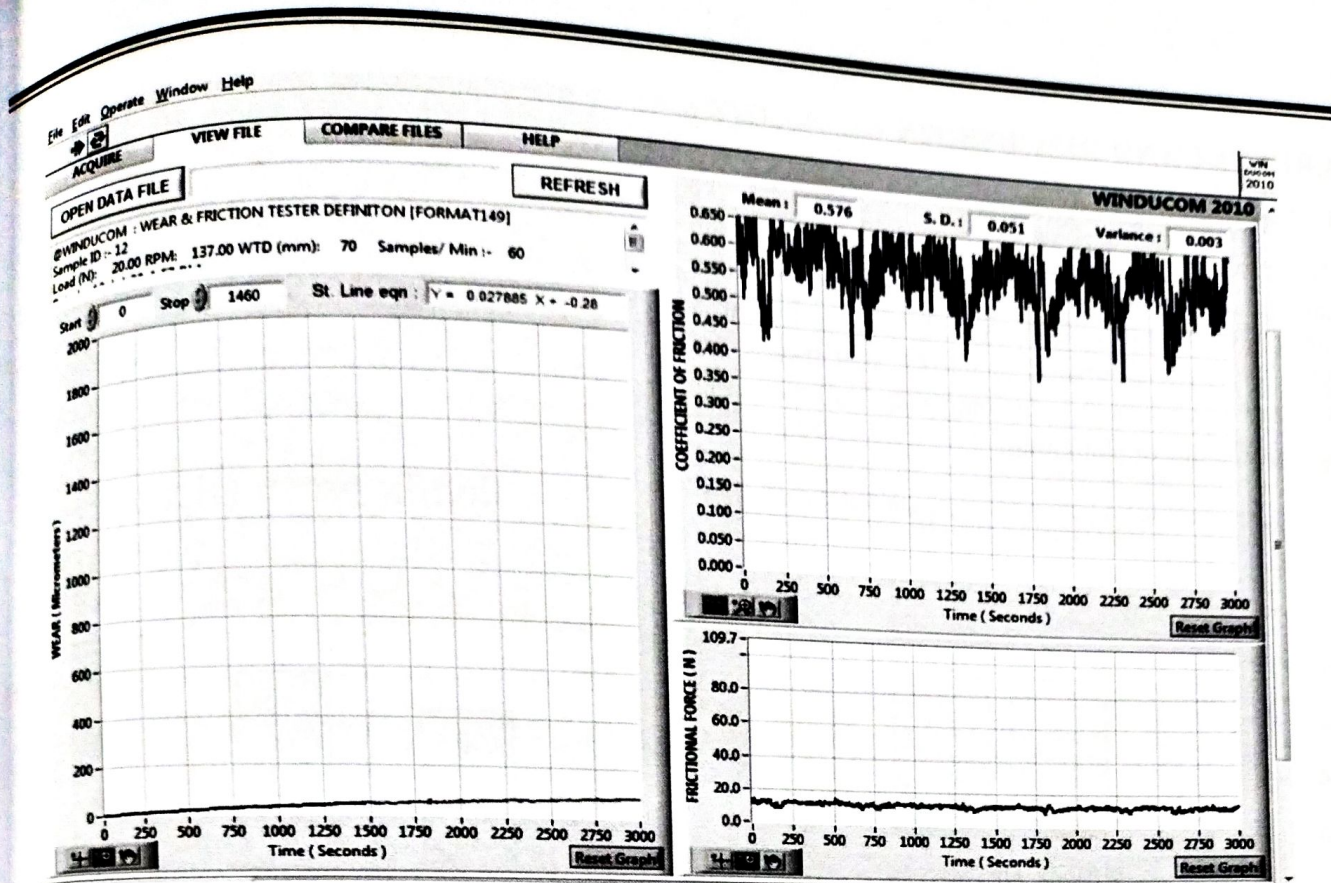


Fig.3. (c)Wear graph at Load = 10N, velocity =0.5m/s and distance = 1500 m.

3.4 Microstructure Test

For the study of microstructure, the castings are examined under the optical microscope. Before going for the inspection, the samples are prepared for surface finishing with a sequence ordered grades of silicon carbide papers, next we apply 1-micrometer aluminium powder paste on disc for polishing for smoother surface finish, in this preparation, the picric acid solution is used as etchant and applied for 10 seconds and washed out with water, after this we taken micro structure pictures by optical microscope. Finally, we analysed the structures of magnesium alloys that are shown below.

3.5 Density and Porosity test

For the castings the density was determined and the values are shown in table 5. By using a water beaker, the volume of the casting is found by dipping it into the water and by using the level in rise of water. The mass of the casting is measured by using a weighing machine. This is done based on the principle of Archimedes. By using the values of mass and volume the density of the castings is found. The formula used to find the density of the casting is given below

$$\text{Density} = \text{Mass/Volume} \quad (1)$$

Table 5. Density values for the castings

Sl.no	Sample	Density(g/cm ³)
1	A15Z1	1.3
2	A25Z1	1.41
3	A40Z1	1.52
4	M60A40	1.55

To find the porosity for the castings the theoretical and actual density values are needed. The theoretical density is measured by using the rule of mixtures. The below is the formula used for porosity

$$P = (1 - (\rho_a / \rho_t)) \times 100 \quad (2)$$

Where, P is porosity of the casting, ρ_a is actual density of the casting and ρ_t is theoretical density of the material. The calculated values of above parameters are shown in Table 6.

Table 6. Porosity and Density values

Sl.no	Actual density (g/cm ³)	Theoretical density (g/cm ³)	Porosity, %
1	1.42	1.84	22.82
2	1.68	1.91	12.04
3	1.82	2.03	10.34
4	1.85	2.02	8.41

4.RESULT AND DISCUSSION

4.1 Hardness test analysis

The detailed information of the hardness values of the castings are shown in the form of graph in figure 5. The graph shows that there is an increment in the hardness value of A25Z1 compared to A15Z1, that means the hardness value is more in the magnesium alloy having high percentage of aluminium.

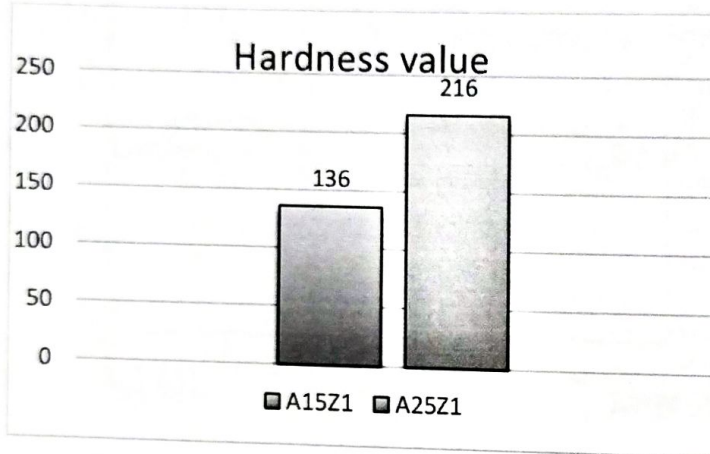


Fig.4. Hardness values Graph

4.2 Wear test analysis

For A15Z1 the wear test is conducted and the wear, coefficient of friction was determined. For the remaining castings the wear test is not conducted due to the brittleness of material. These parameters are represented in the form of graph for the three passes and the graph is shown in the figure 6. In the below graphs we can see the wear and coefficient of friction is increments for every pass.

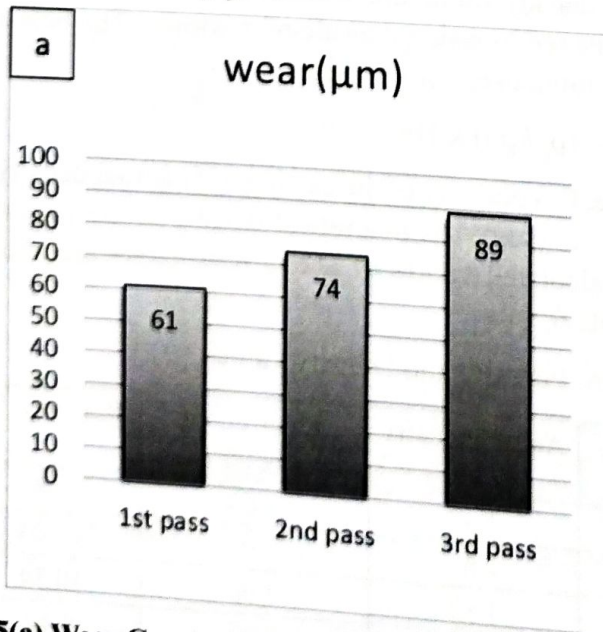


Fig.5(a) Wear Graph

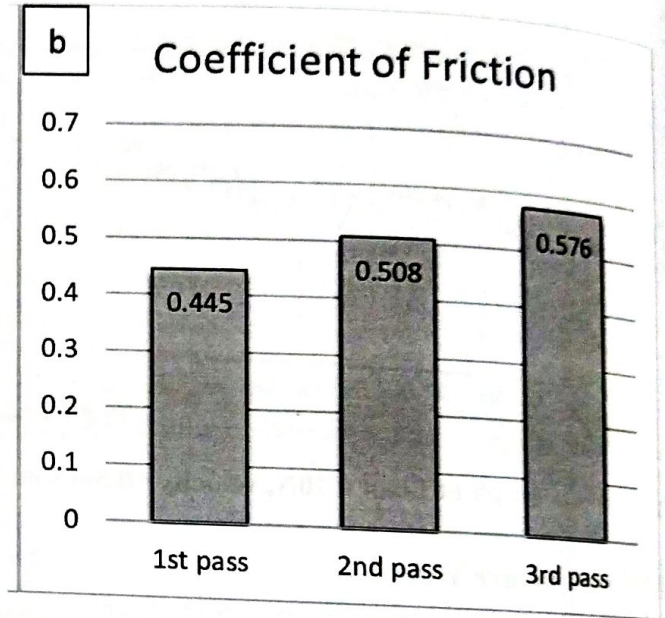


Fig.5(b) Coefficient of friction Graph

4.3 Microstructure analysis

Metallographic investigation is a highly valuable tool for both feature control and investigative purposes. The images that are captured under the optical microscope is shown in the Figure 6. This shows the micro structure of the four different castings. The difference can be observed by seeing these microstructures.

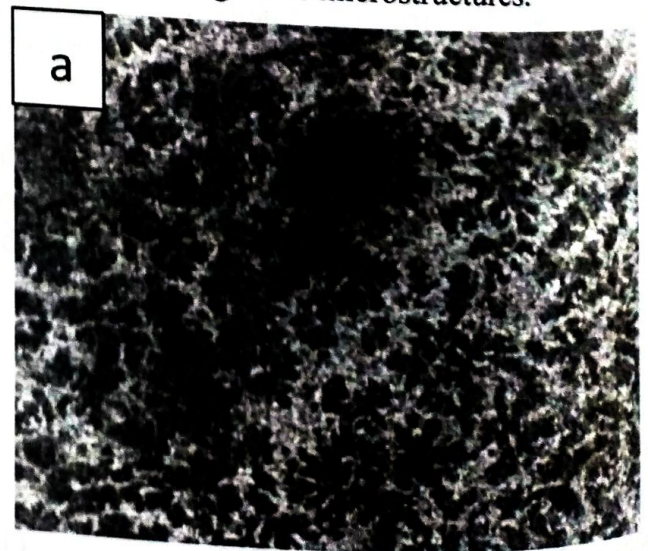


Fig.6. (a) A15Z1

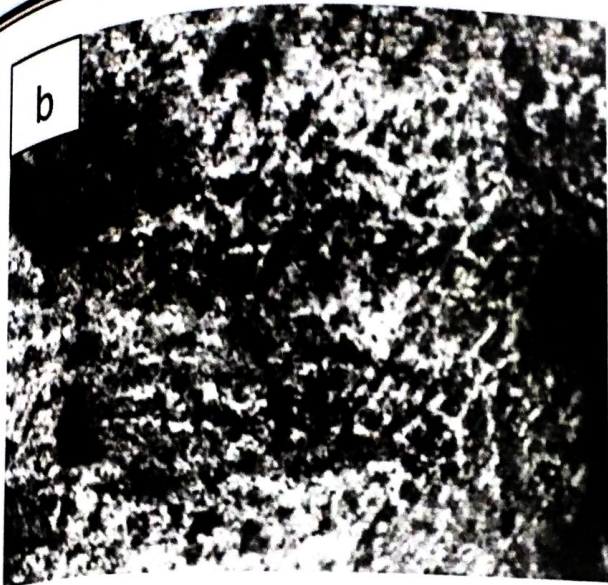


Fig.6. (b)A25Z1

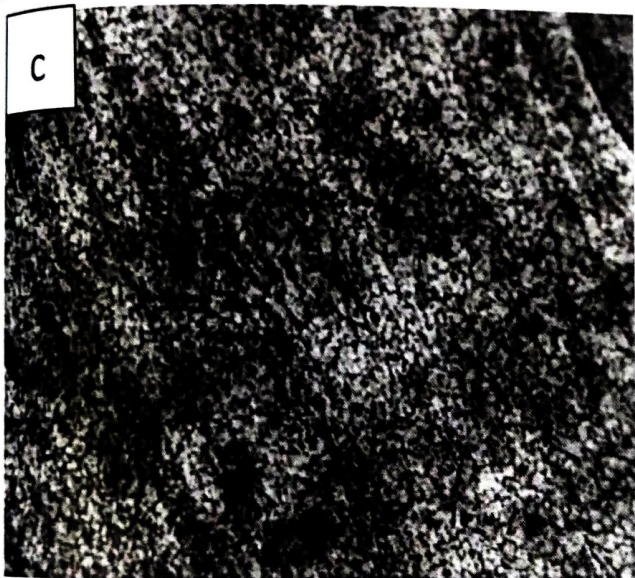


Fig.6. (c) A40Z1

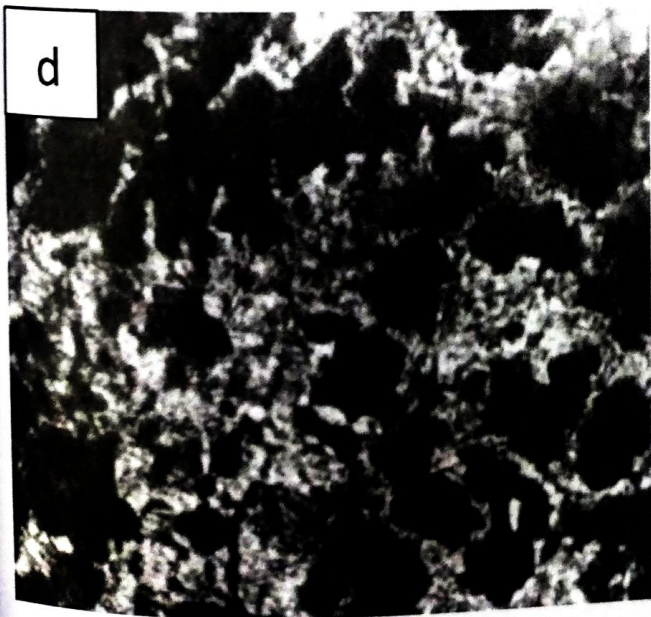


Fig.6. (d)A40M60

4.4 Density and porosity analysis

We calculated density and porosity of samples by theoretical and actual values, by comparing both of them we analysed density was decreased by increasing of magnesium percentage due to its less weight property, porosity had increases by increase in magnesium percentage, we had found A15Z1 had less density with light weight property, from graphs we understood that change in composition of alloy changes its density & porosity values increases with increase of magnesium.

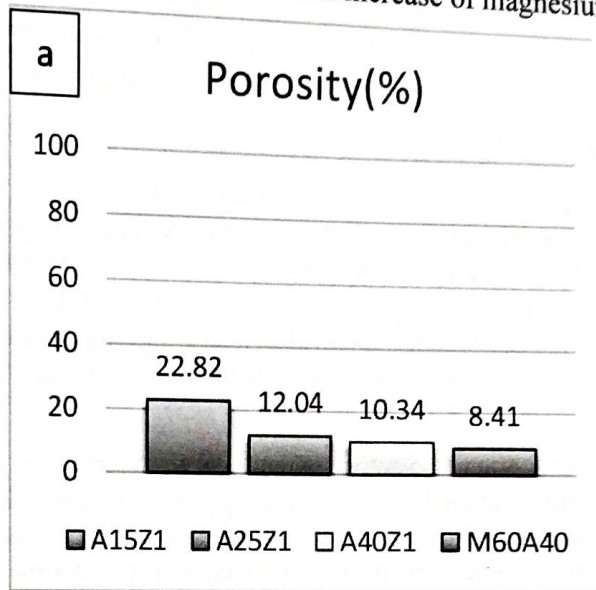


Fig.7 (a) Porosity Graph

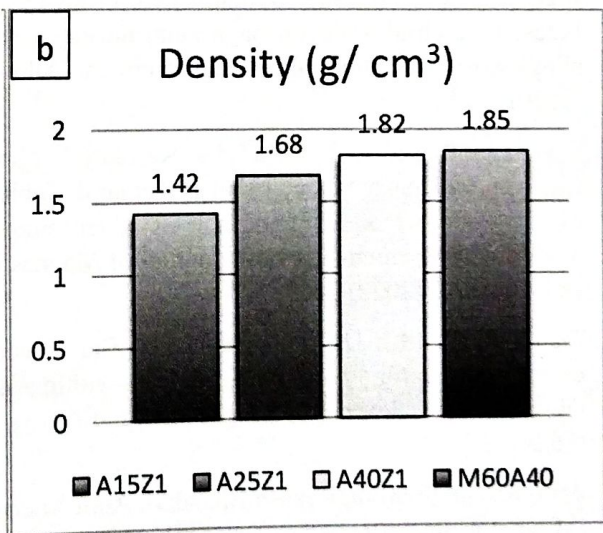


Fig.7 (b) Density Graph

5. CONCLUSION

After conducting Hardness test, we conclude that the hardness value increases with increase in percentage of aluminium in magnesium alloy. In wear test the results shows that the wear and coefficient of friction is getting

more for every increment of a pass. By calculating the porosity, we conclude that the porosity is increases with increase in magnesium percentage in magnesium alloys. While doing this research we are unable able to do the tests for all castings due to their brittleness property. The brittleness is increasing with the increase in Aluminium percentage in magnesium alloys. The A15Z1 is only casting that is examined by all tests and the density of A15Z1 is less compared to other castings. The disadvantage of A15Z1 is the porosity is high when compared to other castings. By studying all of these comparisons we had considered A15Z1 can used for the applications of EV and other low weight applications.

6. REFERENCES

1. A Razal Rose, I Aatthisugan. Fabrication and characterization of Magnesium Metal Composite by Stir Casting. IOP Conference Series: Materials Science and Engineering.912 (2020) 032080 [2]. Alan A. Luo. Magnesium casting technology for structural applications. Journal of Magnesium and Alloys 1 (2013) 2-22.
3. Anil Kumar, Santosh Kumar, N.K. Mukhopadhyay, Introduction to magnesium alloy processing technology and development of low-cost stir casting process for magnesium alloy and its composites. Journal of Magnesium and Alloys 6 (2018) 245–254.
4. Jiangfeng Song, Jia She, Daolun Chen, Fusheng Pan. Latest research advances on magnesium and magnesium alloys worldwide. Journal of Magnesium and Alloys 8 (2020) 1–41.
5. S V Satya Prasad a, S B Prasad a, Kartikey Verma b, Raghvendra Kumar Mishra c, Vikas Kumar d, Subhash Singh. The role and significance of Magnesium in modern day research-A review. Journal of Magnesium and Alloys 10 (2022) 1–61.
6. Tian Li a, b, J.M.T. Davies a, Xiangzhen Zhu. Effect of carrier gases on the entrainment defects within AZ91 alloy castings . Journal of Magnesium and Alloys 10 (2022) 129–145.
7. Arun Kumar Sharma, Rakesh Bhandari, Amit Aherwar , Camelia Pinca-Bretotean. A study of fabrication methods of aluminum-based composites focused on stir casting process. Materials Today: Proceedings 27 (2020) 1608–1612.
8. Aatthisugan, I., Rose, A.R. and Jebadurai, D.S., 2017. Mechanical and wear behaviour of AZ91D magnesium matrix hybrid composite reinforced with boron carbide and graphite. Journal of magnesium and alloys, 5(1), pp.20-25.
9. D. Dash^{1,2*}, S. Samanta², R. N. Rai³ Study on Fabrication of Magnesium based Metal Matrix Composites and its improvement in Mechanical Tribological Properties- A Review. IOP Conf. Series: Materials Science and Engineering 377 (2018)
10. Rajeshkumar Gangaram Bhandare, Parshuram M. Sonawan Preparation of Aluminium Matrix Composite by Using Stir Casting Method. International Journal of Engineering and Advanced Technology (IJEAT) ISSN: 2249 – 8958, Volume-3, Issue-2, December 2013
11. Hailong Shi a , d , Chao Xu b , d , Xiaoshi Hu a , d , Weimin Gan c , Kun Wu d , Xiaojun Wang a , d , *.Improving the Young’s modulus of Mg via alloying and compositing –A short review. Journal of Magnesium and Alloys 10 (2022) 2009–2024
12. Yunpeng Hu¹ Xuan Guo¹ Yang Qiao¹ Xiangyu Wang¹ Qichao Lin² Preparation of medical Mg–Zn alloys and the effect of different zinccontents on the alloy Journal of Materials Science: Materials in Medicine 4,janury ,2022
13. Krishnamohan Thekkepat a , b , c , 1 , Hyung-Seop Han d , 1 , Ji-Won Choi d , Seung-Cheol Lee a , b , c , **, Eul Sik Yoon e , Guangzhe Li d , Hyun-Kwang Seok d , f , Yu-Chan Kim d , f , ***, Jae-Hun Kim g , Pil-Ryung Cha g , *. Computational design of Mg alloys with minimal galvanic corrosion. Journal of Magnesium and Alloys 10 (2022) 1972–1980.
14. Jun Wang, Yuan Yuan *, Tao Chen, Liang Wu, Xianhuan Chen, Bin Jiang, Jingfeng Wang, Fusheng Pan *. Multi-solute solid solution behavior and its effect on the properties of magnesium alloys. Journal of Magnesium and Alloys 10 (2022) 1786–1820.
15. Meysam Mohammadi Zerankeshi a , Reza Alizadeh a , *, Ehsan Gerashi a , Mohammad Asadollahi a , Terence G. Langdon b.Effects of heat treatment on the corrosion behavior and mechanical properties of biodegradable Mg alloys. Journal of Magnesium and Alloys 10 (2022) 1737–1785.

APST

Asia-Pacific Journal of Science and Technology<https://www.tci-thaijo.org/index.php/APST/index>Published by the Research and Graduate Studies Division,
Khon Kaen University, Thailand

Premixed charge combustion in a diesel engine fuelled with biodiesel, n-butanol, and ignition improver blendsGangeya Srinivasu Goteti^{1,*} and Tamilselvan Palsami¹¹School of Mechanical Engineering, VIT University, Chennai, India*Corresponding author: gangeyasrinivasu.2016@vitstudent.ac.in

Received 21 July 2022

Revised 23 November 2022

Accepted 1 December 2022

Abstract

The research aims to achieve optimised combustion by utilising the benefits of both spark ignition engine (SI) and compression ignition (CI) engine combustion properties. This research focuses primarily on gaining the advantages of maximum thermal efficiency and reduced emissions. This research also investigates the usage of biodiesel and an ignition improver with improved operating conditions by supplying n-butanol with preheated air. The experimental work was first conducted for the development of preliminary data using neat diesel. It was then performed using a blend of *Prosopis juliflora* methyl ester (PJME), diesel, and di-ethyl ether as an additive. This blend consists of PJME 25%, diesel 74%, and di-ethyl ether (DEE) 1% on a volume basis and is named B25DEE1. With this blend, improved brake thermal efficiency and reduced emissions were observed. The experiment was repeated by port injecting n-butanol into the preheated air stream (35°C-40°C) in a proportion of 10% volume to the primary injected fuel. This method was used to achieve premixed charge compression ignition. This combustible mixture was named n-butanol vapours (B25DEE1+NB). The engine performance demonstrated improved brake thermal efficiency as well as lower emissions (HC, CO, smoke, and NO_x). Additionally, higher in-cylinder pressures 86.6 bar and heat release rates of 49.12 J/°CA were noted.

Keywords: *Prosopis juliflora* methyl ester, Ignition improver, Cetane number, Diesel engine, Premixed charge compression ignition

1. Introduction

To decrease fossil fuel consumption, there is a need to focus on alternative fuel usage. The selection of alternative fuels must be based on their availability and biodegradability. Its properties must be closer to those of the diesel, which can allow the utilisation of unmodified diesel engines or with little modification for advanced combustion phenomena. Several researchers found various alternative sources that use alcohol-based fuels and biodiesel compounds. Most of the authors concluded that their research findings had shown the suitability of utilising these alcohol fuels and biodiesels with a considerable reduction in emissions and improved performance and combustion characteristics.

Kumar et al. [1] concluded that biodiesel blended with ethanol and preheated inlet air can decrease CO and HC emissions with advanced injection timings. The experimental investigations were conducted by Krishnamoorthi et al. [2] revealed that utilising biodiesel-diethyl ether blends can decrease NO_x emissions and also improve BTE in diesel engines. The improved brake thermal efficiency (BTE) and brake specific fuel consumption (BSFC) and decreased CO emissions were observed by Senthur et al. [3] by preheating the 20% palm oil and blending it with n-butanol, diesel, and a 2000 mg/L butylated hydroxytoluene (BHT) additive. The blends of n-butanol (15%), gasoline (15%), and diesel increased maximum pressures with decreased ignition delay and NO_x emissions. However, when compared to diesel, CO emissions and BSFC were higher, as demonstrated by Prakash et al. [4]. Murthy et al. [5] conducted an experimental analysis using a 5% di-ethyl ether (DEE) and H₂SO₄ solution. This solution was injected into the inlet manifold by high-pressure injection. The engine ran on a palm kernel methyl ester blend. Micro explosions occurred due to the DEE addition. This tendency caused an improvement in the swirl in the combustion chamber and thus reduced the ignition delay period. Tsutsumi et al.

[6] concluded that ignition improvers such as DEE and di-methyl ether (DME), when combined with biodiesel blends in small amounts, can further reduce emissions by increasing the evaporation rate. Utilizing these ignition improvers with biodiesel can improve the cetane number to the required extent. Pugazhivadiv et al. [7] used DEE along with a Pongamia biodiesel blend. The results revealed that DEE additives can decrease emissions like NO_x and smoke. Polyoxymethylene diethyl ethers were used with n-butanol and diesel blends by Huang et al. [8] to achieve improved thermal efficiency and combustion phenomena.

The above literature concludes that the alternative fuels commonly used by researchers are ethyl or methyl esters of biodiesel and alcohol-based fuels for investigating engine performance, emission, and combustion phenomena. Since these fuels are enriched with oxygen and have good miscibility with diesel, Their chemical composition allows them to be used along with diesel with negligible engine modifications. But by increasing the blending percentage of these alcohols and biodiesels with diesel, they can decrease the cetane index further because their cetane index is very low. Because of their enriched oxygen levels, these fuels can also cause increased fuel consumption in comparison to their output power, as Kalargaris et al. [9] demonstrated. Ignition improvers like DEE and DME can be utilised like cetane number improvers with biodiesel to improve the combustion quality. These ignition improvers can reduce the ignition delay period by allowing spontaneous combustion after injection. They can minimise cold-start problems and reduce emissions like NO_x and HC because of higher latent heat of vaporisation and oxygen percentages [10]. The properties of these ignition improvers, like a higher cetane number, higher volatility, a high latent heat of vaporization, a lower auto-ignition temperature, and miscibility with diesel, can allow them to be used as fuel additives. This research work primarily concerns the utilisation of n-butanol vapours and biodiesel blends along with ignition improver DEE.

The bio-oxygenated content is available in the alcohol fuels. They also have increased volatility and mixing properties with diesel compared to other fuels. They can also increase the efficiency of combustion as they have a high oxygen percentage [11], an increased rate of evaporation even at low pressures, a calorific value, a cetane index, and are renewable in nature. Biodiesel compounds offer the benefits of being non-toxic and renewable, with no residues of Sendzikiene et al. [12] utilised the combination of rapeseed methyl ester, diesel, and ethanol to improve the oxygen percentage. With an oxygen limit of 19%, the normal operating condition was observed at a speed of 1200 rpm and 42.42N of torque. But by increasing the oxygen limits to 19.5%, decreased torque and rotational speeds were observed. By increasing the oxygen percentage in the fuel to 25.7 percent, the engine was not activated. The reduced NO_x emission was observed with an increased oxygen percentage in the fuel.

From the above literature survey, it was observed that biodiesels, along with alcohol fuel and ignition improver combinations, can be chosen to increase the oxygen percentage to the required extent. In this present study, the selected qualities of biodiesel *Prosopis juliflora* methyl ester (PJME) are closer to those of diesel. Its seed oil is naturally non-edible. The study is unique in that no combustion evaluations on the use of PJME, n-butanol, DEE, and diesel blends were available.

The seed oil of *Prosopis juliflora* is inedible by nature. *Prosopis juliflora* plant is widely available, and it consists of 44 species throughout the world [13]. The higher the cetane number, oxygen percentage, and heating value of this fuel, the closer it is to diesel, making it a good alternative source for diesel engines. With few or no engine modifications, an alcoholic fuel like n-butanol can be used in conventional compression ignition (CI) engines. Diesel's characteristics are contrasted with n-butanol's and *juliflora* oil methyl esters in Table 1. The fundamental reason for using n-butanol is that it has a higher oxygen percentage, which improves the efficiency of combustion. It also has properties like reduced evaporation pressures, increased heating values, and a high cetane number.

An ignition improver like DEE can improve the combustion quality of biodiesel blends. It can improve the cetane number to the proper extent to maintain smooth engine operation. The ignition lag period can be decreased by adding ignition improvers. They can also minimise the cold-starting problems by improving the diffusion rate. By mixing ignition improvers, NO_x emissions can be reduced significantly due to their elevated latent heat of evaporation. Their high oxygen content may also induce a decrease in HC and CO emissions.

The main objective of this research is to utilise blends of *Juliflora* biodiesel, n-butanol, and ignition improver. The biodiesel blend was meant to decrease conventional fuel usage. The ignition improver is meant to increase the evaporation rate and cetane index. The n-butanol vapours were used to accelerate the reaction rate by further influencing the oxygen content in the test fuel blend and also to reduce the unburned hydrocarbon and carbon monoxide emissions.

Table 1 Properties of the test fuel.

Specifications	Diesel	n-butanol	DEE	PJME	B25DEE1	ASTM D6751 Standard for biodiesel
Cetane Index	50	17	>125	49	50.5	47-65
Stoichiometric A/F ratio	14.95	11.17	11.1	12.25	14.24	-
Oxygen (wt %)	0	21.58	21	12	3.21	11
Carbon (wt %)	86.12	64.82	64.86	77	83.62	77
Hydrogen (wt %)	13.87	13.60	13.5	12	13.4	12
Lower Calorific Value (kJ/kg)	43390	33100	33900	39500	42330	~33342
Kinematic Viscosity (cSt) at 40°C	3.9	2.63	0.23	4.90	4.09	4.0-6.0
Density (kg/m ³) at 15°C	838	810	713	920	857	874.73

2. Materials and methods

The standards of American society for testing and materials (ASTM) D6751 and EN 14214 are applied for the preparation of biodiesel blends. By adhering to these guidelines, the test fuels were prepared by maintaining the blend density below 860 kg/m³, the kinematic viscosity below 4.1 cSt, and the heating value of the blends above 35 MJ/kg.

The test fuel blend consists of 25% biodiesel and 1% ignition improver DEE (Diethyl Ether) and the remaining diesel on a volume basis and is named B25DEE1 (Juliflora Methyl Ester 25%, Diesel 74%, and DEE 1%). The 25% biodiesel was chosen because it attained a higher brake thermal efficiency in the previous experimental analysis when compared to the 15% biodiesel blend [14]. The ignition improver DEE was chosen due to its higher heating value and cetane index when compared to DME [15].

In the next stage, the n-butanol was port injected into the preheated (35°C-40°C) inlet air stream in a proportion of 10% to the main injected fuel (B25DEE1), and this combustible mixture was named B25DEE1+NB. From no load to maximum load, a compression ratio of 18 was used with the diesel and test fuel blends. The main objective of injecting n-butanol into a preheated air stream is to supply n-butanol in the vapour state into the engine cylinder. This can increase the reaction rate and decrease the physical delay period. This can also make the concept of pre-mixed charge combustion more practicable.

2.1 Experimental set up

The test rig is represented schematically in Figure 1. Its technical characteristics are listed in Table 2. The test rig consists of a conventional CI engine coupled to a dynamometer. It was also provided with five gas analyzer and a smoke meter. The experimental setup consists of provisions for measuring combustion-related data and is connected to the data acquisition system. An average value of all the test readings was noted by conducting a series of trials at the stabilised condition of the engine with applied loads. This common rail direct injection (CRDI) variable compression ratio (VCR) engine works with a programmable open electronic control unit (ECU) for diesel injection, a fuel injector, a common rail with rail pressure sensor and pressure regulating valve, a crank position sensor, a fuel pump, and a wiring harness. This setup can be used to perform heat balance and combustion analysis.

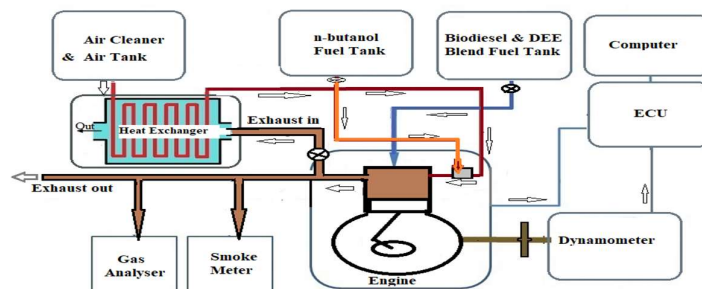
**Figure 1** Schematic view of the test rig along with ECU.

Table 2 Test rig details.

Parameters	Description
Engine	Single Cylinder 4S CI Engine.
Power / Speed	3.5 kW / 1500 rpm
Bore / Stroke / Displacement volume	87.5 mm / 110 mm / 661.5 cm ³
Compression Ratio	18
Main injection pressure/ timing	300 bar/25° before top dead center (BTDC)
Port injection pressure	3 bars (Regulated)
Port injection method	Single, 355° BTDC
Heat Exchanger (for Air pre-heating)	Shell and Tube type
Gas analyzer	Five gas analyzers (AVL DiGas 444N)
Smoke meter	AVL Smoke meter 437°C
Combustion pressure sensor	PCB Piezotronics, USA, Combustion: Range 350 Bar
Crank angle sensor	Kubler Germany, Resolution 1 Deg, 5500 RPM with top dead center (TDC) pulse.

2.2 Analysis of errors and uncertainties

The measured values and uncertainties underwent error analysis using Kline and Mc.Clintock's method [24]. To get results with proper accuracy, the instruments used in this experimental analysis were carefully selected. By evaluating the observed data, it is concluded that the uncertainty values vary between the intervals of ± 0.1 and 2.0%. Based on the results, it is possible to conclude that the uncertainties in the principle value measurements and derived values have no effect on the numerical result uncertainties.

3. Results and discussion

3.1 Performance assessment

3.1.1 Brake thermal efficiency

The ratio of the amount of heat actually converted to braking power to the total heat provided is used to calculate this efficiency. Figure 2 depicts the fluctuation of BTE in accordance with brake mean effective pressure (BMEP).

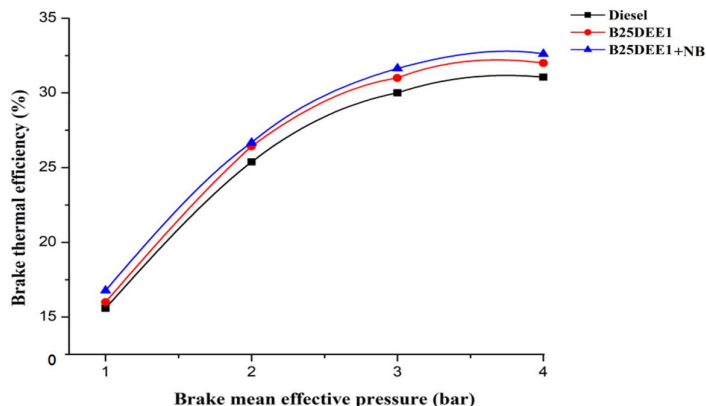


Figure 2 Brake thermal efficiency versus BMEP.

The BTE for the B25DEE1 test fuel blend was higher than diesel. The increased in-cylinder pressure and temperature at maximum BMEP can cause improved evaporation and mix with air [16]. The addition of DEE also improved and maintained the cetane number to the required extent, and it also improved the oxygen percentage. The BTE was improved further in the following stage by introducing n-butanol vapours with air intake into the cylinder. The test fuel B25DEE1 was mixed with n-butanol vapours in the combustion chamber, and this combustible mixture was named B25DEE1+NB. The improvement in BTE was due to n-butanol vapours. These vapours further improved the evaporation rate and brought the heating values and cetane number closer to diesel. The enhanced cetane number and oxygen percentage in n-butanol vapours and biodiesel blends resulted in improved ignition quality, resulting in a higher BTE. The BTE values for diesel, B25DEE1, and B25DEE1+NB were 31.05%, 32%, and 32.61%, respectively, at full load conditions or at maximum BMEP.

3.1.2 Brake specific fuel consumption

This parameter is used to calculate the amount of fuel used in the creation of unit brake power. It also denotes the ability to transfer the fuel's chemical energy into the required work energy. This parameter is influenced by fuel qualities such as oxygen percentage, density, viscosity, and heating values.

From the graph, it is noticeable that as BMEP increased, BSFC decreased. The BSFC for the blend B25DEE1 is slightly higher compared to the combustible mixture B25DEE+NB. The lower heating value of the B25DEE1 blend caused this effect. The reduced BSFC for the combustible mixture B25DEE1+NB was due to the introduction of n-butanol vapours. These n-butanol vapours further influenced the increase in oxygen availability, cetane index, and heating value of the combustible mixture. Figure 3 illustrates the variance of BSFC in relation to BMEP.

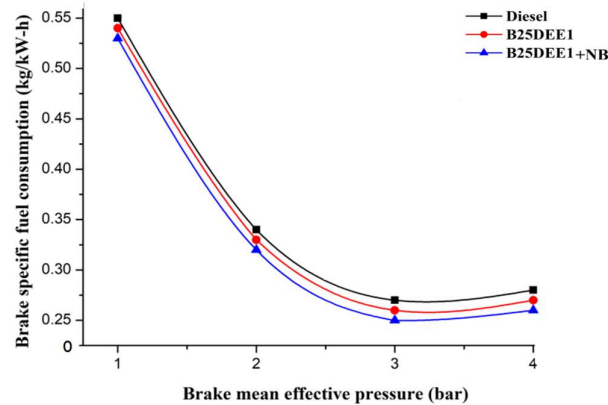


Figure 3 Brake specific fuel consumption versus BMEP.

The BSFC observed at peak BMEP conditions for diesel, B25DEE1, and B25DEE1+NB was 0.281 kg/kWh, 0.270 kg/kWh, and 0.261 kg/kWh, respectively. The saturated fatty acid content in biodiesel can also influence the cetane number, which is comparable to diesel. The cetane number increases with an increase in saturated fatty acids and an increase in chain length [17]. The PJME saturated fatty acid contents, like palmitic acid and stearic acid, consist of straight-line molecular structures, and their percentage was nearly 23% in PJME [18]. The increased density of the fuel blend is also causing it to inject earlier and providing increased mixing time and evaporation. It can lead to better combustion.

3.2 Emission assessment

3.2.1 Carbon monoxide analysis

The emission of CO indicates how effectively the combustion process occurred based on the type of fuel utilized. The unburned hydrocarbons influence the formation of this toxic emission. The type of the mixture, oxygen availability, and reaction rates are the influencing parameters for this emission. Figure 4 depicts CO emissions in relation to BMEP. Incomplete combustion, along with rich mixture and heterogeneous mixture combustion with a decreased oxygen percentage, can improve this emission [19]. CO emissions were found to be higher in diesel than in the test blends. Because the biodiesel, n-butanol, and fuel additives used here have a higher oxygen percentage and a lower carbon percentage on a mass basis than diesel. This emission is only slightly less compared to diesel because biodiesel contains increased levels of unsaturated fatty acids. This can lead to the presence of a double bond and influence poor oxidation. This condition can promote increased emissions of carbon monoxide and hydrocarbons [20]. The addition of DEE suppressed this condition to some extent. The addition of n-butanol vapours (B25DEE1+NB) further decreased this emission as it allowed for further improvement in flame propagation [21]. The improvement in flame propagation caused an improvement in reaction rate.

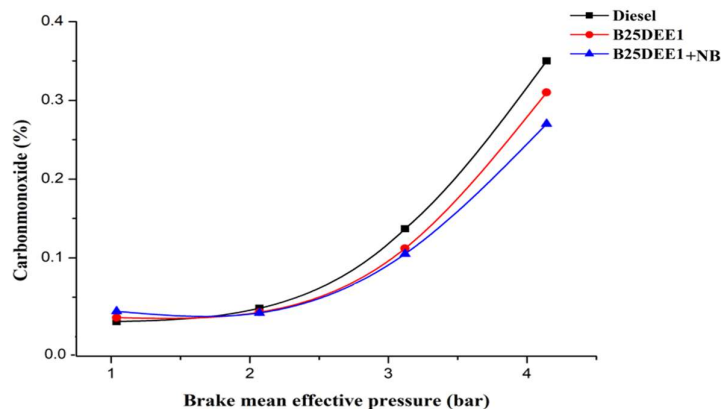


Figure 4 Carbon monoxide versus BMEP.

The CO emission at maximum BMEP conditions for diesel, B25DEE1, and B25DEE1+NB was observed at 0.35%, 0.32%, and 0.28%, respectively. The increased CO₂ results were obtained for both test fuels when compared to diesel. When the fuel decomposes at higher temperatures without enough oxygen, a large amount of carbon will be converted into CO instead of CO₂. The increased oxygen percentages in these fuels led to the conversion of a large quantity of CO into CO₂. The emissions of CO₂ for diesel, B25DEE1, and B25DEE1+NB were observed at 7.63%, 8.54%, and 8.9%, respectively.

3.2.2 Unburnt hydrocarbons analysis

The conditions influencing these emissions are the quality of combustion, fuel atomization, air-fuel mixture, and operating parameters. In Figure 5, the HC emission relative to BMEP is indicated.

The blend strength in the test fuel generally increases the kinematic viscosity and also requires a higher injection pressure. This condition is balanced by adding an ignition improver into the test blend. The increased presence of oxygen and cetane number in the DEE led to an improvement in the combustion process, which in turn decreased the HC emission. When comparing B25DEE1+NB to B25DEE1, there was no significant difference observed for this emission. The HC emissions were not decreased in a considerable manner after adding n-butanol vapours because the improvement in volatility led the air to be overly mixed with n-butanol vapours. This is considered one of the reasons for its ignorable reduction.

The emission of HC may increase if n-butanol is directly injected into the cylinder in liquid form because n-butanol requires a high latent heat of evaporation [22].

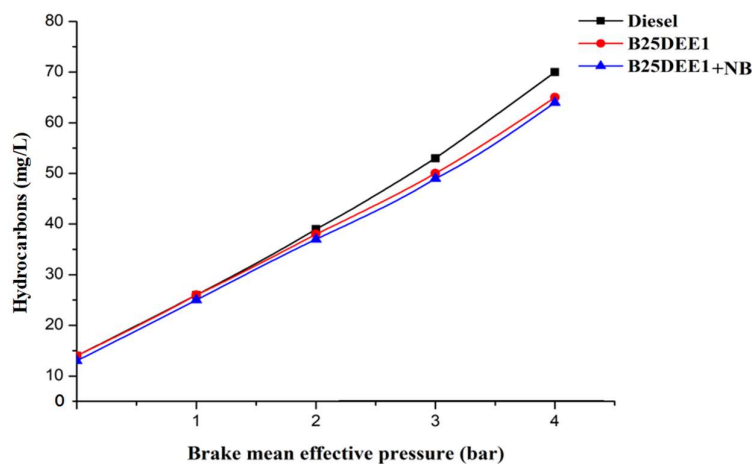


Figure 5 Hydrocarbon emission versus BMEP.

The emission of HC at peak load conditions, or at maximum BMEP for diesel, B25DEE1, and B25DEE1+NB, was observed at 71 mg/L, 65 mg/L, and 64 mg/L, respectively.

3.2.3 Nitrogen oxides analysis

This is the emission that will be produced at higher operating temperatures and the mixture's local stoichiometry. At the highest combustion temperatures and for the longest time at those temperatures, the diatomic nitrogen will be split into monatomic nitrogen. This monatomic nitrogen is highly reactive with oxygen and will produce emissions of NO and NO₂. With a lower heating value of the blends and a better cetane index, this emission can be reduced. For both the test blends, the addition of DEE has taken place since DEE is an ignition improver and, at higher concentrations, it can improve the high latent heat of vaporisation [23]. This condition can lower in-cylinder temperatures, which can reduce NO_x formation. The fluctuation of NO_x emission in relation to BMEP is indicated in Figure 6.

There was no considerable variation between both blends for this emission. These emissions were reduced in a considerable manner compared to diesel. Here, both blends consist of DEE percentages. For the combustible mixture B25DEE1+NB, n-butanol vapours absorbed the most latent heat, resulting in lower NO_x emissions. The emission of NO_x at peak load conditions, or at maximum BMEP for diesel, B25DEE1 and B25DEE1+NB, was observed at 1850 mg/L, 1759 mg/L, and 1752 mg/L, respectively.

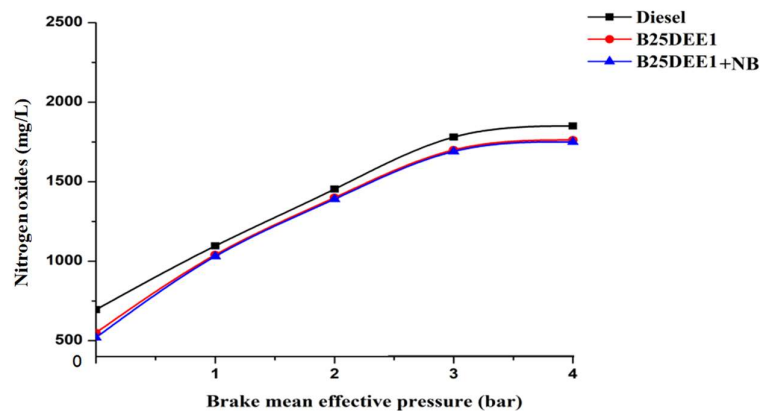


Figure 6 Nitrogen oxide emission versus BMEP.

3.2.4 Smoke opacity analysis

The emission of smoke increases with improper mixing of fuel with air. Figure 7 shows the amount of smoke produced by the test blends versus diesel. As the compression ratio was increased, smoke opacity was reduced for both test fuel blends in comparison to diesel. The introduction of n-butanol vapours and an ignition improver further improved the mixing process of air with test blends. This emission is also influenced by the hydrocarbon ratio and the effectiveness of combustion. As the hydrocarbon ratio is higher for n-butanol in comparison to diesel, it causes lower smoke emissions [24]. This is one of the reasons considered for B25DEE1+NB's reduced smoke emissions when compared to diesel. By encouraging premixed combustion prior to TDC, this emission can be controlled. The premixed combustion phase was improved by utilising n-butanol vapors. This reduction in smoke opacity was also due to higher oxygen percentages in both blends, which resulted in the maximum quantity of carbon to burn. The smoke emission at maximum BMEP for diesel, B25DEE1, and B25DEE1+NB was observed at 57.8%, 53%, and 51%, respectively.

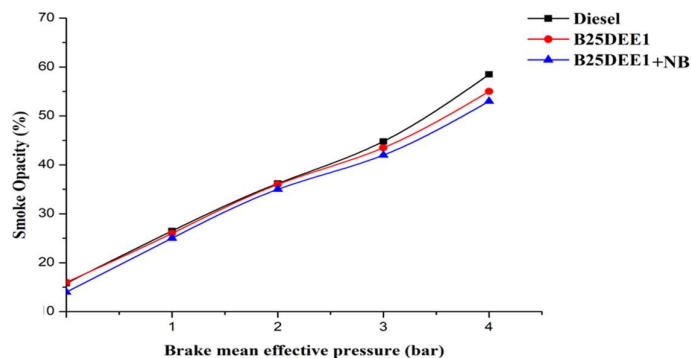


Figure 7 Smoke emission versus BMEP.

3.3 Combustion assessment

3.3.1 In-cylinder pressure analysis

The in-cylinder pressure or gas pressure is affected by the combustion characteristics of the test fuel, as well as the engine's operating parameters. The power output of the engine depends directly on in-cylinder pressure. The combustion phenomenon affects this pressure, which resulted from the fuel's early uncontrolled combustion period [24]. The pre-mixed combustion process occurred after a constant-volume endothermic process. It was also considered one of the causes of peak cylinder pressure with rapid combustion. The constant-pressure endothermic process was also considered diffusion combustion. The fluctuation of in-cylinder pressure with relation to crank angle at maximum BMEP is shown in Figure 8. For the test blends compared to diesel, the maximum in-cylinder pressures were marginally higher. The maximum cylinder pressure was observed for B25DEE1+NB, followed by B25DEE1 and diesel. Both blends had strong peak pressures soon after TDC, demonstrating that, unlike diesel, combustion did not deviate from its regular pattern.

The peak pressure obtained was the result of uncontrolled combustion, oxygen percentage in blends, and calorific value. The availability of oxygen in both DEE and biodiesel, as well as the heating value of biodiesel, which is closer to diesel, were considered impacting parameters for improved cylinder pressure in B25DEE1. The combustible mixture formation increased these pressures further after the addition of n-butanol vapors. The cylinder pressure reached its maximum when combustion began due to a large amount of fuel burned.

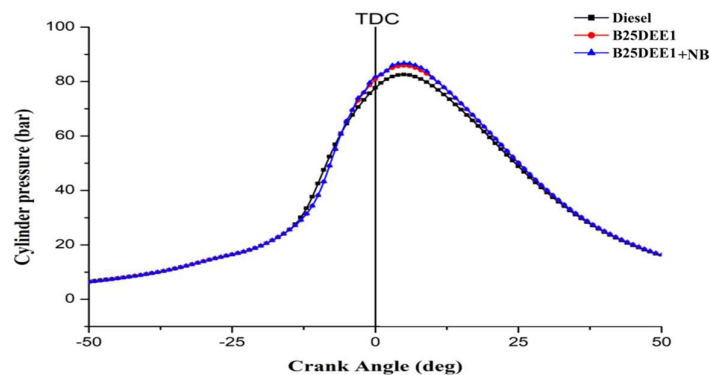


Figure 8 Cylinder pressure versus crank angle.

With more fuel being used during peak times, the working temperature and evaporation rates increased. They could also be a contributing factor to higher cylinder pressures in both test fuels. The peak pressure obtained was 80 bar when fueled with diesel and for B25DEE1, B25DEE1+NB it was 84.7 bar and 86.6 bar respectively.

3.3.2 Heat release rate analysis

A thorough investigation of the combustion methodology is possible with this evaluation of rate of heat release. The net heat release rate can be influenced by operating conditions as well as fuel characteristics. It results from the heat energy that the fuel's chemical energy releases, and it will be enhanced by the fuel-air mixture's rapid burning.

This rapid burning can cause maximum net heat release (NHR) because of the fuel accumulation during the ignition lag period. The variation of NHR in relation to the crank angle at maximum BMEP is shown in Figure 9. The elevated NHR was observed for B25DEE1 compared to diesel because of the accumulation of more fuel during the ignition delay period, which caused a rapid rate of combustion. One of the factors for ignition delay was the increased viscosity of the blend, which affects the physical delay period. The chemical lag period can be influenced by the percentage of oxygen present. The B25DEE1 blend's oxygen level caused it to produce the most NHR compared to diesel. The preheated air can also influence the physical delay period [25]. For the B25DEE1+NB combustible mixture, the NHR was further increased with increased oxygen availability. To some extent, the addition of DEE improved cetane number and evaporation rate. The premixed combustion can also utilise the maximum quantity of vaporised fuel at the end of the ignition delay period. The premixed combustion intensity depends upon the time available for the formation of the combustible air-fuel mixture. Due to this characteristic, both blends performed better than diesel in terms of maximum cylinder pressure and NHR. For all fuels close to 25° BTDC, negative NHR was discovered due to heat absorption during the fuel evaporation phase or the ignition delay phase. The maximum heat release rate (HRR) found for both blends at 6° BTDC. It was observed as 46.5 J/°CA and 49.12 J/°CA for B25DEE1 and B25DEE1+NB, respectively. The maximum HRR for diesel was found at 8° BTDC at 39.38 J/°CA.

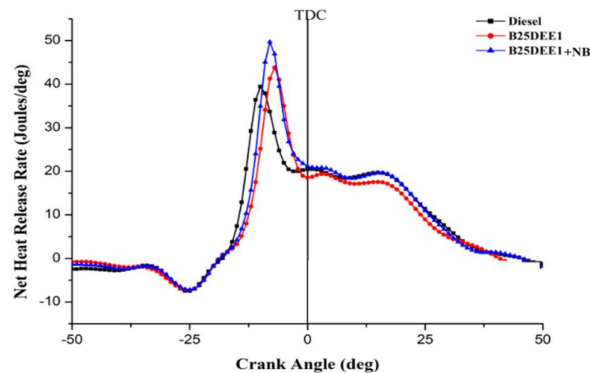


Figure 9 Net heat release rate versus crank angle.

3.3.3 Mass fraction of the fuel burned

The time interval between the initiation of the flame and uncontrolled combustion could be measured by utilising this parameter. This also shows the percentage of fuel consumed in relation to the total quantity of fuel supplied into the combustion chamber per cycle. This is also used to calculate the time between the commencement of the flame and the quick rate of combustion [26].

In comparison to diesel, there was no combustion delay in the early stages of premixed combustion for both test fuel blends. The operating temperatures increased as the n-butanol vapours were added. As a result, the B25DEE1+NB blend's volatility and flame speed became compatible with diesel. The mass fraction burnt (MFB) for both blends compared to diesel is shown in Figure 10. The mass percentage of fuel burned exactly like diesel for both blends at the same crank angle. The mass fraction of the fuel burned near TDC for diesel, B25DEE1, and B25DEE1+NB was 54%, 53.10%, and 53.62%, respectively.

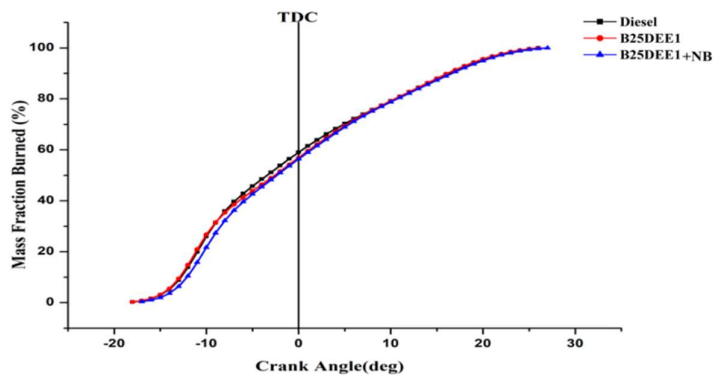


Figure 10 Mass fraction of fuel burned versus crank angle.

3.3.4 Cumulative heat release analysis

It provides information regarding the heat energy obtained by the chemical energy of the fuel. It also indicates the quality of the combustion. Figure 11 indicates the variation of the cumulative heat release rate with crank angle. From the start of the combustion process onward, the test blends followed the same pattern as a standard curve for diesel, but the blend B25DEE1+NB showed a higher cumulative heat release (CHR) when compared to diesel as the combustion process progressed. The rapid rate of combustion of this blend was due to the higher amount of oxygen in it [27]. The ignition delay period could also be regarded as a contributing factor to the rapid rate of combustion that influenced maximum CHR for test blends rather than diesel. The maximum CHR was observed at 0.92 kJ, 1.01 kJ, and 1.05 kJ for diesel, B25DEE1, and B25DEE1+NB, respectively.

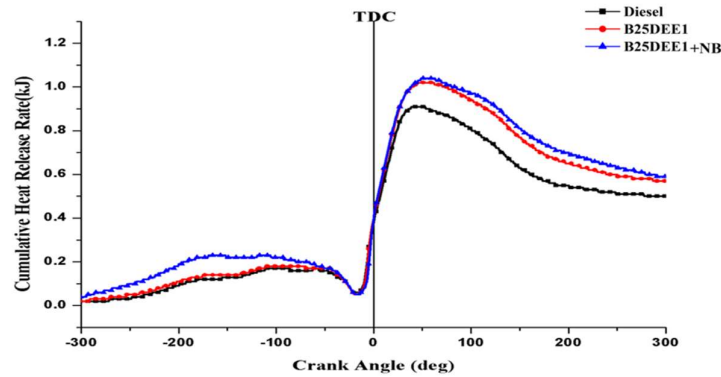


Figure 11 Cumulative heat release versus crank angle.

4. Conclusion

The experimental work for both test fuel blends has obtained the following statements when compared to diesel at maximum BMEP conditions. The higher BTEs were observed for both test blends because of increased oxygen percentages and an improved combustion strategy. The cetane index and oxygen contents were also increased to the required extent with the addition of DEE. The emissions of CO, HC, smoke, and NO_x for both test fuel blends were slightly reduced. The in-cylinder pressures were higher immediately after TDC, revealing that both test fuel blends had no unusual combustion behaviour in comparison to a diesel with a crank angle, and no unusual pressure rise was observed. Increased maximum cylinder pressures were observed for both test fuel blends. The combustion process was normal, and no considerable abnormalities were observed. Due to its minimal vaporisation pressures and quick burning process, the introduction of n-butanol vapours resulted in high peak pressures as compared to diesel. The NHR observed was higher for the test fuel blends compared to diesel. This study also comes to the conclusion that because both test fuel blends had higher viscosities than diesel, higher injection pressures were needed for them.

All of the preceding has demonstrated that n-butanol vapours, along with biodiesel and DEE, can be added to diesel in modest amounts to reduce conventional diesel fuel use and pollutants. Additionally, it enhances a premixed-charged compression ignition (PCCI's) combustion phenomenon for CI engines.

5. References

- [1] Kumar KS, Raj RTK. Effect of fuel injection timing and elevated intake air temperature on the combustion and emission characteristics of dual fuel operated diesel engine. *Procedia Eng.* 2013;64:1191-1198.
- [2] Krishnamoorthi M, Malayalamurthi R. Availability analysis, performance, combustion and emission behavior of bael oil - diesel - diethyl ether blends in a variable compression ratio diesel engine. *Renew Energy.* 2018;119:235-252.
- [3] Senthur PS, Asokan MA, Prathiba S, Ahmed S, Puthan G. Effect of additives on combustion, performance and emission behaviour of pre heated palm oil/diesel blends in DI diesel engine. *Renew Energy.* 2018;122:196-205.
- [4] Prakash T, Edvin GV, Leenus JM, Nagalingam B. Effect of ternary blends of bio ethanol, diesel and castor oil on performance, emission and combustion in a CI engine. *Renew Energy.* 2018;122:301-309.
- [5] Satyanarayana Murthy YVV. Performance of tobacco oil-based bio- diesel fuel in a single cylinder direct injection engine. *Int J Phys Sci.* 2010;5(13):2066-2074.
- [6] Tsutsumi Y, Iijima A, Yoshida K, Shoji H, Lee JT. Combustion characteristics during operation on DME and methane fuels. *Int J Automot Technol.* 2009;10(6):645-652.
- [7] Pugazhvadivu M, Sankaranarayanan G. Investigations on a diesel engine fuelled with biodiesel blends and diethyl ether as an additive. *Indian J Sci Technol.* 2009;2(5):31-35.
- [8] Huang H, Liu Q, Teng W, Pan M, Liu C, Wang Q. Improvement of combustion performance and emissions in diesel engines by fueling n-butanol/diesel/PODE3-4 mixtures. *Appl Energy.* 2018;227:38-48.
- [9] Ioannis K, Guohong T, Sai G. Combustion, performance and emission analysis of a DI diesel engine using plastic pyrolysis oil. *Fuel Process Technol.* 2017;157:108-115.
- [10] Byungchul C, Xiaolong J, Young KK, Gilsung J, Chunhwan L, Inchul C, Chi SS. Effect of diesel fuel blend with n-butanol on the emission of a turbocharged common rail direct injection diesel engine. *Appl Energy.* 2015;146:20-28.

- [11] Tamilselvan P, Nagarajan G. Combustion and emission characteristics of a diesel engine fuelled with biodiesel having varying palmitic acid, stearic acid and oleic acid in their fuel composition. *Int J Oil, Gas and Coal Technol.* 2014;8(3):353-368.
- [12] Sendzikiene E, Makareviciene V, Janulis P. Influence of fuel oxygen content on diesel engine exhaust emissions. *Renew Energy.* 2006;31(15):2505-2512.
- [13] Patnaik P, Abbasi T, Abbasi SA. *Prosopis (Prosopis juliflora): blessing and bane.* *Trop Ecol.* 2017;58(3):455-483.
- [14] Tamilselvan P, Goteti GS. Experimental analysis of VCR engine operated with prosopis juliflora biodiesel blends. *Int J Renew Energy Res.* 2020;10:978-987.
- [15] Goteti GS, Tamilselvan P. HCCI combustion in a diesel engine using oxygenated fuels and various operating parameters. *Int J Renew Energy Res.* 2017;7:1166-1173.
- [16] Savariraj S, Ganapathy T, Saravanan CG. Performance and emission characteristics of diesel engine using high-viscous vegetable oil. *Int J Ambient Energy.* 2012;33(4):193-203.
- [17] Mohebbi M, Reyhanian M, Hosseini V, Muhamad Said MF, Aziz AA. Performance and emissions of a reactivity controlled light-duty diesel engine fueled with n-butanol-diesel and gasoline. *Appl Therm Eng.* 2018;134:214-228.
- [18] Rajeshwaran M, Raja K, Marimuthu P, Duraimurugan MD. Biodiesel production and optimization from *Prosopis julifera* oil – a three step method. *Int J Adv Eng Technol.* 2016;6(2):214-224.
- [19] Tamilselvan P, Goteti GS. Performance, emission and combustion characteristics of VCR CRDI diesel engine fuelled with n-butanol blends. *Int J Automot Mech Eng.* 2019;16(3):6825-6843.
- [20] Tamilselvan P, Nagarajan G. Combustion and emission characteristics of a diesel engine fuelled with biodiesel having varying saturated fatty acid composition. *Int J Green Energy.* 2013;10:952-965.
- [21] Tamilselvan P, Nagarajan G, Sasikumar M. Performance and emission characteristics of a diesel engine using blends of biodiesel by varying saturated fatty acid compositions. *Int J Chemtech Res.* 2016;9(9):508-513.
- [22] Imtenan S, Masjuki HH, Varman M, Varman M, Sajjad H, Arbab MI. Effect of n-butanol and diethyl ether as oxygenated additives on combustion–emission–performance characteristics of a multiple cylinder diesel engine fuelled with diesel–jatropha biodiesel blend. *Energy Convers Manag.* 2015;94:84-94.
- [23] Subbarayan MR, Senthil Kumaar JS. A study of performance and emissions of direct injection diesel engine fuelled with cotton seed oil methyl ester and pumpkin seed oil methyl ester and its blends with diesel using exhaust gas recirculation. *Biofuels.* 2015;6:171-177.
- [24] Zehra Ş, Orhan D, Orhan NA. Experimental investigation of n-butanol/diesel fuel blends and n-butanol fumigation-evaluation of engine performance, exhaust emissions, heat release and flammability analysis. *Energy Convers Manag.* 2015;103:778-789.
- [25] Bang-Quan H, Xu C, Chang LL, Hua Z. Combustion characteristics of a gasoline engine with independent intake port injection and direct injection systems for n-butanol and gasoline. *Energy Convers Manag.* 2016;124:556-565.
- [26] Rajesh Kumar B, Saravanan S, Rana D, Nagendran A. A comparative analysis on combustion and emissions of some next generation higher-alcohol/diesel blends in a direct-injection diesel engine. *Energy Convers Manag.* 2016;119:246-256.
- [27] Ahmed IE, Ookawara S. Performance, combustion, and emission characteristics of a diesel engine fueled with Jatropha methyl ester and graphene oxide additives. *Energy Convers Manag.* 2018;166:674-686.



Contents lists available at ScienceDirect

Materials Today: Proceedings

journal homepage: www.elsevier.com/locate/matpr

Effect of fly ash and alccofine as cementitious materials on M40 grade concrete

Arunchaitanya Sambangi ^{a,*}, Nagarjuna Kundeti ^a, Sai Charan S. ^b, Reshma Srimani S. ^c, Abhilash Nadukuditi ^d

^a Department of Civil Engineering, Seshadri Rao Gudlavalluru Engineering College, Gudlavalluru 521356, Andhra Pradesh, India

^b Department of Civil Engineering, Sir C R Reddy College of Engineering, Eluru 534007, Andhra Pradesh, India

^c Department of Civil Engineering, Ramachandra College of Engineering, Eluru 534007, Andhra Pradesh, India

^d Department of Civil Engineering, Andhra Loyola Institute of Engineering and Technology, Vijayawada 520008, Andhra Pradesh, India

ARTICLE INFO

Article history:

Available online xxxx

Keywords:

Fly ash

Alccofine

Compressive strength

Split tensile strength

Flexural strength

ABSTRACT

Concrete is the most widely utilized building material in civil engineering projects of all kinds. Concrete is more attractive than other construction materials due to its strength properties. Cement, which accounts for about 5% of worldwide CO₂ emissions, is a key component of concrete. To make concrete more environmentally friendly, appropriate replacements will be added to the cement. The present study deals with fly ash and alccofine as supplementary cementitious materials for the M40 grade of concrete. The cement is replaced with 5%, 10%, 15% and 20% fly ash by weight of cement and fly ash is optimized. The fly ash optimized cement concrete is further replaced with 5%, 10%, 15% and 20% alccofine by weight of fly ash in cement to form a ternary concrete. The strength properties are studied on total 10 mixes, mechanical properties such as compressive, flexural and split tensile strengths were determined. At optimum level of fly ash the strength exhibited 55.22 MPa. The maximum compressive strength of 62.74 MPa was obtained for the mix with 15% fly ash and 15% alccofine at 28 days. Split tensile and flexural strengths were also followed the similar trend. Alccofine and fly ash combination can be a sustainable building material.

Copyright © 2024 Elsevier Ltd. All rights reserved.

Selection and peer-review under responsibility of the scientific committee of the International Conference on Advances in Construction Materials and Structures.

1. Introduction

Concrete is the most adaptable building material since it can be constructed to endure the roughest surroundings while still taking on the most creative shapes. With the help of innovative chemical admixtures and supplemental cementitious materials (SCM's), engineers are always pushing the boundaries to increase their performance [1,2]. Most concrete mixtures now include supplemental cementitious material as a cementitious component. The majority of these materials are byproducts of other processes. SCM's key advantages are its capacity to replace a specific proportion of cement while still retaining its cementitious properties, lowering the cost using portland cement. Fly ash, silica fume, powdered granulated blast furnace slag, steel slag, alccofine and other byproducts or industrial waste materials that can be used as SCM's have accumulated as a result of rapid industrialization [3,4]. These

byproducts not only help to recycle waste materials, but they also improve the qualities of concrete in both fresh and hydrated forms. India's rapidly expanding manufacturing sector has produced a wide range of hazardous wastes that have given rise to environmental concerns. That's why these industrial leftovers have to find their way into civil engineering projects. A byproduct of the cement industry, Alccofine is an ultra-fine supplementary cementitious concrete material made from slag. The particle size distribution is one of a kind due to the granulation process being tightly regulated. The finer particles it contains more than cement, fly ash, rice husk ash, etc. boost its hydraulic property, pozzolanic reactivity, and packing density of paste component [5–9]. Two commercial forms of alccofine exist, 1101 and 1203, respectively. In contrast to the latter, the former alccofine is a good source of calcium silicate. Its specific surface area is greater than 12,000 cm²/g, and its specific gravity is between 2.8 and 2.9 [10,11]. Alccofine's beneficial impacts on the concrete's long-term sustainability and the surrounding environment have made it a popular mineral addition. Among their many important contributions to concrete, poz-

* Corresponding author.

E-mail address: arunchaitanya0@gmail.com (A. Sambangi).

<https://doi.org/10.1016/j.matpr.2023.03.192>

2214-7853/Copyright © 2024 Elsevier Ltd. All rights reserved.

Selection and peer-review under responsibility of the scientific committee of the International Conference on Advances in Construction Materials and Structures.

zolans alter the interfacial transition zone (ITZ) and reduce porosity through a process called pozzolanic reaction [12,13]. The mechanical characteristics of concrete, especially when subjected to harsh conditions, can be improved with the help of extra cementitious pozzolans, which are used to strengthen the material [14,15]. The particle size and granulation of alccofine (AL), a recent ultra-fine complementary cementitious material, are very small. Compared to the effects of other admixtures like fly ash (FA) and rice husk ash, this substance has had the greatest positive impact on concrete characteristics and performance [16]. The increased specific surface area of ultrafine-grained particles in AL has a profound effect on enhancing all aspects of metal and concrete characteristics in both their fresh and hardened states. AL is a byproduct of the steel and iron industries and is composed primarily of slag and glass [17,18]. S.C.Boobalan et al. [19] study reviews Alccofine-based High Performance Concrete strength qualities. Alccofine was added to High Performance Concrete in varied quantities. Alccofine materials accelerate concrete strength and durability. Alccofine 1203 is a microfine mineral ingredient for concrete and mortars that minimises water demand and hydration heat, improving concrete strength and durability over time. Alccofine-based High Performance Concrete research. Alccofine's low calcium silicate compound increases concrete pH to protect against corrosion, speeds shuttering removal, improves pumpability, durability, and permeability. B.L.N. Sai Srinath et al. [20] summarises numerous studies on alccofine's use as an SCM in concrete. Alccofine as SCM improves concrete's fresh, mechanical, and durability. At all ages, cement-alccofine increased mechanical and durability. S. Prakash Chandar et al. [21] concretes mechanical properties were tested at different times, MK and AL's ideal partial cement replacement was 10% in the range of 0%, 5%, 10%, and 15%. Metakaolin (MK) and AL at 10% replacement have higher compressive strengths than conventional concrete of the same ratio. Microstructural research on concrete showed how pores and C-S-H (calcium-silicate hydrate) gel form in early and late hydration. This study found that partial cement substitution can minimise CO₂ emissions and preserve its properties. B. Harish et al. [22] Concrete of different grades (M30 to M70) was partially replaced with alccofine at 0, 5%, 10%, 15%, and 20% to reduce hydration heat and create a durable concrete. Alccofine-admixed concrete was compressed, split tensile, and flexed. To improve workability, chemical admixtures were utilised in concretes above M50 grade with a W/B ratio of 0.28–0.35.

1.1. Objective of the study

The main purpose of this project is to investigate the effects of partial cement replacement with fly ash and alccofine in concrete under various curing conditions. An experiment was conducted to see if fly ash and alccofine might be used to partially replace cement. The concrete grade of M40 and the curing times of 7 and 28 days of the concrete specimens were among the criteria taken into account in this investigation.

The cement is replaced by 5%, 10%, 15% and 20% fly ash by weight, and the fly ash is tuned. To make ternary concrete, the optimal fly ash concrete is further replaced by 5%, 10%, 15% and 20% alccofine by weight of fly ash in cement. The strength characteristics of ternary concrete for M40 grade are currently being investigated.

2. Materials

The cement used for this study was OPC 53 grade as per IS 12269. It has a relative density of 3.12 and other physical and chemical compositions are tabulated in Table 1. Commercially

available low calcium alccofine was procured and used in this investigation. The properties of the alccofine were with fineness 12000 cm²/gm, relative density of 2.88 which is lower than the cement. Fly ash was collected from the locally available RMC plant, the physical and chemical properties were presented in Table 2. River sand was used as fine aggregate and crushed stone as coarse aggregate. The detailed mix compositions were tabulated in Table 3.

3. Test methods

To assess the mechanical properties of M40 grade concrete, the following methods were adopted.

3.1. Unconfined compression test

150 × 150 × 150mm cubes tested against compression. Cubes were cast and tested under AMIL 2000kN compression testing machine as per IS 516. At the ages of 7 days and 28 days nine different mixes were cured under normal tap water. After removing specimens from curing, these cubes were tested.

The compressive strength has been calculated by the formula, Compressive strength = applied load/cross sectional area

3.2. Split tensile strength

Split tensile strength of M40 grade concrete with fly ash and alccofine, specimens of size 150 mm dia and 300 mm length was cast in the laboratory. Specimens were cured at 7 days and 28 days, later tested under CTM as per IS 5816.

The split tensile strength has been calculated by the formula, Split tensile strength = $2P/\pi LD$

where, P = compressive load on the cylinder

L = length of the cylinder
D = diameter

3.3. Flexural strength

Beams specimens of 100x100x500mm size were tested to assess the flexural strength of M40 grade concrete with fly ash and alccofine. Three specimens for each mix were cast to determine the flexural strength as per IS 516.

The modulus of rupture is denoted by "f_{cr}".

$$f_{cr} = PL/bd$$

where, P = load on the beam

L = length of the beam
b = width of the beam
d = depth of the beam

4. Results and discussions

4.1. Unconfined compressive strength

150x150x150mm cubes were tested against compressive strength and the detailed results were depicted in Fig. 1 and Fig. 2. The study was conducted in two phases. In the first phase, fly ash(FA) reduced the 7 day strength from 31.82Mpa to 26.42 MPa. It was observed that due to the increase of FA in cement showed a markable loss of strength in early ages. However, 28 days compressive strength gets increased with the rise of FA content in

Table 1

Chemical composition of Cement, Fly Ash and Alccofine.

Composition%	SiO ₂	Al ₂ O ₃	CaO	Fe ₂ O ₃	MgO	SO ₃	K ₂ O	L.O.I
Cement	18.08	3.49	62.64	3.61	0.6	1.64	0.71	2.29
Fly Ash	65.04	14.77	1.35	2.74	0.33	-	0.86	1.98
Alccofine	31.23	20.62	31.15	8.36	6.9	0.4	-	1.21

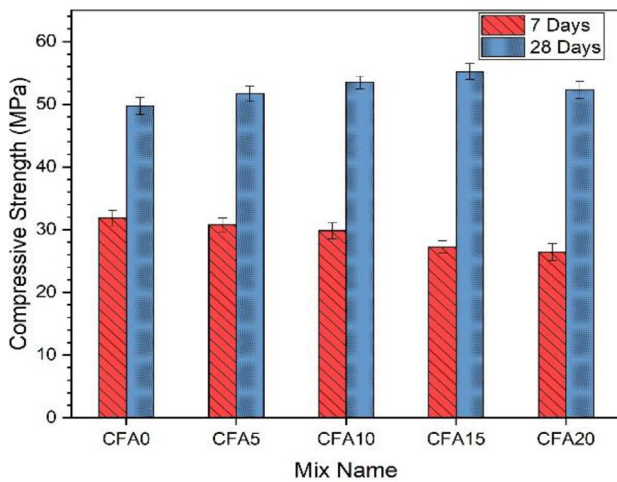
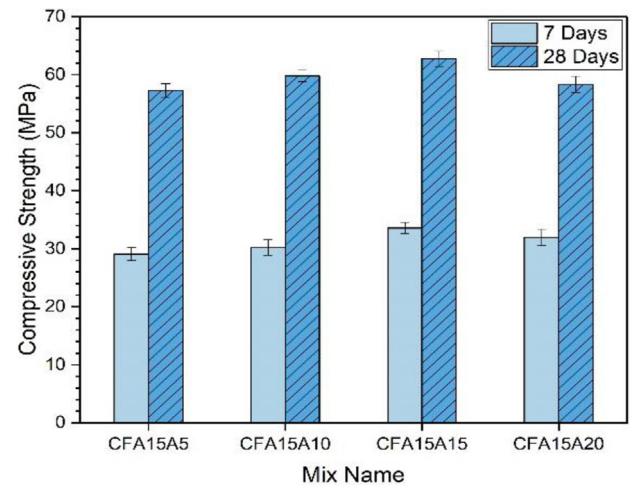
Table 2

Physical properties of materials used in the study.

Properties	Cement	Fly Ash	Alccofine	Fine Aggregate	Coarse Aggregate
Relative Density	3.13	2.34	2.88	2.68	2.8
Water Absorption	-	-	-	1.1%	0.5%

Table 3Mix composition in kg/m³.

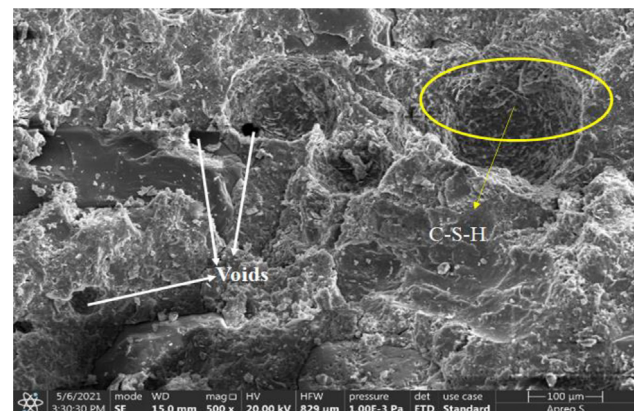
Mix	Cement	Fly Ash	Alccofine	Fine Aggregate	Coarse Aggregate	Water
CFA0	425	-	-	755	1182	150
CFA5	403.75	21.25	-	755	1182	150
CFA10	382.5	42.5	-	755	1182	150
CFA15	361.25	63.75	-	755	1182	150
CFA20	340	85	-	755	1182	150
CFA15A5	358.06	63.75	3.19	755	1182	150
CFA15A10	354.87	63.75	6.38	755	1182	150
CFA15A15	351.68	63.75	9.56	755	1182	150
CFA15A20	348.49	63.75	12.75	755	1182	150

**Fig. 1.** Compressive strength of FA mixes.**Fig. 2.** Compressive strength of alccofine mixes.

the cement. Which was about 6 MPa from the conventional mix. The formations of ettringite and secondary C-S-H gels were reasons for the enhancement of the strength.

On the other hand, alccofine enhanced the strength of concrete even at early ages than the conventional mix. This was due to the reaction of fine particles available in the alccofine. In the same scenario, the 28 days unconfined compressive strength showed the similar results. At 7 days, with 5% has 29.09 MPa, 10% has 30.21 MPa, 15% has 33.56 MPa and 20% has 31.95 MPa. The maximum resistance against the gradually applied load is 62.74 MPa which was obtained at 15% FA and 15% alccofine. This enhancement of compressive strength may be due to the reaction of fine alccofine particles [1].

SEM images of the mixes were presented in Fig. 3, Fig. 4 and Fig. 5, which are conducted on samples collected from cubes after conducting compressive strength. Fig. 3 represented the control

**Fig. 3.** SEM image of CFA0.

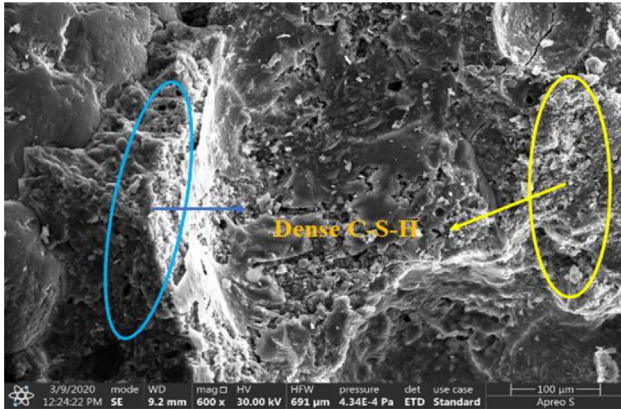


Fig. 4. SEM image of CFA15.

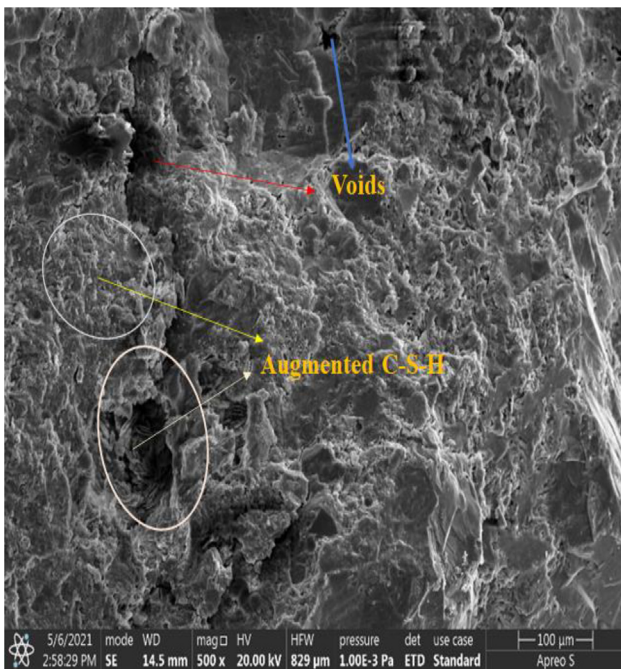


Fig. 5. SEM image of CFA15A15.

mix (CFA0), the microstructure of the conventional concrete contains voids and C-S-H. However, with the fly ash as well as alccofine enhanced the strength properties by the development of dense C-S-H as shown in Fig. 4. Similarly, augmented C-S-H was observed in the concrete matrix. Hence, these are due to the formation of secondary calcium silicate hydrate gel by the pozzolanic action.

4.2. Split tensile strength

The results obtained from the experimental investigation on split tensile strength were similar to the compressive strength. FA affected the early split tensile strength at 7 days in a negative manner. By the increase of FA in cement, it reduced the availability of C_3S in cement which is responsible for the early age strengths. Later at 28 days the available portlandite reacted with silica to form a dense calcium silicate hydrate in concrete matrix. The ultimate strength was attained at 15% FA in cement (i.e., 3.73 MPa) presented in Fig. 6.

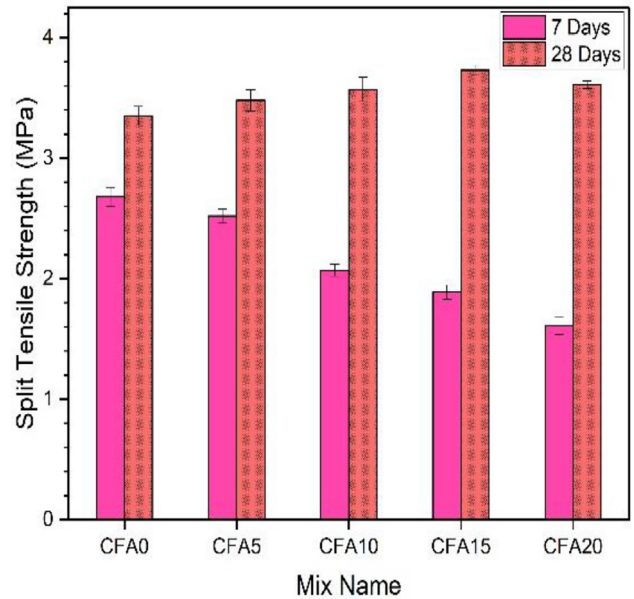


Fig. 6. Split tensile strength of FA mix.

Alccofine in cement as FA replacement enhanced the split tensile strength at 7 days as well as 28 days. The maximum strength attained for CFA15A15 mix at both the ages i.e., 3.11 MPa and 4.27 MPa. Alccofine at 5%, 10%, 15% and 20% achieved 3.95 MPa, 4.07 MPa, 4.27 MPa and 4.13 MPa respectively shown in Fig. 7.

4.3. Flexural strength

The flexural strength of M40 concrete with FA as secondary cementitious material degraded from 3.97 MPa to 2.86 MPa at 7 days. The maximum flexural strength obtained for the conventional mix at the early age of concrete. By the further replacement of FA obtained the least flexural strength. Nonetheless, 28 days showed better results with the FA in concrete matrix. The enhanced strengths were from 4.98 MPa to 5.51 MPa shown in

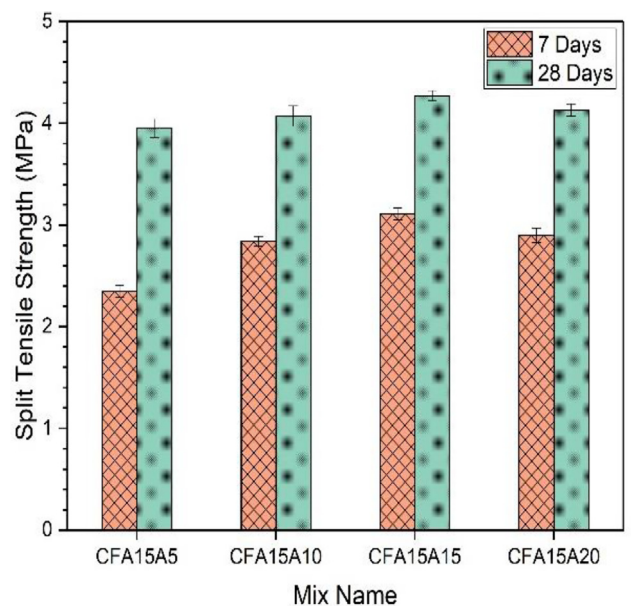


Fig. 7. Split tensile strength of alccofine mix.

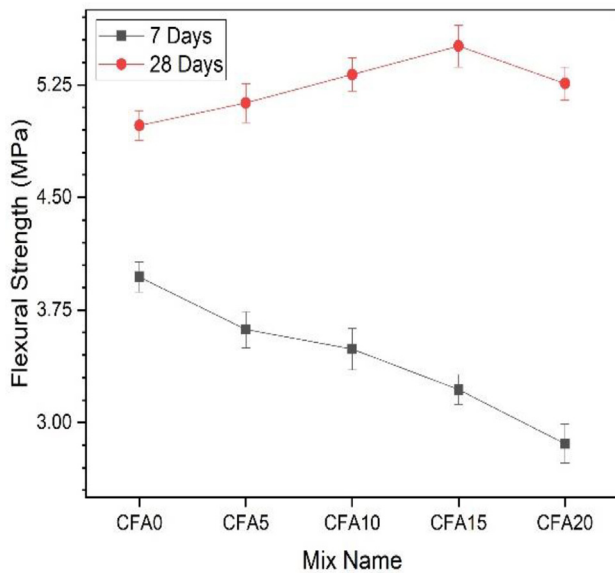


Fig. 8. Flexural strength of FA mix.

Fig. 8. From the results it was concluded that optimum dosage of FA as 15% depicted in Fig. 8.

With the optimum FA content in the cement, alccofine showed favorable results at both the ages were obtained. The lowest average particle sizes of the alccofine gets hydrated easier than the FA particles. The ultimate strengths were attained for CFA15A15 mix i.e., 5.94 MPa shown in Fig. 9.

5. Conclusions

- When cement was replaced by 15% of fly ash and 15% of alccofine gives high compressive strength of 62.74 N/mm². It was observed that the increase in compressive strength was 20.7% when compared with the nominal mix. Further replacement of alccofine leads to decrease in compressive strength.

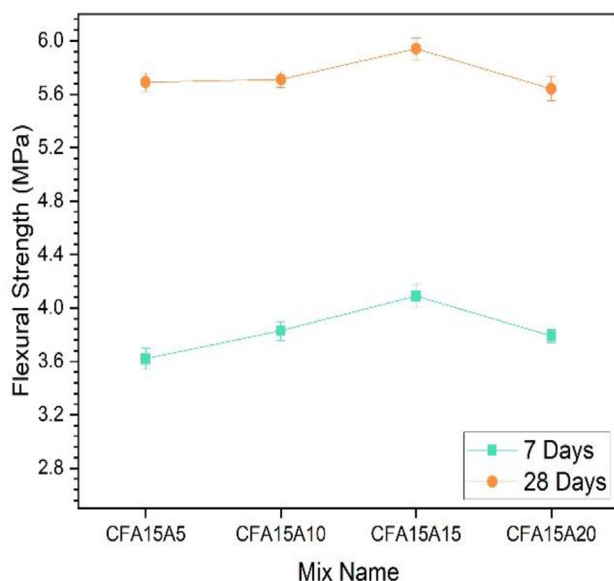


Fig. 9. Flexural strength of alccofine mix.

- It was observed that split tensile strength was increased by 21.54% when the concrete mix containing 15% fly ash and 15% alccofine as a replacement of cement, when compared with the nominal mix. Beyond 15% replacement of alccofine leads to a decrease in the split tensile strength.
- The flexural strength was increased by 16.16% when the concrete mix containing 15% fly ash and 15% alccofine as a replacement of cement, when compared with the nominal mix. At later replacements the flexural strength of the concrete has been decreased.

Authors Contribution

Mr. Sambangi Arunchaitanya contributed to the conceptualization, investigated the research and supervised the project. Mr. Nagarjuna K and Mr. Sai Charan S validated the results, Mrs Reshma S contributed on writing- original draft and Mr. Abhilash N contributed writing- review & editing. All authors read and approved the final manuscript.

Data availability

No data was used for the research described in the article.

Declaration of Competing Interest

The authors declare that they have no known competing financial interests or personal relationships that could have appeared to influence the work reported in this paper.

Acknowledgment

No funding is available for this study.

References

- B.V. Kavyateja, J. Guru Jawahar, C. Sashidhar, Effectiveness of alccofine and fly ash on mechanical properties of ternary blended self compacting concrete, Mater. Today Proc. 33 (2020) 73–79, <https://doi.org/10.1016/j.matpr.2020.03.152>.
- B. Venkatesan, M. Venuga, P.R. Dhevasenaa, V. Kannan, Experimental study on concrete using partial replacement of cement by Alccofine fine aggregate as iron powder, Mater. Today Proc. 37 (2021) 2183–2188, <https://doi.org/10.1016/j.matpr.2020.07.648>.
- A. Narender Reddy, T. Meena, A study on compressive behavior of ternary blended concrete incorporating alccofine, Mater. Today Proc. 5 (5) (2018) 11356–11363, <https://doi.org/10.1016/j.matpr.2018.02.102>.
- D. Parveen, M.T. Singhal, B.B. Junaid, A. Jindal, Mehta, Mehta, Mechanical and microstructural properties of fly ash based geopolymer concrete incorporating alccofine at ambient curing, Constr. Build. Mater. 180 (2018) 298–307, <https://doi.org/10.1016/j.conbuildmat.2018.05.286>.
- B.B. Jindal, B.B. Jindal, D. Singhal, S.K. Sharma, Parveen, Suitability of ambientcured alccofine added low-calcium fly ash-based geopolymer concrete, Indian, J. Sci. Technol. 10 (2017) 1–10, <https://doi.org/10.17485/ijst/2017/v10i12/110428>.
- A. Mohan, K.M. Mini, Strength and durability studies of SCC incorporating silica fume and ultra fine GGBS, Constr. Build. Mater. 171 (2018) 919–928, <https://doi.org/10.1016/j.conbuildmat.2018.03.186>.
- S. Kavitha, T. Felix Kala, Evaluation of strength behavior of self-compacting concrete using alccofine and GGBS as partial replacement of cement, Indian, J. Sci. Technol. 9 (2016) 1–5, <https://doi.org/10.17485/ijst/2016/v9i22/93276>.
- B.V. Kavyateja, J.G. Jawahar, C. Sashidhara, Durability performance of self compacting concrete incorporating alccofine and fly ash, Int. J. Eng. Trans. B Appl. 33 (2020) 1522–1528, <https://doi.org/10.5829/ije.2020.33.08b.10>.
- R.R. Kundanati, T. Malpani, V. Sairam, Study on Mechanical Properties of Mortar using Alccofine and Graphene Oxide, in: Mater. Today Proc., Elsevier Ltd, 2019, pp. 2431–2438. <https://doi.org/10.1016/j.matpr.2020.03.369>.
- A. Saloni, V. Singh, Sandhu, Jatni, Parveen, Effects of alccofine and curing conditions on properties of low calcium fly ash-based geopolymer concrete, Mater. Today Proc. 32 (2020) 620–625, <https://doi.org/10.1016/j.matpr.2020.02.763>.
- G.G.K. Reddy, P. Ramadoss, Influence of alccofine incorporation on the mechanical behavior of ultra-high performance concrete (UHPC), Mater. Today Proc. 33 (2020) 789–797, <https://doi.org/10.1016/j.matpr.2020.06.180>.

- [12] J. de Brito, R. Kurda, The past and future of sustainable concrete: a critical review and new strategies on cement-based materials, *J. Clean. Prod.* 281 (2021), <https://doi.org/10.1016/j.jclepro.2020.123558>.
- [13] R. Ramkrishnan, B. Abilash, M. Trivedi, P. Varsha, P. Varun, S. Vishanth, Effect of mineral admixtures on pervious concrete, *Mater. Today Proc.* 5 (11) (2018) 24014–24023, <https://doi.org/10.1016/j.matpr.2018.10.194>.
- [14] G.G.K. Reddy, P. Ramadoss, Performance evaluation of ultra-high performance concrete designed with alccofine, *Innov. Infrastruct. Solut.* 6 (2021) 1–11, <https://doi.org/10.1007/s41062-020-00375-y>.
- [15] K. Thangapandi, R. Anuradha, P.O. Awoyera, R. Gobinath, N. Archana, M. Berlin, O.B. Oladimeji, Durability phenomenon in manufactured sand concrete: effects of zinc oxide and alccofine on behaviour, *SILICON* 13 (4) (2021) 1079–1085, <https://doi.org/10.1007/s12633-020-00494-2>.
- [16] P.N. Reddy, B.B. Jindal, B.V. Kavyateja, A. Narender Reddy, Strength enhancement of concrete incorporating alccofine and SNF based admixture, *Adv. Concr. Constr.* 9 (2020) 345–354, <https://doi.org/10.12989/acc.2020.9.4.345>.
- [17] B. Sagar, M.V.N. Sivakumar, An experimental and analytical study on alccofine based high strength concrete, *Int. J. Eng. Trans. A Basics* 33 (2020) 530–538, <https://doi.org/10.5829/IJE.2020.33.04A.03>.
- [18] P. Narasimha Reddy, B.V. Kavyateja, Durability performance of high strength concrete incorporating supplementary cementitious materials, *Mater. Today Proc.* 33 (2020) 66–72, <https://doi.org/10.1016/j.matpr.2020.03.149>.
- [19] S.C. Boobalan, V. Aswin Srivatsav, A. Mohamed Thanseer Nisath, A. Pratheesh Babu, V. Gayathri, A comprehensive review on strength properties for making Alccofine based high performance concrete, *Mater. Today: Proc.* (2021), <https://doi.org/10.1016/j.matpr.2021.01.278>.
- [20] B.L.N. Sai Srinath Chandan, Kumar Patnaikuni, K.V.G.D. Balaji, B. Santhosh Kumar, M. Manjunatha, A prospective review of alccofine as supplementary cementitious material, *Mater. Today: Proc.* (2021), <https://doi.org/10.1016/j.matpr.2021.03.719>.
- [21] S. Prakash Chandar, R. Santhosh, Mechanical properties and microstructural analysis of metakaolin and alccofine in M40 grade concrete, *Mater. Today Proc.*, (2022), <https://doi.org/10.1016/j.matpr.2022.06.100>.
- [22] N.R. Bhotla Harish, M.S. Dakshinamurthy, K. Jagannadha Rao, A study on mechanical properties of high strength concrete with alccofine as partial replacement of cement, *Mater. Today: Proc.* (2021), <https://doi.org/10.1016/j.matpr.2021.11.037>.



Effect of Covid-19 Pandemic on Foreign Direct Investment: Indian Perspective

Subba Rayudu Thunga^{1*} and Lavanya P B²

¹Associate Professor, Andhra Loyola Institute of Engineering and Technology, Vijayawada, Andhra Pradesh, India,

²Assistant Professor, Andhra Loyola Institute of Engineering and Technology, Vijayawada, Andhra Pradesh, India

Received: 01 June 2022

Revised: 20 June 2022

Accepted: 23 July 2022

*Address for Correspondence

Subba Rayudu Thunga

Associate Professor,

Andhra Loyola Institute of Engineering and Technology,

Vijayawada, Andhra Pradesh, India,

Email: rayudu.thunga@gmail.com,



This is an Open Access Journal / article distributed under the terms of the **Creative Commons Attribution License** (CC BY-NC-ND 3.0) which permits unrestricted use, distribution, and reproduction in any medium, provided the original work is properly cited. All rights reserved.

ABSTRACT

Capital inflows are the most important source of investment for developing economies like India and acts as an engine for fostering economic growth. But the world economy has been witnessing a great difficulty for the last two years due to Covid pandemic. This has impacted the investment pattern across the business environment. The pandemic has created great uncertainty on investments. World foreign direct investment inflows fell by half up to second quarter of 2020 and the measures taken by governments could not encourage investments at global level. Investors' preference also changed because of pandemic from investments in primary and manufacturing sectors to other desirable sectors. Keeping in view the above objective the key aim of this research is to get out the outcome of Covid epidemic on foreign direct investment flows from different countries to India using yearly data for the time period 2018 to 2022. The study is based on secondary sources. Data were analyzed using parametric test. The results shows foreign direct investments differ significantly between the countries and sectors. However it does not differ significantly between the years. The study limits to foreign direct investment flows from few countries to select sectors. The findings will be valuable to the policy makers for attracting more funds into the desirable sectors for fostering economic development.

Keywords: Covid-19 pandemic, Crisis, Foreign Direct Investment (FDI), Lockdown, Priority sectors.





INTRODUCTION

Investments are the key for economic development (Liesbeth et al., 2008) and human progress (Torabi, 2015), due to that it is an important to increase the wealth of nation as well as individuals. Among the many investments, FDI has a crucial Impact on the fiscal development of a country, as a form to attract funds to develop and progress the nation and the quality of human capital (Simionescu & Naros, 2019). FDI is an investment made by investor or company of one country in another in various forms. It facilitates in advancement of a nation in terms of technology, human potential and enhances economic growth (Alfarro, 2017). FDI can also signify an input for inclusive growth in specific sectors (Cicea et al., 2019). Increase of GDP and Quality of human life is a yardstick for the development of a country (Botha et al., 2020). During 1990s Foreign Direct Investments was proved to be the most significant source of investment for developing countries. (Mahmoodi & Mahmoodi, 2016). The positive consequence of investment in FDI is that it has less volatile to economic cycle. It is a boost for the emerging economies like India for its economic growth. This paper is going to examine the effect of covid-19 pandemic on foreign direct investment with Indian perspective.

Literature review

Internationalization is a driving force integrating economies across the globe (Velde, 2005) and develops economies (Iqbal et al., 2012). It has significant impact of capital movement among various nations (Hill & McKaig, 2015). Host countries derive many benefits with the inflows from foreign nations (Büthe & Milner, 2008). Technical, Skill, managerial gaps of nations, people and business can be bridged with FDIs (Masron et al., 2012). FDI creates job opportunities, helps in fostering GDP, infrastructure, competition and enhance productivity of the host nations (Edrak et al., 2014). Similar outcomes were found in the study of Yucel (2014) and Yildirim and Tosuner (2014). Foreign Direct investment in any country is influenced by multiple factors. Political Environment is one of the important factors of FDI flows Büthe and Milner (2008). Governments of emerging economies are making efforts to encourage overseas inflows by liberalized policies (Masron et al., 2012). Study of Wang and Wong (2011), proved that various incentives such as tax and financial assistance to MNCs attracts more potential foreign inflows. Many studies pointed out the negative consequences of FDIs on host countries. Investors and business entities are pulling out the profits from host to home countries (Hill & McKaig, 2015). Emerging economies are facing the trouble of over dependence on foreign inflows and irregular inflows and investment low priority and less- tech industries creating pressure on domestic firms Chen et al. (2010). The negative consequences lead to restricted entry of FDIs by those nations.

Objectives of the study

The purpose of present research is to know the conceptual framework of foreign direct investment and examine the effect of covid-19 epidemic on foreign direct investment flows from different countries to India for the time period 2018 to 2022.

Research hypothesis

H₀₁ = Foreign Direct Investment do not differ significantly between the years

H₀₂ = Foreign Direct Investment do not differ significantly between the countries

H₀₃ = Foreign Direct Investment do not differ significantly between the sectors

Methodology of the study

Sources for data collection

The data has been gathered from secondary sources which include annual reports of Reserve Bank of India, journals, magazines.





Techniques for data analysis

Information collected from different sources was examined with statistical technique of analysis of variance without replication

Analysis and Discussion

Figure 1 depicts that growth rate of inflows to Indian economy from other countries during the study period recorded positive growth except Mauritius and Germany. Switzerland recorded highest growth rate followed by US, Cayman Island, UK, Canada, Netherlands and Singapore. Figure 2 exhibits growth rate of inflows in various sectors to India. Analysis revealed that all the selected sectors showed a positive growth rate between 2018 to 2022 except for communication services and Electricity & other energy generation sectors. Education and R & D has highest inflow potential followed by mining, computer services, manufacturing, hospitality, transport, retail & wholesale, construction and financial services.

Inference

Since the value of F is 1.11 which is less than 2.92 therefore, we accept the null hypothesis concluding that overseas investments not differ between the years. The value of F 23.28 is more than 2.16 therefore; we reject the null hypothesis concluding that overseas investments differ between the countries

Inference

Since the value of F = 0.52 is less than 2.92 hence, we accept null hypothesis concluding that overseas investment not differ between the years. The value of F 4.72 is more than 2.16 therefore; we reject null hypothesis concluding that overseas investments differ between the sectors.

CONCLUSION

The study has found that there are significant differences between countries and sectors regarding foreign direct investment flows to India. Additionally, foreign direct investment flows do not differ significantly between the years. The present study is not free from limitations. Firstly, the study has been conducted based on secondary data. Secondly, the study covers a period of five years i.e. 2018 to 2022. Thirdly, the study has considered foreign direct investment flows of 11 countries. The limitations of this study can provide a scope for further qualitative study in the field of foreign direct investment from many countries; further studies can also continue the effect of government policy initiatives in specific sectors and its impact on foreign direct investment. The study concluded that foreign inflows are not sufficient for fostering economies like India. Especially more investment support is required in priority sectors such as manufacturing, energy, hospitality and other priority and growing sectors for fostering economic growth. Therefore, this study has a significant contribution to the government and policy makers to attract more funds in to the desirable sectors.

REFERENCES

1. Abdouli, M., & Hammami, S. (2017). Investigating the causality links between environmental quality, foreign direct investment and economic growth in MENA countries. *International Business Review*, 26(2), 264–278.
2. Azman Saini, W. N. W., Baharumshah, A. Z., & Law, S. H. (2010). Foreign direct investment, economic freedom and economic growth: International evidence. *Economic Modelling*, 27(5), 1079–1089.
3. Amar Iqbal Anwar & Mazhar Mughal, 2012. "Economic Freedom and Indian Outward Foreign Direct Investment: An Empirical Analysis," *Economics Bulletin*, AccessEcon, vol. 32(4), pages 2991-3007.
4. Botha, I., Botezatu, M. A., & Coanca, M. (2020). Innovative calculation model for evaluating regional sustainable development. *Economic Computation and Economic Cybernetics Studies and Research*, 54(3), 5–24.



**Subba Rayudu Thunga and Lavanya**

5. Büthe, T., & Milner, H. V. (2008). The Politics of Foreign Direct Investment into Developing Countries: Increasing FDI through International Trade Agreements? *American Journal of Political Science*, 52, 741-762.
6. Bakhsh, K., Rose, S., Ali, M. F., Ahmad, N., & Shahbaz, M. (2017). Economic growth, CO2 emissions, renewable waste and FDI relation in Pakistan: New evidences from 3SLS. *Journal of Environmental Management*, 196, 627–632. <https://doi.org/10.1016/j.jenvman.2017.03.029>
7. Billas, V. (2020). FDI and economic growth in EU13 countries: Co integration and causality tests. *Journal of Competitiveness*, 12(3), 47–63.
8. Chen, C.-M., Melachroinos, K., & Chang, K.-T. (2010). FDI and Local Economic Development: The Case of Taiwanese Investment in Kunshan. *European Planning Studies*, 18, 213-238.
9. Carbonell, J. B., & Werner, R. A. (2018). Does foreign direct investment generate economic growth? A new empirical approach applied to Spain. *Economic Geography*, 94(4), 425–456. <https://doi.org/10.1080/00130095.2017.1393312>
10. Chaudhary, N. (2018). Foreign direct investment and economic growth in India. *Pacific Business Review International*, 10(12), 113–118.
11. Cicea, C., & Marinescu, C. (2021). Bibliometric analysis of foreign direct investment and economic growth relationship. A research agenda. *Journal of Business Economics and Management*, 22(2), 445-446.
12. De Andrade, A. G., & Quing, Y. (2015). The role of foreign direct investment on economic growth. In *Proceedings of the 12th International Conference on Innovation and Management* (pp. 1110–1114).
13. Dinh TT-H, Vo DH, The Vo A, Nguyen TC (2019). Foreign Direct Investment and Economic Growth in the Short Run and Long Run: Empirical Evidence from Developing Countries. *Journal of Risk and Financial Management*. 2019; 12(4):176. <https://doi.org/10.3390/jrfm12040176>
14. Edrak, B. B., Gharleghi, B., Fah, B. C. Y., & Tan, M. (2014). Critical Success Factors Affecting Malaysia' SMEs through Inward FDI: Case of Service Sector. *Asian Social Science*, 10, 131-138
15. Furková, A. (2012). Does foreign direct investment affect economic growth? Evidence from OECD countries. In *Proceedings of the International Conference Quantitative Methods in Economics. Multiple criteria decision making XVI* (pp. 56–61).
16. Ghasem Torabi (2015, May 1). Foreign Direct Investment and Human Development: The Law and Economics of International Investment Agreements. *Journal of Human development and capabilities*, 15(2), 316-317.
17. Hill, C., & McKaig, T. (2015). *Global Business Today* (4th Canadian ed.). Toronto: McGraw-Hill Ryerson.
18. Hagan, E., & Amoah, A. (2020). Foreign direct investment and economic growth nexus in Africa New evidence from the new financial fragility measure. *African Journal of Economic and Management Studies*, 11(1), 1–17.
19. Hakimi, A., & Hamdi, H. (2016). Trade liberalization, FDI inflows, environmental quality and economic growth: A comparative analysis between Tunisia and Morocco. *Renewable and Sustainable Energy Reviews*, 58, 1445–1456.
20. Hlavacek, P., & Bal Domanska, B. (2016). Impact of foreign direct investment on economic growth in Central and Eastern European countries. *Inzinerine Ekonomika-Engineering Economics*, 27(3), 294–303.
21. Hussain, M. E., & Haque, M. (2016). Foreign direct investment, trade, and economic growth: An empirical analysis of Bangladesh. *Economies*, 4(2).
22. Iamsiraroj, S. (2016). The foreign direct investment-economic growth nexus. *International Review of Economics & Finance*, 42, 116–133.
23. Khamphengvong, V., Xia, E., & Srithilat, K. (2017, July). The relationship among FDI, trade openness and economic growth: Empirical evidence from Lao PDR. In *4th International Conference on Industrial Economics System and Industrial Security Engineering (IEIS)* (pp. 1–6). Kyoto, Japan.
24. Kondyan, S., & Yenokyan, K. (2019). The effect of foreign direct investment on economic growth. *Eastern Economic Journal*, 45(4), 532–564.
25. Laura Alfaro (2017, March). Gains from Foreign Direct Investment: Macro and Micro Approaches. *The World Bank economic review*, 30(1), S2-S15.
26. Liesbeth Colen, Miet Maertens and Jo Swinnen LICOS (2008, September). Foreign direct investment as an engine for economic growth and human development: a review of the arguments and empirical evidence. LICOS Centre for Institutions and Economic Performance, Working Paper No. 16 - September 2008 Prepared for the IAP P6/06 Project, Working Package FDI-1.





Subba Rayudu Thunga and Lavanya

27. Maria-Simona Naroş (2019, June). Foreign Direct Investment and Human Capital Formation. Journal of Intercultural Management, 11(2), 163-178.
28. Majid Mahmoodi & Elahe Mahmoodi (2016, February). Foreign direct investment, exports and economic growth: evidence from two panels of developing countries. Economic Research-Ekonomska Istraživanja 29(1), 938-949.
29. Tajul Ariffin Masron, Zulkornain Yusop (2012, November). The ASEAN investment area, other FDI initiatives, and intra-ASEAN foreign direct investment. Asian Pacific Economic Literature, 26(2), 88-103.
30. Velde, D. W. (2005). Globalisation and Education: What Do the Trade, Investment and Migration Literatures Tell Us? London: Overseas Development Institute.
31. Vijayalakshmi, R., Palanisingham, V., Lingavel, G., & Gurumoorthy, T. R. (2019). Factors determining in foreign direct investment (FDI) in India. International Journal of Recent Technology and Engineering, 8(2), 722–729.
32. Yildirim, D. C., & Tosuner, O. (2014). The Effects of FDI on Human Capital Stock in Central Asian Turkic Republics. Eurasian Journal of Business and Economics, 7, 51-60.
33. Yucel, G. E. (2014). FDI and Economic Growth: The Case of Baltic Countries. Research in World Economy, 5, 115-134.
34. Yulek, M., & Gur, N. (2017). Foreign direct investment, smart policies and economic growth. Progress in Development Studies, 17(3), 245–256.
35. <https://www.rbi.org.in/Scripts/AnnualReportPublications.aspx?year=2022>
36. <https://www.cescube.com/vp-fdi-in-india-during-covid-19-pandemic>
37. <https://www.scirp.org/journal/paperinformation.aspx?paperid=108158>
38. <https://essaypro.com/blog/research-paper-format>

Table 1- Country-wise Foreign Direct Investment flows to India (pre and post Covid) (US\$ billions)

Year	Singapore	US	Mauritius	Netherlands	Switzerland	Cayman Islands	UK	Japan	UAE	Germany	Canada
2017-18	12.2	2.1	15.9	2.8	0.5	1.2	0.8	1.6	1	1.1	0.3
2018-19	16.2	3.1	8.1	3.9	0.3	1	1.4	3	0.9	0.9	0.6
2019-20	14.7	4.1	8.2	6.5	0.2	3.7	1.3	3.2	0.3	0.5	0.2
2020-21	17.4	13.8	5.6	2.8	0.2	2.8	2	1.9	4.2	0.7	0
2021-22	15.9	10.5	9.4	4.6	4.3	3.8	1.6	1.5	1	0.7	0.5
Average	15.28	6.72	9.44	4.12	1.1	2.5	1.4	2.24	1.5	0.78	0.32
Growth rate	30.33	400	-40.88	64.29	760	216.67	100	6.25	0	-36.36	66.67

Source: RBI

Table 2- Sector-wise Foreign Direct Investment flows to India (US\$ billions)

Year	Manufacturing	Computer services	Communication Services	Retail & Wholesale trade	Financial services	Education, R&D	Transport	Construction	Hospitality	Mining	Electricity & other energy generation
2017-18	9	3.4	9.1	4.6	4.6	0.4	2.5	2.8	0.5	0.1	2.8
2018-19	9.6	3.7	6.5	4.9	7.2	0.9	1.2	2.3	0.8	0.3	2.6
2019-20	9.6	5.1	7.8	5.1	5.7	0.8	2.4	2	2.7	0.3	2.8
2020-21	9.3	23.8	2.9	3.9	3.5	1.3	7.9	1.8	0.3	0.2	1.3
2021-22	16.3	9	6.4	5.1	4.7	3.6	3.3	3.2	0.7	0.4	2.2
Average	10.76	9	6.54	4.72	5.14	1.4	3.46	2.42	1	0.26	2.34
Growth rate	81.11	164.71	-29.67	21.63	2.17	800	32	14.29	40	300	-21.43

Source: RBI





Subba Rayudu Thunga and Lavanya

Table: 3- Country-wise Foreign Direct Investment flows to India

	Sum of squares	Df	Mean square	F	Critical value
Between years	12.737	3	4.24568	1.114250267	2.92
Between countries	887.357	10	88.7357	23.28807514	2.16
Error	114.31	30	3.81035		
Total	1014.4	43			

Table: 3- Sector-wise Foreign Direct Investment flows to India

	Sum of squares	Df	Mean square	F	Critical value
Between years	17.24091	3	5.74697	0.52171	2.92
Between sectors	519.9364	10	51.99364	4.719985	2.16
Error	330.4691	30	11.01564		
Total	867.6464	43			

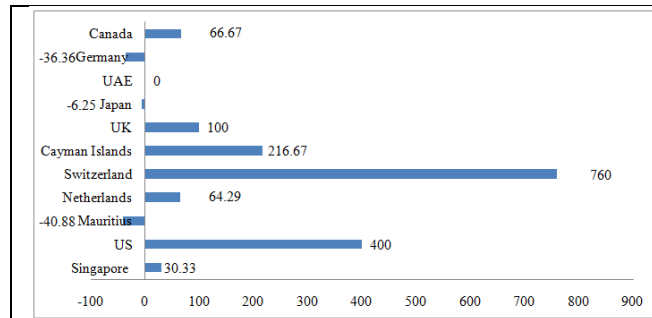


Figure: 1-Country-wise Growth rate of FDIs from 2017-18 to 2021-22

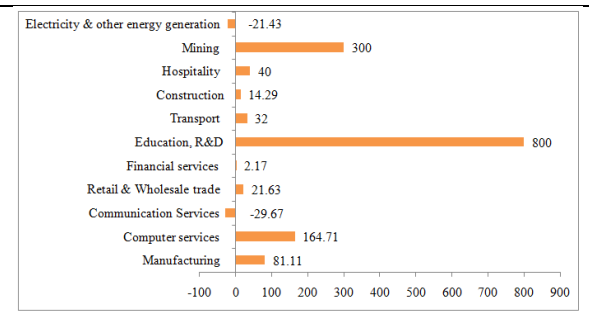


Figure: 2-Industry-wise Growth rate of FDIs from 2017-18 to 2021-22

